



HAL
open science

The Production and Characterisation of High Purity Ozone and Experimental and Modelling Studies of Anomalous Oxygen Isotope Effects in the Formation of Carbon Dioxide from Irradiated Mixtures of Carbon Monoxide and Ozone or Oxygen

Daniela Simone

► **To cite this version:**

Daniela Simone. The Production and Characterisation of High Purity Ozone and Experimental and Modelling Studies of Anomalous Oxygen Isotope Effects in the Formation of Carbon Dioxide from Irradiated Mixtures of Carbon Monoxide and Ozone or Oxygen. Other [cond-mat.other]. Université Pierre et Marie Curie - Paris VI, 2014. English. NNT : 2014PA066091 . tel-01023002

HAL Id: tel-01023002

<https://theses.hal.science/tel-01023002>

Submitted on 11 Jul 2014

HAL is a multi-disciplinary open access archive for the deposit and dissemination of scientific research documents, whether they are published or not. The documents may come from teaching and research institutions in France or abroad, or from public or private research centers.

L'archive ouverte pluridisciplinaire **HAL**, est destinée au dépôt et à la diffusion de documents scientifiques de niveau recherche, publiés ou non, émanant des établissements d'enseignement et de recherche français ou étrangers, des laboratoires publics ou privés.

**THÈSE DE DOCTORAT
DE L'UNIVERSITÉ PIERRE ET MARIE CURIE**

Spécialité : Physique

École doctorale : « La physique, de la particule à la matière condensée »

réalisée au

**Laboratoire d'Etudes du Rayonnement et de la Matière
en Astrophysique et Atmosphère (LERMA2)**

présentée par

Daniela SIMONE

pour obtenir le grade de :

DOCTEUR DE L'UNIVERSITÉ PIERRE ET MARIE CURIE

Sujet de la thèse :

**The Production and Characterisation of High Purity Ozone
and Experimental and Modelling Studies of Anomalous
Oxygen Isotope Effects in the Formation of Carbon Dioxide
from Irradiated Mixtures of Carbon Monoxide And Ozone or
Oxygen.**

soutenue le 25 Juin 2014

devant le jury composé de :

M ^{me}	Amaëlle Landais	Rapporteur
M ^{me}	Maud Rotger	Rapporteur
M.	Thomas Röckmann	Examineur
M.	Lahouari Krim	Président
M.	Matthew S. Johnson	Co-Directeur de thèse
M.	Christof Janssen	Directeur de thèse

Abstract

The ozone formation reaction $\text{O} + \text{O}_2 + \text{M} \rightarrow \text{O}_3 + \text{M}$ is a unique example of a chemical reaction that leads to an anomalous isotopic composition of the products, most likely due to symmetry - breaking effects in the reaction. So far, results on other chemical systems that might show similar effects are spurious, even though such claims concerning reactions other than the formation of ozone have been made repeatedly. This applies in particular to the spin forbidden $\text{O} + \text{CO} + \text{M} \rightarrow \text{CO}_2 + \text{M}$ reaction, where two studies report a mass-independent fractionation of about 8%. Nevertheless, the presence of ozone in these experiments raises questions as to the validity of this assertion. We thus make a new attempt to study the $\text{O} + \text{CO} + \text{M}$ reaction in the photoreactor at CCAR (University of Copenhagen) where reagents and contaminants are monitored on-line by FTIR. This study combined with the analysis of the spectral distribution of the employed lamps and isotope kinetic modeling lead to a complete re-interpretation of previous experiments. We conclude that available measurements are more compatible with the hypothesis that no mass-independent isotope anomaly takes place in the $\text{O} + \text{CO}$ reaction. We propose that all observations can be completely explained by an isotope transfer from ozone, involving photolytic production of $\text{O}(^1\text{D})$ that in turn leads to OH radicals, which then rapidly form CO_2 from reaction with CO.

We also present a method to produce pure ozone samples and derive an upper limit on nitrogen oxide contaminations based on mass spectrometer measurements. These values will serve as benchmark values for future studies of ozone absorption cross sections in the IR and UV.

***Key words:* ozone, isotopic fractionation, isotope anomaly, mass spectroscopy, FTIR, photolysis, carbon monoxide, kinetic modeling.**

Résumé

La réaction de formation de l'ozone $O + O_2 + M \rightarrow O_3 + M$ est un exemple unique de réaction chimique qui mène à une composition isotopique anormale des produits, probablement due à une brisure de symétrie. L'existence d'autres réactions chimiques présentant des effets isotopiques similaires est encore controversée malgré des études affirmant que de telles réactions existent. Ainsi, deux études sur la réaction $O + CO + M \rightarrow CO_2 + M$ indiquent un fractionnement indépendant de la masse de 8% environ. Néanmoins, la présence de l'ozone dans ces expériences soulève des questions en ce qui concerne la validité des résultats. Nous avons donc étudié à nouveau la réaction $O + CO + M$ dans le photoréacteur installé au CCAR (Université de Copenhague) où les réactifs et les contaminants sont surveillés par spectroscopie FTIR. Cette étude combinée avec l'analyse de la distribution spectrale des lampes utilisées et la modélisation cinétique des isotopes mènent à une réinterprétation complète des expériences précédentes. Nous concluons que les mesures disponibles sont plus compatibles avec l'hypothèse qu'aucune anomalie isotopique indépendante de la masse n'a lieu dans la réaction $O + CO$ et que toutes les observations peuvent être complètement expliquées par un transfert isotopique à partir de l'ozone.

Nous présentons également une méthode pour produire des échantillons d'ozone à haute pureté et déterminer une limite supérieure des contaminations par les oxydes d'azote basée sur des mesures par spectrométrie de masse. Ces valeurs pourront être utilisées comme référence pour de futures études sur les sections efficaces d'absorption de l'ozone dans l'IR et l'UV.

Mots clés : ozone, fractionnement isotopique, anomalie isotopique, spectroscopie de masse, FTIR, photolyse, monoxyde de carbone, modélisation cinétique.

Contents

1	Mass Independent Fractionation and Ozone Atmospheric Chemistry	1
1.1	Properties of ozone	1
1.1.1	Physico-chemical properties of ozone	2
1.2	Ozone in atmospheric chemistry	2
1.2.1	The layers of Earth's atmosphere	2
1.2.2	Ozone chemistry in the atmosphere	4
1.3	O(¹ D) in the atmosphere	7
1.4	Atmospheric Ozone and the Climate System	8
1.5	Ozone hole	8
1.6	Cycles of tropospheric pollutants	9
1.7	Isotope terminology	11
1.8	Isotope dependence of the zero point energy	14
1.9	Origins of mass-dependent isotopic fractionation	15
1.9.1	Isotope fractionation in the thermodynamic equilibrium	16
1.9.2	Isotope fractionation in irreversible processes	16
1.9.3	Isotopic fractionation factors	17
1.10	Mass independent fractionation	18
1.10.1	Isotope anomaly from self shielding	21
1.10.2	Magnetic Isotope Effect	21
1.11	Ozone isotopic anomaly	22
1.11.1	Atmospheric measurements	22
1.11.2	Laboratory measurements	23
1.12	Theory of MIF in ozone	26
1.13	MIF in other relevant atmospheric compounds	27
1.13.1	Study of MIF in O + CO reaction	29
1.14	The PhD project and structure of the manuscript	30
2	Generation of pure ozone samples	33
2.1	Ozone generation by electric discharge	33
2.2	Experimental setup	34
2.3	Ozone decomposition in pressure sensors	34
2.4	Mass spectrometer	36
2.5	Experimental procedure	40
2.6	Impurities in ozone samples	42
2.6.1	General considerations	42
2.6.2	Evaluation of individual nitrogen containing impurities	42
2.6.3	Quantitative estimate of the sum of nitrogen containing contaminants	45
2.7	Short chapter summary and outlook	47

3	Analysis of previous studies on O + CO	49
3.1	The experiment of Bhattacharya and Thiemens (1989)	49
3.2	The experiment of Pandey and Bhattacharya (2006)	54
3.3	Motivation for further investigation on O + CO	57
4	Relative rate study of O + CO	59
4.1	Relative rate method	59
4.2	Smog chambers	60
4.3	The Copenhagen photoreactor	62
4.4	Experimental procedure	62
4.5	Chamber chemistry	65
4.6	Data analysis and semi quantitative interpretation	66
4.7	OH tracer experiments	70
4.8	Short chapter summary and outlook	71
5	O(³P) and O(¹D) production from O₃ photolysis	73
5.1	Wavelength dependence of O(¹ D) production from O ₃ photolysis	73
5.2	Branching ratio between O(¹ D) and O(³ P) production	78
5.2.1	Experimental setup	78
5.2.2	Lamp spectra	79
5.2.3	Spectral Emission of Halogen Tungsten lamps	81
5.2.4	Spectral Emission of LED lamps	85
5.3	Summary and Discussion of Obtained Branching Ratios	88
5.4	Short Chapter Summary	89
6	Isotope Kinetic Modeling	91
6.1	Software Tools	91
6.1.1	The Kinetic Preprocessor – KPP	91
6.1.2	Mathematica	92
6.2	Oxygen Isotope Models	92
6.2.1	General Remarks	92
6.2.2	Definitions and terminology in chemical kinetics	92
6.2.3	Isotope abundances	95
6.3	Accuracy and Biases	97
6.4	Modeling of experiments	102
6.4.1	Modeling of experiment at CCAR	102
6.4.2	Modeling of the experiment of Pandey and Bhattacharya	105
6.4.3	Ground state oxygen chemistry	105
6.4.4	Full modeling including excited state and isotope chemistry	108
6.5	Short chapter summary	113
7	Summary and Conclusion	115
A	Spectroscopy and FTIR	119
A.1	Basics of molecular spectroscopy and FTIR	119
A.1.1	Spectroscopy	119
A.1.2	Fourier Transform Infrared Spectroscopy (FTIR)	124
B	Statistical Models on Ozone Photolysis	129
B.1	Full statistical model	129
B.2	Statistical model restricted to singly substituted species	134

<i>CONTENTS</i>	iii
C Reaction Schemes for the CCAR Experiments	137
D Reaction Schemes for the PB06 Experiments	139
Bibliography	146

Chapter 1

Mass Independent Isotope Fractionation (MIF) and Ozone Atmospheric Chemistry

This chapter gives a short review of ozone atmospheric chemistry, the role of oxygen isotopes and the ozone isotope anomaly that manifests as a mass independent fractionation effect.

1.1 Properties of ozone

Ozone, also called trioxygen according to IUPAC nomenclature is the triatomic, and rarer, allotrope of the chemical element oxygen and it is therefore denoted by the chemical formula O_3 . Its discovery is generally attributed to the german chemist Christian Friedrich Schönbein (1799-1869) who performed extended studies of electric discharges in oxygen and identified it as the first ever observed allotrope of a chemical element. He also proposed the name "ozone" which comes from the ancient greek word "ὄζων" (to smell), and relates to the strong and characteristic odor that was produced in these experiments. [1]. However, it seems that the Dutch chemist Martin van Marum has effectively produced and observed ozone during his electrolysis experiments much earlier in 1789 [2]. At that time, however, the smell was still attributed to the general phenomenon of electricity and the electrically excited oxygen was not deemed a chemically different species.

Despite of its low abundance as a trace gas, ozone is an important constituent of the terrestrial atmosphere and plays a fundamental role for the existence of life on Earth. It naturally occurs in the stratosphere ($\sim 90\%$) where absorbs the harmful solar ultraviolet radiation, whereas its presence at the ground level in the troposphere ($\sim 10\%$) is noxious for life and extremely pollutant due to its strong oxidation capacity. Nowadays, levels of 30-40 ppb¹ of ozone have been recorded in the remote troposphere [4], even if the concentration is steadily increasing and could reach a value of 70 ppb by the year of 2100 [5]. According to OSHA (Occupational Safety and Health Administration) (<https://www.osha.gov>), the exposure level for a human being has a threshold level of 0.2 ppm for no more than 2 hours.

¹1 ppb or parts per billion, 1×10^{-9} , 1 ppm or parts per million, 1×10^{-6} are units commonly used to indicate mixing ratio of atmospheric gases which is defined as the ratio of the amount of substance considered in a given volume to the amount of all constituent of air in that volume. In the SI system they are expressed respectively as nmol/mol and $\mu\text{mol/mol}$ [3].

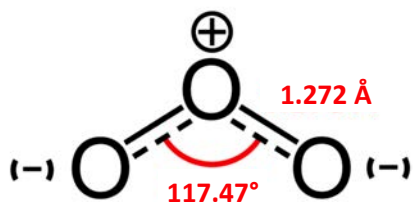


Figure 1.1: Chemical structure of ozone molecule.

Interatomic distance	1.272Å
Bond angle	117.47°
Molar mass	48 g · mol ⁻¹
Dipole moment	0.53373 D
Dissociation energy (298 K)	106.6 kJ · mol ⁻¹

Table 1.1: Some physical-chemical properties of ozone [6].

1.1.1 Physico-chemical properties of ozone

Spectroscopic investigations have revealed a non-cyclic triatomic structure of the ozone molecule. The oxygen atoms are situated at the corners of a bent, open triangle with a bond angle of 117.47° and an interatomic distance of 1.272 Å [6] as schematically represented in figure 1.1. Its main physico-chemical properties are summarised in table 1.1. At room temperature, ozone appears as a pale blue gas. At 161 K (boiling point) it condenses into a dark blue liquid and it solidifies at 80 K (melting point) in violet - black color. Due to its chemical structure, which can be regarded as a hybrid resonance characterized by one single and one double bond, ozone is extremely unstable with a dissociation energy of 106.6 kJ · mol⁻¹ [6]. It can easily decompose to form molecular oxygen. The process of decomposition is exothermic and may lead to explosion if ozone is present in high concentration. The breaking of the bond and the consequent presence of an isolated oxygen atom makes ozone highly reactive and oxidant. It can therefore cause substantial damage to vegetables and crops and can harm human and animal tissues of respiratory system. This compound can also substantially damage materials such as metals, plastics and rubbers. This can impact negatively on economy.

Nevertheless if used with care and in low concentration, the use of ozone has many industrial applications and it is employed for removing contaminations, sterilization, improving water quality, food protection and the storage of fruits and vegetables.

1.2 Ozone in atmospheric chemistry

1.2.1 The layers of Earth's atmosphere

The terrestrial atmosphere can be divided into several layers, which becomes evident from the temperature distribution shown in figure 1.2. Starting from the ground level, the lowest layer is the troposphere which extends to about typically 8 km in polar latitudes and 18 km at the equator. With about 90 % of the total mass of the atmosphere, practically all of the weather phenomena occur in the troposphere, where the temperature continuously decreases with altitude since the Earth's surface is warmed by solar radiation and the energy is distributed upwards into the troposphere through a mixing of the air. Above the troposphere, a layer of dynamically stable stratification is situated: the stratosphere. It is characterized by the positive temperature gradient and extends up to about 50 km below which 99.9 % of the mass atmosphere is contained. The stratosphere-troposphere interface is called tropopause. The positive temperature gradient is caused by efficient absorption of (UV). The third layer, namely the mesosphere, extends up to 85 km with a decrease of temperature followed by the mesopause and the thermosphere characterized by temperature values up to 200 K. This

part of the atmosphere is the most exposed to solar radiation and as consequence most of the particles are ionized (ionosphere).

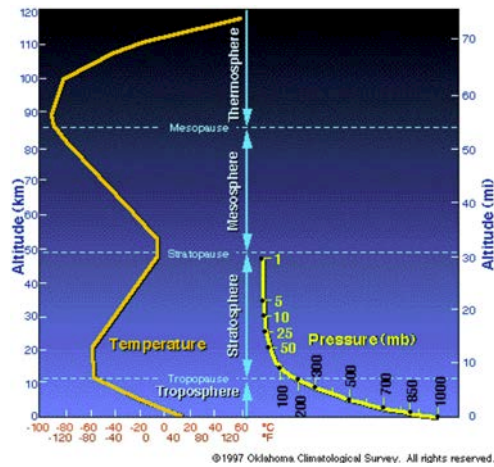


Figure 1.2: Vertical profile of temperature and pressure in the atmosphere in function of altitude. The atmospheric layers between ground level and 120 km are also indicated.

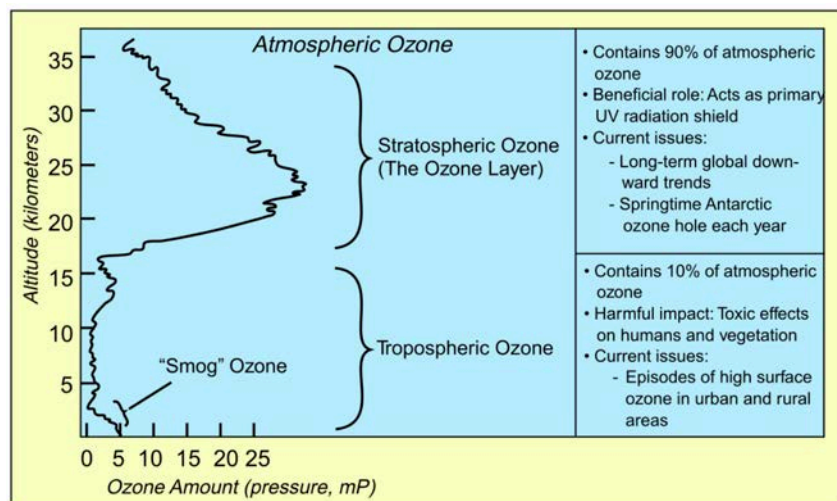


Figure 1.3: Vertical profile of ozone in the atmosphere in function of altitude. The main features related to tropospheric and stratospheric ozone are illustrated. The picture has been taken from 1999 EOS Science Plan (Revisited) Chapter 7 - Ozone and Stratospheric Chemistry (Schoeberl).

The main components of atmosphere are nitrogen (N_2), oxygen (O_2) and argon (Ar). Less amounts of other species are present, such as greenhouse gases like CO_2 , CH_4 , water vapor and O_3 as well as dust, aerosols or antropogenic gases. The amounts of the most important atmospheric compounds are reported in table 1.2. Ozone is present in troposphere and mostly in the stratosphere (figure 1.3) where it form the so called "ozone layer" since it acts as a shield for the harmful UV radiation from the Sun.

Compound	Mole fraction (%)
N ₂	78.084
O ₂	20.946
Ar	0.934
CO ₂	0.03976
Ne	0.001818
He	0.000524
CH ₄	0.000179

Table 1.2: Chemical composition of the atmosphere [7]. CO₂ value refers to January 2014 and has been taken from *Ed Dlugokencky and Pieter Tans, NOAA/ESRL (www.esrl.noaa.gov/gmd/ccgg/trends/)*.

1.2.2 Ozone chemistry in the atmosphere

Among the atmospheric layers, ozone resides mostly in the stratosphere and its chemistry includes both production and destruction. The first mechanism proposed is the Chapman cycle which cannot explain the actual amount on ozone observed in the atmosphere. Thus other ozone destructive mechanisms have been taken into account.

The Chapman mechanism

The photochemical model which describes the dynamics of ozone in the stratosphere is the Chapman mechanism [8] according to which the dissociation of molecular oxygen O₂ by UV radiation below 240 nm produces atomic oxygen which can then recombine with O₂ to form O₃ following the reactions (1.1) and (1.2) where M is an inert molecule (in the atmosphere generally N₂ and O₂) that stabilizes the reaction by removing excess energy.



The ozone molecule produced in reaction (1.2) is then photolysed by ultraviolet or visible photons according to



However, reaction (1.3) is not the ultimate sink for ozone, since the oxygen atom may undergo reaction (1.2) to reform ozone. According to Chapman cycle O₃ is lost due to the reaction between ozone and atomic oxygen O



The Chapman cycle is schematically represented in figure 1.4 where the kinetics of processes is resumed. Effectively it can be found that reactions (1.2) and (1.3) are much faster than 1.4. Therefore a rapid cycle between O and O₃ takes place while a slower one holds between O₂ and (O+O₃). For this reason the high reactive O and ozone as usually referred as a chemical family called odd oxygen O_x = O₃ + O produced globally by process (1.1) and destroyed by reaction (1.4).

On one side the Chapman mechanism explains the ozone distribution with altitude in the stratosphere but on the other side it predicts an amount of ozone which is higher than the one actually measured. This discrepancy can be solved considering that ozone is not

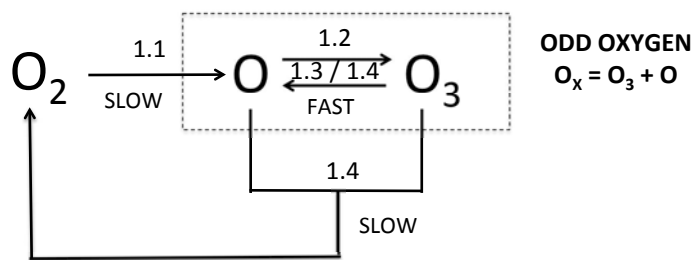


Figure 1.4: Scheme of the Chapman mechanism. Comparing the velocity of processes, the whole cycle can be seen as an exchange between molecular oxygen and odd oxygen (see text). The numbers on the arrows refer to the reaction number according to section 1.2. Picture has been adapted from <http://acmg.seas.harvard.edu>.

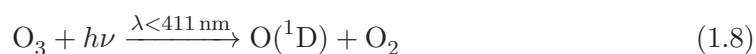
destroyed solely by the Chapman mechanism but also referring to other cycles which occur in the atmosphere.

Other cycles involving ozone in the atmosphere

- Hydrogen catalytic cycle
Oxydation of water vapor produces OH which originates a cycle representing an important sink for O_3 in the stratosphere.



where $O(^1D)$, oxygen atoms in the excited state, are produced by ozone photolysis by



Reactions (1.6) and (1.7) are responsible for ozone loss *via* the following net reaction



which does not consume the OH radical. The catalytic cycle terminates only if hydrogenperoxide reacts with the hydroxyl radical to form water and molecular oxygen



- Nitrogen catalytic cycle
Nitrogen oxide that enters the cycle may be provided by reaction of excited oxygen and nitrous oxide



or by lightning events, that dissociate N_2 , and subsequently forms NO by reaction with

O₂. NO then might undergo the following cycle



which is a null cycle, because odd oxygen is conserved. During daytime this cycle rapidly couples NO to NO₂ on the order of a minute or so, which motivates the introduction of NO_x (= NO + NO₂) as a new chemical family for reactive nitrogen oxide compounds. Interestingly, a fraction of the NO₂ reacts in the following way



and thus provides a catalytic cycle for O₃ destruction *via* the above mentioned net reaction (1.9). The cycle terminates with loss of NO_x radicals by



Note that reaction (1.15) cannot take place during night, since there is no O(¹D) available to form OH from H₂O.

- Halogen catalytic cycles

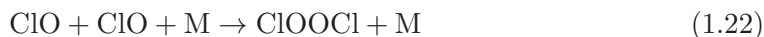
Chlorine atoms are produced by photolysis of chlorofluorocarbons (CFCs) in the stratosphere. They can undergo a cycle similar to the nitrogen catalytic cycle that destroys ozone



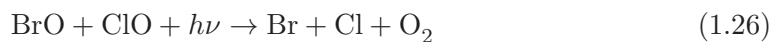
The cycle terminates with the reactions



In polar regions, ozone loss is accompanied by particular high ClO concentrations and the relevant cycles are



and



which also provide catalytic conversion from odd to even oxygen.

1.3 $O(^1D)$ in the atmosphere

The chemistry of ground state oxygen atoms, $O(^3P)$, from (1.1) or (1.3) is very simple and mostly due to the high abundance of O_2 , which is a preferred reaction partner. It requires substantial amounts of energetic photons in the first hand to dissociate O_2 by UV *via* reaction (1.1). As such, this chemistry is only relevant in the upper atmosphere and cannot account for much of the tropospheric chemistry. $O(^1D)$ from (1.8), on the contrary, is much more reactive and initiates a complex chemistry [9], which is at the heart of atmospheric oxidation [10]. Since the groundbreaking work of Weinstock [10] and Levy [9], $O(^1D)$, its reaction pathways and production channels from the UV absorption of ozone have therefore been object of many studies over the last decades [see 11–14, for example].

Excited atomic oxygen is present only in extremely small concentrations, because collisions of $O(^1D)$ with the main air components (N_2 , O_2 , Ar) lead to efficient de-excitation into the ground state at a much higher rate than what would correspond to its radiative lifetime of about 140 s [15]. The importance of $O(^1D)$ is essentially due to its reaction with water vapor H_2O (1.5) and, to a lesser extent, with N_2O (1.11):



Both reactions provide radicals from rather stable molecules.² Reaction (1.5) is the ultimate source of the atmospheric hydroxyl radical, OH, which is an important agent of (chemical) energy transfer and exchange in the atmosphere [16]. Due to its high reactivity, its chemical lifetime is short and their stationary concentration is low (ca. 3×10^6 molecules cm^{-3} [17]). Furthermore, OH concentrations show seasonal and day/night cycles because OH formation is triggered by UV radiation. In addition, OH concentration tends to decrease with increasing altitude, as the air becomes cooler and dryer. It also decreases with increasing latitude, because both the water vapor concentrations and sunlight intensity decreases when approaching the polar regions. OH is the most important oxidizing species in the troposphere and transforms many trace components into water-soluble forms, which can then be removed from the atmosphere by dry or wet deposition. OH initiated oxydation thus keeps atmospheric concentrations of trace compounds low, even when these are continuously released in the atmosphere by anthropogenic and natural sources. The OH radical has therefore been denominated “detergent of the atmosphere”. The most important reaction partners for the OH radical are carbon monoxide, CO and methane, CH_4 .

OH can also be formed from reactions other than (1.5). These are the photolysis of nitrous acid, HONO [18], the dark reaction of alkenes with ozone and NO_3 [19], and photolysis of formaldehyde or other carbonylic compounds [20]. Reaction (1.11) provides the formation of reactive nitrogen in the form of nitric oxide from the stable green house gas N_2O . As OH, NO is a free catalyst which causes ozone depletion in the stratosphere and, at the same time, depending on the amount of hydrocarbons present, can decrease ozone production [7].

²In chemistry a radical, also called free radical, is an atom, molecule or ion with at least one unpaired electron. The unpaired electron usually makes a radical a highly reactive species. Even though radicals are generally short-lived due to their reactivity, long-lived radicals (such as molecular oxygen) also exist.

into the stratosphere, where they reach altitudes at which they can be photolyzed to liberate reactive halogen gases. These lead to a continuous destruction of ozone via the reactive cycles presented in section 1.2.2.

Another and much more prominent loss of ozone occurs during the so called ozone hole events, first reported by Farman et al. [24]. These take place under the very special atmospheric conditions of polar winters (mostly in the Antarctica). Due to the lack of solar radiation, the stratospheric temperature strongly decreases and leads to formation of a very stable dynamic system: the polar vortex that is an enclosed and non-irradiated air mass which circles around the pole. Within this air mass low temperatures are reached that allow formation of liquid and solid Polar Stratospheric Clouds (PSCs). On the liquid or solid surfaces of PSCs several reactions can occur which convert the inactive chlorine reservoir to active (*i.e.* ozone destructing) substances. During the late winter (September) when the solar radiation begins to irradiate the Antarctic, photolysis and formation of large amounts of active chlorine occurs with a subsequent onset of the ozone destroying cycles. In the Arctic, similar processes occur, but they are generally much less significant than in the Antarctic, because temperatures are higher than at the South Pole, leading to less PSCs and a vortex that is less stable.

1.6 Cycles of tropospheric pollutants

Unlike stratospheric ozone, tropospheric ozone can directly harm ecosystems, animals and humans due to its toxicity. Tropospheric ozone is chemically produced by the so-called ozone precursors: nitrogen oxides (NO_x), carbon monoxide (CO) and Volatile Organic Compounds (VOCs), that are released into the atmosphere as air pollutants and which mostly stem from factory emissions, engine exhaust and power plants. In the presence of these pollutants and solar irradiation smog may form, the term “smog” having been coined at the beginning of the last century as contraction of the two words “smoke” and “fog” in order to describe the effect on visibility that is due to the accompanying formation of particulates.

As in the stratosphere, ozone formation near the Earth’s ground is due to photochemical activity. The source of the oxygen atoms for ozone formation is provided by the photolysis of nitrogen dioxide (NO_2).



which is then followed by



The nitric oxide formed in reaction (1.13) reacts rapidly with ozone reforming NO_2



As in the stratosphere, this process does not cause a net gain of ozone, but maintains a dynamic equilibrium between O_3 , NO and NO_2 that depends on the solar actinic flux and the concentration of nitrogen oxides. Further reactions must be taken into account in order to explain pollution events where ozone concentrations are increased: these result from the simultaneous presence of NO_x and VOCs which lead to the overall reaction [4]



via a series of reactions.

This series is generally started by the reaction between one of the ozone precursors and the hydroxyl radical OH which produces HO_2 that then reacts with nitrogen monoxide NO to produce NO_2 . Without O_3 being consumed and thus bypassing reaction (1.12), the dynamic

equilibrium between NO and NO₂ in reactions (1.13) and (1.12) is thus perturbed and shifted towards NO₂, which upon photolysis produces O atoms and thus leads to the formation of ozone. The dynamic equilibrium established by the rapid photochemical cycling between nitrogen oxides and ozone will thus react by increasing the ozone concentration. The following reaction chain, which involves the precursor molecule methane (CH₄) illustrates the chemistry [25]. First, attack of OH produces the methyl radical



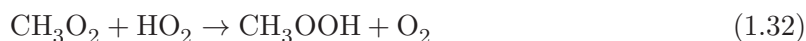
which then reacts with molecular oxygen to form the methylperoxy radical (CH₃O₂).



The methylperoxy radical combines with nitric oxide NO and produces a methoxy radical CH₃O and nitrogen dioxide NO₂, followed with a consequent formation by photolysis of an oxygen atom that can react with O₂ producing O₃



Another sink for CH₃O₂ is the reaction with HO₂



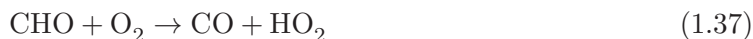
The methoxy radical (CH₃O) produced in reaction (1.31) undergoes reaction with O₂ to form formaldehyde (CH₂O) and HO₂



Formaldehyde can either photolyze in the two possible channels (1.34 and 1.35) to form respectively CHO radical or carbon monoxide (CO) or react with OH to form CHO as well



The CHO radical reacts with O₂ forming CO and HO₂



Carbon monoxide is then oxidized through OH originating an ozone producing cycle which can be summarized as



and which proceeds by the following individual reaction steps



If formaldehyde is destroyed by OH attack *via* (1.36), the methane cycle leads to net ozone production according to



because under high NO_x conditions, formation of HO_2 is equivalent to formation of NO_2 via (1.41), which then provides the O atom for ozone formation. For other VOCs, the oxidation scheme is similar and also leads to an increased production of ozone in the presence of nitrogen oxides.

1.7 Isotope terminology and quantification of isotopes and isotope effects

Atoms are composed out of a nucleus which contains N neutrons (n) and Z protons (p^+) surrounded by a negatively charged distribution of electrons (e^-), which compensates for the positive charge of the nucleus. The mass number $A = N + Z$ of an atom is defined as the sum of nucleons, *i.e.* the number of protons and neutrons. A nuclide of an element X is an atom with a specific combination of nucleons. It is described by the notation A_ZX_N or, because $N = A - Z$, more often by A_ZX . Even more concise is the notation AX , which is already unambiguous, because the element name uniquely defines the number of electrons and thus the proton number Z . Another common notation is obtained by linking the fully written elemental name to the mass number using a dash, such as carbon-12 and oxygen-16 for ${}^{12}\text{C}$ and ${}^{16}\text{O}$.

Nuclides with the same value of Z but different N are called “isotopes”, coming from the greek words “ἴσος” and “τόπος”, signifying “same” and “location, place”, thus meaning the same location in the table of chemical elements, because of the identical chemical structure that is determined by the electrons [26]. Isotopes are stable if they do not show any sign of radioactive decay. Isotopes with half-life greater or comparable to Earth’s age ($4.5 \cdot 10^9$ years) are called primordial, implying that stable isotopes are necessarily primordial. Because nucleons (n, p) are fermions ($I = 1/2$), isotopes have different nuclear spins.

Molecules contain several atoms (often also different elements) and thus can contain various isotopic combinations. According to the IUPAC Gold Book [27], two terms are used to specify isotopic variants of molecules. “Isotopologues” denote molecules which differ in their isotopic composition, *i.e.* ${}^{16}\text{O}_2$ and ${}^{16}\text{O}^{18}\text{O}$ are two isotopologues of the O_2 molecule. The term comes from the contraction of the two words “isotopic” and “analogue”. Isotopomers are molecular species having the same (isotope) chemical formula and are thus composed out of the same isotopes, but situated in different positions in the given molecule. For example ${}^{16}\text{O}^{18}\text{O}^{16}\text{O}$ and ${}^{16}\text{O}^{16}\text{O}^{18}\text{O}$ are two isotopologues of the ozone molecule with the overall sum formula ${}^{16}\text{O}_2^{18}\text{O}$. The term comes from the contraction of the two words “isotopic” and “isomer”. No accepted terminology has yet been found to describe the set of all isotopic variants of a molecule.

For the light elements, only few stable isotopes exist. Table 1.3 gives some information on the three stable isotopes of oxygen : ${}^{16}\text{O}$, ${}^{17}\text{O}$ and ${}^{18}\text{O}$, and according to the CIAAW³, there are 19 elements with exactly one stable isotope with atomic numbers Z ranging from 4 (Be) to 79 (Au).

Different isotopes of a chemical element are characterized by different physical properties (mass, radioactive lifetime, nuclear spin, . . .), but have almost identical chemical properties. Masses are mostly expressed using the unified atomic mass unit u (or dalton, $1 \text{Da} = 1u$),⁴

³Commission on Isotopic Abundances and Atomic Weights: <http://www.ciaaw.org>

⁴Note that the unified atomic mass is a non-SI unit, whose use is accepted.

that is related to the definition of the mole. The mole is the SI unit for amount of substance measurements. It is defined as the number of atoms in 12 g of ^{12}C . The universal constant that converts between amount of substance and this number is the Avogadro constant N_A , whose current best value is [28]

$$N_A = 6.0221456(23) \cdot 10^{23} \text{ mol}^{-1} \quad [3.8 \cdot 10^{-7}]. \quad (1.43)$$

Here, we have used the standard conventions to express standard uncertainty $u(N_A)$ as digits in parantheses and relative standard uncertainties ($u_r(N_A)$) as dimensionless value in square brackets.

The unified mass unit u , or the atomic mass constant m_u is derived from the definition of the mole and is defined as the mass of a ^{12}C atom. We thus have:

$$1u = m_u = \frac{1}{12}m(^{12}\text{C}) = 1 \text{ g mol}^{-1}/N_A = 1.6605377(63) \cdot 10^{-27} \text{ kg} \quad [3.8 \cdot 10^{-7}]. \quad (1.44)$$

A related and dimensionless quantity is the relative atomic mass $A_r(X)$ (or atomic weight in the older literature) of an entity X , that could be an electron, nucleon, ion etc.:

$$A_r(X) = m(X)/m_u. \quad (1.45)$$

If X is an element, where stable isotopes iX occur with relative abundances x_i , $\sum_i x_i = 1$,⁵ its relative atomic mass is given by the abundance weighted isotope masses

$$A_r(X) = \sum_i x_i \cdot A_r(^iX) = \sum_i x_i \cdot m(^iX)/m_u \quad (1.46)$$

The relative atomic mass of an isotope $A_r(^iX)$ thus is related to the mass $m(^{12}\text{C})$ of carbon-12 (^{12}C) and $A_r(^{12}\text{C}) = 12$.

Since the mole is the SI unit for amount measurements, absolute isotope abundances are specified in terms of molar abundances $n(^iX)$. Absolute abundances N on the atomic scale can be obtained using the Avogadro constant:

$$N(^iX) = n(^iX)N_A \quad (1.47)$$

The use of absolute amounts is not very useful inasmuch as they are extensive quantities that depend on sample size. A more useful notation would thus employ amount (mole) fractions or abundance ratios:

$$x_i = \frac{n(^iX)}{\sum_j n(^jX)} = \frac{N(^iX)}{\sum_j N(^jX)}, \quad (1.48)$$

where j extends over all isotopic variants of the entity X . The disadvantage of this quantification scheme is that it requires the measurement of all isotopes. It is thus for practical reasons that the most frequently employed quantification scheme in stable isotope studies is based on the amount ratio of just two isotopes, generally using the naturally most abundant species as a reference. The most abundant isotopic species is generally also the one that is measured most easily. The *isotopic ratio* between a rare iX and the most abundant jX isotope is commonly denoted by the letter R [29]:

$$^iR = \frac{n(^iX)}{n(^jX)} = \frac{N(^iX)}{N(^jX)} \quad (1.49)$$

Taking the oxygen molecule as an example, the isotopic ratios are $^{17}R = n(^{17}\text{O})/n(^{16}\text{O})$

⁵ x_i is defined further below on p. 12.

and $^{18}R = n(^{18}\text{O})/n(^{16}\text{O})$. Depending on the reservoir species, this may still require the measurement of more than two isotopic compounds.

With BO and, again, O₂ as examples, we get

$$^{17}R(\text{BO}) = \frac{n(^{17}\text{O})}{n(^{16}\text{O})} = \frac{N(^{17}\text{O})}{N(^{16}\text{O})} = \frac{[{}^9\text{B}^{17}\text{O}]}{[{}^9\text{B}^{16}\text{O}]}, \quad (1.50)$$

and

$$^{17}R(\text{O}_2) = \frac{n(^{17}\text{O})}{n(^{16}\text{O})} = \frac{N(^{17}\text{O})}{N(^{16}\text{O})} = \frac{2[{}^{17}\text{O}_2] + [{}^{16}\text{O}^{17}\text{O}] + [{}^{17}\text{O}^{18}\text{O}]}{2[{}^{16}\text{O}_2] + [{}^{16}\text{O}^{17}\text{O}] + [{}^{16}\text{O}^{18}\text{O}]}, \quad (1.51)$$

where we have used square brackets to specify the number density

$$[X] = N(X)/V \quad (1.52)$$

as the number N of an entity X in a specified volume V .

The isotopic ratio of an element is not identical within different chemical compounds or physical phases due to isotopic fractionation effects (see section 1.9). Instead variations of R are observed throughout nature. These variations are conveniently expressed as relative deviations from a standard ratio R . These deviations are called δ -values and defined in the following way:

$$\delta = \frac{R_s}{R_r} - 1 \quad (1.53)$$

where R_s and R_r are the isotopic ratios of the isotope in the sample and the reference compound, respectively. Positive values of δ denote an enrichment (of the rare and mostly heavy isotopes), negative values a depletion. δ -values being usually quite small, they are commonly expressed in the dimensionless units of “percent” (10^{-2} , %), “per mil” (10^{-3} , ‰) or “per meg” (10^{-6}). The ratio of isotopic ratios of two samples A and B is called fractionation factor α

$$\alpha_{A-B} = \frac{R_A}{R_B}. \quad (1.54)$$

Since isotopic fractionation factors have usually values close to unity, it is common to define the fractionation constant ϵ as the difference between the fractionation factor α and one:

$$\epsilon = \alpha - 1, \quad (1.55)$$

which like δ , is expressed in units of “percent” (10^{-2} , %), “per mil” (10^{-3} , ‰) or “per meg” (10^{-6}).⁶ Despite the apparent similarity between the definitions of δ and ϵ , there is a difference in significance between the two quantities. The δ -value specifies the isotopic composition with respect to a reference value, that had been chosen for reasons of measurements, whereas ϵ specifies the fractionation (and thus the difference in isotopic composition) of two reservoirs or substances that are linked to each other by a physico-chemical process with which this fractionation constant can be associated.

As previously explained, the enrichment or the depletion of a sample is measured in comparison to a standard with known isotopic composition and as close as possible to the compound under study. It should also be homogeneous, stable and non dangerous [30]. The necessity of using international reference materials comes from the fact that the abundance of heavy isotopes is usually very low and its measure can therefore be easily affected by instabilities in the system during the measurement. It is consequently convenient to measure the isotopic composition of a sample with respect to a standard with a known isotopic com-

⁶Note that the literature is somewhat ambiguous on sign in the definition of ϵ , which is sometimes also defined as $1 - \alpha$.

position. The use of an internationally accepted reference substance as a standard makes it easier to compare measurements performed in different laboratories [31]. Nowadays, several standard substances are recommended by IUPAC for oxygen isotope measurements [32]:

- Standard Light Antarctic Precipitation (SLAP): is a standard (H_2O , liquid) based on the isotopic composition of Antarctic precipitation and used to quantify oxygen-18 and hydrogen-2.
- Vienna Standard Mean Ocean Water (VSMOW): This standard substance (H_2O , liquid) is based on the isotopic composition of distilled sea water collected from several oceans. It is the current standard for the stable isotopes of oxygen-17, oxygen-18 and hydrogen-2, but it is not distributed anymore because the stock got exhausted. A replacement is currently in preparation.
- Vienna Pee Dee Belemnite (VDPB): is a standard based on the isotopic composition of the Cretaceous marine fossil *Belemnitella americana* (CaCO_3 , solid), from the PeeDee Formation in South Carolina (United States). It is a reference substance for amounts of the stable isotopes carbon-13 and oxygen-18.

Isotope	Relative atomic mass A_r	Mole fraction x_i (%)	Nuclear spin I
^{16}O	15.994914223(25)	99.757(16)	0
^{17}O	16.99913150(22)	0.038(1)	5/2
^{18}O	17.9991604(9)	0.00205(14)	0

Table 1.3: Relative atomic masses and abundances of the stable oxygen isotopes in VSMOW according to De Laeter et al. [33]. The isotopic composition of VSMOW is representative for the natural abundance of oxygen isotopes on Earth. Standard uncertainties are given in parentheses.

1.8 Isotope dependence of the zero point energy

Much of the natural variations found in the distribution of isotopes is due to thermodynamical differences between isotopic molecules. These are mostly caused by quantum mechanical effects that atomic masses have on the density of molecular states, and thus on the partition function that determines the thermodynamic properties of a molecule, such as density, vapour pressure, etc. [34–36]. This creates physico-chemical phenomena with implications in other fields such as astrophysics and chemistry, geophysics and biology. In terms of physical chemistry, we particularly note that the bond strength shows a dependency on the isotopic composition. In general, the chemical bond in a molecule containing the heavier isotope is more stable than the one which contains the lighter molecule (see Fig. 1.6). A greater amount of energy is thus required to break the isotopically heavier molecule as compared to its lighter counterpart.

Considering the simple case of a diatomic where we approximate the atomic interaction around the minimum by a harmonic potential,⁷ the lowest energy level E_0 , also called *zero point energy* (ZPE) is given by $E_0 = h\nu/2$ where h is the Planck constant and ν the classical vibration frequency. This frequency, and thus E_0 , is related to the force constant k and the

⁷Here we make the assumption that the Born-Oppenheimer approximation holds according to which the electronic potential is independent of nuclear masses.

reduced mass of the two atoms $m_r = (m_1 m_2)/(m_1 + m_2)$, by

$$\nu = \frac{1}{2\pi} \left(\frac{k}{m_r} \right)^{1/2} \quad (1.56)$$

This means that the zero point energy of a vibrational molecule always lies above the minimum of its potential energy curve. The $1/\sqrt{m}$ dependence of the zero point energy further implies that the difference between E_0 and the minimum of the potential is larger for a molecule composed out of light nuclides than that composed out of the heavier isotopes, as is demonstrated for the isotopologues of H_2 in figure 1.6.

As an aside we can already note that spectral properties (that are based on both rotational and vibrational motions, see section 1.9) also depend on the isotopic composition, providing another possible mechanism for isotopic fractionation through the interaction with photons.

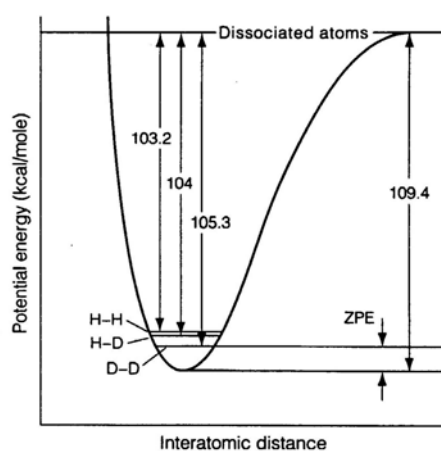


Figure 1.6: Energy level diagram for the isotopologues of H_2 . Picture taken from [37].

The lower dissociation energy of light isotopologues also facilitates chemical reactions and increases their reaction rates when compared to the heavier isotopologues [38]. Similar fractionation effects hold for phase changes, such as evaporation and condensation processes that are particularly relevant for fractionation effects in relation to Earth's hydrological cycle. Due to their quantum mechanical nature, these isotope effects are more important at low than at high temperatures.

1.9 Origins of mass-dependent isotopic fractionation

Isotope substitution always changes the mass of an atom or molecule and therefore changes its physico-chemical behaviour. This chapter gives a short overview of the different processes that lead to isotope fractionation between different phases and reservoirs. In general, one distinguishes between reversible or irreversible processes. Isotope fractionation can originate from both, equilibrium and non-equilibrium effects. The main agent which causes isotope fractionation in reversible processes is linked to isotope thermodynamics and thus, according to statistical physics, requires a quantum mechanical treatment, taking zero point energy effects into account. In irreversible processes, further fractionation occurs due to atomic or molecular dynamics, which depends on the inert or effective masses, and can be described classically [39].

1.9.1 Isotope fractionation in the thermodynamic equilibrium

Equilibrium isotope fractionation or fractionation during reversible processes describes the partitioning of isotopes between chemical compounds or different phases of the same species in reactions that have come to equilibrium. One may write



where subscripts 1 and 2 refer respectively to the light and heavy isotope contained in the species (or phases of the same compound) A and B. This kind of fractionation takes place in closed and well-mixed systems at chemical/thermodynamic equilibrium where the rate constants of the forward and backward reactions of each isotope are the same. However, the amount ratios of isotopes are different in each compound or phase. The equilibrium constant for the reaction (1.57) is

$$K = \frac{([A_2]/[A_1])^a}{([B_2]/[B_1])^b} \quad (1.58)$$

For elements with low mass, such as hydrogen, carbon or oxygen, equilibrium fractionations can be large.

1.9.2 Isotope fractionation in irreversible processes

Processes referred to as non-equilibrium or irreversible processes are related to systems out of thermodynamic equilibrium where the direct and inverse rates (for a phase change or for a chemical reaction) do not have the same value. Reactions are thus unidirectional and reaction products are physically isolated from the reactants. Examples of these systems are incomplete or unidirectional chemical reactions, evaporation, effusion or diffusion processes. In the latter case, it is evident that isotopes are diffused as a function of the inert masses involved.

Considering the kinetic theory of gases, all molecules in a gas have the same average kinetic energy and Graham's law of diffusion holds [30]

$$\frac{v_1}{v_2} = \sqrt{\frac{m_2}{m_1}} \quad (1.59)$$

where m_1 , m_2 , v_1 and v_2 represent respectively the molecular masses and the velocities of two isotopic molecules (indices 1 and 2). The $v \propto 1/\sqrt{m}$ dependence leads to lower translational velocities for the heavier species as compared to the lighter ones, that diffuse faster. This leaves a residual compound enriched in the heavier isotopes, when gas is removed by diffusion, such as in a molecular beam created from a fixed gas reservoir. The same principle applies to a phase change process, such as unidirectional evaporation. In this case, the flow through the phase boundary ($\propto [X]v$, where $[X]$ is the number density of the species X) is higher for the lighter than for the heavier isotope.

It must be noted that kinetic isotope fractionation in unidirectional chemical reactions is not entirely due to the above outlined mass dependent kinetic isotope effect (KIE). Zero-point energy differences also come into play (see section 1.8). This is evident from the complete statistical physical treatment of reaction rates in transition state theory. As an example, let's consider the following reaction that passes through the transition state $[ABC]^\ddagger$:



where the index i specifies the respective isotopes and A, B and C designate atoms or small

molecules. The rate ratio is given by [40–42]:

$$\alpha = \frac{k_2}{k_1} = \left(\frac{\nu_2^\ddagger}{\nu_1^\ddagger} \right) \left(\frac{f_{\text{ABC}_2^\ddagger}}{f_{\text{ABC}_1^\ddagger}} \right) \left(\frac{f_{\text{BC}_1}}{f_{\text{BC}_2}} \right) \quad (1.61)$$

where the ν_i^\ddagger are the imaginary frequencies of the reaction coordinate in the transition state, $f_{\text{ABC}_i^\ddagger}$ the reduced partition functions of the transition state, and f_{BC_i} the reactant partition functions. The imaginary frequencies are associated with effective masses (similar to a real harmonic oscillator in eq. (1.56)) and the ratio thus contributes. However, the product of partition functions

$$\left(\frac{f_{\text{ABC}_2^\ddagger}}{f_{\text{BC}_2}} \right) \left(\frac{f_{\text{BC}_1}}{f_{\text{ABC}_1^\ddagger}} \right) = \frac{K_2^\ddagger}{K_1^\ddagger} \quad (1.62)$$

in eq. (1.61) constitutes the ratio of thermodynamic equilibrium constants between the transition state and the reactant configurations, thus adding zero-point-energy effects associated with surmounting the activation barrier of the reaction. Normally, lighter isotopes have a smaller activation energy and they thus tend to react more rapidly than their heavier counterparts. Lighter isotopes are therefore more easily transferred onto the product side of a reaction where they become concentrated, causing the residual reactants to become enriched in the heavy isotopes. In this case the KIE is called to cause normal kinetic isotope fractionation. When the heavier isotope is transferred more efficiently than the lighter one, one speaks about an inverse kinetic isotope fractionation [43].

Non-equilibrium isotope fractionation can also be produced in biological processes such as breathing or metabolic processes [44].

1.9.3 Isotopic fractionation factors in equilibrium and non-equilibrium processes

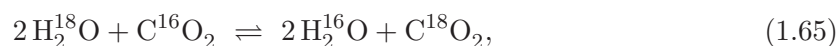
The isotopic fractionation factor α (see (1.54)) expresses the magnitude of isotopic fractionation between two reservoirs/compounds A and B which can be either in equilibrium or taking part in a unidirectional reaction as reactant or substrate and product. For the fractionation factor in equilibrium, we recall

$$\alpha_{A-B} = \frac{R_A}{R_B} \quad (1.63)$$

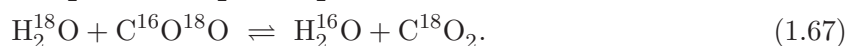
where R_A and R_B are the isotopic heavy/light ratios introduced in section 1.7. If isotopes are randomly distributed within the compounds A and B, α can be related to the equilibrium constant K of the reaction by

$$\alpha = K^{1/(ab)} \quad (1.64)$$

where a and b are the stoichiometric coefficients of equation (1.57). As an illustration, let's look at the isotope exchange between carbon dioxide and water



which proceeds in a sequence of oxygen isotope exchange reactions



Comparing with the definition in equation (1.57), we find $A = \text{CO}_2$, $B = \text{H}_2\text{O}$, $a = 1$ and $b = 2$ and ^{16}O and ^{18}O correspond to isotopes 1 and 2, respectively. If we define $q =$

$R_A/(1 + R_A)$, $o = 1/(1 + R_A)$, we find

$$\frac{2[\text{C}^{18}\text{O}_2] + [\text{C}^{16}\text{O}^{18}\text{O}]}{2[\text{C}^{16}\text{O}_2] + [\text{C}^{16}\text{O}^{18}\text{O}]} = \frac{2q^2 + 2q(1 - q)}{2o^2 + 2o(1 - o)} = \frac{q}{o} = R_A = \sqrt{\frac{q^2}{o^2}} = \sqrt{\frac{[\text{C}^{18}\text{O}_2]}{[\text{C}^{16}\text{O}_2]}}, \quad (1.68)$$

because of the statistical distribution of isotopes within a species that we assume. We thus obtain

$$\alpha_{A-B} = \frac{R_A}{R_B} = \sqrt{\frac{[\text{C}^{18}\text{O}_2]}{[\text{C}^{16}\text{O}_2]}} \bigg/ \left(\frac{[\text{H}_2^{18}\text{O}]}{[\text{H}_2^{16}\text{O}]} \right) = \sqrt{\frac{[\text{C}^{18}\text{O}_2][\text{H}_2^{16}\text{O}]^2}{[\text{C}^{16}\text{O}_2][\text{H}_2^{18}\text{O}]^2}} = K^{1/2}, \quad (1.69)$$

which well confirms eq. (1.64).

It must be noted, however, that the equilibrium constants for the two reaction steps (1.66) and (1.67) are of the order of 2 and 1/2, respectively, because the density of states enters in the partition function for the calculation of the equilibrium constant. The twofold-symmetry of the homonuclear $^{16}\text{O}_2$ and $^{18}\text{O}_2$ molecule reduces the density of states by a factor of 2 as compared to the heteronuclear molecule $^{16}\text{O}^{18}\text{O}$. In classical calculations of the rotational partition function, this is taken into account by a factor $1/\sigma$, where σ is the so called symmetry number under rotations. This statistical factor, however, does not contribute to isotope fractionation (see also sec. 6.2.3).

In the case of non-equilibrium isotope fractionation, α is calculated as the difference in isotopic ratios between the new system to which molecules are added by the unidirectional process and the bulk system from which this infinitesimal amount of compound is removed [30, 29]. Let thus B be the bulk phase and add dN_1 and dN_2 molecules to the new empty A phase by a kinetic process (evaporation, reaction, etc.). The fractionation factor will then be given by

$$\alpha = \frac{R_A}{R_B} = \frac{(dN_2/dN_1)}{(N_2/N_1)} = \left(\frac{dN_2}{N_2} \right) \bigg/ \left(\frac{dN_1}{N_1} \right) = \frac{d \ln N_2}{d \ln N_1} \quad (1.70)$$

where, as before, indices 2 and 1 denote heavy and light isotopes, respectively. The incremental flow of an individual isotope i from phase B to A is assumed to occur by the rate equations,

$$\frac{dN_i}{dt} = k_i N_i \quad \Leftrightarrow \quad \frac{d \ln N_i}{dt} = k_i \quad (1.71)$$

where k_i is the isotopic rate constant for the unidirectional process. We thus find that the fractionation factor

$$\alpha = \frac{R_A}{R_B} = \frac{k_2}{k_1} \quad (1.72)$$

corresponds to the ratio of rate coefficients for the isotope specific reactions. Note that our definition of α and the convention to use the bulk reservoir as “reference” leads to a rate ratio where the rare/heavy isotope rate appears in the numerator and the reference rate in the denominator.⁸

1.10 Mass independent fractionation

As has been discussed above, isotope fractionation due to mass differences provides an evident mechanism for explaining much of the observed isotope variability in nature, but there are notable exceptions to this behaviour. First, given the physical origin of these mass dependent effects, the size of these effects is limited by the relative mass differences and the involved force constants, which gives an upper limit of about 8% for the fractionation of ^{18}O

⁸Note that the inverse ratio can also be found in some books.

[34]. This variability is actually observed in nature, where stable compounds, like Antarctic precipitation can be highly depleted $\delta_{\text{SMOW}}^{18}\text{O} = -62.8 \text{ ‰}$ and nitrous oxide dissolved in anoxic sea water from the Black Sea can reach enrichments as high as $\delta_{\text{SMOW}}^{18}\text{O} = 109 \text{ ‰}$ [45]. Apart from N_2O , nitrate can also show significant ^{18}O enrichments of up to 80 ‰ [45].

However, much higher values that exceed these limits have been observed. ^{18}O isotope enrichments in stratospheric ozone on the order of 300 to 400 ‰ were reported as early as in 1981 [46], but these high values were later questioned [47]. Nevertheless, very recent and more reliable remote sensing [48] and mass spectrometer measurements [49] still report maximum values of as high as $\delta_{\text{SMOW}}^{18}\text{O}(\text{O}_3) \simeq 200 - 250 \text{ ‰}$ and $\delta_{\text{SMOW}}^{18}\text{O}(\text{O}_3) = 150 \text{ ‰}$, respectively, which corresponds to two or three times the predicted $\pm 80 \text{ ‰}$ range, even though ozone generally is a shortlived compound that rapidly interacts with atmospheric oxygen.

Another important feature is a tight correlation between isotope effects in the ^{17}O and ^{18}O isotope composition that is predicted by the aforementioned effects. Indeed, a power law is expected for equilibrium isotope effects [e.g. 39]

$$\frac{{}^{17}R_A}{{}^{17}R_B} = \left(\frac{{}^{18}R_A}{{}^{18}R_B} \right)^\lambda \quad (1.73)$$

where, as before, the subscripts A and B refer to two different reservoirs or phases and λ takes a value of about $1/2$. For small fractionation effects, the isotope ratios can be considered approximately a linear function of the differences in the reciprocal masses of the isotopically substituted species [50] and the relationship between the ratios of $^{17}\text{O}/^{16}\text{O}$ and $^{18}\text{O}/^{16}\text{O}$ is approximately determined by the relation between δ values

$$\delta^{17}\text{O} = \lambda \times \delta^{18}\text{O}. \quad (1.74)$$

λ can then be interpreted as the slope in a three isotope plot $\delta^{17}\text{O}$ as function of $\delta^{18}\text{O}$. For molecular oxygen the value for λ according to statistical theories [35, 51, 36] is [39, 42]

$$\lambda = \left(\frac{1}{m_{16}} - \frac{1}{m_{17}} \right) / \left(\frac{1}{m_{16}} - \frac{1}{m_{18}} \right) \quad (1.75)$$

where m_{16} , m_{17} and m_{18} are respectively the masses of three oxygen isotopes ^{16}O , ^{17}O and ^{18}O , which amounts to $\lambda = 0.531$ when the expression is evaluated using current recommendations (see Table 1.3). This value may vary by a few percent, depending on the details of the fractionation mechanism [52]. Relation (1.73) is generally accepted to hold for both equilibrium effects and kinetic processes at low temperatures [53].



According to (1.74), all natural material should thus form an array in an oxygen three isotope plot [54] with a slope of about 0.5. This is called Terrestrial Fractionation Line (TFL) and defined by Terrestrial and lunar rocks which show enrichments [55] compatible with these mass dependent fractionation processes. Interestingly, marked and unexpected exceptions from this general behaviour have been observed. This non-standard fractionation pattern is often named “non mass dependent fractionation” or “mass independent fractionation” (MIF). The first strong deviation from the TFL was reported in studies of meteoritic materials [56]. The three isotope plot in figure 1.7 shows that refractory meteoritic material exhibits an important departure from the TFL and forms with a slope of about 1. At that time, the explanation for this anomaly was attributed to nuclear processes (*e.g.* cosmic rays, spallation, nucleosynthesis) since it was believed that a purely chemical mechanism could not give rise to isotope effects independent of mass [50]. Nevertheless the observation of mass independent

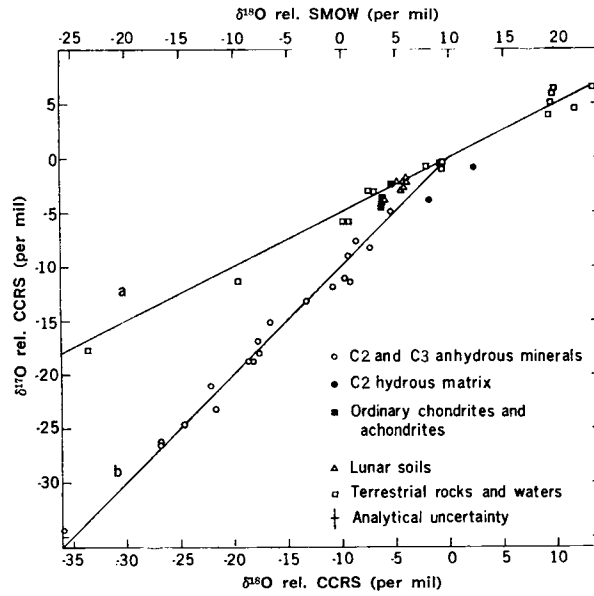


Figure 1.7: Oxygen isotopic composition of several meteoritic sources. Picture taken from [56]

fractionation processes in chemical reactions has well been confirmed in laboratory experiments under “non-nucleosynthetic” conditions. The first clear laboratory experiments that produced a deviation from the standard mass-dependence (eq. (1.74)) and showed that $^{17}\text{O}_2$ (or $^{16}\text{O}^{17}\text{O}$) can react faster (up to 13%) than both $^{16}\text{O}_2$ and $^{18}\text{O}_2$ (or $^{16}\text{O}^{18}\text{O}$) [57–59], thus clearly demonstrating the influence of nuclear spin on some chemical reactions. Later, Thiemens et al. [60] performed an electric discharge in molecular oxygen and found that product ozone is almost equally enriched in both heavy oxygen isotopes, thus pointing to still another possible origin of non-nucleosynthetic mass-independent fractionation. At that time photochemical self-shielding was put forward as the most likely explanation. It took seven more years to clearly identify the thermal reaction of ozone formation from ground state constituents to be at the basis of this observation [61].

One way to report on mass-independent fractionation is to observe three isotope slopes $\lambda \neq 1/2$. Due to some natural variability of λ in standard mass dependent processes some caution must be taken to assure that the difference is significant [52, 62]. This is certainly the case for $\lambda = 0.6 \dots 1$. The departure from a mass dependent fractionation can also be expressed by a single number, the so-called “ ^{17}O -excess” $\Delta^{17}\text{O}$ which is defined as

$$\Delta^{17}\text{O} = \delta^{17}\text{O} - \lambda \times \delta^{18}\text{O} \quad (1.77)$$

where the reference value of $\lambda \simeq 0.5$ must be clearly specified to avoid disambiguities [63].

Figure 1.8 shows that a large ^{17}O excess is present in stratospheric and tropospheric ozone. Note that a number of atmospheric oxygen-bearing molecules and deviate from the mass dependent rule do not lie on the TFL array. Laboratory experiments as well as field surveys [65] confirm that the anomaly is likely inherited from ozone *via* atmospheric oxidation processes. The measurement of the triple oxygen isotope composition of all these different compounds thus allows to get important additional insight on the history and origin of the diverse molecules, in particular about their link to ozone and to atmospheric oxidation chemistry. However, this also depends on how well the ozone isotopic composition is understood and characterized (see section 1.11).

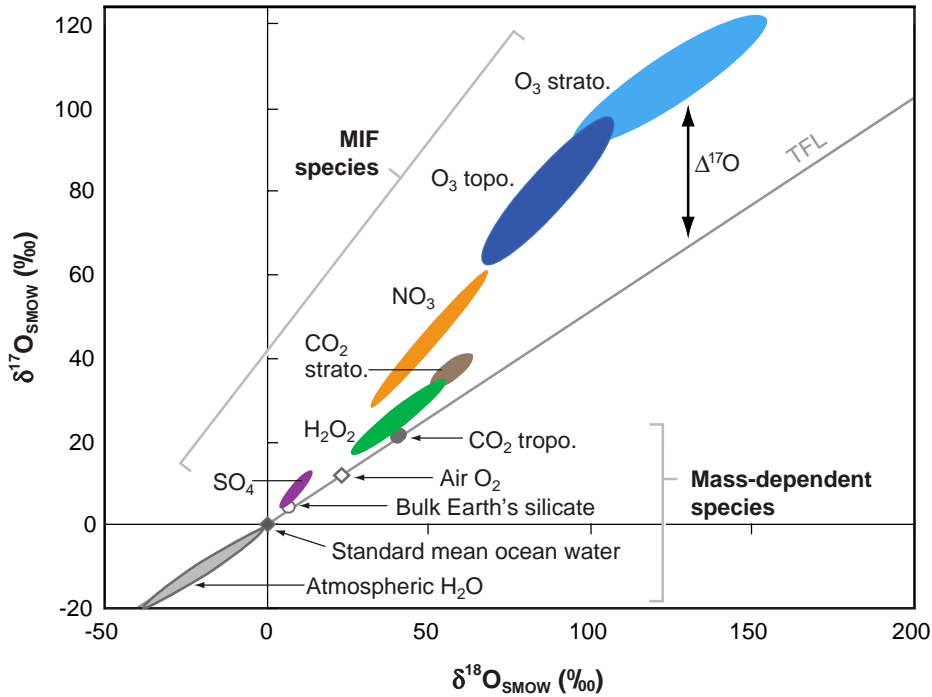


Figure 1.8: Three isotope plot of different oxygen containing atmospheric species. The ones which do not lie on the TFL are characterized by a mass independent fractionation effect. Picture taken from [64].

1.10.1 Isotope anomaly from self shielding

The most commonly accepted explanation for the oxygen isotope anomaly observed in the meteorites, particularly in chondrites, is self-shielding of carbon monoxide in the early solar nebula [66]. Self shielding is due to isotope selective absorption of light, which leads to abundance dependent penetration depths. Since ^{16}O is the most abundant isotope (see Table 1.3) its penetration depth is much shorter than that of the rarer isotopes. CO possesses well separated absorption lines in the far-ultraviolet (FUV) region between 91.2 nm and 110 nm and the early active sun may have served as intense source of UV light. Photodissociation in cold surface regions of the nebula, could preferentially decompose the heavier molecules, leading to a mass independent depletion of the gas phase material that forms water and gets, according to the model, accumulated in the disk. The chondritic material forms in early stages and has the same composition as the initial solar nebula (and the sun), only the dissociated products condense later (as water) and provide the building blocks for the terrestrial planets, for which the model predicts a mass independent enrichment. The predictions of this model agree with the recent oxygen isotope composition of the solar wind by the GENESIS mission [67].

1.10.2 Magnetic Isotope Effect

In general, the nuclear spin has little effect on chemical reactions, because hyperfine energy corrections are mostly negligible as compared to electronic energies. However, the nuclear spin can interact with the magnetic moments of the electrons and provides a “nuclear-electronic hyperfine coupling”. This coupling term vanishes in the absence of a nuclear magnetic moment, and the simultaneous presence of zero and non-zero nuclear spin isotopes therefore

provides the basis for the “nuclear spin isotope effect” or “magnetic isotope effect” (MIE) [59], which is completely independent from nuclear masses. The effect of nuclear spin has particularly well been documented in the liquid phase and plays a role in radical pair reactions. These provide reaction pathways via triplet or singlet systems. A singlet-triplet or intersystem crossing (ISC) is usually avoided due to spin conservation. However, a simultaneous (nuclear and electronic) spin-flip conserves angular momentum and magnetic isotopes therefore provide an allowed pathway for ISC, thus opening up reaction channels that are completely forbidden for non-magnetic isotopes, such as the recombination of a triplet radical pair $R\cdot R$ to form the diamagnetic molecule $R-R$ [68]. Associated isotope fractionations therefore are sizable ($\sim 13\%$) [69, 59].

In the three isotope system, only ^{17}O is magnetic (see Table 1.3). The isotope fractionation therefore concerns only this isotope, while ^{16}O and ^{18}O remain unaffected, such as in the thermal decomposition of endoperoxides in which a singlet biradical can decompose to form singlet oxygen $\text{O}_2(^1\Delta)$ or undergo spin conversion to the triplet state and form $\text{O}_2(^3\Sigma)$. Since conversion from singlet to triplet is faster for biradicals containing magnetic ^{17}O , $\text{O}_2(^3\Sigma)$ is exclusively enriched in ^{17}O while the singlet product has been observed to be depleted [57].

1.11 Ozone isotopic anomaly

As can be observed from the three isotope plot shown in figure 1.8, atmospheric ozone is strongly and anomalously enriched in the heavy isotopes. As a matter of fact, ozone formation is the prototype of a mass-independent reaction and has played a central role in the discovery of MIF. For this reason, the main measurements and results concerning both, atmospheric ozone and ozone produced in the laboratory are reviewed here.

1.11.1 Atmospheric measurements

The first observation of very high heavy isotope enrichments in atmospheric ozone has been reported in the early '80s when mass spectrometric experiments installed on balloons measured enhancements in ^{18}O at altitudes of about 32 km [70]. At that time it was hypothesized that photodissociation of the second most abundant oxygen isotopologue, $^{16}\text{O}^{18}\text{O}$, would act as a strong ^{18}O source due to the twofold increased density of states [71]. Only a few years later sizeable enrichments in ^{17}O containing ozone have been measured, with $\delta^{17}\text{O}$ -values of similar magnitude than $\delta^{18}\text{O}$ [72] but it took laboratory experiments to attribute the effect to the formation of ozone [61]. At the same time theoretical studies on the exchange reaction in the atmosphere demonstrated that the O atom exchange is sufficiently fast that any increased abundance of ^{18}O should be rapidly diluted under atmospheric conditions [73, 74]. Other campaigns based on different measurement techniques confirmed the previous observations [75]. Recent analysis on high altitude stratospheric ozone samples collected during balloon flights confirmed an additional UV photolysis-induced isotope effect which accounts for 1/4 of the total enrichments measured [76, 48], the latter having been predicted on theoretical grounds [77]. 4/5 of the observed fractionation, however, is due to temperature and pressure variations that impact the ozone isotope composition via the ozone formation reaction.

Speculations of an additional ozone formation channel [78, 79] via



are probably irrelevant. The channel had been proposed because reactions of vibrationally excited O_2 showed a sharp increase in the rate of disappearance when the threshold energy of the above reaction was reached at $\nu = 26$, but the experiments could not provide actual evidence for ozone formation and theoretical studies by Lauvergnat and Clary [80] could not

support the finding that ozone was actually formed in the above reaction. If operative, it could lead to an additional ozone enrichment of 3% in equatorial regions at high (42 km) altitudes [81].

Tropospheric measurements are relatively sparse. The first measurements [82] had shown values of $\delta^{17}\text{O} = 71\text{‰}$ and $\delta^{18}\text{O} = 91\text{‰}$ for ozone cryogenically trapped and converted to ozone. These values were in agreement with the predicted $\delta^{17}\text{O}$ from laboratory studies but presented a lower enrichment in ^{18}O which could be due to systematic errors and extra fractionation in tropospheric ozone [83]. Other measurements [84] confirmed the occurrence of tropospheric ozone anomaly with typical values of $\delta^{17}\text{O} = 66\text{--}78\text{‰}$ and $\delta^{18}\text{O} = 82\text{--}91\text{‰}$. Very recently, precise measurements of $\Delta^{17}\text{O}$ became available by means of a new filter based measurement technique [85], confirming the previous values.

1.11.2 Laboratory measurements

The first observation of an anomalous enrichment in ozone generated in laboratory dates back to few years after the first observation of very high isotope enrichment in atmospheric ozone: ozone was formed in an electric discharge and it was found that $\delta^{17}\text{O} \simeq \delta^{18}\text{O}$ [86]. This pioneering experiment is considered the starting point for many further investigations, because the origin of the effect was completely elusive at that time. The main issue in the following experiments has been to identify the relevant reaction and the molecular mechanism behind the observed isotopic fractionation. To this end, the influence of temperature and pressure [87], [88] on fractionation processes in ozone generated by photolysis [89] or electric discharge [90] has been investigated. The use of the photolytic recycling technique [87] with visible light instead of electric discharge or UV dissociation of O_2 as a means to generate ozone further allowed to unambiguously identify the reaction from ground state reactants as the sole source of the observed isotope anomaly. On the basis of this experiment [87], self-shielding or other molecular processes had to be ruled out.

Concerning the pressure dependence, several studies performed at 321 K [87] and at room temperature [88] recorded a quite constant high enrichment ($\simeq 13\%$ for $\delta^{18}\text{O}$ and $\simeq 11\%$ for $\delta^{17}\text{O}$) at low pressures below 100 torr and a strong decrease as pressure increases as shown in figure 1.9.

Follow up studies then aimed at investigating the temperature dependence of the isotope effect. Ozone was therefore produced from $\text{O}(^3P) + \text{O}_2(^3\Sigma_g)$ in the gas phase, controlling both temperature and pressure. Both of these experiments were performed at constant pressures of 50 [87] and 45 Torr [92], respectively. They observed an increase in $\delta^{17}\text{O}$ and $\delta^{18}\text{O}$ as temperature rose (figure 1.10). δ values for ^{17}O changed from 36 ‰ at 130 K to 117 ‰ at 361 K, while for ^{18}O the δ increased from 26 ‰ to 146 ‰ over the same temperature range.

The aim of laboratory measurements was also to understand how isotopic fractionation effects were related to molecular mass or molecular symmetry. Therefore, multi-isotope studies where ozone isotopologues with masses ranging from 48 to 54 u have been performed and electric discharge [93] as well as photolytic recycling [94] has been used for the generation of ozone. In these studies, large isotopic effects have been found in the asymmetric molecules as shown in figure 1.11, where the highest enrichment is recorded for the isotopologue $^{16}\text{O}^{17}\text{O}^{18}\text{O}$. The symmetric and homonuclear molecules $^{17}\text{O}_3$ and $^{18}\text{O}_3$, on the contrary, were both depleted. The observation that $^{49}\text{O}_3$ and $^{50}\text{O}_3$ are characterized by the same enrichment, independent on the composition of the initial O_2 gas (natural abundance or highly enriched), lead to the conclusion that the isotope anomaly is an intrinsic molecular effect.

Nevertheless, results obtained in subsequent kinetic investigations seemed to question the hypothesis of a symmetry driven isotopic fractionation [95]. These experiments looked at individual reaction rates for four ozone formation channels, two producing symmetric

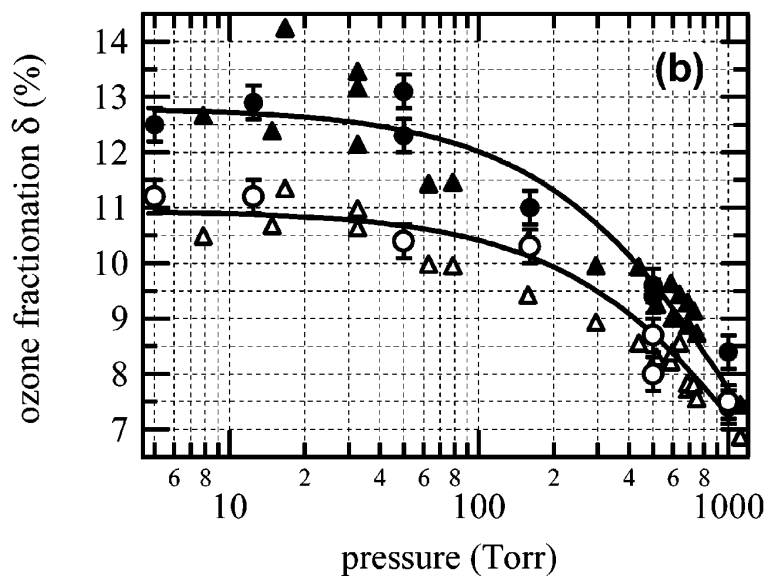


Figure 1.9: Pressure dependence for $\delta^{17}\text{O}$ (open symbols) and $\delta^{18}\text{O}$ (closed symbols). Triangles and circle refer to values calculated at room temperature [88] and at 321 K [87] respectively. Best fit curves for data from [87] have been evaluated in [91]. Picture taken from [83].

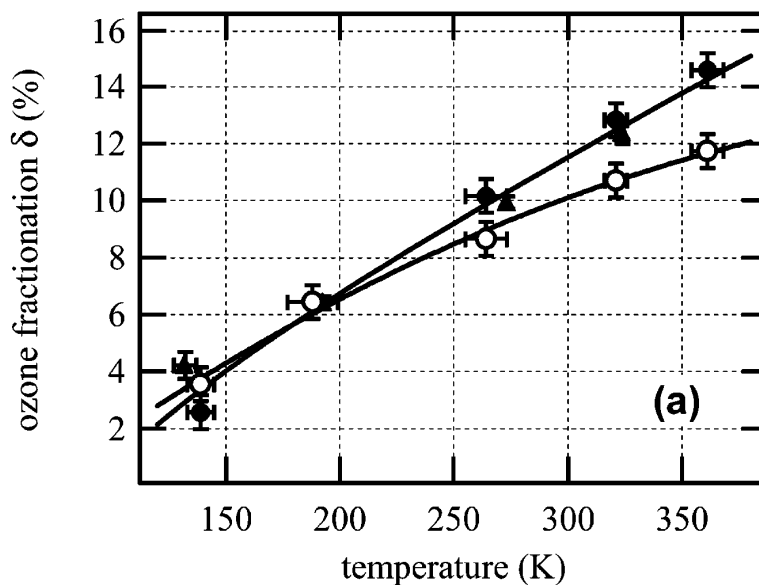


Figure 1.10: $\delta^{17}\text{O}$ (open symbols) and $\delta^{18}\text{O}$ (closed symbols) dependence of temperature between 130 K and 360 K. Triangles and circle refer to values calculated at 45 torr [92] and 50 torr [87] respectively. Picture taken from [83].

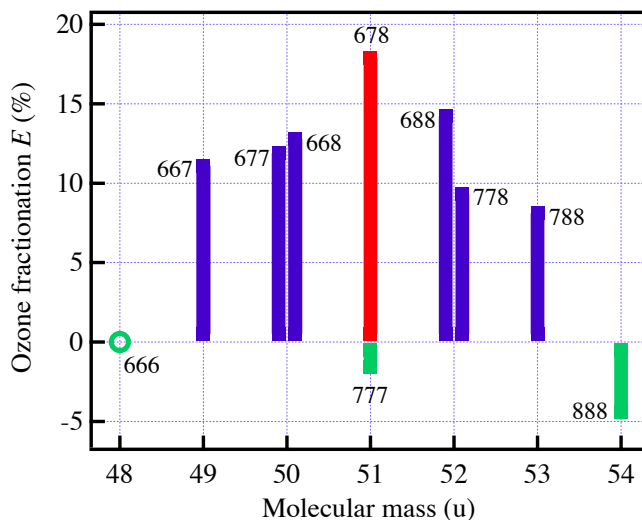


Figure 1.11: Measured enrichments for ozone isotopes. Numbers 6, 7 and 8 refer to oxygen isotopes ^{16}O , ^{17}O and ^{18}O respectively. Picture taken from [56]

molecules ((1.79) and (1.82)) the others ((1.80) and (1.81)) leading to symmetric ozone.



If the dominant fractionation process was ruled by molecular symmetry, the rates of reaction which lead to symmetric ozone should have similar values and differ from the values that yield asymmetric molecules. Nevertheless, this has not been observed. It was found that the rate coefficient of reaction (1.81) is about 60% higher than the rate measured for reaction (1.80). In addition reaction (1.80) is by 10% slower than reaction (1.79), while reaction (1.81) was measured to be about 50% faster than reaction (1.79). These values have been confirmed by later experiments which measured the relative rates of further isotopic variants. The study also confirmed that the collisions forming ozone are end-on reactions and that molecular symmetry does not play the dominant role in the enrichment process [96].

The pressure and temperature dependence of individual rate coefficients has also been investigated. It has been found [91] that if the total pressure increases the low ozone rate formation through reaction $^{18}\text{O} + ^{16}\text{O}^{16}\text{O}$ which has a value of 0.92 if compared to the reaction 1.79 does not change whereas the higher rate of reaction $^{16}\text{O} + ^{18}\text{O}^{18}\text{O}$ reduces its value. Moreover, the low rate coefficient ratios decrease as temperature increases while large ratios have no temperature dependence [92].

Finally, studies on the bath gas dependence of isotope enrichments of ozone formed in the presence of Ar, Kr, Xe, O_2 , CO_2 , CH_4 and SF_6 have shown that except for SF_6 , where the ^{17}O excess completely disappears at 0.1 MPa [97], the nature of the bath gas has little or no effect [97, 91].

1.12 Theory of MIF in ozone

As illustrated in the previous section, both atmospheric and laboratory measurements have shown an anomalous isotopic fractionation in ozone, characterized by almost mass-independent enrichments for heavier oxygen atoms in O_3 molecules. Moreover, the rate coefficients of individual ozone formation channels differ by as much as 60%. The origin of isotopologue enrichments could be attributed to both the association reaction (1.2) together with all the possible isotopic variants and the exchange of isotopes through reactions



which equilibrate the isotopic composition between atoms and molecules, because they proceed at much faster rates than the ozone formation process. Consequently the heavier atoms ^{17}O and ^{18}O are distributed in a such way that, due to differences in the zero-point energy of equilibrium definition states of reaction (1.83) and (1.84), the heavy oxygen atoms are depleted and ozone isotopologues should be as well. Indeed this expected behaviour is found in the homonuclear molecules $^{17}O_3$ and $^{18}O_3$. However, as explained in section (1.11), a strong enhancement is observed for all heteronuclear ozone molecules. This points to a kinetic origin of the effect and has therefore been sought in isotope effects of the rate coefficients of individual isotopic reactions. Once a theory can predict the individual rate coefficients of the ozone formation reaction, the ozone isotope puzzle has been solved.

According to the energy transfer mechanism, ozone formed in reaction (1.2) is actually produced in two consecutive steps. The first step is the bimolecular association between an oxygen atom and a molecule to form a metastable ozone molecule O_3^* , which can also dissociate back to reactants (reaction (1.85)). The second step consists in removal of energy from the excited ozone molecule via the collision with an inert reaction partner M (reaction (1.86)).



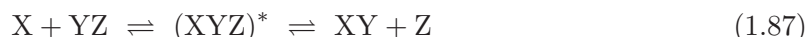
Any theoretical description therefore requires at least the electronic potential surface (PES) for the $O + O_2$ surface and, to a first approximation, the details of the interaction with the third body partner M can be neglected. This is even more motivated by the fact that the choice of the individual collider molecule M does not play a role [91], except for the particular choice of $M = SF_6$.

A theoretical explanation which is in good agreement with the experimental observations is provided by a modified RRKM (Rice-Ramsperger-Kassel-Marcus) approach [98], according to which the measured rate values could be explained combining two temperature dependent empirical parameters, namely ΔE and η , whose values needed to be adapted for reproducing the experimental data.

In the model, ΔE is the average energy transfer per collision and a value of 210 cm^{-1} has been chosen. The η parameter designed to describe a difference in statistical behaviour between asymmetric and symmetric molecules has been chosen to be 1.18. The parameter is attributed to a difference in the “effective density of states” of the metastable $(O_3)^*$. Its physical rationale is provided by the fact that the small ozone molecule is far from being a statistical molecule, where the internal energy can flow freely between all different rovibrational states, an assumption made by RRKM. On the contrary, strong non-statistical behavior has been observed in scattering experiments [99], but it is reasonable to assume that energy redistribution is more efficient for asymmetric than for symmetric molecules. This is

due to less quantum mechanical restrictions that apply to the coupling between different degrees of freedom for asymmetric than for symmetric molecules. It should be noted that this hypothesis remains to be tested and that, so far, no theoretic approach can quantitatively predict the degree of deviation between symmetric and asymmetric molecules.

As shown experimentally [100], two parameters essentially suffice to predict the isotopic effects in ozone formation. Symmetric ozone molecules are formed at approximately equal rates. Asymmetric molecule formation, on the contrary, occurs at strongly variable rates (up to 60%), which correlate with the difference in ZPE between the two possible dissociation channels in the following scheme:



If O_2 molecules on the left (YZ) and right (XY) sides are different, their ZPE will differ too and, depending on the direction taken in the process, the isotope exchange reaction is endothermic or exothermic. Low energy states which have the largest lifetimes are only accessible from endothermic reactants. An endothermic exchange therefore implies an increased lifetime of $(XYZ)^*$, whereas an exothermic process implies the inverse. Ozone formation that shares reactants with an endothermic exchange will therefore be increased with respect to a reaction that shares reactants with an exothermic exchange.

The linear correlation between ozone rate coefficients (leading to asymmetric product molecules) and the difference of zero point energies (ΔZPE) in the isotope exchange reaction (1.87) shows that this mass dependent effect is dominant. However, extrapolation of the correlation for ($\Delta ZPE = 0$) also shows that there is a symmetry selection that favors formation of asymmetric molecules, visible as an offset in the correlation of Ref. 100. η in the modified RRKM theory has accordingly been chosen to match the experimental value of 1.18.

In summary, the rates for ozone production can be motivated by mass dependent effects (differences of ZPE) and a non-mass dependent symmetry selectivity. However, parameters need to be adjusted to match the experimental observation and no theoretical prediction is yet possible as to the size of the effect as well as to the applicability to other molecular systems.

1.13 MIF in other relevant atmospheric compounds

Figure 1.8 demonstrates large ^{17}O -excesses for ozone (from 20‰ to 40‰) associated with extremely high enrichments of the heavy isotopes. But anomalous oxygen enrichments have also been found in other atmospheric species such as sulfates, nitrates or carbon monoxide [101–104]. Here, we give an overview of these species without being exhaustive. We rather focus on those species where the mass-independent character has clearly been demonstrated, *i.e.* either a link to ozone has been established or a reaction or processus has been identified, where the deviation from standard mass-dependence (eq. (1.73)) is evident (as opposed to processes with slightly different scaling factors λ that are within the range of standard mass-dependent processes).

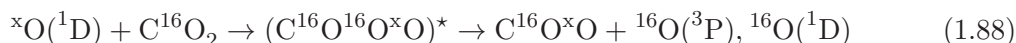
Note that many oxygen bearing molecules carry a ^{17}O -excess and both observations and laboratory experiments suggest that most of the isotope effect is inherited from ozone during oxidation processes rather than being generated directly in formation reactions that form the above mentioned compounds. The isotope transfer between O_3 and other atmospheric species is feasible due to ozone being a central molecule for atmospheric oxidation, either as a precursor for the oxidizing radicals OH and NO_3 , or as a direct oxidizing agent. This makes O_3 a prominent molecule in the atmosphere and $\Delta^{17}O$ in other species can be considered as tool to trace the link to ozone.

We note that in analogy to the $O + O_2$ reaction other reactions have been suggested

as possible origins of an oxygen anomaly, mostly in order to explain the mass independent behavior in meteorites [56]: These were⁹ $\text{O} + \text{SiO}$, $\text{O} + \text{Si}_2\text{O}_2$, $\text{O} + \text{CaO}$, $\text{O} + \text{FeO}$ [105]. Indeed, in a recent experiment on the oxidation of silicon monoxide an anomalous enrichment of product SiO_2 has been found and the $\text{SiO} + \text{OH}$ reaction has been proposed to cause the observed isotope composition [106]. However, these experiments are complex and difficult to interpret and ozone has probably also been present such that the attribution of an anomaly to a single reaction step is presently impossible.

In this context atmospheric carbon monoxide (CO) is particularly interesting, because associated isotope signatures seem to be independent of ozone formation. The importance of CO in the atmosphere comes from the fact that it is the main atmospheric reactant of the hydroxyl radical OH , and therefore determines the atmospheric oxidation capacity. The main sources of carbon monoxide are atmospheric oxidation of CH_4 and volatile organic compounds (VOC) as well as combustion processes (*e.g.* biomass burning, fossil fuel burning, ...). Its concentration in the atmosphere varies seasonally, although its cycle is not very repeatable [107]. Depending on the source from which it has been generated, CO can exhibit different isotope composition but it has been observed that its $\Delta^{17}\text{O}$ is anti-correlated to its concentration, thus indicating that the anomaly is linked to the sink reaction $\text{CO} + \text{OH}$. Effectively, laboratory experiments [108] on the $\text{CO} + \text{OH}$ reaction measured a ^{17}O -excess of about 4.5‰ for the reactant CO . The reaction proceeds through an unstable intermediate state, HOCO^* , which can re-decompose into reactants, stabilize through a collision with a third body or proceed to the products. The isotope signature therefore shows a pressure dependence, but enrichments do not fall to zero in the low pressure limit. Unlike ozone formation, it is the reactants and not the products that have ^{17}O in excess of ^{18}O ($^{17}\text{O} > 0$). In addition, the observed fractionation values are much smaller than in the case of ozone.

Another relevant atmospheric species is carbon dioxide (CO_2), because right after water, it is the most important green house gas. Several studies [109–111] have shown that stratospheric CO_2 is endowed by an anomalous isotopic enrichment. Mid and polar latitude data align along a slope of about 1.71, indicating that carbon dioxide is favorably more enriched in ^{17}O than in ^{18}O . It has been suggested that this signature is due to an isotope transfer from O_3 to CO_2 *via* $\text{O}(^1\text{D})$ [103]. According to this mechanism, $\text{O}(^1\text{D})$ radicals react with CO_2 in order to form an intermediate short lived complex CO_3^* that readily disintegrates into CO_2 and $\text{O}(^3\text{P})$ (or $\text{O}(^1\text{D})$), [112]):



Several explanations have been proposed in order to explain the isotope transfer from ozone to CO_2 [83]:

- Statistical mixing between $\text{O}(^1\text{D})$ and CO_2 reservoirs;
- Isotope transfer which includes additional mass-dependent fractionation in the CO_3^* metastable state;
- Isotope transfer which includes additional mass-independent fractionation in the CO_3^* metastable state;
- A mass-independent anomaly in the CO_3^* metastable state, which is independent of ozone.

The last hypothesis, however, can likely be ruled out, because the exchange has only been observed in the presence of ozone and energetic UV. As a necessary consequence, the ozone

⁹ For the $\text{O} + \text{CO}$ reaction please see the next section 1.13.1.

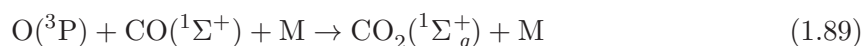
isotope composition is somehow transferred because exchange with O_2 cannot quench the isotope anomaly in O1D and experiments under high CO_2 concentrations still show the effect [113, 114]. These laboratory studies show that the relevant parameters for the isotope exchange between the two species are the isotopic composition of the reactant $O(^1D)$ produced from ozone molecules, the possible fractionation in the photolysis of O_3 which is supposed to be mass-dependent and a possible isotope effect in the CO_3^* complex.

Finally, among the main atmospheric species, particular attention needs to be paid to sulfur oxides and related compounds due to the fundamental role of sulfur in the biogeochemical cycle. The isotope anomaly observed in sulfate (SO_4^{2-}) has been studied [102] trying to understand the origin for this effect. In particular in the gas phase the oxidation pathway is driven by the hydroxyl radical OH whereas in the aqueous phase the pathways have been identified involving reactions with O_3 , H_2O_2 and O_2 . It has been found that none of these pathways can give rise to a mass-independent oxygen signature in the product sulfate.

Interestingly, even tropospheric water may show signs of mass-independent fractionation. However, $\Delta^{17}O$ of tropospheric water is extremely small (in the range from 20 to 80 ppm [115]) and mostly due to mixture of transport and equilibrium fractionation¹⁰. However, the interannual variability of $\delta^{18}O$ and $\Delta^{17}O$ of precipitation from a snowpit near Vostock, Antarctica, has been measured and $\Delta^{17}O$ showed a large variability of 40 ppm and an anticorrelation with $\delta^{18}O$ [116]. This could not be explained by climatic variations. It was therefore concluded that the observations reflect the influence of stratospheric water. Stratospheric water is predicted to be mass-independently fractionated due to its coupling to ozone chemistry *via* production by reaction of OH with CH_4 [117]. The extremely low H_2O concentrations at the elevated Vostock site (4000 m, $T = -50^\circ C$) could make stratospheric precipitation a significant source, despite the very low stratospheric abundance of about 4 ppm. The stratospheric/mass-independent origin of the precipitation water is further supported by the observation of other stratospheric tracers (Tritium, ^{10}Be) [116]. A real-time and high resolution measurement of these tracers, and in particular $\Delta^{17}O$, by spectroscopic techniques therefore provide interesting and new opportunities to further study stratospheric precipitation events.

1.13.1 Study of MIF in $O + CO$ reaction

The spin forbidden CO_2 formation reaction



which is isoelectronic to $SiO + O$ and 100 times slower than the ozone formation reaction has been object of studies in order to identify a possible mass-independent fractionation in the product CO_2 and to further elucidate the conditions on chemically producing mass independent fractionations. Indeed, two studies [118, 119] claim a MIF due to reaction (1.89), but interpretation is not straightforward due to the presence of ozone and the possibility of side reactions in the experiments. These have used photon irradiated mixtures of oxygen or ozone and carbon monoxide to trigger reaction (1.89). As has been discussed before, the OH + CO reaction provides a very efficient pathway for CO_2 formation, and OH might have been created from the reaction of ozone derived $O(^1D)$ reacting with water traces, thus providing a possible isotope transfer pathway from ozone to carbon dioxide.

These two experiments will be discussed later in greater detail (see chapter 3), but it

¹⁰The smallness of δ -values and the involvement of processes with λ in the range of 0.518 - 0.528 requires that equation (1.73) is correctly linearized through the use of an unambiguous three-isotope plot: $\ln(1 + \delta^{17}O) = \lambda \ln(1 + \delta^{18}O)$. A correspondingly adopted definition of the ^{17}O -excess is given by $\Delta^{17}O = \ln(1 + \delta^{17}O) - \lambda \ln(1 + \delta^{18}O)$, $\lambda = 0.5281$ [115].

needs to be pointed out that both studies have generated significant amounts of $O(^1D)$, thus making the proposed transfer pathway a valid hypothesis. While the more recent of these studies [118] claims to have avoided efficient production of $O(^1D)$ from ozone photolysis, the use of a halogen lamp which provides a high energy tail of photons makes this assertion generally questionable and this is dealt with in another chapter of this thesis.

As a summary, only two studies on $O + CO$ exist. Both of these have used significant amounts of O_3 to initiate the reaction. Unlike $O + O_2$, however, only bulk isotope compositions have been measured so far and no information of isotopic rate coefficients is currently available in the $O + CO$ system.

1.14 The PhD project and structure of the manuscript

My PhD has been part of the INitial TRaining in Mass Independent Fractionation (INTRAMIF), which is a Marie Curie Initial Training Network (ITN) within the framework of FP7 PEOPLE initiative of the European Commission. The focus of this ambitious project has been to better understand and employ MIF in atmospheric species by building an interdisciplinary network involving ESRs and PIs from different fields such as atmospheric and climate science, molecular physics, hydrology and oceanography. The network was composed by 8 academic institutions in 5 countries, University of Copenhagen (Denmark), University of East Anglia (United Kingdom), University of Utrecht (Netherlands), CNRS and CEA (France), University of Bern (Switzerland), and 8 non-academic partners. The link among the different ESRs involved is shown in figure 1.12. The main goal of the ESR1 INTRAMIF

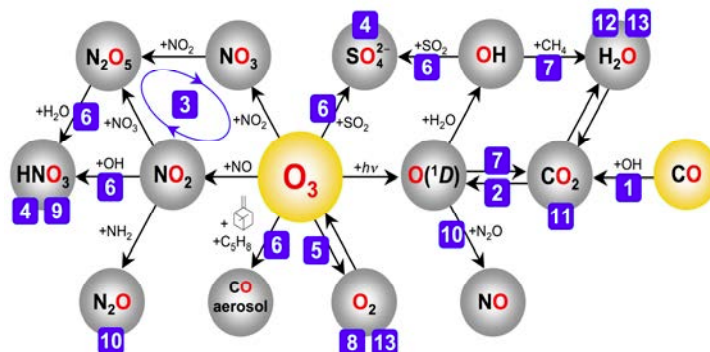


Figure 1.12: Link among different projects in the INTRAMIF network.

project, which has been jointly organized by the CNRS and the Copenhagen Center for Atmospheric Research (CCAR), was to get further insight into the physical origin of mass independent fractionation by experimentally investigating termolecular association reactions of the type $O + XO + M \rightarrow XO_2 + M$, where O is an oxygen atom, X another atom which takes part in the reaction and M an inert molecule. As discussed before, a large non mass dependent fractionation in ozone formation has been demonstrated both in atmospheric and laboratory experiments. Anomalous enrichments have been observed in other atmospheric species, such as nitrates, sulfates and carbon monoxide but only two studies [119, 118] yet claim a strong isotope anomaly in the $O + CO$ reaction. Nevertheless, this interpretation is somewhat ambiguous due to the presence of ozone in both of these experiments and an isotope transfer from ozone to CO_2 cannot be excluded with certainty. Therefore, the current

experimental knowledge on isotope effects in the $O + CO$ reaction is somewhat questionable and the reaction requires further investigations, which are provided within this thesis.

The aim of this thesis can be summarized by the following points:

- Perform new experiments on the $O + CO + M$ reaction by generating oxygen atoms from ozone photolysis in a photochemical reactor where reagent and contaminants can be monitored on-line by Fourier Transform Infrared Spectroscopy (FTIR). Unlike the previous bulk experiments, this study should allow for the measurement of individual rate coefficients or rate coefficient ratios.
- Systematically study and characterize the light sources employed for ozone photolysis in order to avoid the formation of electronically excited oxygen atoms which provide a path for transfer of the isotope anomaly from ozone to CO_2 ;
- Reinterpret the previous experiments on MIF in the $O + CO + M$ reaction on the basis of the new study and an isotope kinetic analysis which takes into account the spectral distribution of employed light sources.

In addition during my PhD I took part on an ongoing project on precision laboratory measurements of the UV cross section of ozone and its isotopes. In particular I contributed to the characterization of pure ozone samples employed for these studies quantifying the contamination of nitrogen oxides. This work is described in chapter 2. Chapter 3 is then devoted to the detailed analysis of a previous experiment on $O + CO$, followed by chapter 4 on CO_2 formation experiments at the photoreactor facility of CCAR in Copenhagen. These require a detailed analysis of the spectral properties of the different light sources, which are described in chapter 5. In chapter 6 some fundamentals of isotope kinetic modeling are recalled and it will be used to analyze our and the previous study of Pandey and Bhattacharya [118] using our photochemical isotope model. In the last chapter we conclude on our results and provide some outlook for future work.

Chapter 2

Generation of pure ozone samples

Ozone generation has a wide range of laboratory and industrial applications (*e.g.* water purification, disinfection, etc.). Spectroscopic or kinetic investigations and accurate concentration measurements depend on the availability of high purity samples. Ozone concentration measurements, in particular, rely on the availability of pure ozone samples in as much as the reference method for ozone concentration measurements is based on the absorption cross section of ozone at 253.65 nm [120], which can only be determined experimentally using samples of known concentration, *ie* pure ozone. Actually, sizeable discrepancies ($\sim 4\%$) in spectroscopically derived atmospheric or laboratory ozone concentration data exist [121–124]. These are most likely linked to the inconsistency of the spectroscopic database due to the difficulty of absolute absorption measurements and the preparation of well characterized ozone samples [125].

In this chapter, we will describe a mass spectrometric approach for deriving an upper limit on nitrogen oxide contaminations that could be present in ozone samples produced in the ozone generation facility developed in the SMILE group. Ultimately, these samples will serve to determine absolute ozone absorption cross sections and intensities in the UV and IR [126, 127].

2.1 Ozone generation by electric discharge

Due to its fragility and reactivity, ozone needs to be generated on site at the time of use. A widely used laboratory technique relies on the dielectric barrier discharge (DBL) also known as “silent discharge” in oxygen [128].

In this process, ground state molecular oxygen (O_2) is dissociated by electron collisions (reaction (2.1)). Electrons are provided by means of an (AC) electric field between two electrodes (planar or circular) that are separated from the discharge volume by a dielectric layer. The advantage of this configuration is that the electrode material does not react with the discharge gas. This leads to ozone formation *via*



Because O atoms also provide a sink for the ozone molecules through



conversion degrees are limited and usually don’t exceed several percent. In order to render the conversion more efficient, ozone may be produced at liquid nitrogen temperatures ($\simeq 77$ K).

At these temperatures, ozone is continuously removed from the gas phase by condensation and near complete conversion ($> 90\%$) becomes possible.

2.2 Experimental setup

The setup used for ozone generation and pressure measurement is displayed in figure 2.1. For the contamination measurements, we have built a duplicate system which is shown in figure 2.2.

We first describe the system for absorption measurements and then the duplicate system. Ozone is generated by electrical discharge in pure molecular oxygen in a 2.5 dm^3 volume spherical reactor (DR) connected in the lower part to a cylindrical extension (30 cm length and 5 cm diameter) which can be immersed in a dewar containing liquid nitrogen (LN_2). To this extension, two copper electrodes are attached from the outside. They are driven by a custom build HV generator, operating at 20 kHz and providing up to 15 kV. Another LN_2 cold trap (CT) is used to store and clean ozone before measurements. The N_2 vapor of this cold finger can be pumped in order to decrease the temperature of the liquid between 78 and 64 K. This consequently lowers the vapor pressure of ozone below 2 mPa [129]. The cold finger is connected to a glass buffer spiral (BS), which is composed by two parts, each 1.5 m long. The two parts can be isolated by a glass-teflon valve. The use of glass-metal transitions is limited and they are only used to connect the system respectively to the turbo molecular pump (TMP), to the temperature stabilized pressure transducers (B_1 and B_2) and to the oxygen bottle. The system is coupled to an absorption cell (AC) for quantitative absorption spectroscopy and there are ports to transfer samples to a mass spectrometer.

For the impurity measurements presented in this thesis, a similar glass system has been built with a 0.25 dm^3 cylindrical discharge reactor, also equipped with external copper electrodes. Ozone produced in this reactor could be collected in several cold fingers and transferred in front of the mass spectrometer system (see section 2.4). Cold fingers labelled as CT_1 and CT_2 are used to store oxygen before the discharge or store other gases before let them mix with ozone. The pressure in this section of the system is measured by the temperature stabilized pressure transducer B_1 whereas B_2 monitors the pressure in the reactor during the discharge. The cold finger CT_4 is employed to cryogenically transfer with LN_2 the gas from the volume close to the discharge reactor to the mass spectrometer and to store it before filling the mass spectrometer for the measurements. The gas pressure is measured by the transducer B_3 . In this system the volume comprised between the cold finger CT_1 and B_2 is made of glass while the region before the mass spectrometer is composed by metal tubes.

In both the systems most of the glass vacuum part is made by 8 mm inner diameter Pyrex tubing and valves are made of glass and teflon fitting (Glass Expansion, Australia). In metal part of the system used for the impurity measurements bellows valves (Swagelok) are employed.

2.3 Ozone decomposition in pressure sensors

The effect of metal surfaces on ozone may be seen from registering the pressure signal in a metallic pressure sensor (MKS 690) stabilized at 45°C . Figure 2.3a shows the rise of the pressure after release of ozone into the sensor. The observed pressure increase is due to the net reaction



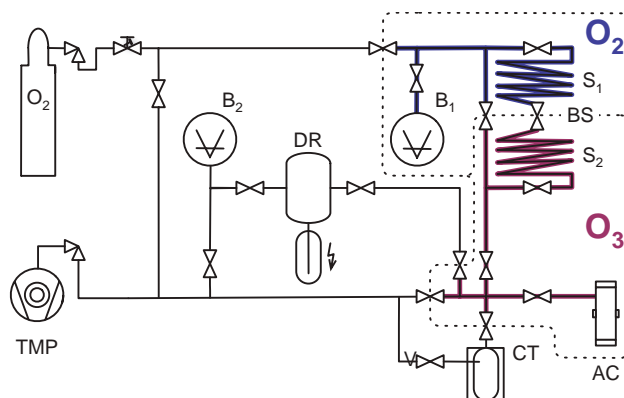


Figure 2.1: Scheme of the gas handling and buffer system used for generation of high purity ozone samples. TMP - turbo molecular pump; B1, B2 - 10 Torr and 1000 hPa Baratron, respectively; AC - absorption cell; BS - buffer spiral, consisting out of two spirals S1 and S2 that can be isolated from each other; DR - discharge reactor; CT - cold trap, V - glass valve. Gas lines that are filled with molecular oxygen and ozone are indicated through areas confined by dotted lines and by dark gray (blue) and light gray (red) color, respectively.

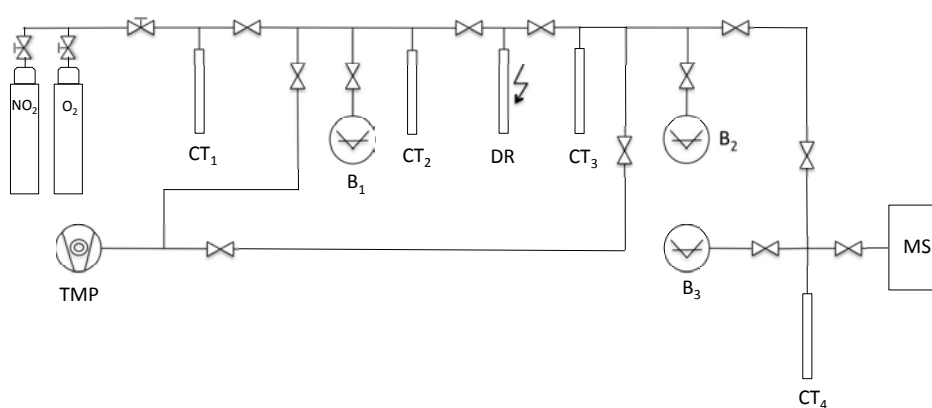


Figure 2.2: Scheme of gas handling used for measuring the impurity in ozone samples. TMP - turbo molecular pump; B1, B2, B3 - 10 Torr and 1000 hPa Baratron, respectively; CT1, CT2, CT3, CT4 - cold fingers; DR - discharge reactor, MS - mass spectrometer.

and implies that contact with the sensors leads to “contamination” with O_2 to an extent, which cannot be easily quantified. This can also comprise the accuracy of the pressure measurement, even if this effect as well as the contamination in ozone can be reduced by decreasing the surface to volume ratio. This is also due to the heat released in the decomposition process, which might contribute to an increase of the temperature in the pressure sensor leading to a less precise accuracy in the measurement. A strategy for precise ozone pressure measurements is therefore to use an inert buffer gas in the sensor. If this gas is pressure balanced with ozone in other parts of the apparatus, the pressure in the sensor can be read off quite reliably. The value will also faithfully reflect the ozone pressure in the absorption cell (AC, figure) for example, as long as diffusion of the buffer gas into the ozone volume and diffusion of ozone into the pressure sensor is negligible. This, however, can be achieved by proper adjustment of the diffusion length *via* introduction of a buffer spiral, for example. The right panel of figure (2.3) shows the effect of the buffer gas using the same pressure sensor and thus the minimization of contamination with O_2 induced from decomposition of ozone on metal surfaces.

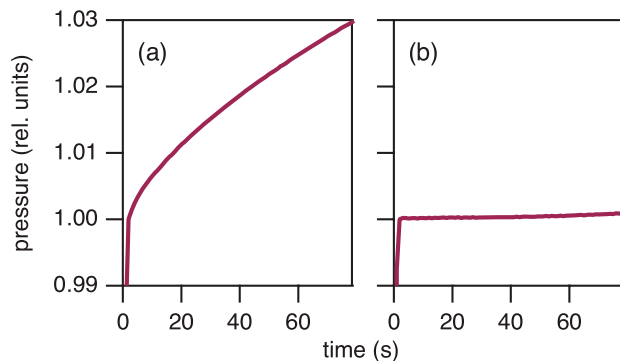


Figure 2.3: Pressure signal recorded during an experiment. The left panel (a) refers to a measurement of pure ozone, in the right panel (b) ozone and O_2 as buffer gas have been used.

2.4 Mass spectrometer

A mass spectrometer has been used as a gas analyzer for the nitrogen content of ozone samples generated by our dielectric barrier discharge setup. The particular instrument used is a double-focussing Mattauch-Herzog spectrometer [130], constructed and fabricated at the University of Minnesota. It has a sensitivity of $\eta = 7 \cdot 10^{-5}$ A/Pa and a mass resolution of $(M/\Delta M)_{1\%} = 56$. The general operation principle of a mass spectrometer which discriminates ions based on their mass over charge ratio (m/z), is schematically shown in figure 2.4: the main components are the ion source, the electric analyzer, the magnetic analyzer and a ion detector.

The gas under study is injected through a slit (1.27 mm \times 2.54 mm) into the ion source, shown in picture 2.5. There, molecules are ionized by electron impact and then accelerated. This region, named “box” or “shield”, has a cylindrical shape and its potential can be varied between +300 and +2400 V.

The ionizing electron beam is generated by a thin filament made from a tungsten-rhenium alloy and bent into the shape of a sharp pin. The electron beam is collimated by a perpendicularly oriented field of a permanent magnet of about $4 \cdot 10^{-2}$ Tesla, which forces the electrons

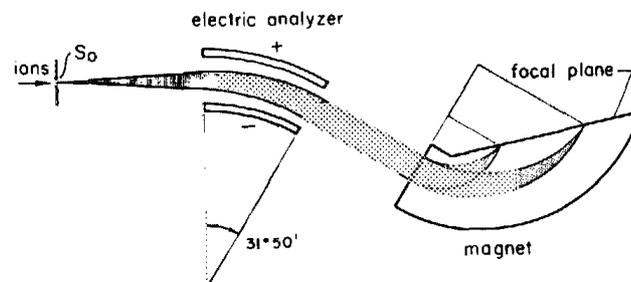


Figure 2.4: Schematic representation of a Mattauch-Herzog double focusing mass spectrometer. Picture taken from [131].

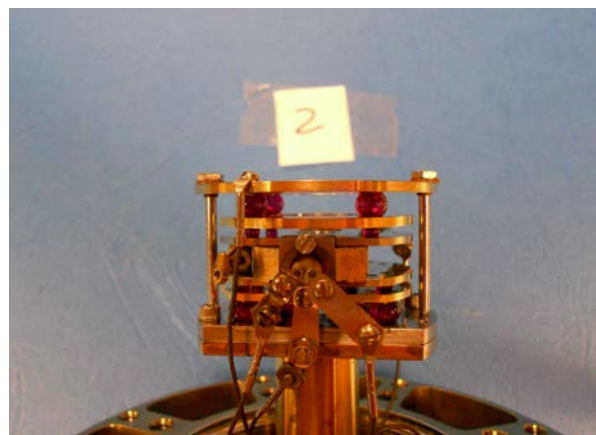


Figure 2.5: Picture of the ion source. The different plates as well as the sapphire balls used to insulate them are visible. The upper plate is the ion repeller below which the shield is mounted. The lower plates are those used to accelerate ions to the analyzer.

on a circular path and thus increases the ionization efficiency by augmenting the length of the path in the ion source region. Emitted electrons are then attracted by another, positively charged, filament which acts as electron trap. The potential of the emitting filament is usually set between 20 V and 100 V below the value chosen for the box, whereas the trap potential is about 27 V higher than the shield value.

The ions formed by electron impact are drawn towards the analyzer by two pairs of symmetric plates providing a positive potential, which decreases with distance from the shield. The efficiency of ion extraction is increased by means of the ion repeller which is placed between the injection slit and the ionizing region and kept at a potential between 100 and 105 % of the shield value. The extraction plate pair closest to the shield has a potential between 90 and 100 % of the shield while the second pair potential is between 70 and 90 % of the potential in the ion forming region. By varying these values it is possible to optimize the focussing of the ion beam that passes through the mass spectrometer entry slit of the ground plate. All plates in the ion source are made of Nichrome V alloy and insulated from each other by sapphire balls.

Once the positive ions leave the source, they pass the cylindrical electrostatic analyzer consisting of two coaxial electrodes which form a curved slit with radius r_e . The two electrodes produce a radial field, with the inner electrode being on a more negative potential than the outer one. The analyzer thus acts as an energy selector by only allowing ions to pass, where the centrifugal force of the ion on the curved trajectory is balanced by the electrostatic force created by the radial field E_r of the analyzer plates:

$$mv^2/r_e = eE_r, \quad (2.5)$$

where m is the ion mass, v its velocity, E_r the radial field strength on the curved trajectory of radius r_e and e the unit charge. Because the kinetic energy E_{kin} of the ion is determined by the accelerating potential U ,

$$E_{kin} = mv^2/2 = eU \quad (2.6)$$

equation (2.5) can be written as

$$r_e = 2U/E_r. \quad (2.7)$$

Energy filtering is evident from this equation, because by selecting E_r and r_e , only ions with a certain kinetic energy (defined by the accelerating potential U) can pass. Note that this filter does not provide a mass filter, because the ion mass does not enter into the transmission formula. Mass filtering is provided by the magnetic analyzer, which is placed behind the electrostatic analyzer. It provides a homogeneous magnetic field B perpendicular to the plane of motion. The Lorenz force F_B exerted on the ions in the magnetic analyzer is

$$F_B = evB, \quad (2.8)$$

where the vectorial character of the quantities could be ignored due to the motion being perpendicular to the field. Again, the Lorenz force needs to be balanced by the centrifugal force in order to keep the ions on a circular trajectory:

$$F_B = evB = mv^2/r_m, \quad (2.9)$$

where v is the tangential speed and r_m is the radius of the orbit described. This equation can be rearranged and rewritten as

$$mv = Ber_m, \quad (2.10)$$

which demonstrates that the magnetic field acts as a momentum analyzer, if ions on a partic-

ular orbit with radius r_m are selected by installing an exit slit at the corresponding position. Using the kinetic energy equation (2.6), the above equation is commonly written in the form of the so-called mass spectrometer equation¹

$$\frac{m}{e} = \frac{B^2 r_m^2}{2U}, \quad (2.11)$$

which gives the mass over charge ratio m/e as a function of the mass spectrometer parameters (U , B , and r_m).

The above relations provide a perfect imaging of the ions in the source to the exit slit of the mass spectrometer, provided that these are initially at rest and that the ion beam does not diverge. In reality this condition is not met and ions have initial kinetic energy that does not come from the electrostatic acceleration. In order to obtain a good resolution, one considers the effect of inhomogenities in the direction and velocity. These are compensated by the double focussing geometry of the Mattauch-Herzog configuration. In the discussion of the double focussing technique, we follow the description of Roboz [132]. Velocity focusing describes the imaging of a beam of ions which are homogeneous in mass and initial direction but which have an inhomogeneous initial velocity distribution. Once the beam is accelerated by the electrostatic field, a (velocity or energy) spectrum is produced in plane B of figure 2.6, which seems to originate from point E. The faster ions will be bent less than the slower ones. As an effect of the magnetic field and the speed dependent Lorenz force, faster ions will be bent more than the slower ones leading to focussing of the different velocities in a single point which depends on the mass. The velocity focussed spectrum therefore is located on the line g in figure 2.6.

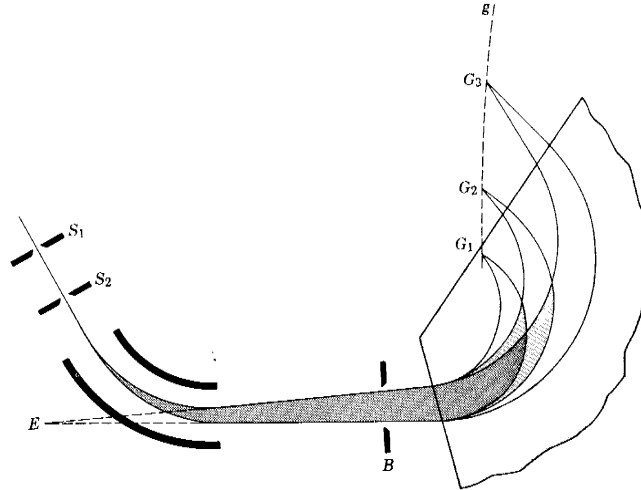


Figure 2.6: Principle of velocity - focusing. Picture taken from [132].

Figure 2.7 illustrates the combined effects of velocity and direction focussing in the mass spectrometer. Depending on their velocities, a slightly diverging beam of ions is direction focused after the electric analyzer (slit B). The different trajectories are then mass separated

¹The equation is often expressed in derived SI units by

$$m/e = 4.83 \times 10^{-5} B^2 r_m^2 / U$$

with r_m in cm, m in u, B in gauss and U in V.

by the action of the magnetic field. As before, this leads to velocity focussing (line g) if we look at the two diverging bundles having different velocities, and to direction focussing if we consider one bundle with homogeneous velocity. The interaction with the magnetic field is longer for ions that enter the field under a smaller angle of incidence. Generally, the points of direction focussing do not coincide with the points of velocity focussing, thus the two initial velocity bundles in the slit E are imaged to two different direction focussing points on the focusing line r .

If the two lines can be superposed by a proper choice of parameters, double focusing is achieved.

In the Mattauch-Herzog configuration [130] of our mass spectrometer the deflection angles ϕ_e and ϕ_m of the electric and magnetic fields are oriented in the opposite direction, $\phi_m = 90^\circ$ is chosen and the detectors of the mass spectrum are located directly within the exit plane of the magnetic field. The double focussing condition then requires that ϕ_e is equal to 31.8° [132].

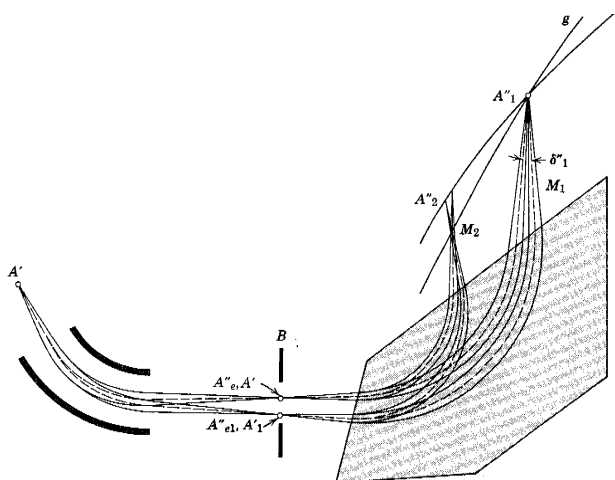


Figure 2.7: Double - focusing principle in mass spectrometry. Picture taken from [132].

2.5 Experimental procedure

Pressure measurements

As already explained in section 2.1, ozone is generated by an dielectric barrier discharge in molecular oxygen. The reactor (DR) is first filled with molecular oxygen (99.9995%, Alphagas 2, Air Liquid) and when a pressure between 40 hPa and 45 hPa is reached the valve connecting the reactor with the rest of the system is closed. On the external part of the cylindrical extension two electrodes are fixed and the lower reactor part with the electrodes is immersed into LN₂. The discharge is then started ($U \simeq 10\text{kV}$, $f = 20\text{kHz}$) and stopped once the pressure has decreased to about one half of the initial value. This avoids the build up of a delocalized low pressure discharge which extends to all the reactor volume and allows for interaction between plasma constituents (electrons, ions, ...) and the teflon fittings that could possibly create contaminants and impurities.

After the discharge, the ozone sample is pumped for a few minutes. Since molecules of oxygen can also be trapped in the liquid, the mixture is evaporated, re-condensed and

pumped once again. By taking off the liquid nitrogen ozone is now ready to be released into the gas phase and fill the volumes of the system to clean all of them. Once this has occurred the valve to the discharge reactor is closed and ozone again condensed and pumped continuously for about 30 min until the pressure does not reach the value of $1 \cdot 10^{-5}$ Pa. A value lower than this cannot be reached due to the vapor pressure of ozone. Therefore the cold trap is cooled down, the valve to the turbo pump closed and the valve which connects the discharge reactor to the system is opened while ozone is admitted to the spiral, the Pyrex tubing in front of the absorption cell and the transducer B_1 . The amount of O_3 is monitored by the transducer and once the desired pressure is reached the cold trap is opened to let the ozone condense inside it. When all the ozone is condensed, the cold trap is closed and the rest of the vacuum system is pumped.

Thereafter, the spiral S_1 and the volume in front of the transducer (blue region in figure 2.1 labeled as " O_2 ") are prepared. They are filled with an amount of molecular oxygen equal to the estimated ozone amount. The valve V is kept closed and at the same time the cold trap is warmed using a water bath in order to heat ozone and fill the absorption cell (or the mass spectrometer in some cases). Once ozone is released into the cell, the valve connecting the trap to the vacuum system is closed in order to avoid the diffusion of less volatile impurities such as water or carbon dioxide. Then ozone is expanded into the still evacuated part of the buffer spiral S_2 and the valve between the two spirals is opened immediately in order to equilibrate the pressure in both spiral arms. The value of the pressure is then read from the sensor B_1 and the absorption cell is closed.

Impurities measurements

The goal is to determine an upper limit for the content of nitrogen oxides in the ozone samples. Due to their reactivity (with ozone) and the possibility of heterogeneous reactions, these nitrogen oxides are difficult to quantify (see section section 2.6 below). Our analysis will therefore be based on the simulation of the ozone generation procedure using oxygen gases with known degrees of contamination through nitrogen containing gases and on studying how contaminated samples are transferred in the trapping process. In order to keep the original system as clean as possible, these laboratory simulations have been performed at the duplicate system that is directly connected to a mass spectrometer.

In the duplicate system, ozone is generated following the procedure explained in the previous section. Due to the slightly larger diameter of the discharge reactor, initial oxygen pressures are kept somewhat below 40 hPa in order to ignite the discharge. When the pressure reaches one half of the initial oxygen pressure the discharge is stopped and the condensate pumped for few minutes. By taking off the LN_2 bath from the discharge reactor and simultaneously cooling down the cold finger CT_3 ozone is then transferred and stored. Other gases (NO_2 or CO_2) can be introduced and stored in the cold finger CT_2 . In case it is condensible it is frozen and the condensate is pumped for few minutes in order to get rid of impurities. Ozone and the other gas are let mix in the volume including the discharge reactor, CT_2 and CT_3 and therefore are transferred in the volume in front of the mass spectrometer by cooling down the cold finger CT_4 . The valve between this volume and the rest of the vacuum system is then closed and the connection to the mass spectrometer is opened. In this way the gas enters the mass spectrometer in which it can be analyzed.

2.6 Impurities in ozone samples

2.6.1 General considerations

A main contaminant of ozone samples generated in the vacuum system is molecular oxygen. O_2 gas might be trapped with ozone at the cold surface during the process of discharge ozone generation. It might also diffuse into the sample volume when used as a buffer gas during the pressure measurements or arise from the in-situ decomposition of ozone. Another possible source is air leakage during the handling process, which also adds nitrogen N_2 and argon Ar as primary contaminants. In addition, H_2O , always being present in a vacuum system, has to be considered as a potential pollutant as well as CO and CO_2 that may stem from oxidation of organic materials (through ozone). Other possibly relevant impurities are nitrogen oxides (N_2O , NO_2 , NO, NO_3 , N_2O_3 , N_2O_4 , N_2O_5) and the corresponding acids (HNO_2 and HNO_3) which can arise from traces of air that can be present during the discharge.

From a practical point of view, contaminants in the ozone sample can be divided into noncondensable and condensable species. Non-condensibles have been estimated in previous measurements by simply analyzing the residual gas which resides in the cold trap after the freezing back the ozone after a measurement. The main components have been found to be O_2 and N_2 , the former originated in ozone decomposition process, the latter entering in the vacuum system during or after the recovery of ozone. In principle CO could also be present in the system as impurity and like N_2 it has a main peak at $m/z = 28$. However, it is unlikely that CO comes from impurities during the discharge, because it would most likely form CO_2 under these conditions. While CO_2 condenses with O_3 , the remaining CO would stay in the gas phase where it would be pumped away. The main explication for the presence of CO in ozone is the degassing from the epoxy adhesive used to glue the windows in the absorption cell or reaction of ozone with the adhesive.

Several condensable and non-condensable contaminants (H_2O , CO_2) have been previously measured by VIS light and by laser absorption spectroscopy in the infrared (IR-TDLAS). For species with a weak absorption in the IR, such as N_2O , a multi-pass cell (50 m of absorption path) was employed. The absorption signal for all the condensable impurities was less than the detection limits of about $0.1 \text{ mmol mol}^{-1}$. A summary of the ozone purity analysis and results obtained from previous studies performed in the vacuum system employed in this thesis and using different measurement methods are displayed in table 2.1. Quantification of the contamination by nitrogen containing oxygen species will be discussed in the remainder of this chapter.

2.6.2 Evaluation of individual nitrogen containing impurities

Within the discharge, a variety of nitrogen oxides can be formed if small amounts of air and thus of N_2 are present. N_2O is chemically very stable and does not react with ozone. Once formed, it could thus potentially be transferred into the ozone sample. IR laser absorption spectroscopy on samples transferred into the absorption cell confirmed insignificant and negligible contamination by N_2O with observed mole fractions of $(0.3 \pm 0.3) \text{ mmol mol}^{-1}$ (see table 2.1).

Higher oxides (NO, NO_2 , NO_3 , N_2O_3 , N_2O_4 , N_2O_5) mostly react with ozone and with each other. What is more, these oxides may stick to the surface and form acids with H_2O molecules that are adsorbed there. The gas phase chemistry of these species can be modeled easily [133], but there will remain large uncertainties linked to the role of heterogeneous chemistry.

Nevertheless, chemical kinetic arguments can be made to demonstrate that concentrations of NO and NO_2 should be extremely low. Larger molecules, on the contrary, should be efficiently removed by the different evaporation and recondensation cycles as well as by the

impurity	method ^b	mole fraction ^a	
		measurand (mmol mol ⁻¹)	uncertainty (mmol mol ⁻¹)
H ₂ O	IR-TDLAS ^c	-0.10	0.17
CO ₂	IR-TDLAS ^d	0.07	0.07
nitrogen oxides			
N ₂ O	IR-TDLAS ^e	0.3	0.3
NO ₃	VIS-TGMAS ^f	-0.01	0.06
total (H _x NO _y) ^{g, h}	MS	0.5 ⁱ	
O ₂ + N ₂	<i>p</i> , MS	1 ⁱ	
CO	<i>p</i>	0.01 ⁱ	

^aMole fractions based on the measurement of a particle number density n have been obtained by referencing to the typical ozone sample size of 3.33 hPa at 295 K: $n_{ref} = 8.18 \times 10^{24} m^{-3}$.

^bIR-TDLAS – infrared tunable diode laser absorption spectroscopy; VIS-TGMAS – visible light tunable grating monochromator absorption spectroscopy; *p* – pressure measurement, MS – mass spectrometry

^cabsorption line at 1868.054020 cm⁻¹

^dabsorption line at 2284.590978 cm⁻¹

^eabsorption line at 1133.050970 cm⁻¹

^fabsorption band at 662 nm

^gsee section 2.6.3

^hH_xNO_y = N₂O + NO + NO₂ + N₂O₃ + N₂O₄ + N₂O₅ + NO₃ + HNO₂ + HNO₃

ⁱupper limit

Table 2.1: Results of the ozone purity analysis

cryogenic transfer of ozone samples into the measurement cell. Reaction of ozone with NO or NO₂ is described by the following rate equation

$$\frac{d[O_3]}{dt} = k_{NO_x}[O_3][NO_x] \quad (2.12)$$

where the values for the rate coefficients k_{NO_x} are $3.2 \times 10^{-17} \text{ cm}^3 \text{ s}^{-1}$ and $1.7 \times 10^{-14} \text{ cm}^3 \text{ s}^{-1}$ for NO₂ and NO, respectively. In the samples transferred to the absorption cell, the decay of ozone has been measured repeatedly and a typical rate of $r = [O_3]^{-1}d[O_3]/dt = -0.2\%/h$ or $5.6 \times 10^{-5} \text{ s}^{-1}$ has been observed. Assuming that all of the ozone decay is due to any of the two oxides, we can rearrange eq. (2.12)

$$\frac{[NO_x]}{[O_3]} = \frac{-r}{k_{NO_x}[O_3]}, \quad (2.13)$$

and obtain an upper limit for the two species using the corresponding rate coefficients. Because ozone samples in the cell were at a pressure of about 3.3 hPa, one obtains the following mole fractions: $[NO]/[O_3] = 4 \times 10^{-10}$ and $[NO_2]/[O_3] = 2 \times 10^{-7}$. NO₃ has been determined independently by spectroscopic means, and it has been found to be negligible ($[NO_3]/[O_3] = -0.01 \pm 0.06 \text{ mmol/mol}$).

In order to investigate on the products of the rapid oxidation of NO and NO₂ by ozone, NO₂ has been added to ozone in the gas phase and the products were analyzed by MS.² As a reference, the mass spectrum of pure NO₂ has been taken (figure 2.8) first. As can be seen, NO₂ can be identified by main peak at ($m/z = 30$), which corresponds to a NO⁺ fragment of the parent molecule/ion with $m/z = 46$.

Next, ozone was produced and transferred into the cold finger (CT₃ in Figure 2.2) and

²Note that only NO₂ and not NO has been used, because NO₂ was readily available and because NO would also rapidly react with ozone to form NO₂.

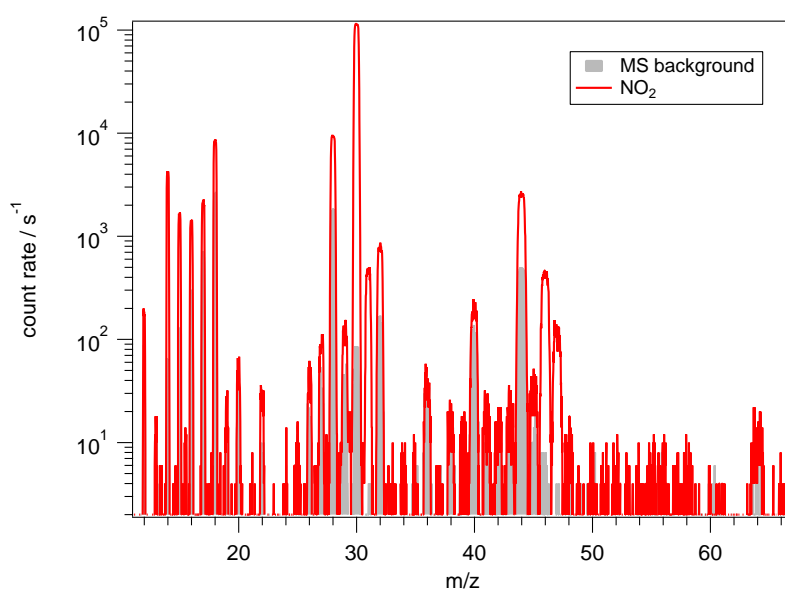


Figure 2.8: Mass spectrum of pure nitrogen dioxide NO_2 in red color. The grey area is the background measured in the mass spectrometer.

NO_2 was added. This was done by introducing an amount of pure NO_2 (Alphagaz, Air Liquide) corresponding to about $[\text{NO}_2]/[\text{O}_3] = 30\%$ into the vacuum system and by then freezing the gas into the ozone containing trap. The two gases were then released into the gas phase and expanded before the MS, where the product could be analyzed. Figure 2.9 shows the time resolved signals on selected m/z numbers of the gas analysis after correction for the empty MS background. As can be seen, most of the signal is on $m/z = 32$, which is due to ozone that has been converted to oxygen either by reaction with NO_x or by catalytic conversion on the metal surfaces of the vacuum system. Note that the ozone conversion is almost complete, but some ozone ($\simeq 1/4$) seems to have survived. This is because the covarying signals $m/z = 32$ and 16 increase upon removal of LN_2 after having pumped on the condensate. Signals at $m/z = 30$ or 46, which would correspond to nitrogen oxides are at least one or two orders lower than what corresponds to the initial $[\text{NO}_2]/[\text{O}_3]$ ratio and at least the $m/z = 30$ signals seems most likely due to background effects in the MS (it covaries with water at $m/z = 18$ and does not show sharp changes due to changing the gas load into the MS). Interestingly, count rates at $m/z = 46$ roughly covary with the sample gas at $m/z = 32$, but the signals differ by three orders of magnitude. It is difficult to interpret these measurements quantitatively. First, we do not know the mass spectra of the potentially relevant nitrogen oxides, whose masses also likely exceed the detection range ($m > 60$ Da). Second, these molecules are to a large extent also difficult to handle due to their stickiness (HNO_3 , for example). A likely fate of the nitrogen oxides is that they get converted to acids that stick to the walls, most likely already in the cold finger where the mixture has been prepared. Even if they get into the mass spectrometer inlet, they might get stuck there too. Signals corresponding to these molecules are therefore expected to be low and ambiguous.

Because of these limitations and also because of the difficulty to set up an adequate system for the measurement of individual compounds, another indirect, but robust approach has been chosen for estimating nitrogen containing contaminants.

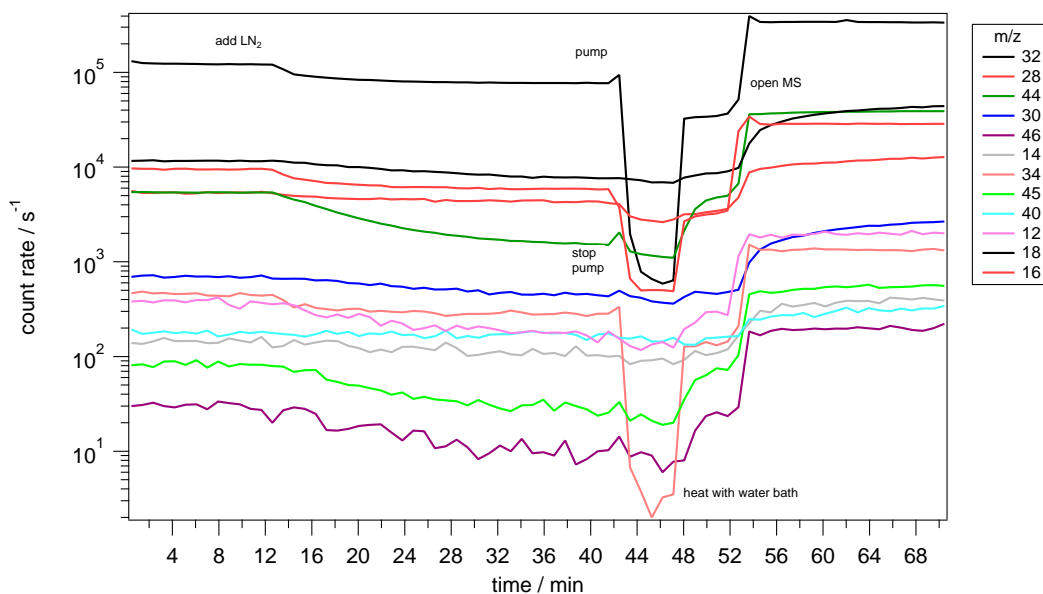


Figure 2.9: Mixture of 9.16 torr of O_3 and 3.6 torr of NO_2 . The gas is transferred in the MS and after $\simeq 12$ min was condensed using LN_2 . The rapid decreasing in the number of counts after 45 minutes is due to several condensations of the mixture using LN_2 followed by pumping of non condensibles and expansions after having closed the valve to the pump. The mixture is then heated with a water bath. Counts due to NO_2 are already low at the beginning of the measurement showing that this compound is lost during the transfer to the MS.

2.6.3 Quantitative estimate of the sum of nitrogen containing contaminants

This alternative analysis leads to an upper limit of the sum of all nitrogen containing contaminations provided that these are derived from N_2 . This is the most likely scenario given the abundance of nitrogen in air and the possibility of small leaks in the glass vacuum system equipped with teflon fitted glass valves. It is therefore assumed that N_2 may have leaked in before or during the oxygen discharge and the estimate is based on mass balance considerations.

Nitrogen (N_2) and pure molecular oxygen (O_2) have been mixed at typical discharge pressures in the 30 hPa range. Then an electric discharge has been performed under normal conditions, *ie.* in the presence of LN_2 to condense out ozone and other unwanted reaction products. By varying the initial $[N_2]/[O_2]$ ratio, the following observation could be made: for $[N_2]/[O_2]$ below 10 mmol/mol the discharge color is purple, whereas for higher values the color tends to be white. Thus, since the color during ozone generation under non-contaminating conditions is purple, it can safely be concluded that leakage of N_2 is restricted to $[N_2]/[O_2]$ mole fractions < 10 mmol/mol. Therefore, a $[N_2]/[O_2] = 1/100$ mixture was prepared from which ozone had been generated in the usual way. The final amount of gas has been kept at 15 % which allows to derive a conservative estimate. The residual gas has then been analysed for N_2 , which by mass balance considerations, implies an upper limit for the nitrogen content in the condensate. Interestingly, the condensate product in the discharge is depleted in nitrogen, because the residual gas is enriched in N_2 by a factor of 6.5 ± 0.2 , as shown in figure 2.10. This is most likely due to the much higher binding energy of N_2 as compared to that of O_2 . Starting from the initial mole fraction $x_i = N_i(N)/N_i(O)$ and corresponding definitions x_c and x_g for the condensed and for the residual gas phase, respectively, we can use the mass

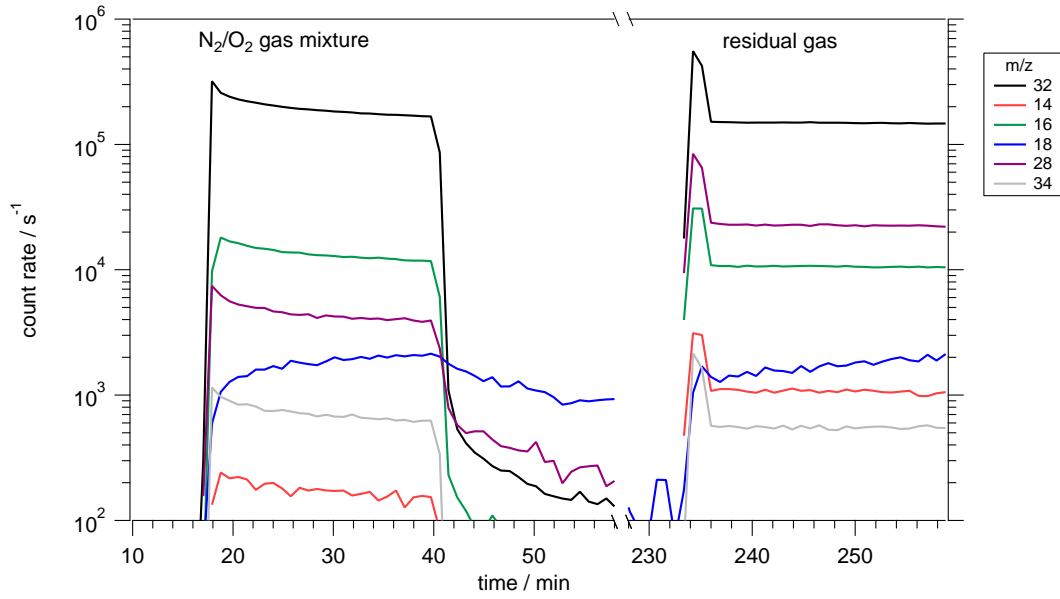


Figure 2.10: Mixture of $[N_2]/[O_2]$ (peaks on the left) and residual gas after a discharge (peaks on the right). The residual gas is enriched in N_2 if compared to the mixture before ozone generation.

balance equations

$$N_g(N) + N_c(N) = N_i(N) \quad (2.14)$$

$$N_g(O) + N_c(O) = N_i(O) \quad (2.15)$$

together with the degrees of conversion

$$f = \frac{N_c(N) + N_c(O)}{N_i(N) + N_i(O)}, \quad (2.16)$$

$$f_O = \frac{N_c(O)}{N_i(O)}, \quad (2.17)$$

$$f_N = \frac{N_c(N)}{N_i(N)}, \quad (2.18)$$

in order to derive the N/O ratio in the condensate

$$x_c = \frac{N_c(N)}{N_c(O)}. \quad (2.19)$$

Let us also introduce the nitrogen enhancement ratios

$$r_c = x_c/x_i \quad (2.20)$$

$$r_g = x_g/x_i. \quad (2.21)$$

After rearranging equations (2.16)–(2.18)

$$(1 + x_i)f = f_O + f_N x_i, \quad (2.22)$$

we can eliminate f_N because of $f_N/f_O = x_c/x_i = r_c$ and obtain

$$f_O = f \frac{1 + x_i}{1 + r_c x_i}. \quad (2.23)$$

Then, we simplify

$$\begin{aligned}
 x_c &= \frac{N_c(\text{N})}{N_c(\text{O})} = \frac{N_i(\text{N}) - N_g(\text{N})}{N_c(\text{O})} = \frac{N_i(\text{N})}{N_i(\text{O})} \frac{1 - N_g(\text{N})/N_i(\text{N})}{f_{\text{O}}} \\
 &= x_i \frac{1 - x_g N_g(\text{O})/N_i(\text{N})}{f_{\text{O}}} = x_i \frac{1 - x_g(1 - f_{\text{O}})N_i(\text{O})/N_i(\text{N})}{f_{\text{O}}} \\
 &= x_i \frac{1 - (1 - f_{\text{O}})x_g/x_i}{f_{\text{O}}} = x_i \frac{1 - (1 - f_{\text{O}})r_g}{f_{\text{O}}}.
 \end{aligned} \tag{2.24}$$

in order to arrive at a second equation in x_i , r_g , r_c and f_{O} :

$$f_{\text{O}} = \frac{1 - r_g}{r_c - r_g}. \tag{2.25}$$

From this we derive

$$r_c = \frac{(1 - r_g) + f r_g(1 + x_i)}{f(1 + x_i) - x_i(1 - r_g)} \tag{2.26}$$

as a function of the observables x_i , r_g and f . In particular, for $f = 0.15 \pm 0.01$, $x_i = (1.0 \pm 0.1)\%$ and $r_g = 6.5 \pm 0.2$ we obtain a reduction of the N/O ratio in the condensate by a factor of $r_c = 11$. If uncertainties are taken into account, a reduction by a factor of 5 or more is still obtained. Because we convert about $f = 50\%$ of the original oxygen, and not $f = 85\%$ as in this simulation experiment, the suppression factor even in this worst case is 8. With this scenario and making the conservative hypothesis that the nitrogen oxides are all monatomic in N (as in HNO_3 for example), this leads to the upper limit for the mole fraction of the nitrogen contaminants of $[\text{HNO}_3]/[\text{O}_3] = 1.3$ mmol/mol.

As discussed before, a further reduction of contamination will likely occur during the release of the ozone sample into the measurement volume. Ozone release is realised by rapidly heating the condensate which leads to evaporation of the more volatile compounds first. The gases NO , O_3 , N_2O , CO_2 , N_2O_3 , $\text{NO}_2/\text{N}_2\text{O}_4$, N_2O_5 , and HNO_3 have respective boiling points at 121.7, 161.8, 184.7, 194.7, 276, 294.3, 303, and 356 K [6]. Except for NO , which should have been converted due to the large abundance of ozone, and for N_2O , which has been investigated separately, N containing compounds will be kept back efficiently in the cold trap upon removal of the LN_2 bath. This should be at least as efficient as the retention of carbon dioxide, which is also released into the gas phase somewhat later than ozone. This retardation effect has been verified by the MS analysis of simulated releases of well prepared O_3/CO_2 mixtures in the duplicate vacuum system. It was found that rapidly evaporated gas contained at least three times less CO_2 than the original gas mixture. If we take this factor into account, the previously given upper limit is again reduced by a factor of three, thus yielding a refined upper limit value of 0.5 mmol/mol for the total of nitrogen contaminants.

2.7 Short chapter summary and outlook

- A vacuum system for the production and quantification of high purity ozone samples has been presented.
- A mass spectrometer system for the analysis of nitrogen containing contaminants has been presented.
- A variety of possible contaminants has been discussed and previously made and spectroscopically based contamination measurements of individual contaminating substances have been summarized.

- Kinetic and thermodynamic arguments have been presented that support a very low contamination by nitrogen containing species.
- Based on a mass spectrometric investigation, an independent and experimentally derived upper limit of 0.5 mmol/mol has been derived for the mole fraction of all nitrogen containing species.
- The present results will allow for ozone cross section measurements with an uncertainty below 1 % at the 95 % level of confidence.
- The results presented in this chapter have been published in Ref. [133].

Chapter 3

Critical analysis of previous experiments on the $O + CO$ reaction

So far, only two experimental studies, one performed by Bhattacharya and Thiemens in 1989 (BT89) [119] the other by Pandey and Bhattacharya in 2006 (PB06) [134], have been devoted to the investigation of the reaction between oxygen atoms and carbon monoxide. Both studies claim that the observed mass independent isotope enrichment of the product CO_2 is due to the thermal gas phase reaction $O + CO + M \rightarrow CO_2 + M$. But the role of ozone that is present in both of these experiments and a possible isotope transfer from ozone to CO_2 has not been discussed in detail, making the conclusion somewhat questionable. This is even more so because the chemical system used to interpret the measurements seems to be incomplete in both cases. In the BT89 experiments, chemistry involving excited oxygen atoms has been neglected despite the energetic light sources used. The PB06 experiment tended to minimize the impact of excited oxygen chemistry by choosing a different light source with dominant emission in the visible, but there was still evidence for an additional CO_2 formation channel. Indeed, this channel was the dominating CO_2 formation pathway, surpassing the gas phase $O + CO$ reaction, but its nature and its isotope fractionation effects are unknown, thus also questioning the proposed explanation.

In this chapter the analysis of the BT89 experiment is revisited and problems of the originally proposed explanations are discussed. Then a new interpretation of the three isotope data is given. It relies on isotope transfer from ozone via excited oxygen atoms and formation of CO_2 via OH. In addition, an overview and a first critical discussion of the PB06 experiment is provided.

3.1 The experiment of Bhattacharya and Thiemens (1989)

In the BT89 experiment mixtures of carbon monoxide and O_2 have been irradiated with UV light emitted from a Hg (180 to 260 nm) or Kr lamp (120 to 160 nm) in a spherical 5.2 l pyrex reactor for time intervals comprised between 16 and 43 hours. For each run molecular oxygen was photolysed in order to produce oxygen atoms which could react with CO to form CO_2 . Once produced, carbon dioxide is continuously condensed out in a LN_2 trap connected to the reaction sphere. The determination of both the enrichments, $\delta^{17}O$ and $\delta^{18}O$, in the produced CO_2 was done by conversion to O_2 , using BrF_5 , which gives CF_4 and O_2 . The oxygen was then analyzed with a mass spectrometer.

The kinetics of these experiments was assumed to occur according to the following se-

quence of reactions:



Molecular oxygen is photolysed by the UV radiation leading to atomic oxygen formation (reaction (3.1)), the last reacting with both O_2 and CO to form respectively ozone and carbon dioxide (reactions (3.2) and (3.3)). These two compounds undergo the photolysis process via reactions (3.4) and (3.5). O atoms may also react with O_3 to annihilate “odd oxygen” (O , O_3) via



Besides processes described by reactions (3.1) - (3.6), the following isotopic exchange reactions must be taken into account



These take place on the same electronic potential surfaces relative to the respective association reactions (3.2) and (3.3). In the low pressure limit both the direct and forward reactions (3.7) and (3.8) are predominant since they occur on a faster time scale as compared to the association reactions. An isotopic equilibrium between atoms and molecules is established with equilibrium constants $K_{1.6}$ and $K_{1.7}$ given by¹

$$K_{1.6} = \frac{[^{16}\text{O}][^{16}\text{O}^{18}\text{O}]}{[^{18}\text{O}][^{16}\text{O}_2]} \quad (3.9)$$

$$K_{1.7} = \frac{[^{16}\text{O}][\text{C}^{18}\text{O}]}{[^{18}\text{O}][\text{C}^{16}\text{O}]} \quad (3.10)$$

From the knowledge of these equilibrium constants which can be calculated from spectroscopic data [136] and from the isotope composition of molecular oxygen and carbon monoxide, the ratio $^{18}\text{O}/^{16}\text{O}$ can be determined. It has been found that at room temperature this ratio is respectively depleted by about 71‰ and 95‰ with respect to molecular oxygen and carbon dioxide [135, 73]. Because CO is at least 175 times more abundant than O_2 , it will essentially not change its original isotopic composition, but molecular oxygen will adjust as to simultaneously fulfill the two equilibria (3.9) and (3.10).

Under the above described experimental conditions, *i.e.* in the presence of UV light ($\lambda < 411$ nm), photolysis products of ozone can also be produced in electronically excited states (see chapter 5). Even CO_2 can be photolysed when the Kr lamp is used. This has been the case in two out of the ten experimental runs carried out. However, the excited state chemistry ($\text{O}(^1\text{D})$, $\text{O}_2(^1\Delta_g)$) is not contained in the set of reactions (3.1)–(3.5) and it is also not discussed in the BT89 paper. However, it is now known that $\text{O}(^1\text{D})$ can transfer the anomalous isotope composition of ozone over to CO_2 [113, 103] by a direct exchange reaction.

¹For an exchange reaction between diatomic molecules and atoms written in the form $\text{ZY} + \text{Y}' = \text{ZY}' + \text{Y}$ where the element Y has two isotopes Y and Y', the equilibrium constant is expressed as $K = \frac{\text{ZY}'/\text{Y}'}{\text{ZY}/\text{Y}}$ being quantities in square brackets the concentrations of the species [135].

Moreover, reaction of $O(^1D)$ with water generates OH, which via



provides an efficient oxidation route for CO, also providing a pathway for transferring the isotopic composition of ozone to CO_2 .

The experimental results obtained by BT89 are shown in the three isotope plot of Figure 3.1, where $\delta^{17}O$ in the product CO_2 is plotted versus $\delta^{18}O$ of the same compound. The δ -values have been calculated relative to a laboratory standard and are reported in Table 1 of the BT89 paper. The data form a line with a slope of about 0.82 covering a range of 50.5 ‰ in $\delta^{18}O$. The points obtained in experiments performed with the Hg lamp (circles in Figure 3.1) cover a more restricted range of 28 ‰ for $\delta^{18}O$ whereas the two highest enrichments have been obtained using the Kr lamp as light source (squares in Figure 3.1).

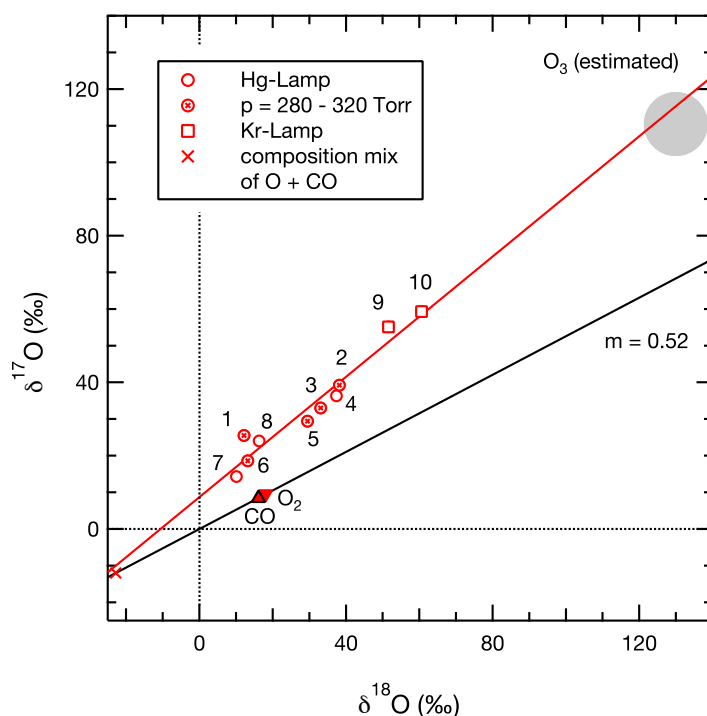


Figure 3.1: Three isotope plot showing the isotopic composition of CO_2 produced in BT89 experiments. Circles and squares refer to CO_2 in Hg - Lamp and Kr - Lamp experiments respectively and the red line is a fit through all of them. Initial CO and O_2 composition are given by solid up and down triangles and lie on the black line which is the mass dependent fractionation line with a slope of 0.52 and passing through the origin of the diagram. The red cross is the combined isotopic composition of $O(^3P)$ and CO whereas the grey circular area is the estimated composition of ozone produced in the experiments.

According to BT89 the slope of 0.82 in the three isotope plot of Figure 3.1 is exclusively due to formation of CO_2 from O and CO (reaction (3.3)) and it is supposed that the reaction induces a mass-independent fractionation similar to the ozone forming reaction (3.2), where product molecules are enriched in both the heavy oxygen isotopes. The authors also note that CO_2 formed from the O + CO reaction should be depleted with respect to the standard as indicated by the red cross (“isotope composition mix”) in Figure 3.1, if there is no fractionation associated with the CO_2 formation reaction itself. This is due to the depletion of the atomic reservoir via the atom exchange reactions (3.7) and (3.8). Reactions involving isotopic exchange (3.10) and eventual photolysis of CO_2 in the case of the Kr lamp likely

occur in a mass dependent way.

Nevertheless, the interpretation has one major drawback, apart from the neglect of excited state chemistry. It cannot explain the large spread in the δ -values of the experimental data which determines the slope of the array (28 ‰ for $\delta^{18}\text{O}$), because carbon dioxide is formed under almost constant experimental conditions, *i.e.* pressure, temperature and reaction extent are not varied very much. Isotope fractionation produced by a mass independent O + CO process should therefore lead to a unique isotope composition represented by a single point on the three isotope plot. The coordinates of this point are fixed by the initial composition of carbon monoxide, by the equilibrium constant (3.10) and the kinetic isotope fractionation in reaction (3.3).

More precisely, the runs have been performed while the temperature has been kept at the constant value of 298 K, and the total pressure has been varied in the 200 – 400 Torr (270 – 530 hPa) range, but variations in pressure do not seem to be causally related to the observed variability of the CO₂ isotopic composition. If, for the moment, the analysis is restricted to the Hg-lamp experiments (8 out of 10 runs), we note that a variation in $\delta^{18}\text{O}$ of 16.3 ‰ and 21.1 ‰ is observed for two pairs of runs performed at identical pressures. One pair at 320 Torr, the other one at 400 Torr (points 5&6 and 4&8). Thus, more than half of the total spread does not depend on the absolute pressure. In addition, five experiments (circles with a cross in Figure 3.1) have been made at pressures in the 280 – 320 Torr pressure range, thus by varying the pressure less than 14%. However, these data cover already a variation of 26 ‰ in $\delta^{18}\text{O}$, which is very close to the total span of 28 ‰. Taking into account also the two Kr-lamp experiments at pressures of 310 and 280 Torr the spread in $\delta^{18}\text{O}$ is extended to 48.4 ‰ with the data still following the same three isotope line and with pressures still being restricted to the 280 – 320 Torr range. At this point it must be concluded that pressure is not at the origin of the observed variability of the data.

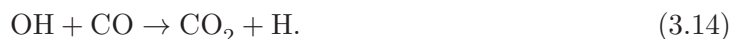
Furthermore, the initial pressure of CO does not significantly change during the runs since formation of CO₂ is slow. In fact, only a fraction of less than 0.7 ‰ of the initial CO is converted to carbon dioxide. As a consequence no Rayleigh-type fractionation pattern along a line through the initial CO reservoir will be created. In addition, initial O₂/CO ratios vary only between 1/178 and 1/423 causing some variability in O-atom source strength, but not in their isotopic composition which is, instead, settled by equations (3.7) and (3.8).

The last experimental condition that could have impacted the isotope composition of CO₂ and thus have caused the observed spread of enrichments are changes related to CO₂ photolysis, such as a variability in the lamp intensity. BT89 assume that carbon dioxide photodissociation leads to mass dependent enrichment of the residual gas, while in a later study [137] from the same authors it has been shown indeed that photolysis by Kr depletes photodissociation products in a mass dependent fashion by less than 80 ‰ in heavy oxygen and photolysis by Hg induces an almost exclusive (anomalous) enrichment of up to 150 ‰ in ¹⁷O in the photolysis products. However, the study on CO₂ photolysis [137] used an experimental setup similar to the one used by BT89 and the small photolysis efficiency (< 2% for photolysis times between 15 and 40 hours) should be about the same in the two studies. Since only $\simeq 1.5\%$ of the produced CO₂ was photolysed by the Hg or Kr-lamp runs over several hours, this actually indicates that even a fractionation of less than 80 ‰ during the photolysis process will change the CO₂ isotopic composition by not more than 1.5 ‰, which is an order of magnitude lower than the observed variability in ¹⁸O. As a matter of fact, no change in $\delta^{18}\text{O}(\text{CO}_2)$ has been observed in these photolysis experiments, whereas $\delta^{17}\text{O}(\text{CO}_2)$ has been reduced by 0.8 ‰ during the photodissociation experiment.

It must therefore be concluded that the line of slope 0.82 in BT89 experiments is not due to an eventual mass independent fractionation effect in reaction (3.3) alone, because this cannot explain the data spread, which would need to be explained by a second fractionation

mechanism that follows the same three isotope slope. This is an unlikely case, however. Finally, the difference between Kr and Hg lamps, that is also marked by the same $\delta^{17}\text{O}$ vs $\delta^{18}\text{O}$ slope of 0.82, would also need to be explained.

The preferred explanation must not only justify the isotope variability and the observed mass dependent enrichment, but also the difference between the Hg and Kr lamps. Due to the presence of ozone, formed *via* reaction (3.2) in an anomalous fashion and UV light, a likely explanation is the transfer of the anomaly from ozone to CO_2 through the following scheme



In this mechanism, ozone is photolysed by UV light forming atomic oxygen in its first excited state which then reacts with water which is always present as a trace substance in vacuum systems. OH radicals thus produced in reaction (3.13) will have an isotopic composition related to ozone and by reaction with carbon monoxide (3.14), this will be transferred into the newly formed CO_2 . In this model, carbon dioxide forms by two competing reactions (3.13) and (3.14) with two different isotopic signatures, one transferred from ozone and related to the OH pathway and the other one from the reaction between carbon monoxide and oxygen atoms. Depending on the relative importance of the two pathways, the observed variability can then be explained by the competition of these two pathways. Therefore the CO_2 isotopic composition should be located in a three isotope plot on the mixing line having the two sources as end members. The one end member, related to ozone, is in the upper right corner of the plot (grey area in Figure 3.1) since it is produced in the $\text{O} + \text{O}_2$ reaction with $\delta^{18}\text{O} \simeq \delta^{17}\text{O} \simeq 110\%$ if compared to the initial molecular oxygen composition. The other end member is located in the lower left corner and is related to the $\text{O} + \text{CO}$ reaction which forms CO_2 most likely without any fractionation, because the line goes through the bulk mixing point of O and CO (red cross).

It must be underlined that the above given interpretation not only is capable of motivating the mass independent fractionation pattern and the observed variability. It also seems to provide a rationale for the difference in the $\delta^{17}\text{O}$ vs $\delta^{18}\text{O}$ data along the slope 0.82 line when the different lamps are used. In fact, the yield of $\text{O}({}^1\text{D})$ which determines the role of the $\text{CO} + \text{OH}$ chemistry is related to the lamp emission spectra. Because radiation from the Kr-lamps is more energetic than the Hg-lamp, $\text{O}({}^1\text{D})$ related photochemistry should be more important under Kr-lamp illumination. The isotope enrichments should correspondingly be higher as in the Hg lamp runs, which corresponds to the observations. Note again that the original explanation does not provide such a rationale and that the only difference between the Kr and Hg lamp experiments are photolysis effects that would need to fractionate along the same line as the hypothetical fractionation effects in the $\text{O} + \text{CO}$ reactions. This seems a highly unlikely scenario and would require a third mass independent mechanism (with all three process aligning at the same slope 0.82 line).

Unfortunately, the experiments do not provide much detail about the emission spectra of the lamps and are therefore difficult to model quantitatively and it is questionable whether an analysis of BT89 could go beyond what is presented here. But from the three isotope analysis alone, O_3 to CO_2 isotope transfer without any mass independent fractionation in $\text{O} + \text{CO}$ seems to be a more viable hypothesis than assuming MIF in $\text{O} + \text{CO}$ and a series of other reactions. It is therefore interesting to confront this new hypothesis also with the more recent experiment on $\text{O} + \text{CO}$, presented by Pandey and Bhattacharya (PB06).

3.2 Brief overview and analysis of the experiment of Pandey and Bhattacharya (2006)

The main reason for the PB06 experiment was to improve on the limitation of the previous experiment due to the use of energetic UV for the photodissociation of oxygen and of ozone that builds up during the experiment. The latter would induce excited state photochemistry and thus a possible transfer pathway from ozone to CO₂. PB06 therefore used ozone that was photodissociated with a halogen-tungsten lamp with predominant emission spectrum between 350 and 900 nm as a source for O atoms.

The experiments have been done either in a 5 dm³ or in a 70 cm³ reaction chamber illuminated by the tungsten lamp. A few runs have been made under conditions similar to the BT89 experiments using a Hg-lamp as light source and molecular oxygen as oxygen supply.

Due to the use of mixtures of ozone and CO as starting material (except for the simulation of the BT89 experiments), reaction times are relatively short (< 5.5 h). The observations were similar to the previous experiments, with strong mass independent enrichments of product CO₂ with respect to the hypothetical O + CO combination mix (see Figure 3.2). The observed slope was also similar to the first BT89 experiments.

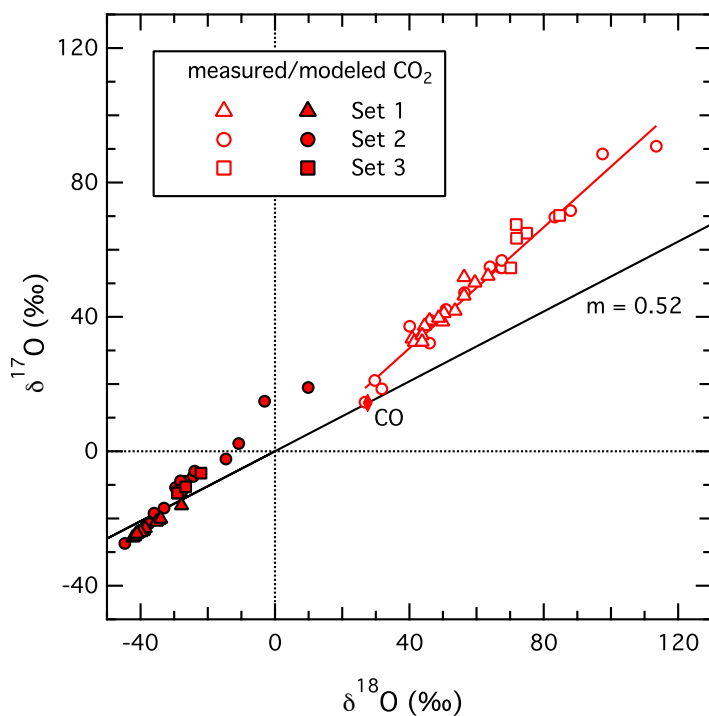


Figure 3.2: Three isotope plot showing the isotopic composition of CO₂ produced and modeled in PB06 experiments. Triangles, circle and squares refers to sets A, AC and AS listed in Table The initial CO composition is given by the solid red rhombus lying on the black line which is the mass dependent fractionation line of 0.52 slope. Open and filled symbols refer to experimental and modeled data respectively.

Interpretation of the experiments is difficult, because the measurements could not be reproduced using an isotope kinetic model. Indeed, kinetic modeling revealed a yet unidentified source of CO₂ in the experiments which exceeded modeled amounts based on recommended rate coefficients for the O + CO recombination (3.3) by factors between 2.8 and 1270. The difficulty of studying the O + CO reaction has been recognized earlier and the large scatter (3 orders of magnitude) in past rate coefficient studies is commonly attributed to the presence of

impurities with hydrogen containing species [138], which provides the possibility of catalytic CO₂ production. It thus seems possible that contaminations could also have hampered the current measurements.

But PB06 rule out significant levels of O(¹D) production from ozone photolysis due to their choice of light source. This would exclude the formation of OH via reaction (3.13) and thus avoid the unwanted HO_x chemistry. This might possibly also rule out the isotope transfer from ozone proposed in the previous section (3.1). Nevertheless, the validity of the hypothesis of negligible O(¹D) levels remains questionable, because of the long wavelength tail ($\lambda < 411$ nm) for O(¹D) production from ozone photolysis [139]. As a matter of fact, the light source being an unfiltered tungsten halogen lamp equipped with a quartz bulb, the lamp emission should extend to the UV, and even into the very strong Hartley band region of the ozone molecule (< 310 nm). Excited oxygen chemistry might thus not only be a source of isotope transfer between ozone and CO₂, it might also explain the discrepancy between observed and modeled ozone quantities.

Pandey and Bhattacharya [134] discuss the issue of a strong and unidentified CO₂ formation channel in their experiments and speculate that either the gas phase reaction occurs at a much faster rate than what is currently recommended [140, 138], perhaps due to the gas mixtures that they use, and that the O + CO reaction also occurs at the surface of the reactor. While an increased gas phase reaction rate due to small additions of ozone and oxygen to carbon monoxide is not a convincing explanation, surface chemistry might well play a role. Given the relative importance of the yet unidentified channel, any conclusion about the (minor) gas-phase process is highly uncertain. If the unidentified source is due to CO₂ formed at the reactor surface, the measurements would imply that the surface process fractionates in a mass-independent fashion. This is unlike ozone, where the surface reaction is strictly mass dependent [141].

The variability of the unidentified source (with strength between 1.8 and 1269 of the gas phase O + CO + M rate) seems to indicate that several factors are involved and the anti-correlation with pressure and reactor size seems to be in favor with the hypothesis of surface chemistry going on. However, this interpretation is still not consistent with the observations. In the set 3 of experiments in the 5 dm³ spherical reactor (see Table 3.1), for example, where 80 μ mol of ozone has been mixed with CO amounts varying between 3.9 and 7.8 mmol, the three body recombination rate constant would need to vary between $\simeq 3$ and 9 times the recommended rate (f in column 6 of Table 3.1), despite 97% of the gas always being pure CO. Moreover, an inverse correlation with pressure is not observed and even if we assume that the rate is three times higher than the recommended value, there are at least 2 runs (AS1 and AS5), where we need an alternative CO₂ formation channel that is at least as fast as O + CO + M. Still, the observed isotope enrichments form a close array of data points, which is very far from the modeled isotope composition assuming no additional mass independent fractionation in the O + CO reaction (open squares in Figure 3.2). This indicates that both reaction pathways (the dominant and the contributing) cause large and similar anomalous fractionations. It is interesting to note that on the relevant time scales, heterogeneous chemistry cannot play any significant role, because it will be slower than the considered gas phase reaction. Table 3.1 gives an overview of the dominant processes, their time scales and the associated number densities. With the exception of heterogeneous CO₂ formation, the relevant reactions are summarized in the sequence (3.2)–(3.4) completed by (3.6), because we can safely assume that the light source does not provide UV light capable of dissociating either O₂ or CO₂, if no O(¹D) can be formed from ozone photolysis. The time constant for O atom diffusion

$$\tau_{\text{diff}} = \frac{r^2}{4D} \quad (3.15)$$

with the reactor radius r , and the diffusion constant D provides a lower limit for the het-

Run	n (cm ⁻³)			f^c	τ (s)			
	CO	O ₃ ^a	O ₂ ^b		O + O ₃ ^d	O + CO + M	O + O ₂ + M ^e	wall diff. ^f
AS1	4.68×10^{17}	8.20×10^{14}	1.21×10^{16}	9.4	0.152	1.06	0.29	1.86
AS2	7.02×10^{17}	6.02×10^{14}	1.26×10^{16}	2.8	0.208	0.47	0.19	2.78
AS3	7.02×10^{17}	7.23×10^{14}	1.23×10^{16}	3.9	0.174	0.47	0.19	2.78
AS4	7.02×10^{17}	5.36×10^{14}	1.28×10^{16}	2.8	0.233	0.47	0.18	2.78
AS5	9.36×10^{17}	1.56×10^{15}	9.77×10^{15}	7.5	0.080	0.27	0.18	3.71

^a O₃ number density corresponding to half the observed final CO₂, between 6 and 16 % of the initial value.

^b upper limit of O₂ number density, assuming that all O₃ has been converted to O₂ and CO₂

^c factor by which k_{O+CO+M} must be increased to match final CO₂. Values taken from Table V in PB06

^d lifetime with respect to the O + O₃ reaction with $n(O_3)$ from column 3

^e lower limit lifetime with respect to the O + O₂ + M reaction from $n(O_2)$ in column 4

^f the diffusional lifetime has been calculated from $\tau_{\text{diff}} = r^2/(4D)$, where D is the diffusion constant of oxygen atoms in O₂ [142] and $r = 10.6$ cm corresponds to the spherical reactor dimension.

Table 3.1: Kinetic analysis of VIS light photolysis experiments of PB06 in 5l reactor (set 3) [134]. Characteristic number densities of CO, O₃ and O₂ and pseudo first order lifetimes with respect to O + O₃, O + CO + M and O + O₂ + M reactions as well as the diffusional time constant are given. Wall diffusion is the time limiting step for heterogeneous CO₂ formation and is by far the slowest reaction.

erogeneous CO₂ formation. Heterogeneous processes depend on the transport of reactants to the surface τ_{diff} and the reaction time τ_r there:

$$\tau_{\text{het}} = \tau_{\text{diff}} + \tau_r. \quad (3.16)$$

If the reaction is limited by diffusion of O atoms due to the ubiquity of CO, the values in Table 3.1 apply immediately. If, as proposed by PB06, activated CO₂^{*} needs to diffuse to the wall, the diffusion times provide an upper limit due to the higher mass and larger collisional diameter of the molecule.² We therefore see that except for the first set, heterogeneous reactions are considerably slower than the gas phase process, even more so if we assume that we underestimate the gas phase rate constant by a factor of three.

Thus, heterogeneous chemistry does not seem to be the unidentified source of CO₂ in the experiments, because it is even slower than the gas phase process, whereas a much faster CO₂ formation channel is required to explain the observations. It might be verified that this applies similarly to the other VIS light measurements at lower pressures and in the smaller reactor. While τ_{diff} might become smaller than the time scale for the gas phase reactions, heterogeneous processes are always slower than the required time scales for the observed CO₂ formation $\tau_O(O + CO + M)/f$. The present experiments therefore also leave room for the alternative hypothesis of an isotope transfer via ozone (reactions (3.12)–(3.14)), which will be explored in chapter 6.9.

It might also be argued that variation in lamp intensity and run time cannot explain the variability of the missing CO₂ source within the PB06 model, because O atoms from ozone photolysis are the only source for CO₂ formation. Once reacted with O₃ to O₂ or with CO to CO₂, these atoms are lost and cannot be recycled. Even in the shortest experiments (90 min), initial ozone has been photolysed more than ten times ($J \simeq 2.5 \times 10^{-3} \text{ s}^{-1}$). Since the dominant loss for O atoms at ozone concentrations of 5 to 10 % of the initial values is reaction with ozone, only a small fraction of the CO₂ will be formed even after very few photolysis time scales, and thus varying the lamp intensity by a factor of two or so should have no impact.

²The authors invoke the possibility that excited CO₂^{*} is stabilized by collisions with the wall.

3.3 Short summary and motivation for further investigation on $O + CO$

The sparsity of the previous experiments as well as the ambiguity related to their interpretation necessitates reinvestigation of isotope effects in the gas phase reaction of oxygen atoms with carbon monoxide, both by experiment and modeling, in order to confirm or disprove the possible existence of a mass independent fractionation effect in the process. Reinterpretation of past data indicate that observed mass independent fractionations are associated with a yet unidentified source channel for CO_2 formation, likely linked to excited oxygen chemistry. New and reliable data on the $O + CO$ reaction might provide fundamental insight into the physical mechanism of symmetry driven mass independent fractionation in chemical reactions.

The second part of this thesis is therefore devoted to a new experimental study of the gas phase $O + CO$ reaction in a photochemical reactor coupled to Fourier Transform Infrared Spectroscopy (FTIR) where O_3 -CO mixtures have been irradiated with light produced by different light sources. Ideally, the experiments provide new rate coefficient data. The setup as well as the results are described in the following chapter. Since $O(^1D)$ free generation of oxygen atoms is crucial for the interpretation of this and also the previous studies, the emission of different light sources, such as a LED and also the tungsten lamp type used by PB06 has been studied in some detail. This is described in chapter 5. Then a isotope kinetic model which takes into excited state chemistry into account is developed and tested in order to interpret our new and previous experiments (chapter 6). Using our lamp data and the model we present the interpretation of our measurements and the PB06 data in chapter 6.

Chapter 4

Relative rate study of the $O + CO$ reaction in a photo-reactor using FTIR spectrometry

As has been discussed previously, two studies [119, 134] claim the occurrence of an anomalous oxygen isotope effect in the reaction between carbon monoxide and oxygen atoms. Interpretation of both of these studies is ambiguous due to the possibility of an isotope transfer from ozone to CO_2 and more investigations are therefore required. So far, only bulk CO_2 has been collected and analyzed in these experiments and no information on individual reactions (rate coefficients) is available. For this reason, it is desirable to develop an experiment which a) will provide this detailed information and b) allows to support or disprove the claim made previously. Fourier Transform Infrared Spectroscopy (FTIR) coupled to a photochemical reactor has already been proven useful to derive isotopic rate coefficients (or ratios thereof) [e.g. 143] and thus seems to be a particularly suited technology. The current chapter describes the setup and results of such an experiment aiming at the study of isotope effects in the $O + CO$ reaction.

The first part of this chapter is devoted to a short presentation of the relative rate method, it briefly summarizes the operating principles of smog chambers and gives an overview of the photoreactor at CCAR (University of Copenhagen) used to perform the experiments. An overview on the FTIR spectroscopic technique is given in Appendix A together with a brief summary of the basic elements of vibrational and rotational spectroscopy. The basic chemistry and the results of individual experimental runs are then presented. Due to apparent discrepancies between the experimental results and the upper limit for CO_2 production via the $O + CO$ reaction, the presence of an interfering reaction must be inferred. Additional tracer experiments based on the relative rate method confirm the presence of OH radicals that strongly impact the oxidation of carbon monoxide. This makes exploration of the current data for the original purpose impossible. The observation also brings the results of the previous experiments into question, which motivates further investigation on the spectral distribution of light sources and chemical modeling which will be described in later chapters.

4.1 Relative rate method

Rate coefficients for gas-phase reactions are often determined as a ratio of rate constants rather than absolute values. Consider a reactive species R, for example a radical, and two compounds which can react simultaneously with R namely A, the species under investigation, and B, the compound with known reaction rate which will be used as reference for the calculation. The relative rate method can be better applied if the reference compound has

a reaction rate of the same order of magnitude as the studied species. Suppose that A and B react with R following the reactions (4.1) and (4.2) characterized respectively by the rate coefficients k_A and k_B :



where P_A and P_B are the products of the reactions. By measuring the concentrations of the reactants A and B, the concentration of the products P_A and P_B or the change in concentration of one of these, it is possible to calculate the ratio k_A/k_B . If, for example, the reactants are monitored, the rate laws are the following:

$$\frac{-d[A]}{dt} = k_A[R][A] \quad (4.3)$$

$$\frac{-d[B]}{dt} = k_B[R][B] \quad (4.4)$$

Combining (4.3) and (4.4) to calculate [R]

$$[R] = -\frac{1}{k_A} \frac{d \ln[A]}{dt} = -\frac{1}{k_B} \frac{d \ln[B]}{dt} \quad (4.5)$$

Integrating from $t = 0$ to time t gives the equation

$$\ln \frac{[A]_0}{[A]_t} = \frac{k_A}{k_B} \ln \frac{[B]_0}{[B]_t} \quad (4.6)$$

where $[A]_0$ and $[B]_0$ are the reactant initial concentrations and $[A]_t$ and $[B]_t$ are the concentrations at time t . Measuring the concentrations of A and B as a function of time, the ratio $\ln([A]_0/[A]_t)$ can be plotted versus $\ln([B]_0/[B]_t)$ since the slope of the line obtained gives the rate constants ratio k_A/k_B . Thus, knowing the absolute value of k_B , an absolute value for k_A can be calculated. A typical relative rate plot is shown in figure 4.1 obtained in a case of study of reaction between CH_3OH and OH [144]. The reference compounds are C_2H_6 and CH_4 and the concentrations are measured using FTIR.

One of the main advantages in using the relative rate method is that the compound R does not need to be measured at all. This is particularly beneficial if the measurement of R is difficult, such in the case of OH, whose measurement is extremely challenging and requires highly specialised techniques.

4.2 Smog chambers

Smog chambers are reaction chambers intended to study atmospheric processes by simulating certain conditions of the real atmosphere. The main purpose of these smog chambers is to have a control on important variables such as pressure, temperature, spectral characteristic of photolysis light sources, composition of the gas mixture, presence and size distribution of aerosols, etc. Smog chambers are well suited for obtaining mechanistic and kinetic data on chemical processes relevant in the atmosphere. For example, reactions of hydrocarbons with OH or ozone or the products from the photolysis of compounds can be studied under varying conditions. These observations can also be used for comparison with kinetic model predictions and therefore for validation of kinetic and modeling data.

Depending on cost and experimental constraints, the design of these smog chambers can

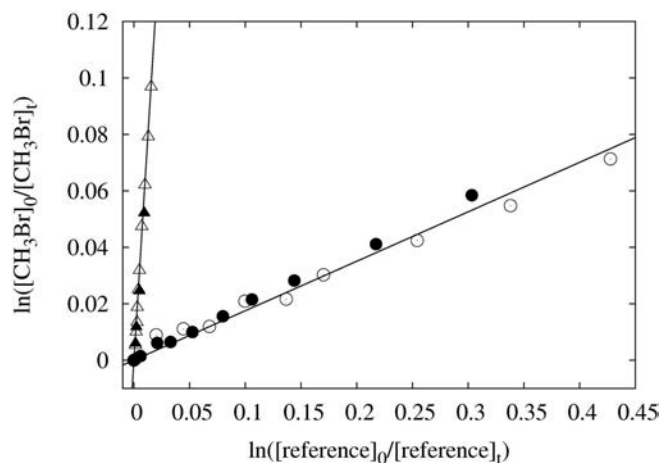


Figure 4.1: Plot of relative rate studies of reaction $\text{CH}_3\text{OH}+\text{OH}$. The reference species are respectively C_2H_6 (circles) and CH_4 (triangles). The picture is taken from [144].

widely vary: the size can be anywhere between a few liters and several cubic meters, the surface material to which the reactants get exposed to can be Teflon for reactors larger than a few cubic meters whereas small chambers are mostly made of glass, quartz or metal.

One advantage of these reactors is that the gas can be evacuated and that pressures below the atmospheric value can be reached if the reactor is sufficiently leak tight. The use of a smog chamber also enables the systematic investigation of individual parameters in experiments under controlled conditions. This is quite different from studies carried on in ambient air where it is often difficult to discern the effect of different and simultaneously varying variables (variation of the light intensity with season and time of the day, cloudiness, etc.). Moreover, the composition of the real atmosphere cannot be varied at will in order to study individual reactions.

As compared to the free atmosphere, smog chambers also suffer from some limitations. One of the most common problems is related to the presence of impurities which originate from compounds that have been used previously or which are due to the wall material itself. Another issue is related to the mere presence of surfaces that provide new (heterogeneous) reaction pathways and which affect approximately 50% of the measurements [145]. When chemical reactions take place on the walls of the chamber, products can desorb into the gas phase changing the observed concentrations of species inside the instrument in a such manner that cannot be entirely interpreted on the basis of known homogeneous gas-phase reactions. To some extent, wall contaminations and loss effects can be reduced by heating the system before starting an experiment or purging the chamber with clean air or ozone under irradiation in order to remove the pollutants out-gassed from the walls. A common strategy used to minimize effects of reactions that take place on the walls is to reduce the surface - to - volume (S/V) ratio by constructing spherically shaped chambers, for example. When spectroscopy is used as an analytic tool, a good alternative is to use cylindrical reactors since this configuration allows long absorption path lengths and relatively low concentrations of reagents [146]. This configuration has therefore been chosen for the photoreactor built at CCAR in Copenhagen, where FTIR spectroscopy is used to follow the chemical composition of irradiated gas mixtures.

4.3 The Copenhagen photoreactor

The photoreactor at CCAR in Copenhagen is schematically represented in figure 4.2. It consists out of a 2 m long cylindrical cell made from quartz (section 3 in figure 4.2) with a total volume of 101.4 dm³, an inner diameter of 250 mm and a 10 mm thick wall. There are two advantages in using quartz as material: the transparency in the UV down to 190 nm and a very low thermal expansion coefficient, which avoids problems of misalignment or damaging in case of large temperature variations and gradients. The temperature of the chamber is controlled by a fan and a heat exchanger. A polyurethane cover assures the insulation from the surrounding, since temperature can reach values of up to 330 K (section 1). An illumination system (section 2) surrounds the cell and it is possible to select among several type of light sources: UV-A, which emit from 315 nm to 400 nm, UV-C with an emission range comprised between 200 nm and 280 nm, sunlamps having a broad UV emission range from about 300 nm to the infrared and LED (Light Emission Diode lamps) with emission in the visible and infrared regions of the electromagnetic spectrum. The lamps are computer controlled using a LabView program that allows to select the lamp type and the number of lamps.

The beam of a FTIR interferometer (Bruker IFS 66v/S) is injected into the White cell optics [147] of the reaction chamber. Two stainless steel flanges are placed at the ends of the cylinder, hosting respectively windows for IR and UV beam and the gas inlet line and the connection to the gas pumping system. The beam from the FTIR is reflected and propagated into the cell by a system of three concave spherical mirrors (section 4a and 4b) covered by a layer of gold which has a high infrared reflectance. They are arranged according to the White's geometry and can be regulated by three micrometric screws in order to keep the alignment of the system. After multiple reflections in the cell, the beam is transmitted to a InSb detector (section 7) under vacuum and cooled down by liquid nitrogen. Further technical details on the photoreactor can be found in [148].

4.4 Experimental procedure

Each experimental run has followed a strict procedure. First, the spectrum of the empty cell has been acquired in order to verify the presence of contaminants. This spectrum is also used as background and is subtracted from the measurement spectrum. Figure 4.4 provides an example of such a background spectrum. Interestingly, traces of water and CO₂ can be identified in the spectrum that has been taken before the cell was filled. These compounds may either be present in the reactor, for example stuck to the walls, or in the transfer optics. In order to minimize the concentration of impurities in the reactor, the chamber is pumped all night long. Sometimes the lamps have been turned on, which increased the temperature and facilitated degassing of compounds stuck to the glass. If the level of impurities was still not low enough, the cell has been filled with ozone and was illuminated. This leads to the formation of O(³P) or O(¹D) radicals that remove contaminants more efficiently [149]. After acquisition of the background spectrum, the cell has been filled: first, ozone has been generated from molecular oxygen gas. Using a commercial discharge generator (model AC-20) from O3 Technology, a steady gas flow was maintained and directed via teflon tubing to a silica gel containing glass trap cooled down to about -78 °C using a mixture of dry ice and ethanol. After the discharge has been finished, oxygen and other condensible species were pumped away and only pure condensed ozone, visible by its characteristic purple color, remained in the trap. The trap was then slowly warmed up by taking off the cooling mixture and ozone was then released into the empty reaction chamber using teflon and stainless steel tubing.

In order to avoid interferences from strong background CO and CO₂, almost pure ¹³C

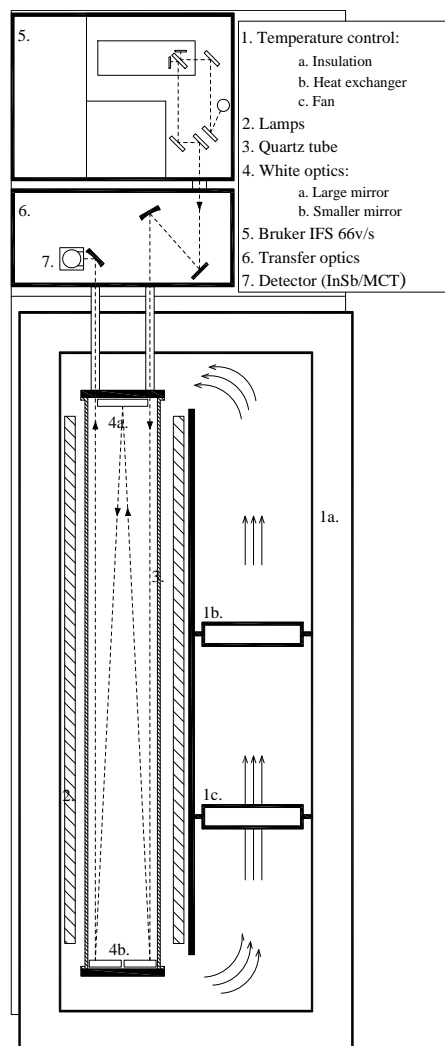


Figure 4.2: Scheme of the photoreactor. The different components are described in section 4.3. The picture has been taken from [148].

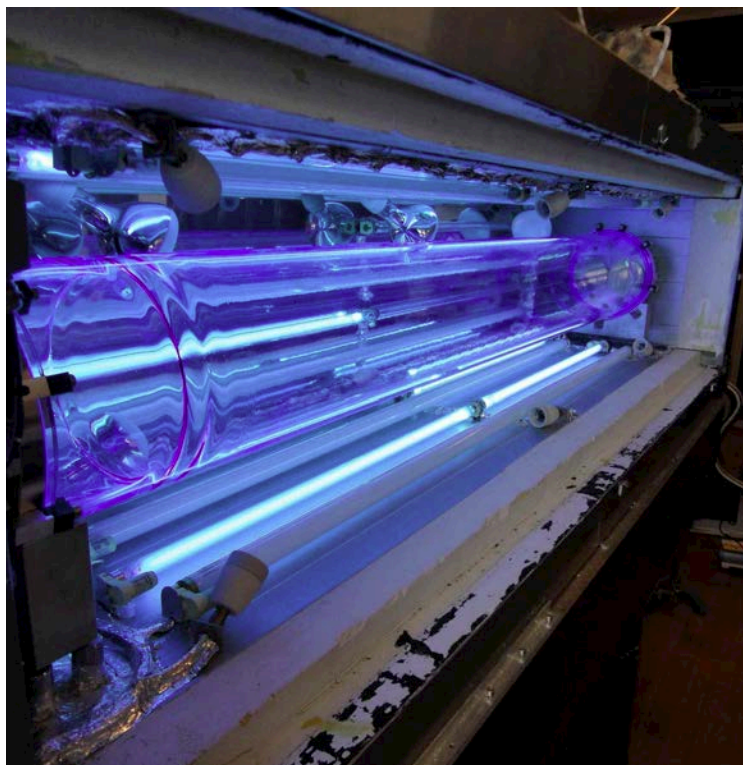


Figure 4.3: Photo of the photoreactor in CCAR. The glass cylindrical chamber is surrounded by lamps and all the system lies in a box internally covered by polyurethane. At the end of the reactor the mirrors used to propagate the beam are visible.

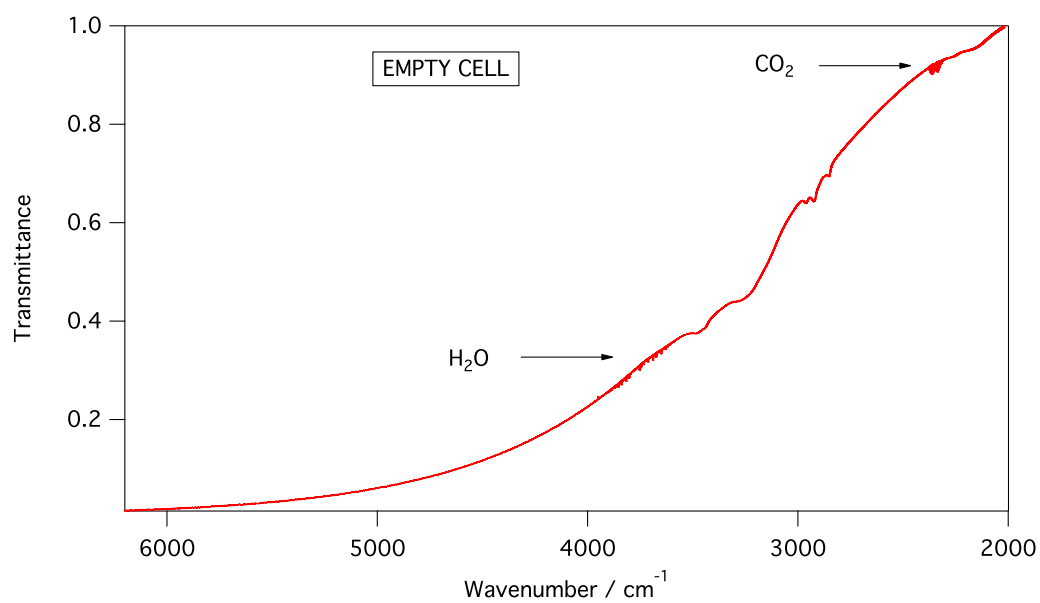


Figure 4.4: Background spectrum of the empty cell. Main absorbers are indicated.

enriched carbon monoxide (99% ^{13}C , $\sim 10\%$ ^{18}O from Isotec Inc.) has been used as a starting material. The $^{13}\text{C}^{16}\text{O}$ lecture bottle is connected to a control volume connected to a pressure gauge, which allows metering of the gas. From this volume, the gas is then released into the cell and flushed with N_2 . Flushing is maintained until the desired final pressure has been reached (between 200 and 980 hPa). Rapid spectra are taken in order to monitor the concentration which must be kept below some value in order to avoid saturation effects in the spectra. The mix of gases is then left to allow for complete mixing and a series of spectra in dark is acquired, because it must be verified whether dark chemistry takes place in the chamber or not. A typical spectrum of the photoreactor filled with ozone, carbon monoxide and nitrogen is shown in figure 4.5. After mixing has been completed, the LED lamps are

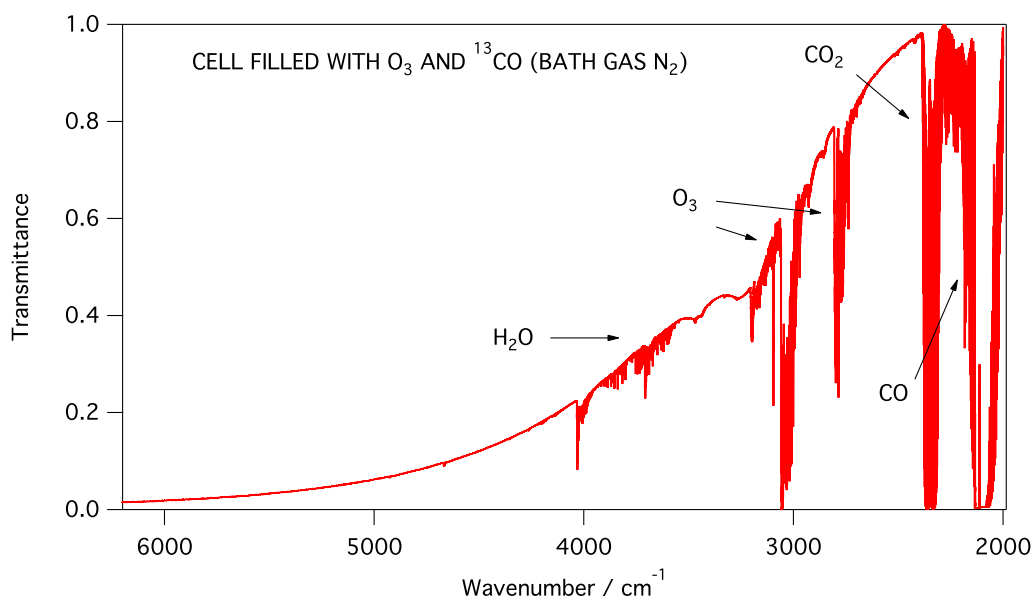


Figure 4.5: Infrared spectrum of the cell filled with ozone, 8 hPa of ^{13}CO and N_2 , total pressure 980 hPa.

turned on to start ozone photolysis and initiate the photochemistry. During overnight runs six lamps have been used for safety reasons; otherwise all twelve lamps were switched on. Photolysis times have been varied between just a few and 20 hours. During an experimental run infrared spectra are registered repeatedly at fixed time intervals. The integration time has been adjusted to the overall photolysis time. Once all spectra have been taken, the lamps are turned off and the chamber is evacuated, first by a mechanical pump and at sufficiently low pressures by a turbomolecular pump. All experiments have been performed at $T = 298\text{ K}$ and spectra were acquired in the wavenumber range between 2000 cm^{-1} and 7000 cm^{-1} displayed by using the OPUS Spectroscopy Software¹ (Bruker, version 5.5).

4.5 Chamber chemistry

The original idea of studying isotope variants of the $\text{O} + \text{CO}$ reaction in a mixture of ozone (or oxygen) and CO is based on a very simple chemical mechanism based on five different

¹<http://www.bruker.com/products/infrared-near-infrared-and-raman-spectroscopy/opus-software/overview.html>

chemical species O, O₂, O₃, CO and CO₂:



The reaction network of only four reactions is initiated by visible light photolysis of ozone (reaction (4.7)). This reaction provides O atoms in their ground electronic state, required for reaction (4.10) to proceed. Molecular oxygen is also produced. Ozone can therefore also be reformed in reaction (4.9). The simultaneous presence of O and the relatively large amounts of initial O₃ also imply that O atoms are efficiently removed by direct reaction with ozone via reaction (4.8), once again leading to the formation of molecular oxygen. As we will see further below, the sequence of reactions (4.7)–(4.9) supplies O atoms and engenders the net conversion of O₃ into O₂. A small fraction of the available O atoms then serves to convert CO into CO₂ via reaction (4.10).

Except for the rate of ozone photodissociation J that depends on the light source and the geometry of the reactor setup, thermal rate coefficients in the above scheme ((4.8)–(4.7)) are well known with reaction (4.10) being the most uncertain: $k_1 = 6.0 \times 10^{-34} \text{ cm}^6 \text{ s}^{-1}$ [150], $k_2 = 8.0 \times 10^{-15} \text{ cm}^3 \text{ s}^{-1}$ [150] and $k_3 = 2.4 \times 10^{-36} \text{ cm}^6 \text{ s}^{-1}$ [151]. The symbol M represents an inert molecule, such as N₂ for example, which provides a reaction partner that can transfer energy in collisions but does not undergo a chemical transformation. The above scheme will be far too simplistic if photons with energies below 411 nm become available, because at these energies excited oxygen atoms might be produced from the photolysis of ozone molecules:



These can react with the water traces present in almost all vacuum system, thus producing the hydroxyl radical OH



which are known to effectively produce CO₂ from the following reaction that is at the heart of atmospheric oxidation and combustion chemistry [152, 153]



Because OH is a highly reactive radical that is regenerated over several reaction steps, rather small concentrations suffice in order to make reaction (4.13) a very efficient source of CO₂. Because this reaction also provides a possible isotope transfer pathway from ozone to CO₂, and because there is also a mass independent isotope fractionation associated with the reaction itself, it must be avoided at all means when studying isotope fractionation in reaction (4.10).

4.6 Data analysis and semi quantitative interpretation

The spectra are analyzed using a spectral fitting algorithm, MALT5 (Multi-Atmospheric Layer Transmission) [154], based on the non-linear least square fitting procedure which generates from reference spectra a synthetic spectrum that is compared with the experimental one. In the fitting procedure the amplitudes of each peak in the reference spectrum is iteratively modified in order to converge to the value in the measured spectrum. Once the best fit is performed, the peak amplitudes in the reference spectrum give the concentration

of the compounds measured in the cell. The reference spectra used by the software are taken from the HITRAN database [155]. As input parameters the program needs to be provided by the names of species which are supposed to be present in the spectrum, their amount, the total pressure, the temperature of the reactor and a wavelength range where the analysis is desired. The software takes also into account several parameters which affect the line shape such as pressure broadening, apodization and resolution. The output given by the program is a file containing the measured, fitted and residual spectra in the region fitted and the fitted parameters (*i.e.* concentrations, ...) with the relative errors. The wavenumber regions chosen for fitting the species presents in the chamber are the following: [3000, 3150] cm^{-1} for O_3 , [2150, 2190] cm^{-1} for $^{13}\text{C}^{16}\text{O}$, [2240, 2380] cm^{-1} for CO_2 and [3810, 3880] cm^{-1} for H_2O . An example of a fitted spectrum (blue curve) compared with a measured one (red curve) and the calculated residual (green curve) is shown in figure 4.6 where the compound under study is the isotope of carbon monoxide $^{13}\text{C}^{16}\text{O}$.

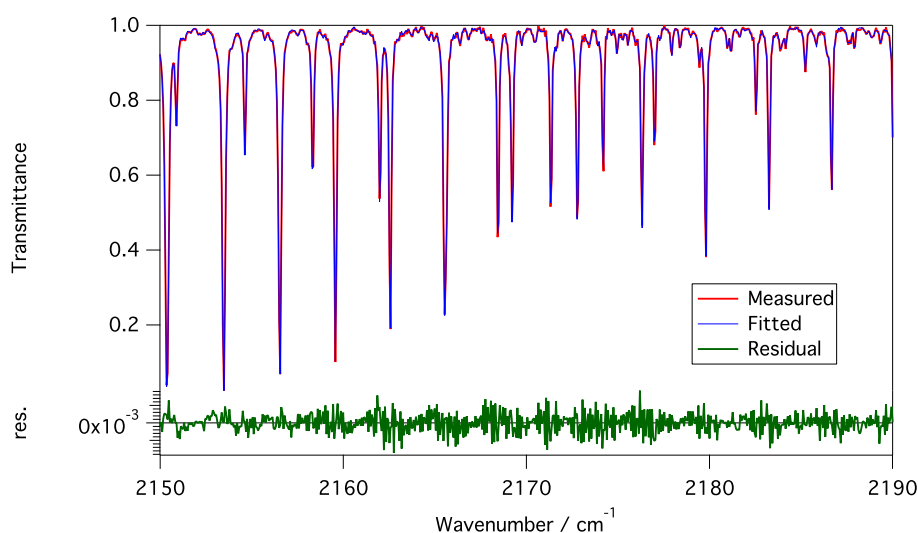


Figure 4.6: Analysis of a spectrum taken during an experiment. In this case the compound examined is $^{13}\text{C}^{16}\text{O}$ whose concentration is 53 ppm in a total pressure of 700 hPa N_2 .

In total twelve experiments were performed at different total pressure and they are listed in table 4.1 where the column “lamps” refers to the number of lamps turned on during the experiment, “time” is the total photolysis time and $[\text{M}]$ is the total concentration of gas in the chamber during the experiment. The initial and the final concentrations of O_3 and $^{13}\text{C}^{16}\text{O}$ are reported as well.

For a preliminary analysis, the stationary state approximation for the concentration of oxygen atoms during an experimental run can be applied:

$$0 = \frac{d[\text{O}]}{dt} = J[\text{O}_3] - k_1[\text{O}][\text{O}_2][\text{M}] - k_2[\text{O}_3][\text{O}] - k_3[\text{O}][\text{CO}][\text{M}]. \quad (4.14)$$

Solving for $[\text{O}]$, one obtains

$$[\text{O}] = \frac{J}{k_1 \frac{[\text{O}_2]}{[\text{O}_3]} [\text{M}] + k_2 + k_3 \frac{[\text{CO}]}{[\text{O}_3]} [\text{M}]}. \quad (4.15)$$

In this expression, $[\text{O}]$ is given as the ratio of the product term over the loss terms. Clearly,

run	lamps	time (h)	[M] (10^{18} cm^{-3})	[CO] (10^{14} cm^{-3})		[O ₃] (10^{16} cm^{-3})		$\Delta[\text{CO}]$ (10^{14} cm^{-3})	[CO ₂] _{max} (10^{13} cm^{-3})
				initial	final	initial	final		
1	6	12	23.8	14.0	9.53	5.00	1.96	4.47	5.94
2	12	3.5	23.8	3.49	2.97	10.5	6.12	0.52	0.86
3	6	16	17.0	9.00	8.17	3.22	1.51	0.83	3.64
4	12	6	17.0	8.39	7.66	3.62	2.34	0.73	2.54
5	12	11	12.1	0.95	0.75	7.86	2.84	0.20	0.38
6	6	3.5	12.1	4.42	4.08	4.05	2.43	0.34	0.28
7	12	12	12.1	1.05	0.89	7.31	3.06	0.16	0.45
8	12	18	12.1	13.6	9.91	11.0	1.77	3.69	8.80
9	12	4	4.86	1.93	1.79	4.58	2.14	0.14	0.11
10	6	15	4.86	1.84	1.61	5.24	1.72	0.23	0.20
11	6	20	4.86	3.25	2.75	4.64	0.86	0.50	0.47
12	12	2.3	4.86	13.6	12.6	10.0	4.41	1.00	0.45

Table 4.1: Experimental results. Concentrations have been determined by the FTIR technique. [M] has been determined by pressure measurement. $\Delta[\text{CO}]$ is the observed loss of CO (initial–final) and $[\text{CO}_2]_{max}$ is an upper limit of CO₂ formed via reaction (4.10). For more details see text.

[O] will be limited by

$$[\text{O}] \leq [\text{O}]_{max} = \frac{J}{k_2}. \quad (4.16)$$

At the very beginning of a run, when the photolysis has just started, equation (4.16) is actually a very good estimate for the O concentration, because the concentration of ozone molecules is high and reaction (4.8) therefore predominates over ($k_2 \gg k_1[\text{M}][\text{O}_2]/[\text{O}_3], k_3[\text{M}][\text{CO}]/[\text{O}_3]$) the competing loss processes (4.9) and (4.10). $[\text{O}]_{max}$ does not change over the course of an experiment. We can use it to obtain an upper limit for CO₂ that is produced during a run. Integration of the rate law for carbon dioxide

$$\frac{d[\text{CO}_2]}{dt} = k_3[\text{O}][\text{CO}][\text{M}] \quad (4.17)$$

is straightforward if we use respective upper limits for O and CO, because [M] and the rate coefficient remain constant and there is no initial CO₂. We thus conclude that the CO₂ concentration is bound by

$$[\text{CO}_2]_{max} = k_3 \frac{J}{k_2} [\text{CO}]_0 [\text{M}] \Delta t, \quad (4.18)$$

where Δt is the duration of a run and $[\text{CO}]_0$ is the initial carbon monoxide concentration. The rate coefficients k_2 and k_3 have been given in section 4.5.

The photolysis rate J depends on experimental conditions. It can be estimated from the initial phase of a photolysis experiment, because the observed ozone loss will only depend on the photolysis and subsequent reaction of O with O₃. This is due to the fact that at the beginning of a run there is no O₂ yet to form new ozone via reaction (4.9) and reaction (4.10), which is the other possibility for O atoms to react with, is just too slow. As a matter of fact, reaction (4.10) only becomes competitive when the ozone concentration has decreased so much that $k_2[\text{O}][\text{O}_3] = k_3[\text{O}][\text{CO}][\text{M}]$. Because we have in our experiments always $[\text{O}_3]/[\text{CO}] > 10$ (see Table 4.1), CO₂ formation via reaction (4.10) accounts at most for 3% of the loss of oxygen atoms and can therefore be neglected. At short times, ozone loss thus obeys the following rate equation

$$\frac{d[\text{O}_3]}{dt} = -2J[\text{O}_3], \quad (4.19)$$

which is solved by a simple exponential decay with characteristic time constant $\tau = 1/(2J)$.

Figure 4.7 is a typical temporal evolution of $[\text{O}_3]$, from which J could be determined.

Note the logarithmic scale of the plot, which demonstrates that the temporal evolution of $[\text{O}_3]$ well follows an exponential decay curve for the first 1 - 2 hours. After about 1.5 hours, reformation of ozone becomes important, leading to a slight decrease of the ozone loss rate. For an arrangement of six lamps, we get $J = 3 - 4 \times 10^{-5} \text{ s}^{-1}$. Using $J = 3.5 \times 10^{-5} \text{ s}^{-1}$,

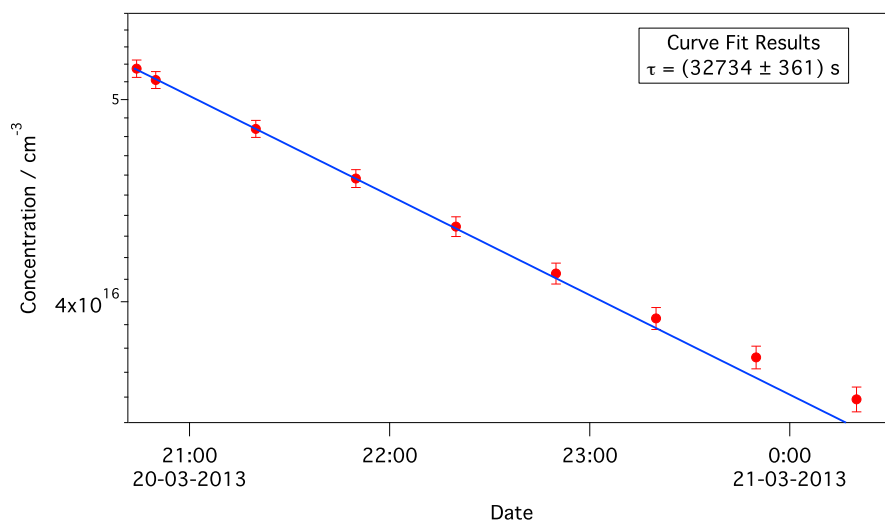


Figure 4.7: Temporal evolution of the ozone concentration during a photolysis experiment. An exponential function has been fitted to the first four data points (corresponding to a photolysis time of 1 hour or less).

the upper limit of CO_2 formed by the $\text{O} + \text{CO}$ recombination reaction could be determined and compared to the observed losses of CO (see last columns in Table 4.1). On average, the observed CO loss ($\Delta[\text{CO}]$) exceeds the upper limit of CO_2 formation via reaction (4.10) by a factor of 5.5. The individual ratios $[\text{CO}_2]_{max}/\Delta[\text{CO}]$ vary between 5 and 44%, indicating that the chemical reaction scheme is incomplete. These numbers also imply that the CO loss is largely dominated by another, yet unidentified process, which prevents that meaningful information on the $\text{O} + \text{CO}$ reaction can be obtained from measuring the apparent loss of CO . The accurate numerical analysis presented later in the thesis (see chapter 6) demonstrates that the discrepancy is even larger than what is implied from our simple estimates in Table 4.1 and that an important CO sink is missing.

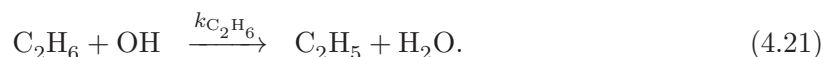
We have thus considered several additional loss pathways for ^{13}CO , such as isotope exchange which would lead to an apparent loss of one isotope, and to a build up of another. We have also investigated heterogeneous losses of CO at the reactor walls, but all these processes must be ruled out. Another hypothesis is that there is still another formation reaction for CO_2 in the gas phase, such as the atmospherically relevant reaction of carbon monoxide with the hydroxyl radical. Hydroxyl could have been present in trace amounts, because of the ubiquity of water in vacuum systems and because $\text{O}(^1\text{D})$ could have been formed in ozone photolysis, leading to formation of OH in the reaction with water (see section 4.5).

In order to put this hypothesis to the test, a tracer, such as ethene or ethane can be added to our reaction mixture. Ethane (C_2H_6) has finally been chosen. It exclusively reacts with OH and the rate coefficient for this reaction is well established and similar to the rate coefficient for $\text{CO} + \text{OH}$. However ethane cannot react with ozone and therefore is a sensitive tracer for OH . If losses of the OH tracer substance and of carbon monoxide occur at proportional rates, the loss of CO can be identified as reaction of carbon monoxide with OH .

4.7 OH tracer experiments

As we have just seen in the previous section, the amount of the observed CO loss cannot be explained assuming that only reactions (4.7) through (4.10) take place in the chamber. Some other processes must occur in the system in order to explain the observed losses of CO.

In section 4.5 the reaction between CO and OH radicals has been pointed out as a possible explanation. Because OH is an effective reagent, but its concentration is very small, direct measurement is difficult and would require a dedicated detection technique. Alternatively, we may use a specific tracer and apply the relative rate method (see 4.1) to the CO, OH and tracer system. We thus consider the competition of the following two reactions



Reaction (4.20) has a rate of $k_{\text{CO}} = (1.4 \pm 0.13) \times 10^{-13} \text{ cm}^3 \text{ s}^{-1}$, whereas the rate coefficient of the tracer reaction (4.21) is $k_{\text{C}_2\text{H}_6} = (2.5 \pm 0.17) \times 10^{-13} \text{ cm}^3 \text{ s}^{-1}$ [150]. As desired, the relative rate $k_{\text{CO}}/k_{\text{C}_2\text{H}_6}$ is therefore of the order 1 and takes the value of 0.56 ± 0.18 , where the uncertainty is given on the 95 % level of confidence.

As explained previously (section 4.1), the relative rate method consists in following the temporal evolution of the two reactants CO and C₂H₆ and then plot $\ln([\text{CO}]_0/[\text{CO}]_t)$ over $\ln([\text{C}_2\text{H}_6]_0/[\text{C}_2\text{H}_6]_t)$. If we correspondingly adapt equation (4.6) to our case, we obtain

$$\ln \left(\frac{[\text{CO}]_0}{[\text{CO}]_t} \right) = \frac{k_{\text{CO}}}{k_{\text{C}_2\text{H}_6}} \ln \left(\frac{[\text{C}_2\text{H}_6]_0}{[\text{C}_2\text{H}_6]_t} \right) \quad (4.22)$$

Figure 4.8 shows the result of our measurements. $\ln([\text{CO}]_0/[\text{CO}]_t)$ over $\ln([\text{C}_2\text{H}_6]_0/[\text{C}_2\text{H}_6]_t)$

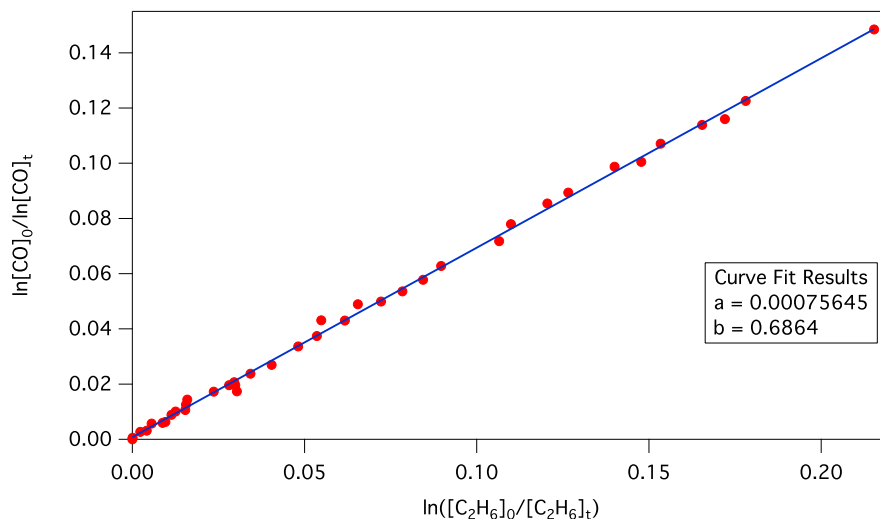


Figure 4.8: Relative rate plot.

data do indeed form a straight line through the origin. An unweighted linear fit yields a value of 0.69 for the slope, which is compatible with the recommended ratio of rate coefficients. It must therefore be concluded that the observed loss of CO is actually due to reaction with OH radicals.

The concentration of OH in the reactor can now be estimated from the decay of [C₂H₆], assuming that [OH] does not vary over time. This certainly is a rough approximation, but will provide an order of magnitude estimate of the OH concentration. Figure 4.9 shows the

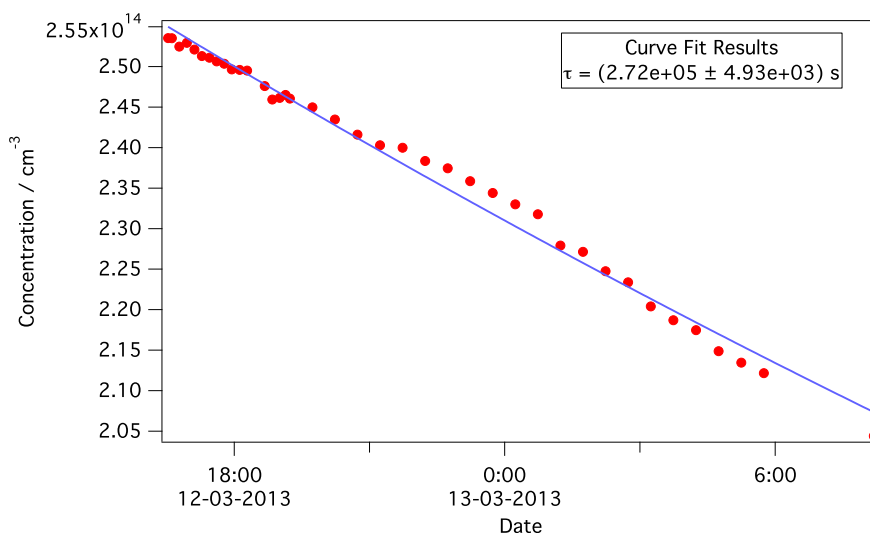


Figure 4.9: Temporal evolution of the ethane concentration in a tracer experiment using ethane and carbon monoxide. Concentrations are given as mixing ratios in ppm (parts per million). The blue line indicates an exponential fit.

ethane concentration during a typical tracer experiment, from which a typical decay time of $\tau = 2.7 \times 10^5$ s is obtained. The steady state hydroxyl radical concentration required to obtain this first order lifetime of ethane can then be obtained from

$$[\text{OH}] = \frac{1}{\tau \times k_{\text{C}_2\text{H}_6}}, \quad (4.23)$$

which gives the value of $[\text{OH}] \simeq 1.5 \times 10^7 \text{ cm}^{-3}$.

Without any further information and detailed modeling, it is difficult to judge whether this value is reasonable and typical for this kind of experiment. We emphasize that we have already employed light sources that greatly reduce UV emission and thus $\text{O}(^1\text{D})$ production. The high ozone concentrations employed in the experiments as well as the fact that the photoreactor has been used to study many reactive species in the past might well explain why there is a OH concentration as high as 10 or 100 times the atmospheric value. However, the problem of contamination is well known in the study of the $\text{O} + \text{CO}$ reaction. According to Tsang and Hampson [140], the scatter of available kinetic data is most likely explained by the presence of contaminants and catalytic reactions such as $\text{CO} + \text{OH}$.

4.8 Short chapter summary and outlook

- Photolytic experiments of O_3 -CO mixtures have been undertaken at the Copenhagen photochemical reactor.
- The setup of the reactor is described.
- The measurements show CO losses that are much larger than what can be explained by the target reaction $\text{O} + \text{CO}$ alone. This prevents to use the current setup and technology for studying isotope effects in the $\text{O} + \text{CO} + \text{M}$ reaction.
- Using ethane as a tracer, OH has been identified to explain the observed CO losses and a typical OH concentration of about 10^7 cm^{-3} has been derived.

- The origin of the OH and possible optimizations of the light sources will be investigated in two later chapters.
- The presence of OH and the effectiveness of the OH + CO reaction provide a pathway to transfer O isotopes from OH to CO₂. This might require reinterpretation of previous experiments where this possibility has been neglected.

Chapter 5

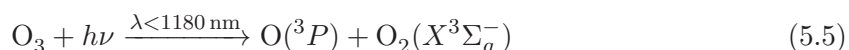
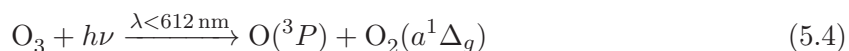
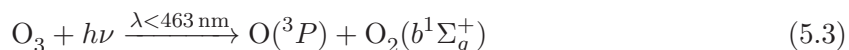
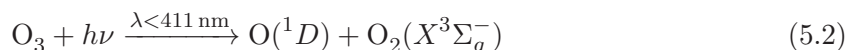
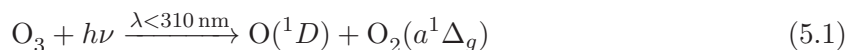
O(³P) and O(¹D) production from photolytic O₃ dissociation using different light sources

This chapter is devoted to the quantitative analysis of dissociation products, notably oxygen atoms, from the photolysis of ozone using different light sources. As it has been discussed before, existing and proposed experiments on isotope effects in the O + CO reaction depend on the exclusive presence of thermal O atoms in their ³P ground electronic state, because excited O(¹D) might provide a direct transfer of the ozone isotope anomaly into CO₂. We therefore investigate the branching ratio r_{BR} for a halogen filled tungsten lamp (at 3400 K color temperature) and a Light Emitting Diode (LED) lamp under various operation conditions. The results will be used to model and interpret our experiment (in chapter 6) as well as the experiment made by Pandey and Bhattacharya (in the following referred as PB06) [134].

We begin by summarizing existing knowledge on the ozone photodissociation process and then discuss our method to determine the O(¹D)/O(³P) production rate ratio. The analysis and results of our measurements for the halogen filled tungsten lamps and LED are presented in two subsequent sections and we conclude this chapter by a short summary of the results.

5.1 Wavelength dependence of O(¹D) production from O₃ photolysis

The reactions (5.1)-(5.5) show the reaction pathways of ozone photodissociation into atoms and diatoms. Depending on photon energy, atomic and diatomic oxygen formed by the photolytic dissociation of ozone might be in their ground states or either or both electronically excited.



Only two of these channels, 5.1 and 5.5, are spin-allowed while the others are spin-forbidden: as shown in figure 5.1, below 310 nm, or in the Hartley band, the first reaction or the singlet channel occurs by direct excitation from the singlet ground state \tilde{X}^1A' to the singlet excited state $^1A'$, also called B. Molecules excited into the B state dissociate, mostly remaining in the excited state (90%), thus leading to singlet products indicated in channel (5.1). About 10% cross over into the repulsive R state, which connects to the ground state potential, thus leading to triplet products of channel (5.5). The energetic threshold of channel (5.1) is somewhat washed out and $O(^1D)$ from this channel may be observed even when irradiating at wavelengths beyond this threshold [156]. This is due to excitation from the tiny population of vibrational hot bands. Just above 310 nm the Huggins band sets on. It is due to excitation in the shallow well of the B state. This will be discussed in some more detail further below. Channel (5.2), for which also experimental evidence has been found ([157], [139]), equally provides $O(^1D)$ and it is speculated that this might be possible until wavelengths up to 411 nm, corresponding to the thermodynamic threshold of this channel. Beyond 411 nm ozone photodissociation occurs in the Chappuis and Wulf bands, which corresponds to excitation in the lowest 1A and 3A states respectively. Dissociation in these bands, however, lacks the energy to produce $O(^1D)$.

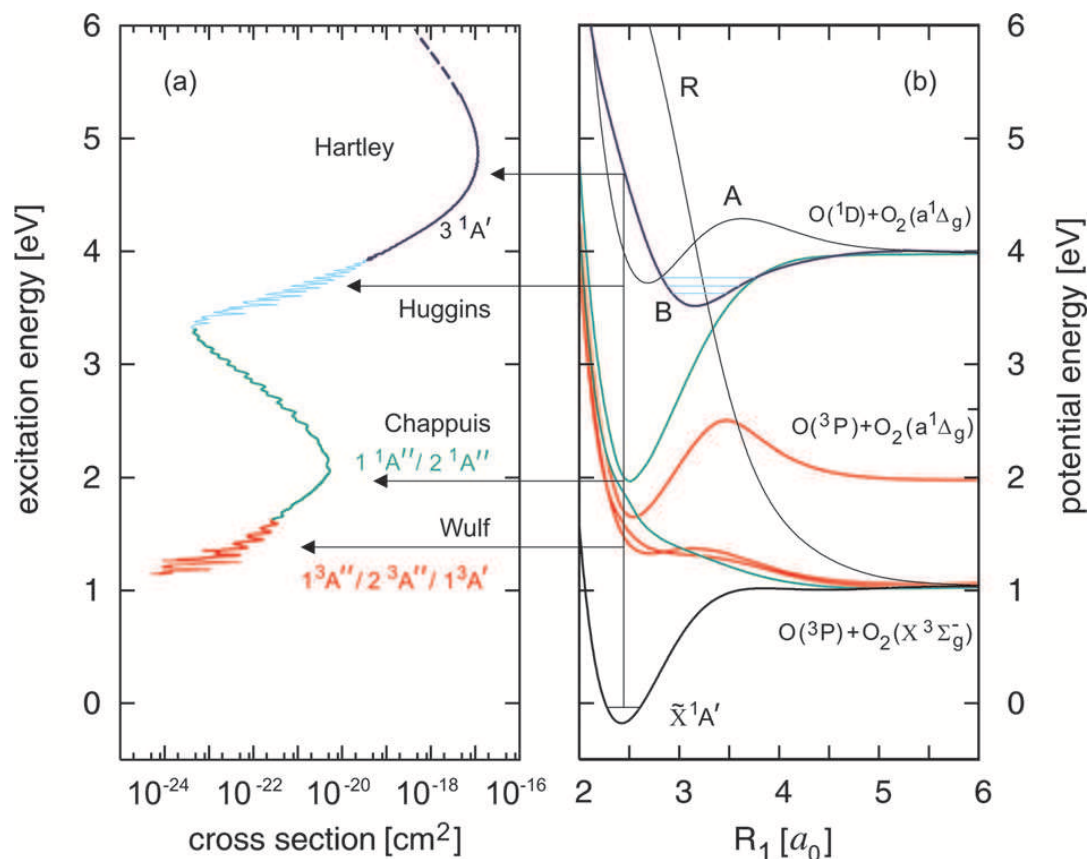


Figure 5.1: Photodissociation of ozone: absorption cross section and electronic potential surfaces. On the left the absorption cross section of ozone is shown as function of the excitation energy. The solid line represents data from [158], the dashed line are data from [159]. On the right the potential energy curves associated to different channels for the ozone photodissociation are shown. Horizontal arrows and colors underline the correspondence between the absorption bands of ozone and its electronic transitions. The data has been taken from [160].

The rate at which a molecule undergoes photolysis essentially depends on three different processes: a) the availability of photons that can be absorbed, b) the effectiveness of the

5.1. WAVELENGTH DEPENDENCE OF O(¹D) PRODUCTION FROM O₃ PHOTOLYSIS⁷⁵

absorption process, and c) the probability for a specific reaction to take place after photon absorption has been occurred. The photodissociation reaction rate or *photolysis rate* is therefore defined as follows

$$J = \int_{\lambda} \sigma(\lambda, T) \Phi(\lambda, T) F(\lambda) d\lambda \quad (5.6)$$

where $\sigma(\lambda)$ and $\Phi(\lambda)$ are respectively the absorption cross section of ozone and the quantum yield at the photolysis wavelength λ , and $F(\lambda)$ is the spectral actinic flux. The latter corresponds to the spectral energy density current (energy per unit area per unit time per unit wavelength irrespective of the direction of the incoming light) which is conveniently given in units of (quanta) $\text{cm}^{-2} \text{s}^{-1} \text{nm}^{-1}$. When we want to specify the photolysis rate for O(¹D) and O(³P) photo-production separately, we can write (5.6) as

$$J[\text{O}(\text{}^1\text{D})] = \int_{\lambda} \sigma(\lambda) \Phi_{\text{O}(\text{}^1\text{D})}(\lambda) F(x, \lambda) d\lambda \quad (5.7)$$

and

$$J[\text{O}(\text{}^3\text{P})] = \int_{\lambda} \sigma(\lambda) \Phi_{\text{O}(\text{}^3\text{P})}(\lambda) F(x, \lambda) d\lambda, \quad (5.8)$$

where $\Phi_{\text{O}(\text{}^1\text{D})}$ and $\Phi_{\text{O}(\text{}^3\text{P})}$ are the respective quantum yields. Note that in general the actinic flux $F(x, \lambda)$ depends on the wavelength and on the geometry of the setting. Because wavelength dependent absorption modifies the actinic flux as a function of the penetration into an absorbing volume, λ and x dependencies are interconnected. However, if we can make the assumption that the absorption is weak, (*i.e.* if attenuation within the absorbing volume is negligible), the x and λ -dependencies are decoupled and we can write F as a product of a geometric factor $g(x)$ and a wavelength dependent term $f(\lambda)$:

$$F(x, \lambda) = g(x) \times f(\lambda). \quad (5.9)$$

In this case, the geometric factor $g(x)$ cancels if we calculate the ratio $J[\text{O}(\text{}^1\text{D})]/J[\text{O}(\text{}^3\text{P})]$, because it can be moved out of the λ integration in equations (5.7) and (5.8). This is helpful if $g(x)$ and so the geometry is unknown, such as in the case of the PB06 experiment. In this case the *branching ratio* $r_{BR}(\text{O}(\text{}^1\text{D})/\text{O}(\text{}^3\text{P}))$ between O(¹D) and O(³P) production is given by the following expression:

$$r_{BR}(\text{O}(\text{}^1\text{D})/\text{O}(\text{}^3\text{P})) = \frac{\int_{\lambda} \sigma(\lambda) \Phi_{\text{O}(\text{}^1\text{D})}(\lambda) f(\lambda) d\lambda}{\int_{\lambda} \sigma(\lambda) \Phi_{\text{O}(\text{}^3\text{P})}(\lambda) f(\lambda) d\lambda} \quad (5.10)$$

where the physical quantities are the same as those used before, except for the presence of $f(\lambda)$ instead of the actinic flux $F(\lambda)$.

The determination of $r_{BR}(\text{O}(\text{}^1\text{D})/\text{O}(\text{}^3\text{P}))$ therefore requires knowledge of the absorption cross section $\sigma(\lambda)$, the quantum yields $\Phi_{\text{O}(\text{}^1\text{D})}(\lambda)$ and $\Phi_{\text{O}(\text{}^3\text{P})}(\lambda)$, and the spectral dependence of the actinic flux $f(\lambda)$. Ozone cross section data are available as a function of temperature and wavelength. Previous measurements have been extensively reviewed by Orphal [161]. However some uncertainties on the consistency of these data remain, (see Guinet et al. [127] and Picquet-Varrault et al. [122] for example), such that accurate ozone cross section measurements are a current priority in laboratory studies for atmospheric research. Nevertheless, for our purpose any of these data will be sufficient and we use the data that has been recently made available on the ACSO-IGACO-O3/UV¹ website.

¹Absorption Cross Sections of Ozone (ACSO) is an activity of O₃ and UV Integrated Global Atmospheric Chemistry Observations (IGACO), which is part of WMO's global atmospheric watch program (GAW):

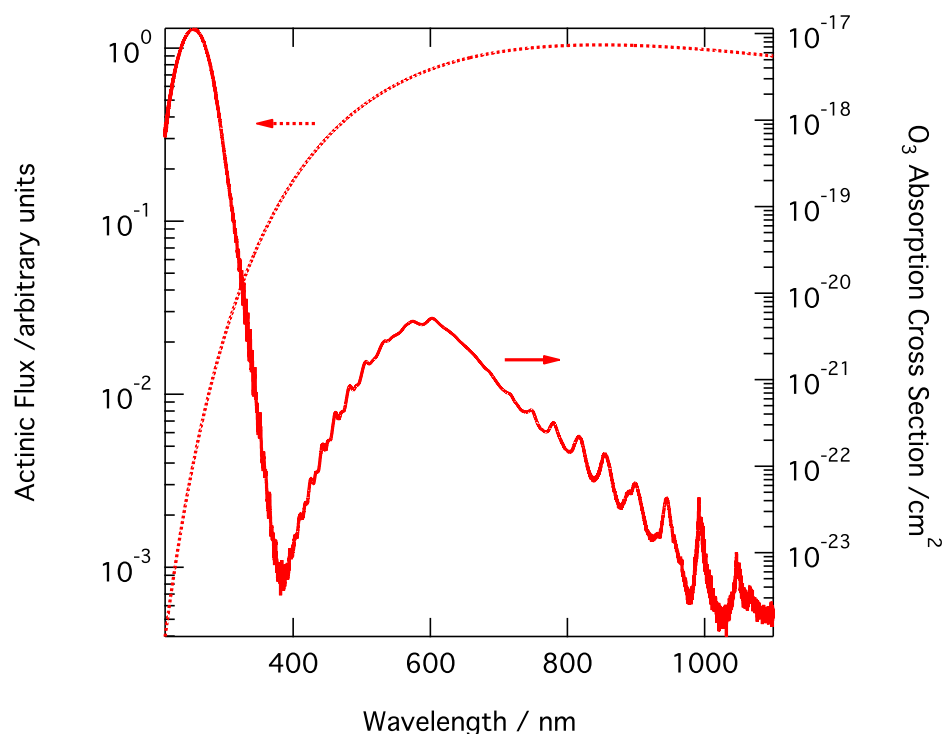


Figure 5.2: Ozone absorption cross section values (right axis) and spectral dependence of the actinic flux for a black body at 3400 K. Note the logarithmic scaling of the vertical axes.

The ozone cross section is plotted in figure 5.2 where the spectral dependence of the actinic flux for a black body at 3400 K is also shown. As demonstrated by the plot, the small UV flux of a thermal radiator is compensated by the strong absorption cross section in the Hartley band.

The quantum yield of $O(^1D)$ formation has been studied extensively, but its wavelength dependence, in particular due to the spin forbidden processes (5.2), is still not fully established. A recent review is given by Matsumi and Kawasaki [162] and current recommendations, such as JPL [150] are based thereon.

As discussed before, the quantum yield is close to unity below the threshold for the spin allowed channel (5.1) (see region I in Fig. 5.3). However, there is a significant and temperature dependent tail of the quantum yield function, which extends to longer wavelengths (zone II). It originates from hot band transitions into the B state and its effectiveness comes from the more than 10 times increased Franck-Condon factor for the $\nu'_3 = 0 \leftarrow \nu''_3 = 1$ as compared to the $\nu'_3 = 0 \leftarrow \nu''_3 = 0$ transition, which explains its strong and positive temperature dependence. Recently, evidence for still another contribution has been found. Smith et al. [157] found a constant $O(^1D)$ quantum yield of 0.12 from wavelengths beyond the long wavelength tail in the region between 328 and 338 nm. Bauer et al. [139] also inferred a wavelength independent $O(^1D)$ yield of $(6.4 \pm 0.6)\%$ over the wavelength range from 305 to 375 nm and further suggested that this value might hold all the way up to 411 nm. This value corresponds to the threshold of the spin forbidden channel, which has been identified to be

5.1. WAVELENGTH DEPENDENCE OF $O(^1D)$ PRODUCTION FROM O_3 PHOTOLYSIS⁷⁷

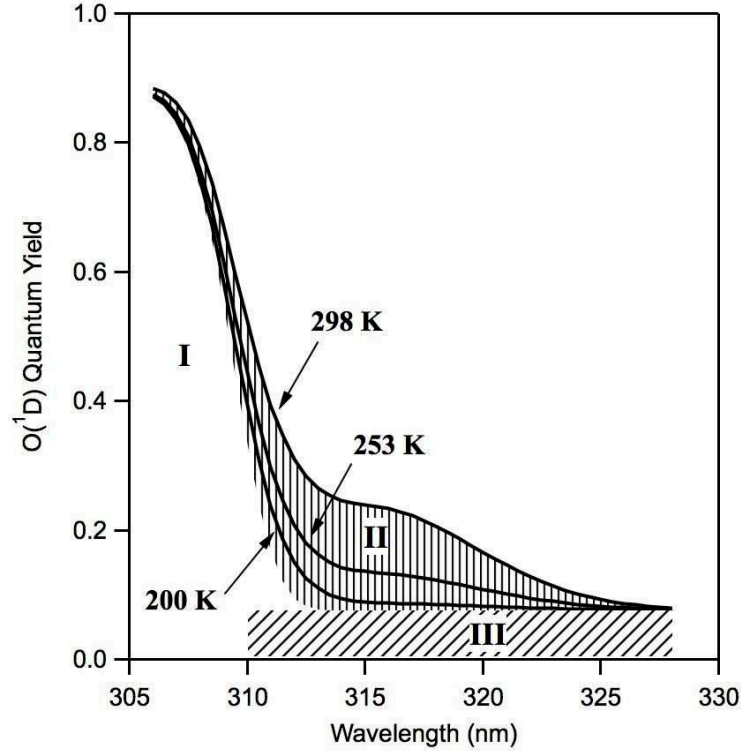


Figure 5.3: $O(^1D)$ quantum yield as a function of wavelength in the range between 305 and 330 nm. The figure is taken from Matsumi and Kawasaki [162]. Roman numbers I - III indicate contributions from different processes, see text.

on the origin of the $O(^1D)$, because temperatures were too low and energies too small that hot band transitions could have played a role in these studies. Based on these investigations, Matsumi and Kawasaki [162] recommend a constant contribution of 0.08 ± 0.04 between 329 and 340 nm, which is an important region for $O(^1D)$ formation in the atmosphere. So far, no recommendation is given for wavelengths larger than 340 nm, because measurements are scarce and the wavelength range is irrelevant for atmospheric studies.

Based on the above discussion and the recommendations given [163, 150], we have used the following parameterisation for the calculation of $\Phi_{O(^1D)}$:

- $\lambda \leq 305$ nm:

$$\Phi_{O(^1D)} = 0.9 \pm 0.09; \quad (5.11)$$

- $305 \text{ nm} < \lambda \leq 328$ nm:

$$\Phi_{O(^1D)} = \left(\frac{q_1}{q_1 + q_2} \right) A_1 \exp \left[- \left(\frac{X_1 - \lambda}{\omega_1} \right)^4 \right] + \left(\frac{q_2}{q_1 + q_2} \right) A_2 \left(\frac{T}{300 \text{ K}} \right)^2 \exp \left[- \left(\frac{X_2 - \lambda}{\omega_2} \right)^2 \right] + A_3 \left(\frac{T}{300 \text{ K}} \right)^{1.5} \exp \left[- \left(\frac{X_3 - \lambda}{\omega_3} \right)^2 \right] + c \quad (5.12)$$

- $328 \text{ nm} < \lambda \leq 411$ nm

$$\Phi_{O(^1D)} = 0.08 \pm 0.04 \quad (5.13)$$

- $\lambda > 411 \text{ nm}$

$$\Phi_{O(^1D)} = 0 \quad (5.14)$$

where

$$q_i = \exp\left(-\frac{\nu_i}{RT}\right) \quad (5.15)$$

and λ is the wavelength, T the temperature and the constant $R = k/(hc)$ the inverse of the second radiation constant, which takes the value of $0.695 \text{ cm}^{-1} \text{ K}^{-1}$. X_i , A_i , ω_i , ν_i and c are fitting parameters with recommended values listed in table 5.1. Note that corresponding uncertainties are 10 % relative for $\Phi_{O(^1D)} > 0.4$ and 0.04 for $\Phi_{O(^1D)} < 0.4$ [163, 150].

	$i = 1$	$i = 2$	$i = 3$
X_i (nm)	304.225	314.957	310.737
ω_i (nm)	5.576	6.601	2.187
A_i	0.8036	8.9061	0.1192
ν_i (cm^{-1})	0	825.518	-
c	0.0765	-	-

Table 5.1: Recommend parameter values used to calculate $O(^1D)$ quantum yield. Taken from [150].

5.2 Experimental determination of the branching ratio between $O(^1D)$ and $O(^3P)$ production for two different lamps

As explained in the previous paragraph, the main products in ozone photolytic dissociation are oxygen molecules and atoms, both in ground and excited states. The branching ratio between $O(^1D)$ and $O(^3P)$ production depends on several factors. On the one hand, molecular properties (σ, Φ) are involved. On the other hand, it is the actinic flux or its spectral dependency provided by the light source which determines to what extent each of these two species are produced. While information on the molecular properties can be inferred from literature data (see previous section), the actinic flux will be specific to a particular experiment and it will depend on the spectral properties of the light source that has been employed. In this section, we will present the experimental determination of the emission spectrum of two different lamp types (LED and halogen tungsten). These have been used either in our own experiments or in other studies on the $O + CO$ reaction. Using the simplifying assumption that the actinic flux can be described as a product of a geometric and a wavelength dependent factor, the $O(^1D)/O(^3P)$ -branching ratio has then been determined according to formula (5.10).

5.2.1 Experimental setup

Figure 5.4 gives a schematic of the experimental setup. It essentially consists out of the light source that is mounted in front of a white diffuser plate (SPECTRALON[®], Labsphere) and a spectrograph with its entry oriented at 90° with respect to the lamp-diffuser axis. The light from the diffuser plate, which has a wavelength independent reflection coefficient is then guided through a slit onto the UV fiber that is connected to a grating spectrometer (BWTEK, model BRC112E-V). Because the tungsten lamp can get very hot, caution must be taken that it does not overheat and that inflammable material is not used in the surrounding. The lamp

has been mounted on a moveable arm so that the distance to the diffuser plate was adjustable in order to match the lamp intensity to the dynamic range of the grating spectrometer.

The spectral resolution of the spectrometer is 1.17 nm at 546 nm, based on a grating with 600 grooves/mm at 400 nm. The instrument can be operated in the wavelength range between 350 nm and 1050 nm. It was observed that the spectrometer needed about 2 hours to stabilize, most likely due to thermal effects when switching on the instrument. After that period, dark signals of about 1000 counts became stable.

Spectra have been recorded in sets of 5 consecutive acquisitions. These have been averaged for evaluation. As will be detailed in the next subsection, the halogen tungsten lamp is equipped with cold reflector. In order to quantify the impact of the reflector on the spectrum emitted from the lamp/reflector combination, it has been necessary to measure the spectrum of the lamp once with and once without reflector.

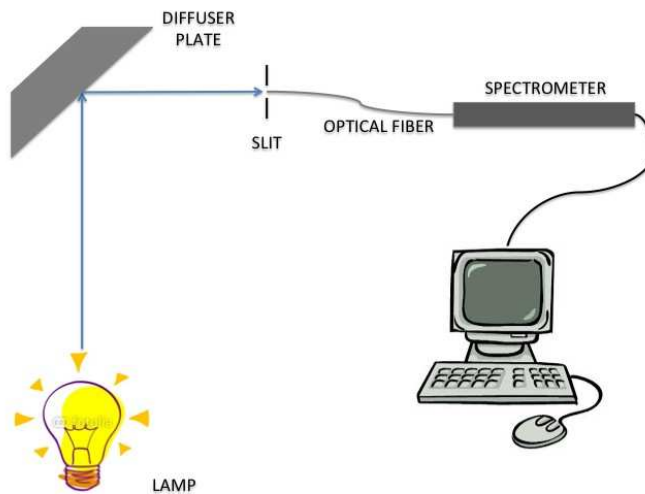


Figure 5.4: Experimental setup for measuring the spectral distribution of lamps.

5.2.2 Lamp spectra

The apparent spectral distribution or raw spectrum $I(x, \lambda)$ of a lamp can be written as:

$$I(x, \lambda) = \phi(x, \lambda) \times \eta(\lambda) \quad (5.16)$$

where $\phi(x, \lambda)$ is the instrument sensitivity (including transmission by the UV fiber) and $\eta(\lambda)$ is the normalized lamp spectrum.² We express I in counts (keeping the integration time always at 11 ms), which are the units directly provided by the spectrometer software. Raw spectra (not shown) show strong spectral structures which are not due to the light sources that have been used. Therefore, the spectrometer's instrument function needs to be determined by employing a lamp with known spectral emission function $\eta_c(\lambda)$. Our calibration lamp was a halogen tungsten lamp (OSRAM, halogen display/optic lamp XENOPHOT[®] HLX 64342, 6.6 A, 100 W), whose spectral emission function $\eta_c(\lambda)$ has been certified by L.O.T. Oriel (Germany) and is given as a list of data points. $\eta_c(\lambda)$ of this lamp is almost a black body

²Any constant factor can be absorbed into the instrumental sensitivity $\phi(x, \lambda)$. $\eta(\lambda)$ can therefore be arbitrarily normalized.

spectrum at 3200 K, which follows Plank's law:

$$\eta_{\text{Planck}}(\lambda, T) \propto \frac{hc^2}{\lambda^5} \frac{1}{\exp\left(\frac{hc}{k\lambda T}\right) - 1}, \quad (5.17)$$

where h is the Plank constant, c the speed of light, λ the wavelength, k the Boltzmann constant and T the temperature. Nevertheless, the provided calibration data show slight deviations from the black body spectrum as shown in figure 5.5. A best fit is obtained when we multiply the Planck function (5.17) by a quadratic polynomial in λ :

$$P(\lambda) = A \left[1 + b \frac{\lambda}{500 \text{ nm}} + c \left(\frac{\lambda}{500 \text{ nm}} \right)^2 \right].$$

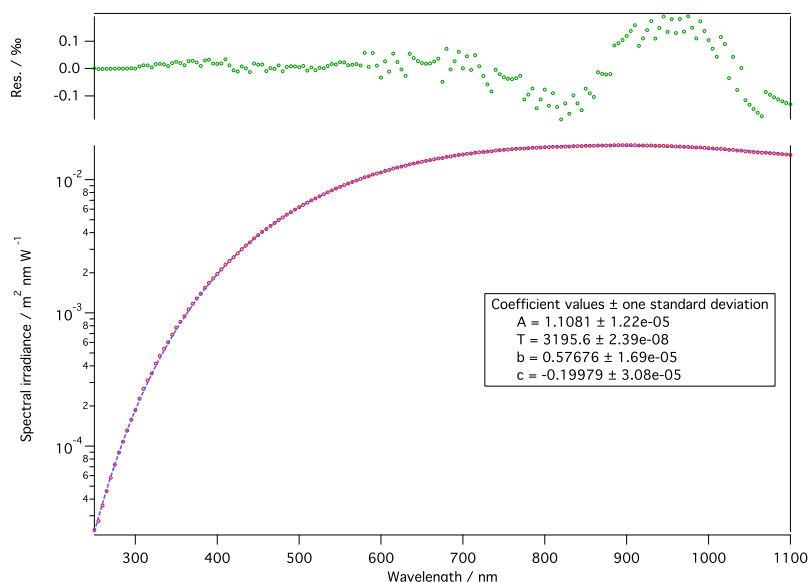


Figure 5.5: Calibration curve of the reference lamp (in red) as provided by Oriel, Germany. An analytic fit (blue) and residuals (green) are also shown. The best fit parameters can be inferred from the box displayed on the graph.

The fit curve in figure 5.5 has then be used to determine the instrument response $\phi(x, \lambda)$ via:

$$\phi(x, \lambda) = \frac{I_c(x, \lambda)}{\eta_c(\lambda)} \quad (5.18)$$

An arbitrary lamp spectrum $\eta_s(\lambda)$ can now be obtained from measurement of the raw lamp signal (I_s) by combining equations (5.16) and (5.18):

$$\eta_s(\lambda) = \frac{I_s(x, \lambda)}{I_c(x, \lambda)} \times \eta_c(\lambda), \quad (5.19)$$

This $\eta_s(\lambda)$ is proportional to the spectral distribution of $f(\lambda)$ in an experiment using the same lamp. With I_s at hand, we can therefore calculate the branching ratio between $O(^1D)$ and $O(^3P)$ production using equation (5.10) when we substitute the spectral dependence $f(\lambda)$ by $\eta_s(\lambda)$ in equation (5.19). The numerical integration had been evaluated using the technical graphing and data analysis software IGOR Pro (Wavemetrics Inc., version 6.2).

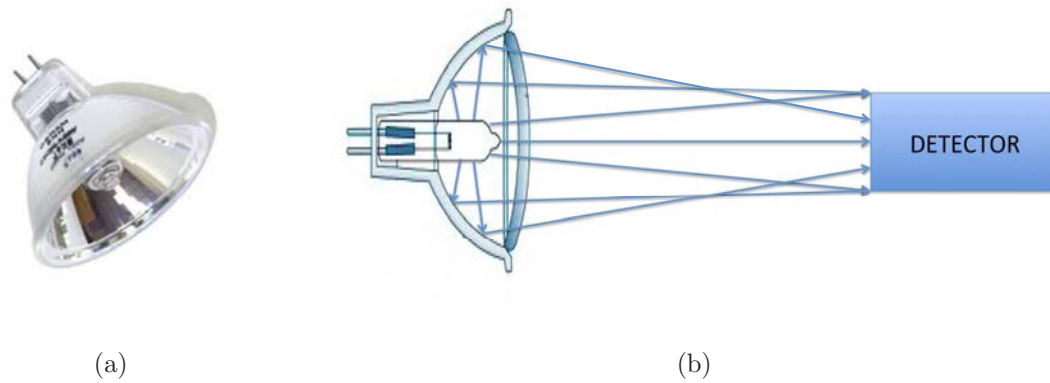


Figure 5.6: Halogen tungsten lamp with cold mirror. **a)** photograph. **b)** imaging properties. Note that the quartz bulb of lamp model no 13163 does not have a window protection, contrary to the scheme that is displayed. The photograph was taken from <http://www.digikey.com> website and the scheme was adapted.

5.2.3 Spectral Emission of Halogen Tungsten lamps

The lamp used in the PB06 experiment [134] is a halogen filled tungsten lamp (model no 13163, 250W, 24V, GX5.3 1CT, color temperature 3400 K) with a quartz bulb that emits substantially in the visible and in the IR. The authors state that its emission essentially occurs between 350 and 900 nm and that there is no emission below 350 nm, even though the high filament temperature and the use of pure quartz as bulb material is in favor of an extended, albeit small lamp emission down to wavelengths in the UV-A and UV-B³. We therefore wanted to verify the lamp spectrum in the UV. The specific lamp type used is equipped with a cold light mirror (picture 5.6a), a dichroic glass which surrounds the bulb and operates as forward focussing element in the visible region while it is transparent in the IR. According to the manufacturer (Philips), the spectrum of the bulb alone (with reflector removed) should be very similar to the spectrum of a reflector free lamp (no 7787 #N3), which exhibits an approximate Planck distribution at around 3400 K (see red curve in Figure. 5.7).

Figure 5.8 shows the spectrum of the reflector-free model 13163 lamp at a nominal temperature of 3400 K as compared to the calibrated lamp with a color temperature of 3200 K.

The observed trend is most easily explained by the ratio of two black body spectra (eqn. (5.17)) at different temperatures. If the reference spectrum is fixed to the nominal value of 3200 K, a temperature of about 3560 K is required to explain the observed variation. It is possible that the lamp temperature exceeds its nominal value of 3400 K due to insufficient ventilation and the result therefore seems reasonable. In any way, our results confirm that the spectrum (at least above 320 nm) of this lamp can well be approximated by a black body spectrum once the reflector has been removed. The use of a filament temperature of 3400 K gives a conservative estimate. This conclusion is compatible with the manufacturer information on the reflectorless lamp model 7787 #N3, where the same type of spectrum has been obtained all over the wavelength range from 300 to 1000 nm. Figure 5.7 reproduces a part of this spectrum between 300 and 800 nm). From the latter data, it can be inferred that the unaltered spectrum of the reflectorless model 13163 bulb in fact corresponds to a black body at 3400 K – at least in a range down to 300 nm. We will see later, that an uncertainty of the order of 100 K in the black body temperature will not have a large impact on the derived $O(^1D)/O(^3P)$ ratio.

³UV radiation can be divided into UV-A (from 400 to 315 nm), UV-B (from 315 to 280 nm) and UV-C (from 280 to 100 nm).

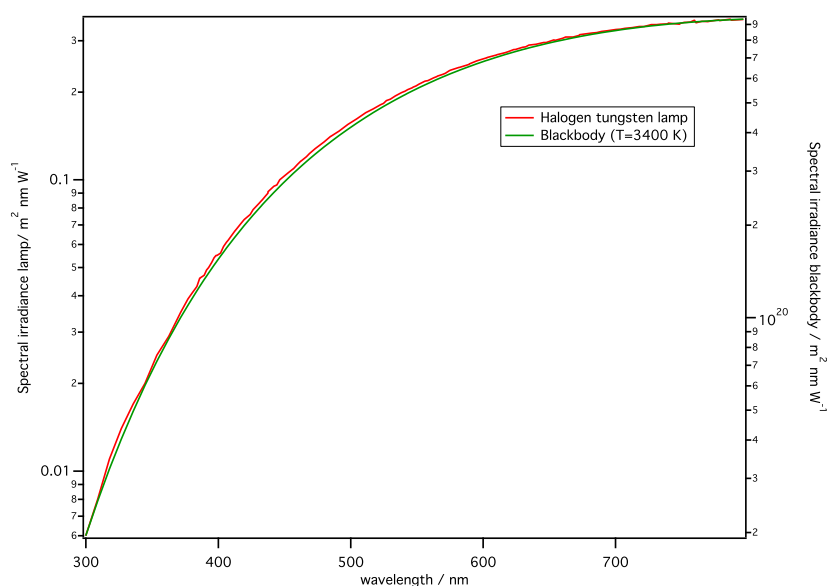


Figure 5.7: Spectral irradiance of a PHILIPS halogen filled tungsten lamp (model 7787 #N3) similar to the one used in PB06 (red curve) and spectral irradiance of a black body calculated at $T = 3400$ K (green curve). The red curve is courtesy of PHILIPS (Eindhoven, Netherlands).

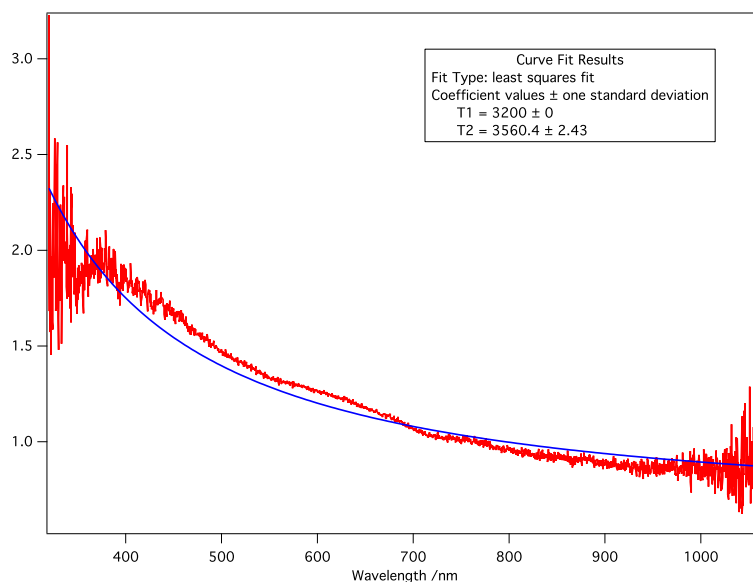


Figure 5.8: Ratio of two halogen lamp spectra. The model 13163 lamp vs. Osram calibration lamp is shown. The ratio of two black body curves (5.17) at different temperatures is also shown, using $T_1 = 3200$ K and $T_2 = 3560$ K.

The emission of the lamp will be modified by the presence of the dichroic reflector, which has therefore also been investigated. A spectrum with the complete lamp at large distance (~ 1 m) from the diffuser has been taken. In this arrangement, light reflected from the mirror will dominate the signal, because it leaves the lamp collimated while the direct light is non-focalised (see fig. 5.6b). From the raw spectra, we have derived the reflectivity of the lamp reflector. The result of our measurements is shown in figure 5.9. The reflectance curve shows a broad bandpass between 400 and 700 nm. The behaviour below 320 nm is not accessible from our measurements and must be guessed. We therefore envisage different scenarios: a) we assume that the reflectance goes down continuously to 0 at 300 nm (“low $O(^1D)$ ”), b) the curve falls off linearly just until 250 nm (“medium $O(^1D)$ ”) or c) stays at a constant value of about 0.7 (“high $O(^1D)$ ”).

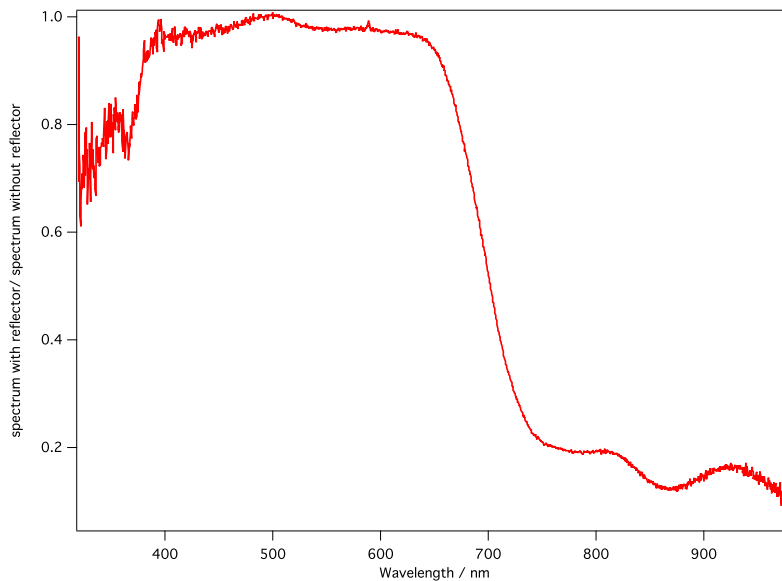


Figure 5.9: Reflectance curve of the dichroic mirror as obtained from lamp spectra measurement

In order to study the impact of the different wavelength regions on the derived branching ratios between $O(^1D)$ and $O(^3P)$ we have calculated these ratios assuming an ideal black body radiator at 3400 K and varied both, upper and lower wavelength integration limits. The results of these numerical calculations are shown in table 5.2. $r_{BR}(O(^1D)/O(^3P))$ might vary between 0 and about 1.6, but the effect of varying the upper cut off (900 or 1100 nm) is very limited ($\sim 1\%$), which can be understood by the fact that both the lamp and the Chappuis bands have maxima that are well below our cutoff wavelengths.

On the other hand, the results are very sensitive to the UV cutoff employed. This is due to the competition between the fall off of the emission towards lower wavelengths and the strong increase of the ozone cross section. Unfortunately, we do not have reliable measurements in these regions, but need to rely on reasonable scenarios that are supported by our investigations. Using $T = 3400$ K we find the following values of $r_{BR}(O(^1D)/O(^3P))$ for the different mirror scenarios a) 0.010, b) 0.389 and c) 1.172. While these values span a range of roughly two orders of magnitude, the numbers indicate a quite significant amount of $O(^1D)$ production even in the most conservative case. We also note that scenario c) and to some extent even b) might overestimate $O(^1D)$ due to the fact that the high ozone cross section in the Hartley band leads to strong absorption, so that the shortest wavelengths will be self-shielded within a small penetration region.

The effect of lamp temperature is not very drastic, however. Table 5.3 gives the results for an ideal black body at 3500 K. Independent of the wavelength cut-off that we chose, the

$T = 3400$ K	low λ_{low} (nm)	Branching ratio	
		$\lambda_{high} = 900$ nm	$\lambda_{high} = 1100$ nm
	200	1.59150	1.58267
	220	1.58981	1.58098
	240	1.53210	1.52353
	260	1.16114	1.15432
	280	0.43077	0.42801
	300	0.05044	0.05010
	320	$9.24159 \cdot 10^{-4}$	$9.17842 \cdot 10^{-4}$
	340	$6.69028 \cdot 10^{-5}$	$6.64421 \cdot 10^{-5}$
	360	$1.07426 \cdot 10^{-5}$	$1.06686 \cdot 10^{-5}$
	380	$6.33821 \cdot 10^{-6}$	$6.29454 \cdot 10^{-6}$
	400	$4.18856 \cdot 10^{-6}$	$4.15970 \cdot 10^{-6}$
	420	0	0

Table 5.2: Branching ratio values calculated for a section of an ideal black body spectrum at $T = 3400$ K. The spectrum was calculated for variable starting wavelengths λ_{low} between 200 and 420 nm and long wavelengths cut-offs λ_{high} of 900 or 1100 nm.

$T = 3500$ K	λ_{low} (nm)	Branching ratio	
		$\lambda_{high} = 900$ nm	$\lambda_{high} = 1100$ nm
	200	1.94598	1.93641
	220	1.94380	1.93423
	240	1.87202	1.86272
	260	1.42045	1.41294
	280	0.52812	0.52500
	300	$6.11211 \cdot 10^{-2}$	$6.07407 \cdot 10^{-2}$
	320	$1.09563 \cdot 10^{-3}$	$1.08864 \cdot 10^{-3}$
	340	$7.73955 \cdot 10^{-5}$	$7.68974 \cdot 10^{-5}$
	360	$1.20555 \cdot 10^{-5}$	$1.19779 \cdot 10^{-5}$
	380	$7.02909 \cdot 10^{-6}$	$6.98382 \cdot 10^{-6}$
	400	$4.62764 \cdot 10^{-6}$	$4.59783 \cdot 10^{-6}$
	420	0	0

Table 5.3: Branching ratio values calculated for a cut of an ideal black body spectrum at $T = 3500$ K. The spectrum was calculated for variable starting wavelengths λ_{low} between 200 and 420 nm and long wavelengths λ_{high} cut-offs of 900 or 1100 nm.

higher temperature leads to a relative increase of $O(^1D)$ by less than 25 %. To be conservative in our estimation of $O(^1D)$, we prefer to stick to the nominal temperature of 3400 K.

5.2.4 Spectral Emission of LED lamps

The branching ratio between $O(^1D)$ and $O(^3P)$ production has also been determined for a commercial LED lamp. This lamp type, a Philips LED (11 Watt, warm white, 2700 K) has been used in the Copenhagen reactor experiments (see chapter 4) in order to minimize production of $O(^1D)$. The derived emission spectrum is shown in figures 5.10 and 5.14.

The lamp is based on a blue led and a remote phosphor element which converts blue photons into longer wavelengths and is characterized by zero emission in the ultra-violet and a strong spectral emission in the visible part of the spectrum at wavelengths above 650 nm. A second minor peak, the original LED wavelength, is present at ~ 450 nm. We have remeasured the lamp spectrum in order to verify that no light is emitted below the threshold of about 380 nm (see raw spectrum in figure 5.10). The spectrum shows the characteristic features of the data supplied by the manufacturer. Nevertheless, we find an offset in the UV region. In order to demonstrate that the offset is not real, but an artifact due to stray light and noise in the spectrometer, additional tests have been made using glass color filters.

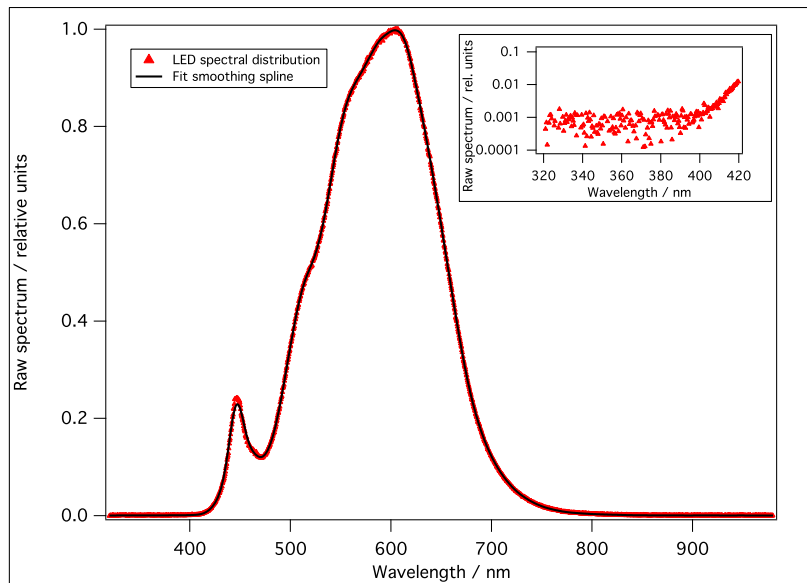


Figure 5.10: Raw spectrum of LED lamp (red triangles) in relative units. A fit to the experimental data with a spline function (black curve) is also shown. In the upper right panel a zoom on the UV region is presented.

Two different optical filters have been used: a long pass filter (Schott GG475, 2 mm thickness, 0.92 reflection factor) with a cutoff at about 475 nm and an ultraviolet band pass (UG5, 2 mm thickness, 0.91 reflection factor) which absorbs in the infrared and at visible wavelengths. The corresponding transmission curves are given in figures 5.11 and 5.12.

Figure 5.13 shows the results of our colour glass filter measurements. When we compare the unfiltered spectrum with the one where the GG475 nm has been introduced just before the entry of the UV fiber, we find that the signal level below 400 nm remains unchanged ($\sim 10^1 - 10^2$ counts), even though the filter transmission is at the 10^{-5} level or below at wavelengths under 450 nm. This clearly indicates that the observed signal does not derive from photons at the corresponding energies, but must be an experimental artifact (stray light

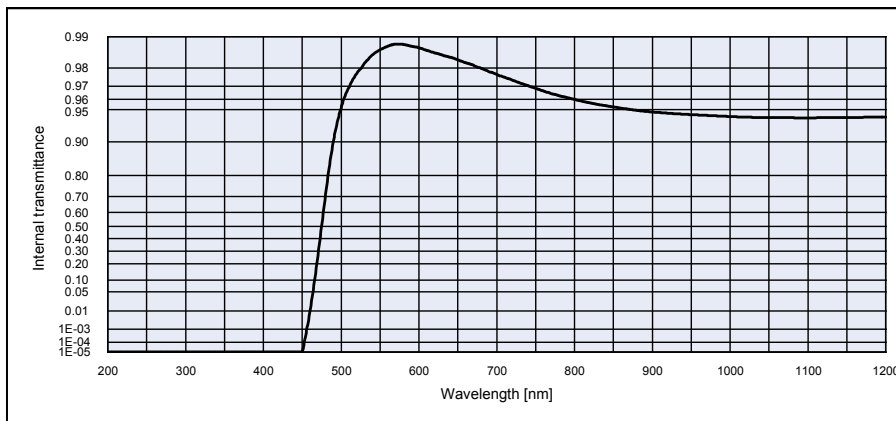


Figure 5.11: Internal transmittance of a SCHOTT Longpass Filter GG475 for 3 mm thickness. Figure reproduced from the filter data sheet.

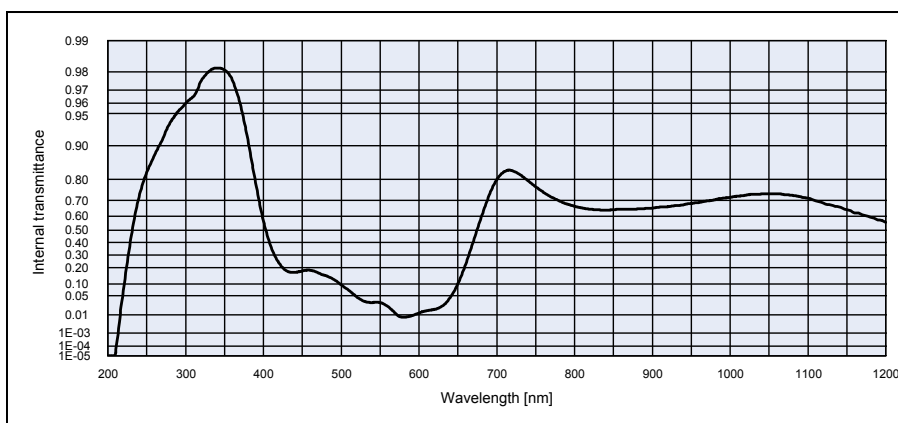


Figure 5.12: Internal transmittance of a SCHOTT Ultra Violet Band Pass Filter UG5 for 1 mm thickness. Figure reproduced from the filter data sheet

or background noise). It is to be observed that the noise background is slightly reduced when we use the UV band pass filter. This indicates that some stray light has been suppressed (due to the reduction of the total number of photons admitted to the spectrometer). The remaining scatter of the data must be explained by the limited dynamic range of our instrument. We note that the white noise of the dark signal (~ 1000 counts), that has already been subtracted, should lead to a maximum offset of up to $\sqrt{2} \times 3 \times \sqrt{1000/5} \simeq 60$, where the individual factors come from background subtraction, from the statistical expansion from $1\text{-}\sigma$ to $3\text{-}\sigma$ and from the $1\text{-}\sigma$ counting noise of a signal that has been obtained from averaging five individual acquisitions, respectively. This value is in very good agreement with our measurement.

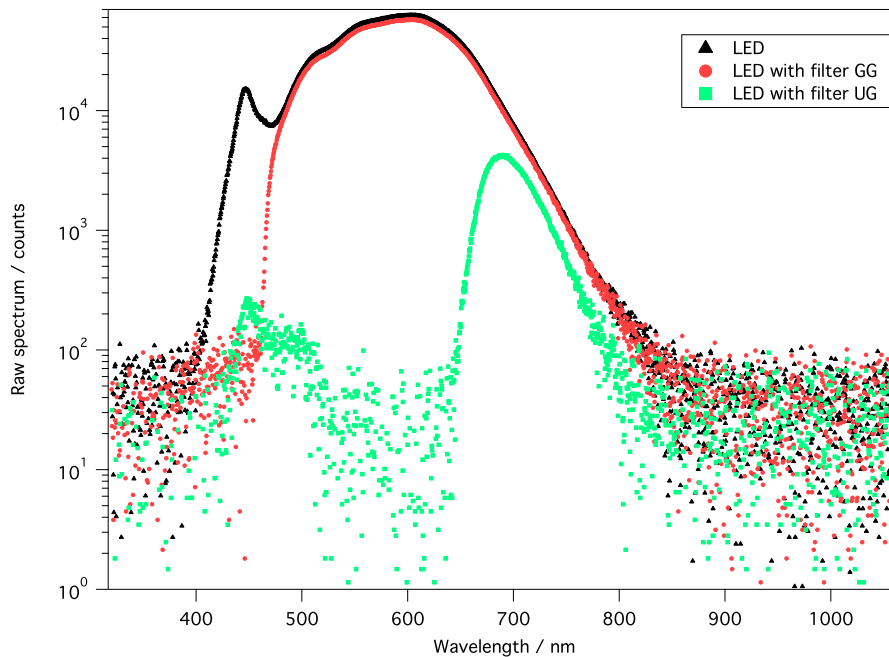


Figure 5.13: Filtered and unfiltered raw emission spectra of a LED. Black triangles indicate the direct measurement signal without any filtering. Red circles and green squares have been obtained by respectively introducing a GG475 long pass and a UG5 UV bandpass colour glass filter in front of the spectrometer entrance.

Stray light and background noise have therefore been removed in the construction of the LED emission spectrum all over the wavelength range from 250 to 1200 nm. For that purpose, the measured emission spectrum (black points) in Figure 5.14 has been extrapolated by exponential growth and decay curves to lower and higher wavelengths, respectively. These curves have been adjusted as to smoothly extend the data in the 413 to 423 nm and the 706 to 748 nm ranges, respectively. The resulting model spectrum, along with the measured data, is shown in figure 5.14.

Following the procedure illustrated in section 5.2.2, the branching ratio $r_{BR}(O(^1D)/O(^3P))$ was calculated from the derived LED spectrum and a value of 1.95×10^{-7} is obtained. If we arbitrarily limit the integration range and start at 320 nm, we get a branching ratio value of 8.4×10^{-8} . This shows that typical branching ratios of the order of only a few 10^{-7} are to be expected when a white LED is used for ozone photolysis. This number is about five to seven magnitudes lower than the range of values (between 0.01 and 1) that has been estimated for the halogen filled tungsten lamps at 3400 K.

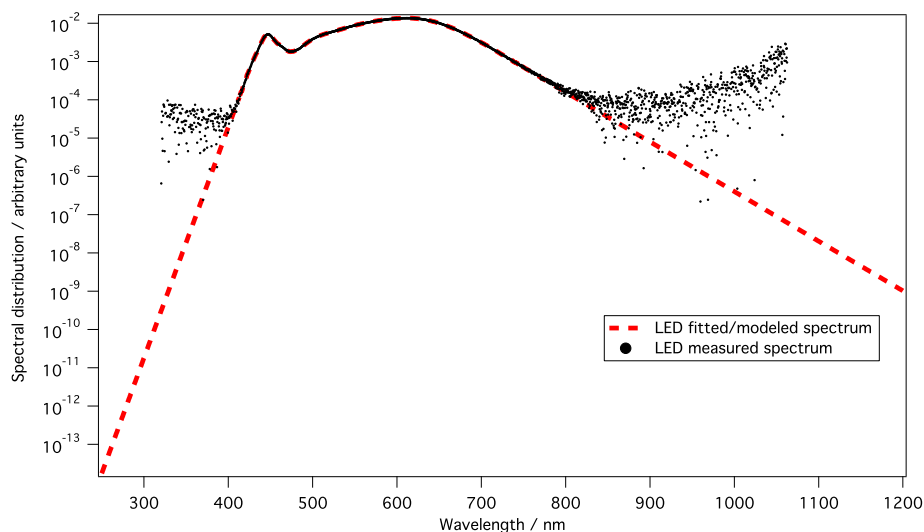


Figure 5.14: Calibrated and extrapolated emission spectrum of the LED. Short and long wavelength tails of the measurement have been extrapolated by ignoring the background noise and stray light.

5.3 Summary and Discussion of Obtained Branching Ratios

The goal of the present chapter has been to determine the $O(^1D)/O(^3P)$ production rate ratio from ozone photolysis used as atom source in experiments on the isotope fractionation in the $O + CO$ recombination reaction. Another goal was to identify and characterize a light source that minimizes $O(^1D)$ production.

In the earliest measurements, a lamp had been used that emitted strongly in the UV and produced large amounts of $O(^1D)$. Only recently, the implementation of a practically $O(^1D)$ free oxygen source based on ozone photolysis using a halogen filled tungsten lamp has been claimed [134]. However, some $O(^1D)$ production must have been occurred, at least through the spin-forbidden reaction channel (5.2). We have therefore investigated more closely the emission characteristics of this lamp. Our measurements and the comparison with manufacturer data shows that this particular lamp produces at least between 1 and 2 % of $O(^1D)$ (see Table 5.4), where the lower number applies to large lamp-sample distances and the larger when the lamp is brought closely to the sample, such that a mix of reflected and direct light illuminates the gas. For several reasons, the estimate of 1 - 2 % is only conservative and other scenarios are also presented in Table 5.4.

In most practical cases, the lamp will be close to the sample to maximize O atom concentrations that are required to study the slow chemical reaction. Because of the black body spectrum of the lamp, much higher photon energies than those used for obtaining this conservative estimate are actually available, irrespective of the mirror material. This is because there will be a significant fraction ($\simeq 30\%$) of photons that enter directly into the reactor volume. Even if these wavelengths are possibly not reflected, $r_{BR}(O(^1D)/O(^3P))$ would be between 10 and 50 % at these geometries. If reflection occurs significantly below 300 nm, however, $r_{BR}(O(^1D)/O(^3P))$ could even be higher, always assuming that the window material used does not selectively absorb incoming photons.

On the other hand, $r_{BR}(O(^1D)/O(^3P))$ will not exceed the value of 2 and it needs to be pointed out that self shielding of ozone might take place at wavelengths below 300 nm, and especially in the maximum of the Hartley band, where the cross section is $1.1 \times 10^{-17} \text{ cm}^2$. This means that ozone columns of 10^{17} cm^2 at 250 nm and of $4 \times 10^{18} \text{ cm}^2$ at 300 nm lead to full ($1/e$) absorption. If we assume typical dimensions of 10 cm for a small reactor, number

Lamp	Branching ratio	Additional remarks	
<i>Halogen Tungsten</i> — w/o reflector	<i>thermal radiator at $T = 3400\text{ K}$</i>		
	0.05	$\lambda_{low} = 300\text{ nm}$	
	0.43	$\lambda_{low} = 280\text{ nm}$	
	1.5	$\lambda_{low} = 240\text{ nm}$	
	1.6	$\lambda_{low} = 200\text{ nm}$	
	reflector dominated	0.01	scenario a, see p. 83
		0.39	scenario b, see p. 83
1.2		scenario c, see p. 83	
<i>LED</i>	$2.0 \cdot 10^{-7}$	full spectrum between 250 and 1200 nm	
	$8.4 \cdot 10^{-8}$	as before, but with low wavelength cutoff at 320 nm	

Table 5.4: Branching ratios $r_{BR}(\text{O}^1\text{D})/\text{O}^3\text{P}$) from ozone photolysis using a incandescent lamp (model 13163 from Philips) and a white light LED. Different assumptions on the reflectivity of the dichroic mirror and on the effective emission range have been made.

densities of 10^{16} cm^{-3} ($\sim 5\text{ hPa}$) or $4 \times 10^{17}\text{ cm}^{-3}$ ($\sim 100\text{ hPa}$) are sufficient to decrease $r_{BR}(\text{O}^1\text{D})/\text{O}^3\text{P}$) due to self shielding in the wavelength ranges that preferentially produce O^1D . For reactors with larger dimensions, critical concentrations are even lower and in these cases, the values with cutoffs $\lambda_{low} = 280$ or 300 nm (or scenario a) might be more realistic.

Table 5.4 also lists characteristic branching ratios $r_{BR}(\text{O}^1\text{D})/\text{O}^3\text{P}$) for a newly employed LED lamp, which is characterized by very little output in the UV. It is clear that this lamp type is well suited for the production of ground state atoms from ozone photolysis.

5.4 Short Chapter Summary

- The photodissociation chemistry of O_3 is reviewed.
- Spectral dependencies of the emission of halogen filled tungsten lamps and of a LED have been investigated.
- Within the limits of our methods (spectral range between 320 to 1000 nm), the continuous black body spectrum of tungsten filament lamps has been confirmed.
- Contrary to what has been assumed in a previous publication [134], O^1D will be produced from O_3 using a halogen filled tungsten lamp (Philips model).
- $\text{O}^1\text{D})/\text{O}^3\text{P}$ production branching ratios have been obtained for the Copenhagen and PB06 experiments.
- While LEDs have very low $\text{O}^1\text{D})/\text{O}^3\text{P}$ branching ratios on the order of a few 10^{-7} , the same branching ratio for the tungsten lamp will be in the 10^{-2} to 1 range.
- LEDs are promising light sources for the generation of ground state atoms from ozone photolysis (for $\text{O} + \text{CO}$ experiments).

Chapter 6

Isotope Kinetic Modeling

Quantitative interpretation of kinetic experiments, such as our study on CO₂ formation from the irradiation of CO/O₃ mixtures, requires the numerical modeling of the chemical rate equations involved. Due to the large number of reactions that take place when isotope variants even in very simple reaction schemes are considered and due to the stiffness of the system of differential equations involved, the use of dedicated software is required. Numerical simulations within this thesis have been performed using simulation code that has been created by the free KPP software package. This software package, as well as the different models and some test scenarios are described in the current chapter. Additional tests have been performed using the commercial mathematical software package Mathematica, which contains numeric solvers for systems of partial differential equations based on different algorithms.

6.1 Software Tools

We shortly describe the two software packages that have been used to interpret our and previous experimental observations.

6.1.1 The Kinetic Preprocessor – KPP

KPP, which stands for Kinetic PreProcessor, is a flexible software environment [164, 165] written in the programming language C for the implementation and solution of systems of coupled ordinary differential equations of chemical reactions networks. Starting from a set of chemical species and a list of reactions, KPP sets up the system of differential equations and allows running and analyzing its temporal evolution. It then generates a computer code for the simulation of the reaction in one out of four programming languages: C, FORTRAN, FORTRAN90 or Matlab. The generation of the simulation code requires the choice of a numerical integration routines, of which several are provided with the distribution of KPP.¹ Some of these are particularly suited to solve stiff reaction networks, such as encountered in atmospheric chemistry problems as well as in the photochemical system studied within this thesis. The executable code can be further adapted and extended. KPP is mostly used in the atmospheric chemistry community and it has been intergrated in global geochemical models (ECCAM, MECCA etc.) [165–167].

In this thesis KPP and the generated simulation codes in C were run on a Macintosh PowerBook under BSD Unix. Isotope kinetic studies require high numerical accuracy, which is due to the smallness of isotope effects (in the sub ‰ down to the 10⁻⁶ range). Since we are aware of only one previous isotope kinetic simulation based on KPP [166], which used on an approximative scheme to be incorporated into a global (3D) chemical transport model,

¹The actual version available at <http://people.cs.vt.edu/~asandu/Software/Kpp/> has version number 2.3.3.

it deemed useful to test the accuracy of the solver and the KPP generated code on our 0D box model set of photochemical reactions. The two sets of photochemical models as well as the test of the accuracy of the KPP generated integrator routine will be presented in the remainder of the chapter.

6.1.2 Mathematica

The commercial Mathematica[®] software package² also provides tools for solving systems of ordinary differential equations (ODEs) and dedicated packages [168, 169] have been developed to assist in the setup and investigation of reaction kinetic systems. However, the rate equations need to be implemented by hand, which is an error prone procedure in the case of large reaction networks. We have therefore used Mathematica only in order to check the impact of using different solver routines on simulating the kinetics neglecting any isotope fractionation, which greatly reduced the number of reactions. This already provided an independent comparison with the results of PB06 (see chapter 3) and also allowed to verify the implementation of the chemical system and the accuracy of the integrators used in our KPP simulations. The runs using the Mathematica software package have been based on version 8.1 of the software and were obtained on a Macintosh PowerBook.

6.2 Oxygen Isotope Models

6.2.1 General Remarks

Two principal models were employed within this thesis to describe CO₂ formation from irradiation of O₃-CO mixtures. The small model assumes that no electronically excited species are generated and that no traces of H₂O and nitrogen oxides are present. Depending on the light source used (see chapter 5), this simplification may or may not be justified, because electronically excited oxygen might form from the photolysis of ozone, thus provoking rich radical chemistry in the presence of water traces. In that case the full model including excited states of oxygen and diverse trace gases with a priori unknown concentrations need to be considered. This model has been simulated including the rare isotopes of oxygen.

6.2.2 Definitions and terminology in chemical kinetics

Starting from a list of n_x different chemical species $\{X_i\}$ and the j chemical reactions R_j between these

$$R_j : \sum_i \nu_{ij} [X_i] = 0, \quad (6.1)$$

where ν_{ij} is the stoichiometric coefficient of compound X_i in reaction j and where the square brackets denote the concentration (number density for reactions in the gas phase). ν_{ij} is positive (negative) if X_i is consumed (produced) in reaction j and 0 if its concentration remains unchanged during reaction. The rate r_j associated with each reaction is given as (see IUPAC Gold Book [170])

$$r_j = -\frac{1}{\nu_{ij}} \frac{d[X_i]}{dt}. \quad (6.2)$$

Note that the related variable

$$\dot{\xi}_j = \frac{d\xi_j}{dt} = -\frac{1}{\nu_{ij}} \frac{dN(X_i)}{dt}, \quad (6.3)$$

²<http://www.wolfram.com/mathematica/>

where $N(X_i)$ defines the molar abundance of molecule X_i , is called the rate of conversion of a reaction. Its use might be more convenient than use of r_j in situations where the volume changes during the course of a reaction. Usually, r_j can be expressed as a function of reactants concentrations, using the so called rate coefficients k_j that establish the relation between the observed rate and reactant concentrations

$$r_j = k_j \prod_{\nu_{ij} < 0} [X_i]^{\nu_{ij}}. \quad (6.4)$$

These constants k_j are independent of molecular concentrations $[X_i]$, but may well depend on pressure, temperature and other physical variables. The exponents ν_{ij} in the product are experimentally determined coefficients that determine the order $l_j = \sum_i \nu_{ij}$ of a reaction. ν_{ij} thus defines the order of reaction j with respect to the concentration of X_i . For elementary reactions, *ie.* a reaction in which one or more of the chemical species react directly to form products in a single reaction step and with a single transition state [170], the order $l_j = 1, 2$ or 3 determines the molecularity of the reaction. Examples for unimolecular ($l = 1$) reactions are photodissociation reactions



where the rate coefficient is often denoted by J instead of k . A molecularity of 2 characterizes bimolecular reactions, such as



or



Note that direct three-body collisions (3B) are extremely rare such that elementary termolecular ($l = 3$) reactions are encountered only in very few cases [see Ref. 171, for example]. Third order reactions, such as ozone formation



therefore almost exclusively occur in consecutive steps of elementary bimolecular collisions. These can be of the Lindeman energy transfer (ET) type, where a non-reactive molecule M , carries away energy from an excited and short lived collision complex O_3^*



Another possibility is the so called Chaperon or radical complex (RC) mechanism, where intermediate van der Waals complexes are formed either via



or by the following route



For practical reasons, rate coefficients of third order reactions which proceed via the energy transfer mechanism in eqs. (6.9) and (6.10) or via the RC mechanisms in eqs. (6.11)–(6.14) are commonly represented as effective rate coefficients for a second order reaction. The pressure

Order	Molecularity of elementary reaction	Rate r	Units of rate coefficient k, J	
			SI	Molecular
1	unimolecular	$k[A]$ or $J[A]$	s^{-1}	s^{-1}
2	bimolecular	$k[A][B]$	$\text{mol}^{-1} \text{m}^3 \text{s}^{-1}$	$\text{cm}^3 \text{s}^{-1}$
3	termolecular	$k[A][B][C]$	$\text{mol}^{-2} \text{m}^6 \text{s}^{-1}$	$\text{cm}^6 \text{s}^{-1}$

Table 6.1: Definitions and terminology of reactions with order up to three. Units for gas phase rate coefficients are given in the SI system as well as in the more commonly used molecular system. $[A]$, $[B]$ and $[C]$ indicate concentrations of three chemical species arbitrarily denoted by A, B and C. These have respective units of mol/m^3 and cm^{-3} in the SI and the molecular system.

dependence of the reaction is thus incorporated into the rate coefficient, which therefore is not independent on concentrations anymore. For the example of ozone formation ($\text{O} + \text{O}_2$), the rate coefficient is defined by the second order rate equation

$$r = \frac{d[\text{O}_3]}{dt} = k_f([\text{M}], T)[\text{O}][\text{O}_2]. \quad (6.15)$$

The recommended parameterisation of k_f for these type of reactions is due to Troe [172–175] and takes the following form

$$k_f([\text{M}], T) = \left(\frac{k_0(T)[\text{M}]}{1 + \frac{k_0(T)[\text{M}]}{k_\infty(T)}} \right) 0.6^{1 + \left[\log_{10} \left(\frac{k_0(T)[\text{M}]}{k_\infty(T)} \right) \right]^2} \quad (6.16)$$

where

$$k_0(T) = k_0^{300\text{K}} \left(\frac{T}{300\text{K}} \right)^{-n} \quad (6.17)$$

and

$$k_\infty(T) = k_\infty^{300\text{K}} \left(\frac{T}{300\text{K}} \right)^{-m} \quad (6.18)$$

are (termolecular) low pressure limiting (k_0) and (bimolecular) high pressure limiting (k_∞) rate coefficients with empirically determined temperature exponents n and m . Fig. 6.1 illustrates the pressure dependence of k_f using ozone formation as an example. Expressions (6.16)–(6.18) thus determine the pressure dependence in the two limiting cases as well as in the so-called fall-off region, which describes the transition between these two. Whether the full parameterisation, or just one of the two limiting cases needs to be considered depends on the reaction and the encountered pressure range. The characteristic concentration

$$[\text{M}]^* = k_\infty(T)/k_0(T). \quad (6.19)$$

describes the pressure range where the falloff occurs. For the ozone formation reaction, $k_0^{300\text{K}} = 6.0 \times 10^{-34} \text{cm}^6 \text{s}^{-1}$ and $k_\infty^{300\text{K}} = 3.0 \times 10^{-12} \text{cm}^3 \text{s}^{-1}$. Thus $[\text{M}]^* = 5 \times 10^{21} \text{cm}^{-3}$.

If $[\text{M}] \ll [\text{M}]^*$ ($[\text{M}] \gg [\text{M}]^*$) the use of the simpler limiting expression $k = k_0(T)$ ($k = k_\infty(T)$) will suffice.

Reaction orders higher than three or non-integer orders always imply a complex reaction mechanism, which can be broken down into elementary steps. Table 6.1 summarizes definition and terminology concerning rate coefficients for elementary reactions.

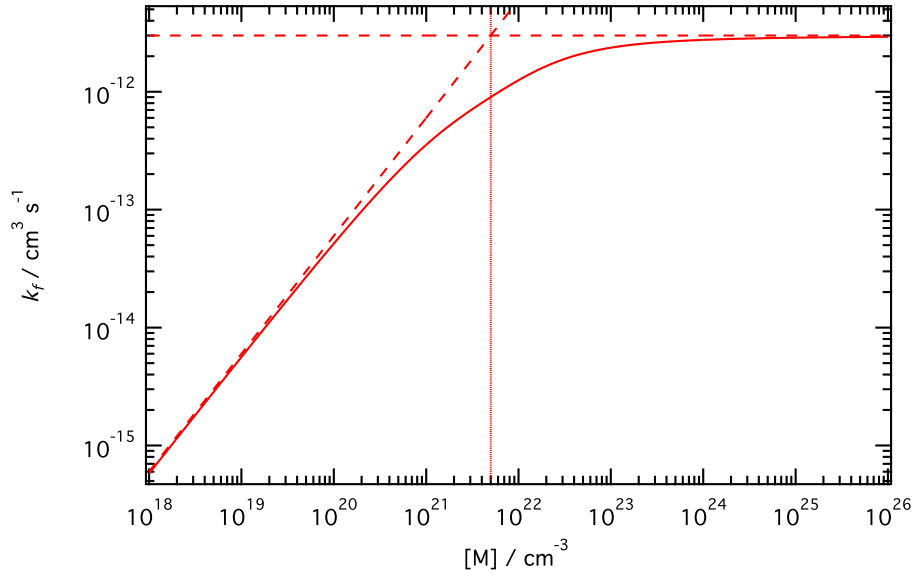


Figure 6.1: Pressure dependence of the effective second order rate coefficient k_f of a three body association or recombination reaction (fall-off curve), using ozone formation as an example. The full expression for the fall off curve at 300 K (eq. (6.16), full line), as well as the low and high pressure limiting cases (dashed lines) are indicated. The intersection of these limiting lines indicates the characteristic transition pressure as number density $[M]^* = 5 \times 10^{21} \text{ cm}^{-3}$ (vertical line).

6.2.3 Isotope abundances

Isotopomer abundances or isotopomer specific enrichments can be easily calculated from modeled molecular abundances. As before, we define the relative atomic abundances, or more precisely the isotopic mole fractions f ,

$$f_{\text{O}} = \frac{N(\text{O})}{N(\text{O}) + N(\text{P}) + N(\text{Q})}, \quad (6.20)$$

$$f_{\text{P}} = \frac{N(\text{P})}{N(\text{O}) + N(\text{P}) + N(\text{Q})}, \quad (6.21)$$

$$f_{\text{Q}} = \frac{N(\text{Q})}{N(\text{O}) + N(\text{P}) + N(\text{Q})}, \quad (6.22)$$

where $\text{O} = {}^{16}\text{O}$, $\text{P} = {}^{17}\text{O}$ and $\text{Q} = {}^{18}\text{O}$. Clearly

$$f_{\text{O}} + f_{\text{P}} + f_{\text{Q}} = 1. \quad (6.23)$$

For VSMOW (Vienna Standard Mean Ocean Water), we have [45]:

$$(f_{\text{O}})_{\text{VSMOW}} = 0.9976206(5), \quad (6.24)$$

$$(f_{\text{P}})_{\text{VSMOW}} = 0.0003790(9), \quad (6.25)$$

$$(f_{\text{Q}})_{\text{VSMOW}} = 0.0020004(5). \quad (6.26)$$

The figures in parantheses give the standard ($k = 1$) uncertainty in the last significant digit and were derived from measurements by Baertschi [176] and Li et al. [177]. For the atomic

ratios, we find

$$({}^{17}R)_{\text{VSMOW}} = 0.0003799, \quad (6.27)$$

$$({}^{18}R)_{\text{VSMOW}} = 0.0020052. \quad (6.28)$$

As has been discussed before, δ values are defined as relative deviations from the reference ($_{ref}$) ratios:

$$\delta({}^iE) = \left(\frac{N_x({}^iE) / N_x({}^jE)}{N_{ref}({}^iE) / N_{ref}({}^jE)} \right) - 1 \quad (6.29)$$

If the reservoir species a and the reference b need to be explicitly specified, we add a corresponding subscript to the δ -value: δ_{a-b} .

The δ value can be expressed in terms of molecular concentrations. For monoxides one obtains a very concise expression

$$\delta_{\text{CO-}ref}(\text{Q}) = \left(\frac{[\text{CQ}]}{[\text{CO}]} / ({}^{18}R)_{ref} \right) - 1 \quad (6.30)$$

taking the ${}^{18}\text{O}$ isotope as an example. For di-oxygenated molecules, such as O_2 , for example, the expression becomes slightly longer:

$$\delta_{\text{O}_2\text{-}ref}(\text{Q}) = \left(\frac{2[\text{Q}_2] + [\text{OQ}] + [\text{PQ}]}{2[\text{O}_2] + [\text{OP}] + [\text{OQ}]} / ({}^{18}R)_{ref} \right) - 1. \quad (6.31)$$

And for a triply oxygenated molecule, such as ozone, expressions may become somewhat lengthy:

$$\delta_{\text{O}_3\text{-}ref}(\text{Q}, \text{O}_3) = \left(\frac{3[\text{Q}_3] + 2([\text{OQ}_2] + [\text{PQ}_2]) + [\text{OPQ}] + [\text{O}_2\text{Q}] + [\text{P}_2\text{Q}]}{3[\text{O}_3] + 2([\text{O}_2\text{Q}] + [\text{O}_2\text{P}]) + [\text{OPQ}] + [\text{OQ}_2] + [\text{OP}_2]} / ({}^{18}R)_{ref} \right) - 1. \quad (6.32)$$

In these equations, we have used atomic ratios for mono, di and tri-oxygenated molecules which are given by

$${}^{18}R_1 = \frac{[\text{CQ}]}{[\text{CO}]} \quad (6.33)$$

$${}^{18}R_2 = \frac{2[\text{Q}_2] + [\text{OQ}] + [\text{PQ}]}{2[\text{Q}_2] + [\text{OQ}] + [\text{PQ}]} \quad (6.34)$$

$${}^{18}R_3 = \frac{3[\text{Q}_3] + 2([\text{OQ}_2] + [\text{PQ}_2]) + [\text{OPQ}] + [\text{O}_2\text{Q}] + [\text{P}_2\text{Q}]}{3[\text{O}_3] + 2([\text{O}_2\text{Q}] + [\text{O}_2\text{P}]) + [\text{OPQ}] + [\text{OQ}_2] + [\text{OP}_2]} \quad (6.35)$$

where we have used carbon monoxide, oxygen and ozone as examples for the molecules containing 1, 2 or 3 oxygen atoms. If we use the definition of the trinomial coefficient

$$\binom{M}{l \ m \ n} = \frac{M!}{l! m! n!}, \quad \text{where } M = l + n + m \text{ and } l, m, n \geq 0 \quad (6.36)$$

we can express the statistical (or combinatorial) abundance of a particular XO_M molecule containing M oxygen atoms using the atomic ratios ${}^{17}R$ and ${}^{18}R$ by noting that

$$\phi(M, n, m; f_P, f_Q) = \binom{M}{l \ m \ n} f_O^l f_P^m f_Q^n \quad (6.37)$$

is a discrete (trinomial) probability distribution which denotes the probability to draw a

particular combination of M balls (l of type 1, m of type 2 and $n = M - l - m$ of type 3), where the respective probability of drawing type 1, 2 and 3 balls is f_O , f_P and f_Q . For such a statistical distribution, we can calculate the expectation value for the number of P atoms in a molecule

$$E(N(P) \text{ in } XO_M) = \sum_m \sum_{l,n} m \phi(M, n, m; f_P, f_Q) \quad (6.38)$$

$$= \sum_m \sum_{l,n} m \binom{M}{l \ m \ n} f_O^l f_P^m f_Q^n \quad (6.39)$$

$$= \sum_m m f_P^m \binom{M}{m} \sum_l \binom{M-m}{l} f_O^l f_Q^{M-m-l} \quad (6.40)$$

$$= \sum_m m f_P^m \binom{M}{m} (f_O + f_Q)^{M-m} \quad (6.41)$$

$$= \sum_m m f_P^m (1 - f_P)^{M-m} \quad (6.42)$$

$$= M f_P, \quad (6.43)$$

where the last transformation is the well known expectation value of a binomial distribution. The average number of P atoms in a XO_M molecule thus is $M f_P$. We can therefore calculate individual isotopologue abundance ratios from the atomic abundances

$$\frac{[XO_l P_m Q_n]}{[XO_M]} = \binom{M}{l \ m \ n} f_O^l f_P^m f_Q^n / f_O^M = \binom{M}{l \ m \ n} ({}^{17}R)^m ({}^{18}R)^n, \quad (6.44)$$

provided that isotopes are statistically distributed within our target molecule. For the particular case of the ratio of the mono-substituted species over the reference molecule, this yields (taking substitution by $Q = {}^{18}O$ as an example)

$$\frac{[XO_{M-1}Q]}{[XO_M]} = \binom{M}{1} \frac{f_Q}{f_O} = M \times {}^{18}R. \quad (6.45)$$

This means that in the statistical case it is sufficient to measure the mono-substituted species with respect to the reference molecule in order to determine δ -values, that are defined in terms of the atomic ratios ${}^{17}R$ and ${}^{18}R$. For $R \ll 1$, we can further expect that this ratio provides a good approximation for R even in the non-statistical case. The agreement should be better, the smaller the value of R .

6.3 Accuracy of Simulations with KPP and Biases in Isotope Kinetic Modelling

In order to understand the biases and numerical limitations of quantitative kinetic isotope modelling, we run the model on the very simple reaction system, consisting out of three chemical (plus one exchange) reactions between the three different species O, O_2 and O_3 :



Rate coefficients for these reactions have been taken from the literature and the photolysis rate $J = 2.65 \times 10^{-4} \text{ s}^{-1}$ has been selected. As initial conditions $[\text{O}_3] = 2.5 \times 10^{16} \text{ cm}^{-3}$ and $[\text{O}_2] = [\text{O}] = 0$ have been chosen, corresponding to a sample of pure ozone that gets converted to O_2 by the impact of visible light. Figure 6.2 shows the results of the kinetic simulation.

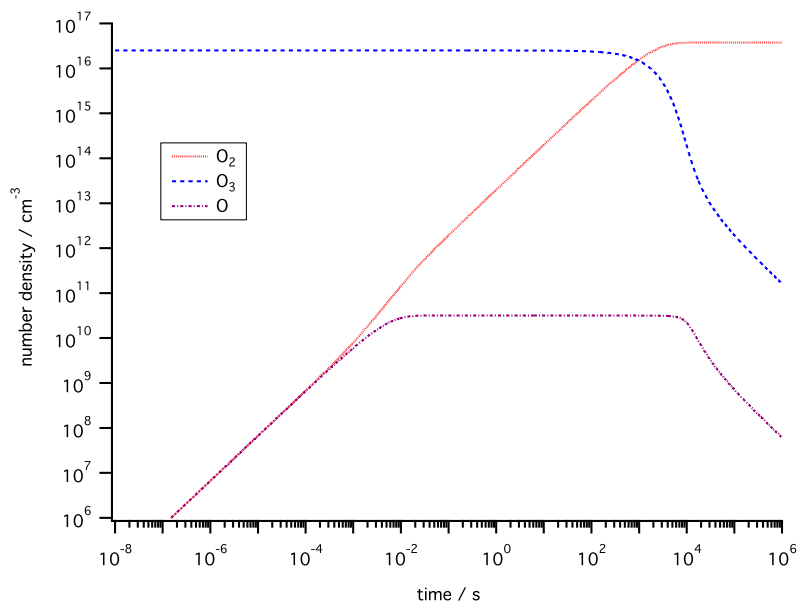


Figure 6.2: Temporal evolution of pure oxygen species upon photolysis of 130 Pa of pure ozone at a constant rate of $J = 2.65 \times 10^{-4} \text{ s}^{-1}$. The simulation shows the mass-conserving transformation of ozone into molecular oxygen.

One infers that the ozone dissociation is negligible up to time scales of about 10^3 to 10^4 s and that oxygen atoms and molecules increase steadily. Oxygen atoms equilibrate after about 1 ms, due to reaction with ozone, O_2 continues to increase until ozone is lost and, as required by mass conservation, the final O_2 number density is 1.5 times the initial ozone.

The complexity of this reaction system is considerably augmented when all stable isotopes of oxygen are included. It then comprises 27 species and 144 reactions, which are detailed in Appendix B. If we assume statistical rates, *i.e.* identical rates taking into account statistical branching ratios (see Table B.4) in the above system, but including all isotopic variants, the kinetics cannot introduce any isotope fractionation between the different species. We therefore expect that δ values stay close to the initial value of the starting compound, which is ozone in our case. The fully statistical model can therefore be used as a reference case to test the accuracy of numerical modeling. It also provides a useful test to check whether an error has been made in the implementation of the isotopic reaction system.

The results of this model are displayed in Figure 6.3. The very high degree of consistency of the modelled δ -values with the reference value of 0‰ which is manifested in deviations $|\delta| < 5 \times 10^{-10} \text{ ‰}$, indicate the level of numerical accuracy that can be achieved using the Rosenbrock integrator. Obviously, it is largely sufficient for our purpose, where a permil accuracy is sought for.

Nevertheless, ambiguities arise when only a subset of isotopes is considered, for example all monosubstituted compounds. There are now 3 atoms, 3 diatoms and 5 ozone species: (O, P, Q, O_2 , OP, OQ and O_3 , OOP, OPO, OQQ, OQO), which interact via 25 individual reactions (see Appendix B.2). Since molecules, and especially reactions, that contain or involve more than one rare isotope are neglected, the expressions for the δ values become

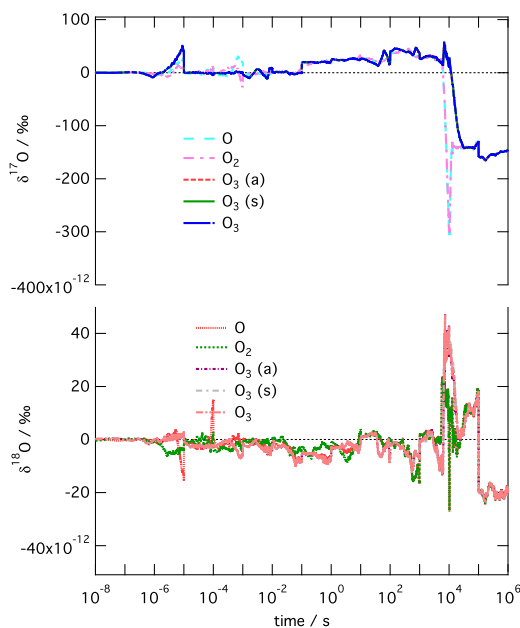


Figure 6.3: $\delta^{17}\text{O}$ and $\delta^{18}\text{O}$ of the full statistical model. All isotopic compounds are considered and $\text{O}_3(s)$, $\text{O}_3(a)$ and O_3 denote symmetric, asymmetric and “total” ozone (*eg.* $[\text{O}_3(a)] = [\text{OOQ}]$, $[\text{O}_3(s)] = [\text{OQO}]$, and $[\text{QO}_2] = [\text{OQO}] + [\text{OOQ}]$). The observed signals $|\delta| < 5 \times 10^{-10} \text{‰}$ are a measure of the numerical accuracy of the integrator used with the KPP software.

necessarily truncated, *eg.* counting atoms for O_2 gives :

$$\delta_{\text{O}_2\text{-ref}}^a(\text{Q}) = \left(\frac{[\text{OQ}]}{2[\text{O}_2] + [\text{OP}] + [\text{OQ}]} \right) / ({}^{18}\text{R})_{\text{ref}} - 1. \quad (6.50)$$

As we have seen before in equation (6.45), the atomic ratio R can be obtained from the abundances of mono-substituted species, provided that isotopes are distributed statistically. Since we consider a diatomic ($M = 2$), this leads to the second definition, which neglects the rare isotopes in the denominator:

$$\delta_{\text{O}_2\text{-ref}}^m(\text{Q}) = \left(\frac{[\text{OQ}]}{2[\text{O}_2]} \right) / ({}^{18}\text{R})_{\text{ref}} - 1. \quad (6.51)$$

Equivalent definitions have to be utilised for molecules that allow for a larger number of substitutions ($M > 2$). For oxygen atoms and mono-oxides, no ambiguity arises and the two definitions are equivalent:

$$\delta^m = \delta^a. \quad (6.52)$$

Applying both of these two definitions to the above truncated photochemical system (6.46) – (6.49) using identical rate coefficients for the different isotopic reactions (*ie* imposing non-fractionating conditions), we see artifacts due to mass balance (see Figure 6.4). The existence of these artifacts and the fact that these are strictly mass-independent (*i.e.* $\delta^{17}\text{O} = \delta^{18}\text{O}$) has been noted previously [178]. In our example, the artifacts take values of up to 7‰. It is interesting to note that both “truncated” definitions lead to the same artifacts even though individual species are shifted differently on the vertical scale, depending on the definition used.

It should be pointed out that only our first approximation (6.50) is effectively mass conserving, while the second in equation (6.51) is not. Since O_3 gets completely converted into O_2 during the course of the experiment, we will find $\delta^a(\text{O}_3, t = 0) = \delta^a(\text{O}_2, t = \infty)$, but

$$\delta^m(\text{O}_3, t = 0) \neq \delta^m(\text{O}_2, t = \infty).$$

The origin of these mass-independent artifacts can be understood from the kinetics of the system. As a matter of fact, truncating the reaction network leads to kinetic fractionation even if equal rates for the different isotopic variants of the same reaction (see Appendix B.2) are chosen. The first mass-independent feature at $t \simeq 10^{-3}$ s, for example, can easily explained by looking at Figure 6.2. From the figure, it is evident that only very little O_3 has been consumed after 1 ms. Thus, concerning ozone, the only reaction that needs consideration is photolysis that occurs at equal rates for all isotopes. Therefore, there is no fractionation of ozone yet. But the number density of oxygen atoms levels off at this time scale (Figure 6.2), indicating that photolytic production of oxygen atoms via reaction (6.46) is balanced by reaction (6.47) with ozone. Despite all reactions having the same rate coefficients



the rate for loss of O is higher than that for P or Q. This is due to the fact that we neglect multiply substituted species. While the heavy atoms only react with the lightest ozone molecule (reactions (6.58) and (6.59)), O can in addition also react with the singly substituted species (reactions (6.54)–(6.57)). Thus, when we ignore the formation of oxygen atoms, we

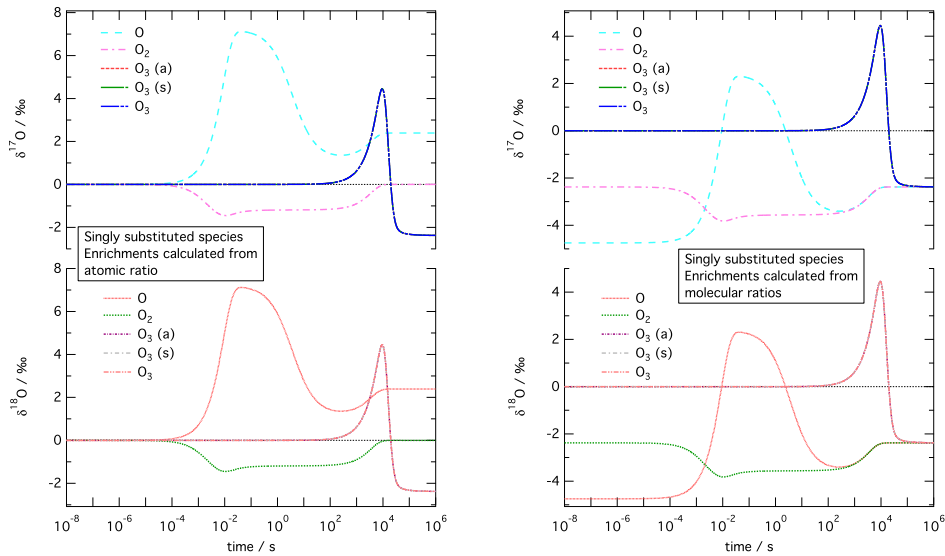


Figure 6.4: Truncated $\delta^{17}\text{O}$ and $\delta^{18}\text{O}$ as a function of reaction time for the simply substituted reaction system (Appendix B.2). O_3 is assumed to have no initial enrichment. $\text{O}_3(a)$ and $\text{O}_3(s)$ respectively indicate asymmetric and symmetric ozone molecules and $[\text{O}_3] = [\text{O}_3(a)] + [\text{O}_3(s)]$. Values on the left are calculated using atomic isotope ratios (δ^a). δ values on the right are calculated using molecular abundance ratios of singly substituted species (δ^m). δ values are based on $R_{ref} = R_{VSMOW}$.

find the isotopic loss rates

$$\frac{d[\text{O}]}{dt} = -k[\text{O}][\text{O}_3] \left(1 + \frac{[\text{OOQ}] + [\text{OQO}] + [\text{OOP}] + [\text{OPO}]}{[\text{O}_3]} \right) \quad (6.60)$$

$$\frac{d[\text{P}]}{dt} = -k[\text{P}][\text{O}_3] \quad (6.61)$$

$$\frac{d[\text{Q}]}{dt} = -k[\text{Q}][\text{O}_3] \quad (6.62)$$

Since heavy ozone has a relative abundance of $\simeq 3(2 \times 10^{-3} + 4 \times 10^{-4}) = 7.2 \times 10^{-3}$, we expect that O atoms get enriched in heavy isotopes by about 7‰. Because this effect acts exclusively on ^{16}O , the fractionation is mass-independent. Similar arguments can be made for the other turn ups and downs in Figure 6.4. At the same time, we see a slight isotope depletion in O_2 , which holds until ozone starts to diminish quantitatively ($t \simeq 10^3 \dots 10^4 \text{ s}$). In order to understand this signal, consider O_2 formation that occurs by photolysis of ozone (which is assumed not to fractionate) and – to equal proportion – by reaction of O with O_3 . Two out of six atoms come from the photolysis which does not fractionate, four out of the six atoms in O_2 come from reaction of oxygen atoms with ozone ($\text{O}_3 + h\nu$ and $\text{O} + \text{O}_3$). If we consider the reaction scheme for the latter reaction, we can set up the rate equations for oxygen molecules that form in this reaction:

$$\frac{d[\text{O}_2]}{dt} = 2k[\text{O}][\text{O}_3] \left(1 + \frac{[\text{P}] + [\text{Q}]}{2[\text{O}]} + \frac{[\text{OOQ}] + [\text{OQO}] + [\text{OOP}] + [\text{OPO}]}{2[\text{O}_3]} \right) \quad (6.63)$$

$$\frac{d[\text{OP}]}{dt} = k[\text{O}][\text{O}_3] \left(\frac{[\text{P}]}{[\text{O}]} + \frac{[\text{OOP}] + [\text{OPO}]}{[\text{O}_3]} \right) \quad (6.64)$$

$$\frac{d[\text{OQ}]}{dt} = k[\text{O}][\text{O}_3] \left(\frac{[\text{Q}]}{[\text{O}]} + \frac{[\text{OOQ}] + [\text{OQO}]}{[\text{O}_3]} \right) \quad (6.65)$$

As before, the rate of O_2 formation induces a fractionation due to the higher order terms that amounts to $1/2 \times 4 \times (2.4) \text{‰} \simeq 4.8 \text{‰}$. Since this source only contributes two third to the oxygen molecules, we get finally a diminution in both the $[\text{OP}]/[\text{O}_2]$ and $[\text{OQ}]/[\text{O}_2]$ ratios by 3.2‰, which leads to δ values that are half this size. This mass independent $\delta = -1.6 \text{‰}$ is in good agreement with the modeling (see Figure 6.4a).

The use of δ^m also produces interesting results (Figure 6.4b), because diatomic and monatomic species are shifted by -2.3 and -4.7‰, respectively. This is due to the systematic offset that is neglected in the denominator when we compare the definition of δ^m to that of δ^a . Depending on the number M of oxygen atoms in the molecules, values are shifted by

$$\delta^m(\text{XO}_M) - \delta^a(\text{XO}_M) \simeq (M - 1)(^{17}\text{R} + ^{18}\text{R}) \simeq (M - 1) 2.4 \text{‰}, \quad (R \ll 1). \quad (6.66)$$

Since the isotopic composition of ozone is used as a reference ($\delta^m(\text{O}_3, t = 0) = 0$), O_2 is depleted by 2.4‰ and atomic oxygen by 4.8‰ when we compare panels a and b in Figure 6.4. At the end of the run this leads to identical δ^m values for all species and, at least in this simple model, δ^m seems to conserve “molecular isotope ratios”. For oxygen atoms, this is immediately evident, because at the end of the run molecular oxygen is the dominant species and atoms are coupled to O_2 via isotope exchange, which gives

$$\frac{[\text{Q}]}{[\text{O}]} = \frac{1}{K} \frac{[\text{OQ}]}{[\text{O}_2]}, \quad (6.67)$$

where $K = 2$ is the equilibrium constant for the isotope exchange in the statistical case. Clearly, this reaction transfers the isotope ratio from molecular into atomic oxygen. Since O

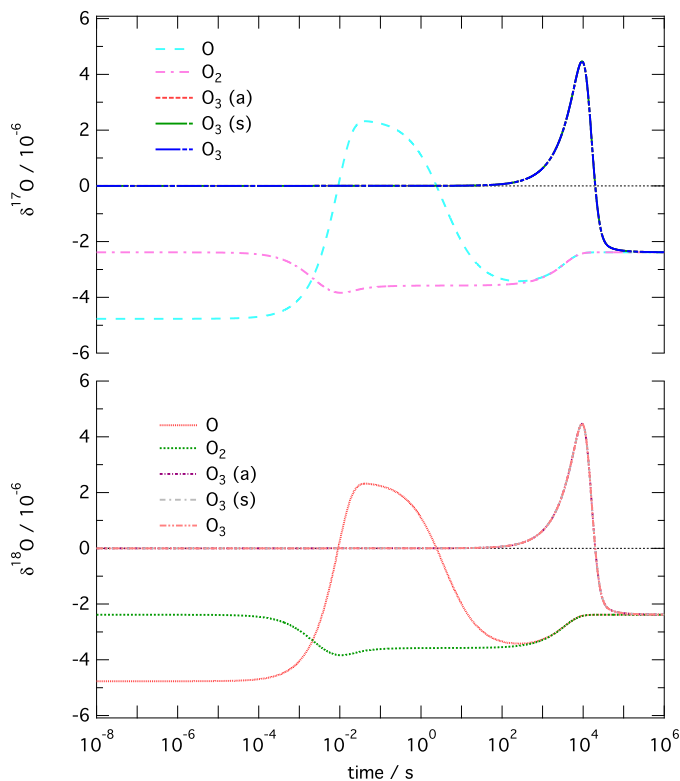


Figure 6.5: Truncated $\delta^{17}\text{O}$ and $\delta^{18}\text{O}$ as a function of reaction time for the simply substituted reaction system (Appendix B.2) as in Figure 6.4b. The heavy isotope content has been artificially reduced by a factor 1000, *i.e.* $R_{ref} = R_{\text{VSMOW}}/1000$.

and O_2 have identical isotope compositions, ozone that forms from these two needs to have the same as well. Because ozone is continuously destroyed without a fractionation in the decomposition process, the ozone levels will always reach a point, where most of the ozone has been formed under conditions where atoms and molecules have been equilibrated.

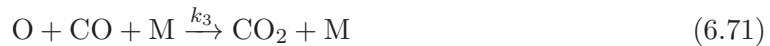
Because the bias by truncation depends on the relative importance of the higher substituted molecules for the isotope budget, the agreement between the truncated modeling and experiments will improve with decreasing values of R , *i.e.* decreasing mole fractions of ^{17}O and ^{18}O containing molecules. This is nicely illustrated in Figure 6.5.

6.4 Modeling of experiments

6.4.1 Modeling of the experiment at CCAR in Copenhagen

As already discussed in chapter 4, the visible light photolysis of ozone in the presence of carbon monoxide produced more CO_2 than expected from simple ground state chemistry between O , O_2 , O_3 and CO in our experiments at the photoreactor facility at CCAR in Copenhagen. Simple kinetic arguments led to a discrepancy by a factor of ten at least (see table 4.1). The tracer experiment using CO and ethane provided strong evidence that radical chemistry involving OH is actually responsible for the observed decomposition of CO during the experimental runs.

Before we try to model this chemistry, we run the kinetic model of the simple ground state chemistry to confirm the back of the envelope calculations presented previously. For the sake of convenience, we repeat the reaction scheme:



The KPP software [165] has been utilized employing the rate constant values shown in table C.1 in Appendix C, where the above reactions take numbers 01, 03, 04 and 36. The most uncertain quantity seems to be the rate constant of the $\text{O} + \text{CO}$ reaction (no. 36 in table C.1), which has been taken from Tsang and Hampson [140]. They recommend the measured value of Slanger et al. [151] $k_{\text{O}+\text{CO}+\text{M}} = 6.5 \times 10^{-33} \exp(-2184 \text{ K}/T) \text{ cm}^6 \text{ s}^{-1}$ where the third body M is CO. These authors also give a value for $\text{M} = \text{N}_2$, which is $k_{\text{O}+\text{CO}+\text{N}_2} = 3.67 \times 10^{-33} \exp(-2184 \text{ K}/T) \text{ cm}^6 \text{ s}^{-1}$ or $2.4 \times 10^{-36} \text{ cm}^6 \text{ s}^{-1}$ at $T = 298 \text{ K}$.

The rate J_1 for ozone photolysis into O and O_2 ground states (reaction (6.68)) is determined by the experimental conditions and has been estimated for each run by matching the model predicted ozone concentration to the observations. As will be seen in a moment, this assumption is justified, even if the total chemical scheme is not complete. The values vary between 1.3 and $6.5 \times 10^{-5} \text{ s}^{-1}$ (See Table 6.2) and are in agreement with those determined in section 4.6.

The other rate constants are well established and were obtained from standard compilations [150, 179]. Table 6.2 compares the modeled relative loss of carbon monoxide $\Delta[\text{CO}]/[\text{CO}]$ to those from the experiments. The modeled values (column “mod. 1”) vary between -0.05 and -0.34%. These values are roughly a factor of 100 lower than those observed experimentally (column “exp.”). The numerical analysis thus confirms our conclusion that the $\text{O} + \text{CO} + \text{M}$ cannot be the dominant source of CO_2 . We note that contaminations by hydrogen compounds have been a common problem in the determination of the rate coefficient for the $\text{O} + \text{CO}$ reaction and it is therefore generally assumed that earlier reports on higher rates for the spin forbidden reaction are due to contamination effects [138]. For the same reason, it is unlikely that we have underestimated this rate coefficient.

run	[M] (10^{18} cm^{-3})	[CO] ₀ (10^{14} cm^{-3})	J_1 (10^{-5} s^{-1})	$\Delta[\text{CO}]/[\text{CO}]$ (%)				[OH](mod. 3) (10^5 cm^{-3})
				exp.	mod. 1	mod. 2	mod.3	
1	23.8	14.0	3.00	-32.2	-0.34	-0.42	-1.12	7.79
2	23.8	3.49	4.05	-14.7	-0.21	-0.23	-0.46	8.43
3	17.0	9.00	1.30	- 9.3	-0.19	-0.25	-0.85	5.37
4	17.0	8.39	1.51	- 8.6	-0.11	-0.13	-0.37	5.50
5	12.1	0.95	2.60	-20.4	-0.19	-0.24	-0.78	7.61
6	12.1	4.42	2.91	- 7.8	-0.09	-0.10	-0.28	7.49
7	12.1	1.05	1.85	-14.7	-0.16	-0.20	-0.71	6.50
8	12.1	13.6	5.05	-27.3	-0.34	-0.48	-1.53	9.47
9	4.86	1.93	3.38	- 7.5	-0.05	-0.07	-0.26	8.47
10	4.86	1.84	1.51	-12.2	-0.08	-0.08	-0.18	1.17
11	4.86	3.25	2.23	-15.4	-0.12	-0.13	-0.27	1.24
12	4.86	13.6	6.49	- 7.5	-0.06	-0.06	-0.21	11.0

Table 6.2: Comparison of experiments at CCAR with model results. Model results correspond to three different scenarios: mod. 1—no $\text{O}(^1\text{D})$; mod. 2—low $\text{O}(^1\text{D})$ and H_2O ; mod. 3—high $\text{O}(^1\text{D})$ and H_2O .

In line with this interpretation of these kinetic studies on $O + CO$, we found that the most likely candidate for rapid oxidation of CO is then hydrogen radical chemistry. This has been confirmed by our tracer experiments with ethane (see chapter 4). A potential source of the OH radical is the reaction of water residuals in the reactor with trace amounts of $O(^1D)$ that are produced in ozone photolysis:



Reaction of OH via



then provides the pathway for CO_2 formation. Moreover, since $O(^1D)$ is a direct product of the photolysis of ozone this mechanism also presents the possibility for transferring the ozone isotope anomaly into the product carbon dioxide. The ethane tracer experiments imply a OH number density of about $[OH] \simeq 1.5 \times 10^7 \text{ cm}^{-3}$. With an extended kinetic model that contains the missing HO_x chemistry, we can now investigate whether these high levels of OH can be explained when we use the lamp data obtained in chapter 5. The investigation of the LED light sources revealed that the output in the UV is low, leading to a very low $O(^1D)/O(^3P)$ branching ratio value of $J_2/J_1 = 2 \times 10^{-7}$. For the model, we have used this value (mod. 2) as well as an upper limit of $J_2/J_1 = 10^{-6}$ (mod. 3). The full scheme of reactions is given in Table C.1 of the appendix C. Initial concentrations for CO , O_3 and N_2 were fixed to the experimental values. The H_2O number density has been set either to $[H_2O] = 2.5 \times 10^{14} \text{ cm}^{-3}$ (mod. 3), which corresponds to an upper limit that has been established by analysis of the FTIR spectra, or a ten times lower value has been utilized (mod. 2). Models 2 and 3 thus are “optimistic” and “pessimistic” scenarios in terms of the importance of the $OH + CO$ reaction as compared to the formation of CO_2 by $O + CO$.

The result of a pessimistic (mod. 3) model run is shown in Figure 6.6. The particular run shows the conditions of experimental run 1 and reveals the expected conversion of O_3 into O_2 and CO_2 . Also, OH is produced in significant quantities $[OH] \sim 10^6 \text{ cm}^{-3}$. But this is still much less than the $\sim 10^7 \text{ cm}^{-3}$ from the tracer experiment. Indeed, as also demonstrated in table 6.2 (column “mod. 3”), the CO loss is in fact increased with respect to the simple model 1, but only by a factor of about 3. This is still much less than what is measured (~ 30). The “optimistic” scenario (mod. 2) shows however, that the setup should be capable of studying the $O + CO$ reaction if it can be secured that H_2O concentration levels stay ten times below the maximum observed value and that other sources of OH can be avoided. By comparing these numbers (mod. 2) with the $O + CO$ only model (mod. 1), we find that the production of CO_2 is dominated by the $O + CO$ reaction with $OH + CO$ producing less than about 25 % of the total CO_2 .

It must be noted that in the reaction scheme the chemistry related to the nitrogen has been neglected, apart from the reaction 10 in Table C.1 which is the quenching of excited state oxygen atoms in the bath gas. $O(^1D)$ and N_2 can also react to produce N_2O with a rate constant $k = 2.80 \cdot 10^{-36} (300 \text{ K}/T)^{0.9} [\text{M}]$ [150] which can consequently undergo a reaction with $O(^1D)$ leading to two pathways having $O_2 + N_2$ and NO as products. Note that for value of pressure in the range 980 - 200 hPa the reaction which is responsible for N_2O formation is about 10^6 times slower than the quenching thus the neglect ion of this process does not significantly affect the modeled chemistry.

For completeness, we have also made the unsubstantiated assumption that the lamps provide much more $O(^1D)$. However, a very high branching ratio $J_2 = 1.2 \times 10^{-2} \times J_1$ would be required in order to match observed losses of CO . This value strongly exceeds what can be justified by our measurements on the spectral lamp properties.

We must conclude that there is a yet unidentified source of OH in our experiment. Several

contaminants that were compatible with our FTIR spectra have been considered (NO_x and various hydrocarbon compounds), but no convincing scenario could be developed that would be compatible with our measurements. We point out that the search for a contaminant is not trivial, because the photoreactor has been used to perform experiments with many other chemical compounds (hydrocarbons, chlorine, greases, ...) in the past. Residues of these might be stuck to the walls of the reaction chamber or in the gas lines. But even after cleaning of the lines and many ozone treatments our results were reproducible and the contaminant could not be identified. The most promising approach would be to completely reconstruct the reactor from scratch using clean materials. This task has only very recently been accomplished and new measurements have still to be made.

To conclude, the experimental photoreactor experiments presently do not allow to study the possible occurrence of a mass independent fractionation effect in the reaction between carbon monoxide and oxygen due to the presence of a dominant but yet unidentified CO_2 formation pathway. The tracer experiment points towards a source of OH that leads to a CO loss which largely outpaces the $\text{O} + \text{CO}$ reaction. The modeling also demonstrates that the experiments are doable in principle. The only prerequisite is that a sufficient degree of cleanness must be reached.

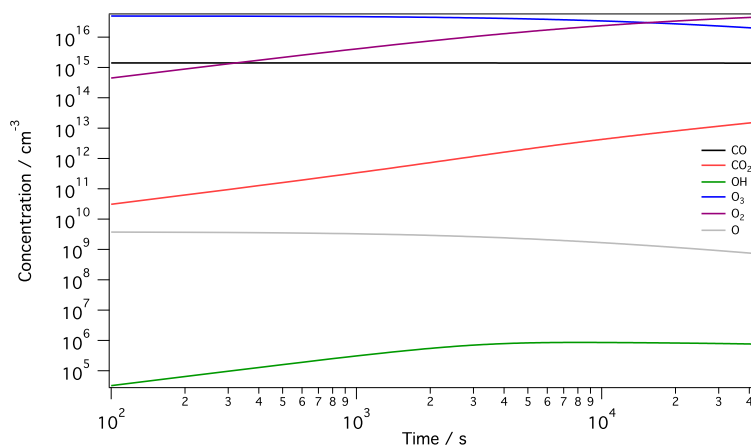


Figure 6.6: Kinetic modeling of the first experimental run. The temporal evolution of some relevant species in the photoreactor are shown. Initial conditions were set to $[\text{O}_3] = 2100$ ppm, $[\text{CO}] = 59$ ppm and $[\text{H}_2\text{O}] = 10$ ppm at a total pressure of 980 hPa N_2 .

6.4.2 Modeling of the experiment of Pandey and Bhattacharya

6.4.3 Ground state oxygen chemistry

Before presenting the isotope kinetic modeling of the experiment of Pandey and Bhattacharya [134] a brief presentation of the experiment including its results is given and the kinetic model proposed by PB06 and its limitations are recalled.

PB06 used two different reactor arrangements and two different light sources to illuminate carbon monoxide - ozone or carbon monoxide - oxygen mixtures. The resulting CO_2 has been extracted and analyzed mass spectrometrically after conversion to molecular oxygen. Here, we restrict ourselves on the tungsten lamp experiments which came in three series: A and AC in a small (~ 70 cm³) cylindrical reactor and AS in a large (~ 5 dm³) spherical reactor. The measurement results are presented in Table 6.3.

The measurements were modeled using the Mathematica software (see section 6.1.2). The set of differential equations was set up from the rate equations corresponding to the system of reactions (6.68)–(6.71). The rate coefficients were chosen according to literature

recommendations and in agreement with the set of PB06. The only modification has been that an adjustable scaling factor f has been added to the rate of the O + CO reaction. This was necessary to match observed CO₂ amounts.

Our modeling reproduced essentially the results from PB06 (column “mod-CO₂” in Table 6.3). There were some differences in the scaling factor f , which in some cases can be very important, however. This is due to the fact that PB86 did not match exactly the produced amount of CO₂, the largest discrepancy between modeled and observed amounts being 21.8 μmol . The extremely large range of f values between 1.2 and 1150 points towards a missing source, that was interpreted as a surface reaction in the original work. Table 6.3 therefore also presents the characteristic lifetimes for diverse processes, as well as the lifetime with respect to the unidentified source of CO₂ formation:

$$\tau_{\text{O}}(\text{X}) = \frac{1}{(f - 1)k_{\text{O}+\text{CO}+\text{M}}[\text{CO}][\text{M}]} \quad (6.74)$$

With the exception of the experimental run A3, f is significantly different from 1 and CO₂ formation is dominated by an unidentified source, which is often 10 to 1000 times faster than the rate of the O + CO reaction in the gas phase. Because of some anti-correlation with pressure, PB06 proposed formation of CO₂ at the reactor surface as the missing source. But the diffusional time constant in table 6.3 disproves this assertion. Except for the lowest pressure measurements, the diffusional time constant is much larger (even up to $10^3 - 10^5$ in experiments A1, A2, AC4, for example) than $\tau(\text{X})$. Experiment AC4 even produces more CO₂ that could ever be explained by the chemistry in (6.68)–(6.71), because the yield of CO₂ is 50 % higher than the initial ozone amount. Such a result is impossible within the simple scheme of reactions (6.68)–(6.71) even if some of the reactions would occur at the surface, because for each photolysed ozone molecule, there is exactly one oxygen atom produced and therefore at most one CO₂ molecule that can be formed. Catalytic reactions would be necessary to explain the observation and the very high yields are strong indicators for an additional chemistry with higher quantum yields. Even conversion rates of nearly 100 % such as in run A2 or in excess of 60 % (A1, A7 and A8) are hardly explained within the model, because the O + O₃ reaction that is an odd oxygen sink is faster than either the gas phase formation of CO₂ or the diffusional time scales.

Contrary to the more common mechanisms of the Eley-Rideal or the Langmuir-Hinshelwood mechanisms for surface reactions, that would directly be limited by atom diffusion, PB06 seem to invoke a “complex stabilization” mechanism, which corresponds to the association of excited CO₂^{*} in the gas phase that then gets deactivated at the reactor walls. If we make the common assumption that the high pressure limiting rate for the O+CO reaction is given by $2k_{ex}$, where k_{ex} is the rate for the Q + CO isotope exchange, an upper limit for this wall stabilization mechanism can be given using the measurements by Jaffe and Klein [180]. They measured the rate with respect to the O + NO₂ → NO + O₂ reaction, which got reevaluated since. Using a more recent recommendation [150], we find $2k_{ex} = 3.7 \times 10^{-15} \text{ cm}^3 \text{ s}^{-1}$, which is half the rate coefficient of the O + O₃ reaction, $k_{\text{O}+\text{O}_3} = 8.0 \times 10^{-15} \text{ cm}^3 \text{ s}^{-1}$. The fraction of O atoms that are available for CO₂ formation will thus depend on the ratio

$$\frac{2k_{ex}[\text{CO}]}{k_{\text{O}+\text{O}_3}[\text{O}_3]} = \frac{1}{2} \frac{[\text{CO}]}{[\text{O}_3]} \quad (6.75)$$

Table 6.3: Measurement and modeling results for the experiment of PB06. The first columns summarize measured amount data as given by Pandey and Bhattacharya [134]. The prefixes “in”, “fin” and “mod” stand for initial, final and modeled amounts. f is an artificial scaling factor by which the rate of the O+CO reaction was increased to match the observed CO₂ amounts (TW stands for this work, PB is the original work). τ_{O} gives oxygen atom life times for characteristic process, such as reaction with ozone, CO₂ formation in the gas phase, wall diffusion and with unknown scavenger (X) to reproduce the observed amounts of CO₂.

run	time (min)	amount (μmol)				scaling factor f		τ_{O} (ms)			
		in.-O ₃ ^a	in.-CO	fin.-CO ₂	mod.-CO ₂	TW	PB ^b	O+O ₃ ^c	O+CO	diff ^d	X
A1	50	59.3	1587	46.0	11.5	16	16.8	0.63	1.2	675	0.084
A2	50	59.3	1633	59.3	12	360	55.0	0.49	1.2	694	0.0032
A3	150	59.3	1633	15.9	9.8	1.2	3.5	1.8	1.2	694	7.8
A4	240	59.3	1587	25.5	13.9	2.9	3.3	1.1	1.2	675	0.65
A5	210	59.3	1582	33.7	13.8	5.5	6.8	0.85	1.3	672	0.28
A6	30	59.3	1313	34.8	7.5	10	10.2	0.83	1.8	558	0.20
A7	40	59.3	1177	42.9	7	22	22.0	0.68	2.3	500	0.11
A8	100	59.3	1189	44.6	8.8	25	27.0	0.65	2.2	505	0.093
A9	330	59.3	1022	30.7	7.9	10	10.8	0.94	3.0	434	0.32
A10	300	59.3	67	14.5	0.1	330	375.0	1.9	700	28	2.2
A11	180	59.3	67	12.2	0.1	220	250.0	2.4	700	28	3.2
A12	180	59.3	25	13.0	0.03	1150	1270.0	2.2	5030	11	4.4
A13	180	59.3	1008	30.3	7.5	9.8	10.9	1.0	3.1	428	0.35
A14	180	59.3	1035	26.1	7.8	6.7	6.6	1.1	2.9	440	0.51
A15	180	59.3	46	4.9	0.07	100	202.0	5.8	1490	20	15
A16	180	59.3	109	7.3	0.2	45	111.0	4.2	264	46	6.0
AC1	120	38.7	129	9.6	0.3	80	96.5	2.9	189	55	2.4
AC2	150	41.3	654	17.7	0.6	11	95.0	0.72	7.3	278	0.72
AC3	65	223	329	104.1	1.4	200	228.0	1.4	29	140	0.15
AC4	120	24	309	37.0	9.7		(80.0)	1.4	33	131	0.0004
AC6	60	45.3	46	12.8	0.05	620	590.0	5.6	1490	20	2.4
AC7	70	43.3	46	6.3	0.05	200	230.0	5.6	1490	20	7.5
AC8	115	47.3	46	11.3	0.06	470	500.0	5.6	1490	20	3.2
AC9	135	50.7	46		0.06		(440.0)	5.6	1490	20	
AC10	140	45.3	1269	30.0	9.3	10	12.0	0.39	2.0	539	0.2
AC11	150	49.3	1269	27.9	9.6	7.0	6.6	0.39	2.0	539	0.33
AC12	120	32	170	14.3	0.4	130	130.0	2.4	109	72	0.87
AC13	65	59.3	1353	35.6	9.8	8.6	8.5	0.36	1.7	575	0.2
AC14	180	31.0	1212	23.7	7.8	13	10.9	0.40	2.1	515	0.18
AC15	115	64.7	386	30.4	1.6	56	60.0	1.2	21	164	0.38
AC16	125	60.7	386	11.3	1.6	10	12.0	1.2	21	164	2.3
AC17	180	45.3	88	9.0	0.15	120	154.0	3.8	406	37	3.4
AS1	180	53.3	3889	13.6	2.4	12	9.4	150	1060	1860	98
AS2	90	53.3	5834	10.0	4.4	3.3	2.8	210	470	2780	210
AS3	360	53.3	5834	12.0	4.5	4.3	3.9	170	470	2780	140
AS4	90	53.3	5834	8.9	4.4	2.7	2.8	230	470	2780	270
AS5	90	53.3	7778	25.9	6.8	10	7.5	80	265	3700	29

^a In the publication given as O₂ equivalent

^b Unclear how numbers in parentheses were determined by Pandey and Bhattacharya [134]. In one instance the amount of CO₂ has not been measured. In the other instance it largely exceeded the amount of initial ozone, thus leaving f undefined in both cases.

^c Assume typical ozone amount of half the observed CO₂.

^d Diffusional time constant for small cylindrical geometry (with diameter $D = 2.9$ cm, A1 – AC17) and large spherical geometry (with diameter $D = 21.2$ cm, AS1 – AS5).

In run A12, at most 12.5 μmol CO₂ can thus be formed by the proposed mechanism, which

corresponds to the measured value. However, this requires that CO_2^* gets wall stabilized before it re-decomposes in the gas phase. Given the diffusional time scales of > 10 ms (which are even larger for CO_2^*), this would require unrealistically long complex life times, which makes this hypothesis very unlikely.

6.4.4 Full modeling including excited state and isotope chemistry

Amount Data

Due to the tremendous discrepancies between ground state chemistry modeling and observations, excited state chemistry according to the reaction scheme in Table D.4 in Appendix D has been taken into account. Isotopes have been modeled using singly substituted species only (see Table D.2). 37 model runs have been performed in agreement with the experimental conditions outlined in Table tab:PBsummary and corresponding to the three sets of experiments using a halogen filled tungsten lamp as a light source. The ozone photolysis rates J_1 and J_2 which determine the $\text{O}(^1\text{D})/\text{O}(^3\text{P})$ production branching ratio have been set close to the experimental value: $J_1 = 2.5 \times 10^{-3} \text{ s}^{-1}$ and $J_2 = 0.05J_1$. The choice of the J_2/J_1 branching ratio is at the lower end of the range ($J_2/J_1 = 10^{-2} \dots 1$) that has been estimated from the investigation of the lamp spectra in chapter 5. A water background of $10 \mu\text{mol/mol}$ in the large reactor and $100 \mu\text{mol/mol}$ in the small reactor has been assumed. Due to the lack of experimental data on the water contamination, this choice has been done deliberately, taking into account the surface to volume ratios S/V of the different reactors and the fact that the 100 dm^3 reactor in Copenhagen already showed a water content of up to $10 \mu\text{mol/mol}$.

Figure 6.7 shows the result of the modeled CO_2 amounts $N(\text{CO}_2)$ compared to the experimental data. Without individually adjusting water contents, the totality of data fairly reproduces the measured values which span the range between 4.9 and $104.1 \mu\text{mol}$. More precisely, the model values do not exceed the measurements by much more than a factor of two and underestimate less than by a factor of five. The relative standard deviation is $\sigma = 50\%$. This outcome has to be compared to the simple chemistry model, where excited oxygen chemistry is completely neglected. As demonstrated in Figure 6.7, model results in this case, especially at low pressures, are underestimated by a factor between 2 and 5000. Including excited state chemistry therefore improves the description of the experiments quite significantly and the agreement can be further ameliorated by varying the water content. However, since there is no independent data on H_2O for these measurements available, this cannot be used as decisive test as to how well our model can reproduce the measurements. These results based on variable water contents are therefore omitted here.

It is certainly interesting to note that what has been first interpreted as the impact of surface chemistry by Pandey and Bhattacharya [134], can well be explained by gas phase chemistry alone if relevant reactions are taken into account. As it has been demonstrated before, the lamp necessarily provides excited oxygen ($\text{O}(^1\text{D})$) atoms and since water is an ubiquitous contaminant with required amounts being reasonable when compared to our study at CCAR, it must be concluded that OH radical chemistry must have played a role in the experiments. More importantly, solely excited state chemistry could possibly explain why $N(\text{CO}_2) = 37 \mu\text{mol}$ in the experiment AC4 has largely exceeded the initial ozone amount of $N(\text{O}_3) = 24 \mu\text{mol}$ (see Table 6.3). This is because the quantum yield γ for generation of species (that are capable of oxidizing CO) from ozone photolysis can be larger than one (via reaction $\text{O}(^1\text{D}) + \text{H}_2\text{O} \rightarrow 2 \text{OH}$, for example), while it must be $\gamma \leq 1$ in the case of the pure ground state mechanism. If it is not an experimental artifact, the particular run AC4 therefore contradicts the proposed surface mechanism, but can likely be explained by $\text{O}(^1\text{D})$ initiated chemistry.

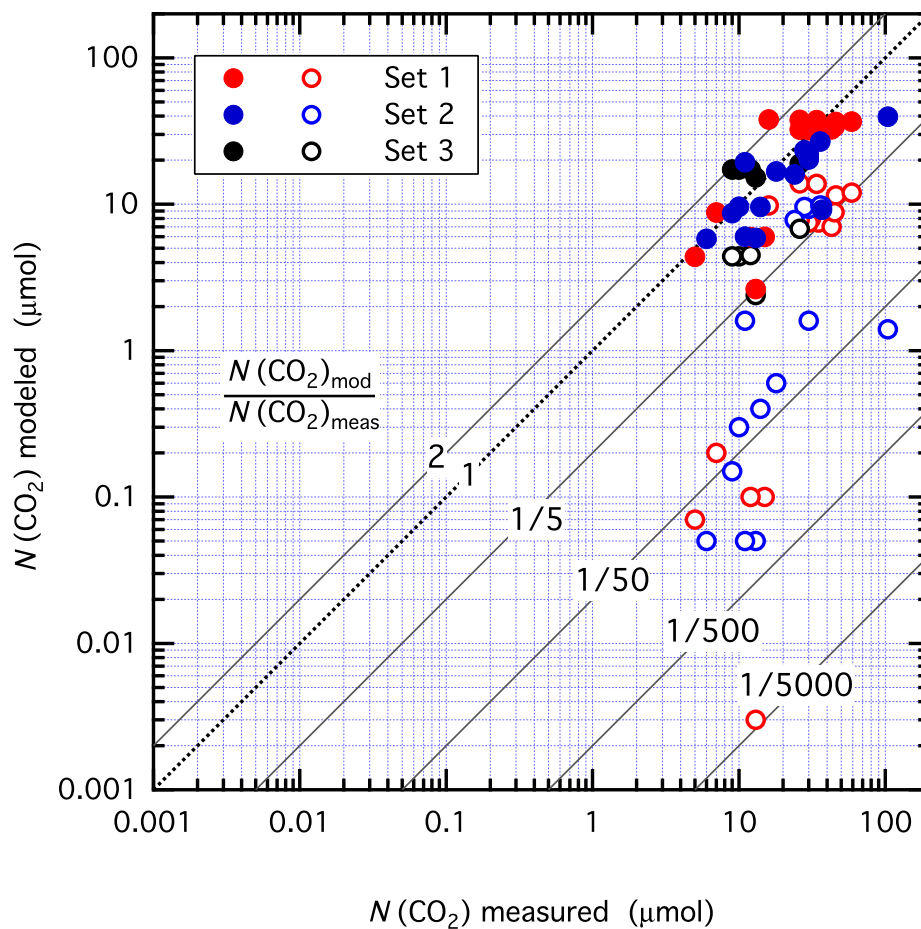


Figure 6.7: Comparison between modeled and measured amounts of CO₂. Measured data are from Ref. 134. Solid circles present actual model results with 10 (large reactor, set 3) or 100 $\mu\text{mol/mol}$ (small reactor, sets 1 and 2) of H₂O. Open circles are modeling results for ground state oxygen and gas phase chemistry ($f = 1$, Ref. 134).

It is clear that the presence of OH not only has a strong impact on the CO₂ formation rate, but also on the CO₂ isotopic composition. Taking into account the isotope chemistry of the singly substituted species therefore will provide a further test for the relevance of chemistry linked to O(¹D) and may also provide an explanation of the observed three-isotope signature in CO₂ without invoking mass independent fractionation in the O + CO + M reaction.

Isotope Composition

The isotope chemical model is given in Appendix D. It is based on known rate coefficients for ozone formation and isotope exchange reactions. Other rates are assumed to be statistically. Initial values of CO and O₃ have been adjusted to the experimental conditions and the isotopic composition of water impurities has been assumed to equal the value of SMOW ($\delta = 0$). CO had an isotope composition of $\delta^{18}\text{O}(\text{CO}) = 28.7\text{‰}$ and $\delta^{17}\text{O}(\text{CO}) = 14.9\text{‰}$ with respect to SMOW. The initial isotope composition of ozone requires some discussion however, because the partitioning of isotopes between the isotopomers (O₃(*a*) and O₃(*s*)) is not uniquely determined by the overall isotope composition that could be determined experimentally. It is likely that this distribution is not statistical, but a temperature dependence is expected that could possibly lead to a statistical distribution with $[\text{O}_3(a)] = 2[\text{O}_3(s)]$ and thus ($\delta^{17}\text{O}(\text{O}_3(s)) = \delta^{17}\text{O}(\text{O}_3(a))$) when ozone is formed at low temperatures [181].

It must be noted that the isotopomer ratio

$$\mathcal{R} = \frac{[\text{O}_3(a)]}{[\text{O}_3(s)]} \quad (6.76)$$

remains constant under constant conditions (T , p , etc.) even when varying amounts of oxygen (O₂) gas are converted into ozone. This is contrary to the total enrichment ($\delta(\text{O}_3)$), which will take the initial oxygen value $\delta(\text{O}_2)$ if the conversion is complete and likely is larger when the degree of conversion is smaller than one. In order to determine the initial isotopic composition of ozone ($\delta(\text{O}_3(a))$, $\delta(\text{O}_3(s))$), we have therefore estimated

$$\beta = \mathcal{R}/2 - 1, \quad (6.77)$$

which is a measure of the degree of asymmetry of ozone. β will be 0 if there is no preference for asymmetric ozone, positive, if there is more asymmetric ozone than in the statistical case and negative if it is less abundant.

Most of the ozone samples (sets 1 and 2) in Table 6.3 have been produced by electrical discharge in oxygen with the reactor being (partly) immersed in LN₂. The ozone isotopic composition could be varied by converting oxygen to a different degree, with highest δ -values corresponding to lowest degrees of conversion. We have derived a value of $\beta = 45.5\text{‰}$ and δ values have been calculated by simultaneously fulfilling eq. (6.77) and the mass balance equation

$$3\delta(\text{O}_3) = 2\delta(\text{O}_3(a)) + \delta(\text{O}_3(s)). \quad (6.78)$$

The result of such an model run (AC17) is exemplified in Figure 6.8. The preference for the asymmetric ozone molecule can be clearly seen, but total initial ozone corresponds to the experimental starting condition. Oxygen atoms quickly equilibrate to negative delta values, which is due to rapid isotope exchange with CO and O₂ and an interesting feature is that ozone enrichments get very high at the end of the experiment when the original ozone has been photolysed and ozone is reformed from the newly created oxygen molecules. From the temporal evolution, the final isotopic composition of CO₂ has been read off for all runs. The resulting three isotope plot of the set 2 & 3 (AC, AS) experiments is given in Figure 6.9.

The three isotope data in Figure 6.9 show that not only the spread but also the absolute

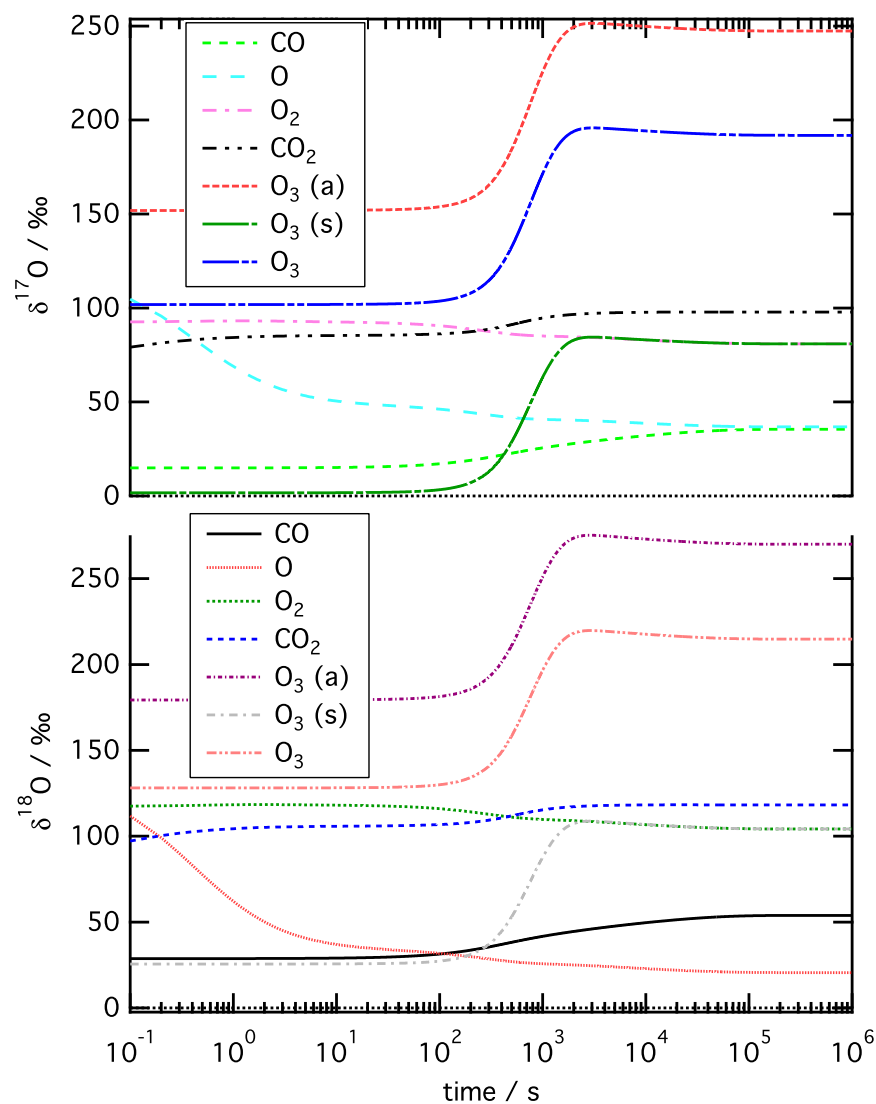


Figure 6.8: Modeled temporal evolution of $\delta^{17}\text{O}$ and $\delta^{18}\text{O}$ of some key species for experimental run AC17 of PB06 (see Table 6.3). $\text{O}_3(a)$ and $\text{O}_3(s)$ designate asymmetric and symmetric ozone isotopomers, while O_3 stands for total ozone $\text{O}_3 = \text{O}_3(a) + \text{O}_3(s)$. δ -values have been calculated using molecular ratios $\delta = \delta^m$ (see equation (6.45)). The experiment was stopped at $t = 9600$ s (vertical line).

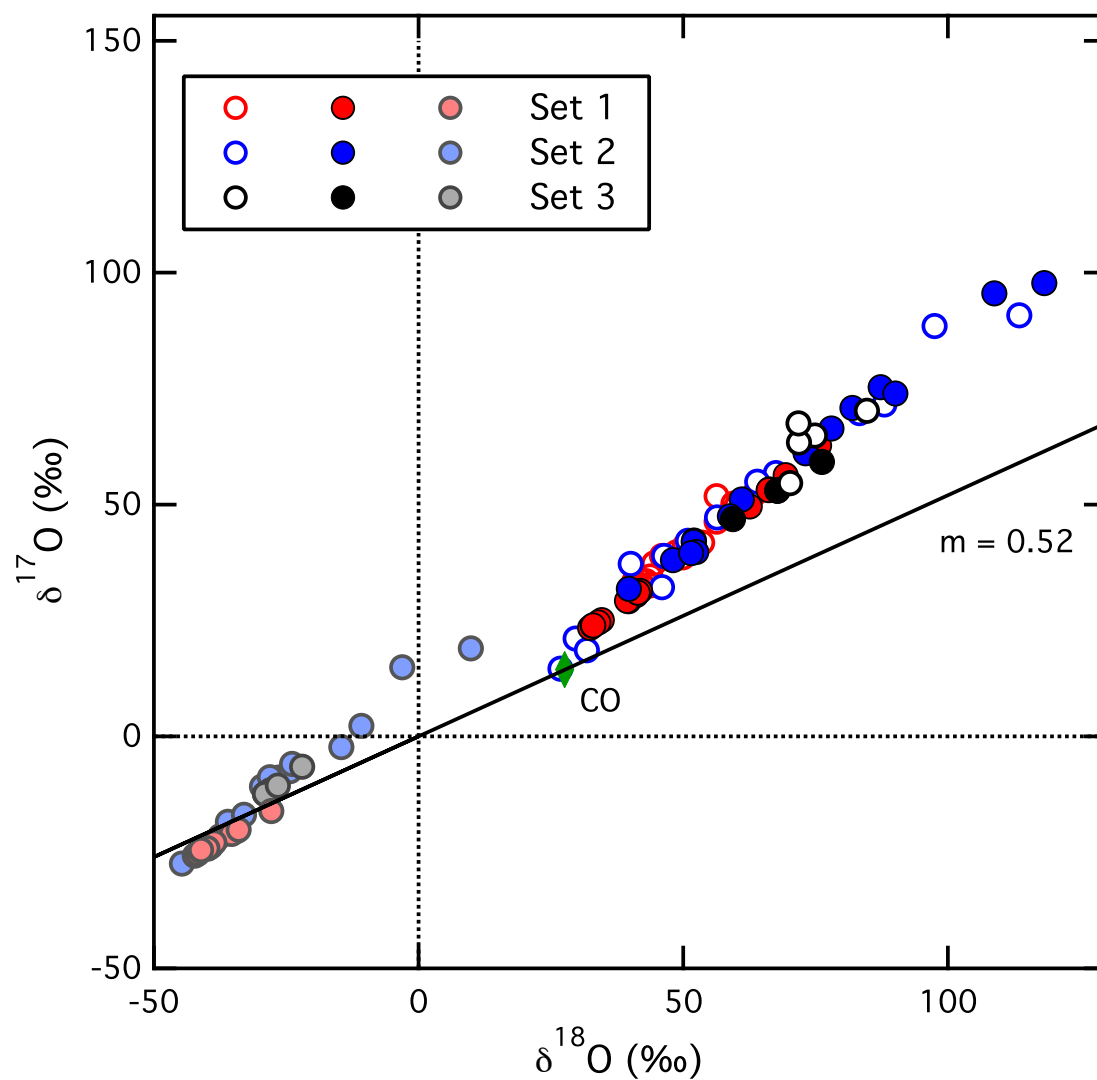


Figure 6.9: Comparison of modeled and measured three isotope data of CO_2 in the PB06 experiment. Set 1, set 2 and set 3 are represented by red, blue and black symbols, respectively. Open symbols are measured results and filled symbols represent modeled values. Shaded symbols are calculated with the simple ground state chemistry model of PB06, according to reactions (6.68)–(6.71).

values of the δ values can be reasonably well reproduced when known excited oxygen chemistry occurs at the assumed levels of H_2O contamination. The agreement is not perfect, however, and some discrepancy might be due to variable and water content. Then, isotope effects in most of the reactions are unknown and have been ignored with the exception of ozone formation and the isotope exchange reactions. Moreover, as demonstrated before, δ values have been determined approximatively and we expect uncertainties of up to 7‰ due to the neglect of multiply substituted compounds. Also, our estimate of the ozone starting composition, *i.e.* the partitioning between asymmetric and symmetric isotopomers may be inaccurate and, finally, there is a considerable uncertainty on the rate coefficient for the $\text{O} + \text{CO} + \text{M}$ formation. Changing the value by 30% will considerably shift the data along the array formed by the measurement points. Given all these different sources of bias, the agreement between modeling and measurement values on the order of about 10‰ to 20‰ must be regarded satisfactory. In particular it must be recognized that while individual δ values are not accurately modeled the alignment of the data along the measured array in the three isotope plot is very well reproduced. Clearly, including water contaminations and the full spectral properties of the light source on the one hand and of the ozone molecule on the other hand unambiguously demonstrates that the mass-independent “offset” (which is on the order of 100‰ if we compare the two model predictions on the set 3 data) between the ground state chemistry model and the measurements can be easily explained by known gas phase chemistry and $\text{O}(^1\text{D})$ mediated isotope transfer from ozone into CO_2 via formation of OH. There is no need to invoke an additional mass independent fractionation in the $\text{O} + \text{CO} + \text{M}$ reaction.

What is more, the above modeling is entirely consistent with the qualitative interpretation of the earlier experiment by Bhattacharya and Thiemens [119]. From the latter we could conclude that if there is a mass independent fractionation in the $\text{O} + \text{CO} + \text{M}$ reaction, it is small and, for the moment, there is no experimental evidence that could prove such an effect. The apparent anomalous isotope fractionation in both the experiments, the one of BT89 and the other of PB06, is largely dominated by isotope transfer from ozone via $\text{O}(^1\text{D})$ and OH. Another important conclusion to draw from this experiment is that great care must be exercised if ozone is present in a oxygen isotope study and possible isotope transfer paths must be excluded in order to avoid unambiguities in the interpretation of the results.

To sum up finally, the ozone formation reaction still seems to be a unique reaction in terms of its strong and anomalous isotope selectivity. It does not seem that analogous recombination reactions of the $\text{O} + \text{XO}$ type in general also show fractionation patterns that are similar to the one of ozone. The question why and how isotope fractionation in the formation of the ozone molecule occurs thus remains an interesting open question.

6.5 Short chapter summary

- The large mass independent fractionation in CO_2 from irradiated mixtures of O_2 and CO has been modeled for the first time.
- Amounts of CO_2 in experiments performed in the photochemical reactor at CCAR have been modeled using lamp data and reasonable H_2O contents.
- Using the same type parameters the anomalous isotopic signature of CO_2 in PB06 could be modeled.
- There is no need to invoke mass independent fractionation in the $\text{O} + \text{CO}$ reaction.
- The model - experiment comparison shows that OH mediated chemistry is an effective isotope transfer pathway from O_3 to CO_2 .

- In the light of the previous BT89 experiments the $O + CO + M$ reaction shows no or a small mass independent isotope signature.

Chapter 7

Summary and Conclusion

In the present PhD thesis an experimental and modeling study of formation of CO_2 in irradiated mixtures of CO and O_3 has been performed with the aim to investigate the isotope fractionation in the spin forbidden reaction $\text{O} + \text{CO} + \text{M} \rightarrow \text{CO}_2 + \text{M}$. A mass independent isotope anomaly has been clearly established in the $\text{O} + \text{O}_2 + \text{M}$ ozone forming reaction both from atmospheric and laboratory studies, but very few is known whether there are other similar reactions that produce comparable isotopic effects. Interestingly two studies, one by Bhattacharya and Thiemens in 1989 [119] (BT89) the other by Pandey and Bhattacharya in 2006 [134] (PB06), observed an anomalous isotope enrichment in CO_2 , which the authors claim to be caused by the $\text{O} + \text{CO} + \text{M}$ reaction. Nevertheless some doubt about this interpretation remains, because both experiments suffer from the presence of ozone which might also have been at the origin of the observed anomalous isotope signature.

The thesis first provides a line of arguments showing that the spread in the BT89 data which form an array in the three isotope plot with a slope of 0.82 cannot be explained by a mass independent fractionation effect in the $\text{O} + \text{CO} + \text{M}$ reaction alone. At least two more anomalous processes would be required to explain the data, which is deemed unlikely. According to the interpretation given in this thesis the data are explained much more convincingly if there is no anomaly in the $\text{O} + \text{CO} + \text{M}$ reaction, but an isotope transfer from ozone via $\text{O}(^1\text{D})$ and OH radicals. The formation of these reactive species in the experiment is feasible due to the use of energetic UV light.

The PB06 experiment had been performed to overcome the limitation due to the presence of UV photons in the BT89 study and a halogen filled tungsten lamp has been used in their experiments. The data show mass independent enrichments in CO_2 similar to the data of BT89 but, at the same time, the measured carbon dioxide amounts were significantly higher than those predicted from the model based on the $\text{O} + \text{CO} + \text{M}$ reaction as the only source of CO_2 . So far there is no rigorous isotope kinetic model which would explain the observations and the occurrence of a mass independent isotope anomaly in the $\text{O} + \text{CO} + \text{M}$ reaction is currently uncertain.

We hereby present a new attempt to study oxygen isotope effects in the $\text{O} + \text{CO} + \text{M}$ reaction in a photochemical reactor at CCAR (University of Copenhagen) where mixtures of O_3 and CO have been irradiated with light produced by Light Emitting Diodes (LED) in order to minimize $\text{O}(^1\text{D})$ production from ozone photolysis. A total number of 12 experiments has been performed using N_2 as bath gas at pressure between 200 and 980 hPa. Species concentration have been monitored by FTIR. As in the PB06 study CO losses in our system exceed what can be explained by the $\text{O} + \text{CO}$ reaction alone, indicating the presence of another source of CO_2 . The $\text{CO} + \text{OH}$ reaction has been identified as the most likely candidate by performing relative rate experiments using ethane as a tracer. According to our measurements OH radicals are present at levels of 10^7 cm^{-3} .

In order to understand the origin of OH in our system an extended study of the spectral emission of the LEDs has been undertaken at LERMA2 in Paris using a calibrated UV - VIS light source. In combination with ozone cross section data, this allowed to calculate the $O(^1D)/O(^3P)$ product branching ratio. For the LEDs, which have been employed for the first time in this kind of investigation, a very low value of a few 10^{-7} has been obtained. By measuring the emission spectrum of a halogen tungsten lamp of the type that has been used by PB06 a much higher value of between 10^{-2} and 1 has been found for this branching ratio. This demonstrates that significant amounts of excited oxygen have been present in the PB06 experiments and that gas phase radical chemistry cannot be excluded.

Kinetic modeling was then used to interpret our measurements at CCAR. In a first step we confirmed that the simple ground state and gas phase chemistry misses observed CO_2 formation rates by a factor of about 100. Then excited state chemistry was included in the model using two scenarios: one based on $O(^1D)/O(^3P) = 2 \times 10^{-7}$ and $[H_2O] = 2.5 \times 10^{13} \text{ cm}^{-3}$ and the other one on $O(^1D)/O(^3P) = 10^{-6}$ and $[H_2O] = 2.5 \times 10^{14} \text{ cm}^{-3}$. These two scenarios correspond to realistic and worst case experimental conditions respectively, but even in the worst case the observed CO_2 production was underestimated by a factor of 30. Because the tracer experiments unambiguously demonstrated the presence of OH radicals at levels that are compatible with the observed decay of CO, we need to conclude that other impurities and more complex chemistry played a role in our experiments. Due to the multitude of chemical compounds that have been investigated in the reactor in the past, it was unfortunately not possible to identify the contaminants. Interestingly, the modeling results show that the $O + CO + M$ reaction can in principle be studied with this type of setup, especially when LEDs are used as light sources. However, the presence of the yet unidentified contaminants necessitates a complete rebuilding of the photoreactor cell and the gas line. This has very recently been done and this kind of experiments can be performed in the near future. Nevertheless, according to our reinterpretation of the BT89 experiment it is not very likely that these experiments will reveal large mass independent anomaly in the $O + CO$ reaction.

Using the halogen filled tungsten lamp data and assuming reasonable levels of water residues in the experiments of PB06, we could provide the first complete modeling of the isotope and amount data. There is a fair degree ($\lesssim 10 - 20\%$) of agreement between the modeled and observed isotope composition of CO_2 . In agreement with the interpretation of the first experiments of BT89, the model supports the hypothesis that an isotope transfer from ozone into CO_2 via $O(^1D)$ and OH takes place, thus causing the unexpectedly high isotope enrichments in product CO_2 .

The available experiments on CO_2 produced from irradiated mixtures of ozone/oxygen and carbon monoxide have therefore been shown to comply with the idea of a simple transfer of the ozone isotopic composition into CO_2 . Evidence for an additional mass independent isotope effect in $O + CO + M$ could not be found and more detailed studies will be required to settle the question whether such an anomaly occurs in the reaction, albeit to a seemingly smaller degree than in the ozone formation reaction. This also leaves open the search for an analogous $O + XO$ recombination reaction that would show an isotope fractionation similar to the one observed in the formation of ozone.

In another part of this manuscript a vacuum system for the production and characterization of pure O_3 samples is described. Generation of pure ozone samples is an important prerequisite for quantitative ozone measurements both in laboratory studies and in atmospheric applications. Current measurements of ozone concentrations are ultimately linked to spectroscopic standards, but they suffer from inconsistencies in the spectroscopic database that become apparent when data from different spectral regions are compared. Absolute measurements based on pure ozone samples are required to tackle this issue, but the quantification of impurities is no straight forward task. While some impurities might be measured

by spectroscopic and thus noninvasive methods, others are much more difficult to quantify, in particular if they can react with ozone in different ways. Nitrogen oxides belong to this class of contaminants and an indirect quantification method based on simulation experiments and mass spectrometric measurements has been devised to find an upper limit of 0.5 mmol/mol in ozone samples generated by the electric discharge method. This low degree of contamination will allow to make absolute ozone cross section and intensity measurements with a relative standard uncertainty better than 0.5 %.

Appendix A

Spectroscopy and FTIR

A.1 Molecular spectroscopy and the Fourier Transform Infrared technique

Fourier Transform Infrared Spectroscopy (FTIR) is a powerful and widely used tool for identifying and characterizing chemical species. It is based on the interaction between infrared light and molecules. In the next sections a brief summary on molecular spectroscopy will be provided and the basic concepts of this spectroscopic technique will be illustrated.

A.1.1 Spectroscopy

The generation of an infrared spectrum is based on the absorption of infrared light by molecules with the consequent transition between quantized energy states. In this section we will give a brief overview on the basic concepts of molecular spectroscopy useful for understanding how a infrared spectrum is generated. A more complete description on this subject can be found in [182].

Vibration

Molecules formed by N atoms have $3N$ degrees of freedom, three representing the translational motion along the perpendicular axes x, y, z and three the rotational motion with respect to the same axes. The number of vibrational modes, that is the number of ways the atoms vibrations can occur in a non linear molecule is thus $3N - 6$. In case of linear molecules, since rotation around the bond does not lead to a displacement of atoms, one of the rotational degrees of freedom is not taken into account and the number of modes is $3N - 5$. The atoms vibrate from their equilibrium positions following harmonic displacements. Solving the problem quantum-mechanically one obtains the set of eigenstate energies

$$E_v = h\nu \left(v + \frac{1}{2} \right) \quad v = 0, 1, 2, \dots \quad (\text{A.1})$$

where h is the Plank's constant, v is the vibrational quantum number and ν is the classical vibration frequency. The frequency is related to the force constant k and the reduced mass m_r , defined for a diatomic molecule as $m_r = \frac{m_1 m_2}{m_1 + m_2}$, by

$$\nu = \frac{1}{2\pi} \left(\frac{k}{m_r} \right)^{1/2} \quad (\text{A.2})$$

The ground state ($v=0$) has an energy of $E_0 = \frac{h\nu}{2}$ called zero point energy. Infrared radiation can originate from a vibrational transition only if the dipole moment μ changes during the transition. Thus homonuclear diatomic molecules (*i.e.* N_2 or O_2) are not active in the IR since their dipole moment, equal to zero due to the absence of electric charge in the molecule, cannot vary during a transition.

Only transitions between states obeying the selection rule $\Delta v = \pm 1$ are allowed. Nevertheless, the harmonic potential needs to be modified in order to better approximate the physical reality. The function which agrees with the experimental results is the empirically derived Morse potential

$$V_{\text{Morse}} = D_e(1 - e^{-\alpha(R-R_e)})^2 \quad (\text{A.3})$$

where D_e is the dissociation energy and α depends on the force constant at the zero point energy k_e

$$\alpha = \sqrt{\frac{k_e}{2D_e}} \quad (\text{A.4})$$

The Morse potential adds to the solutions for the harmonic oscillator previously introduced a term of anharmonicity x_i which causes a shift down in the energy levels if compared to the harmonic oscillator as shown in figure A.1 and contributes to the potential energy which is then given by

$$E_v = h\nu\left(v + \frac{1}{2}\right) - h\nu x_i\left(v + \frac{1}{2}\right)^2 \quad (\text{A.5})$$

This anharmonicity modifies the selection rule allowing transitions with $|\Delta v| > 1$. In spec-

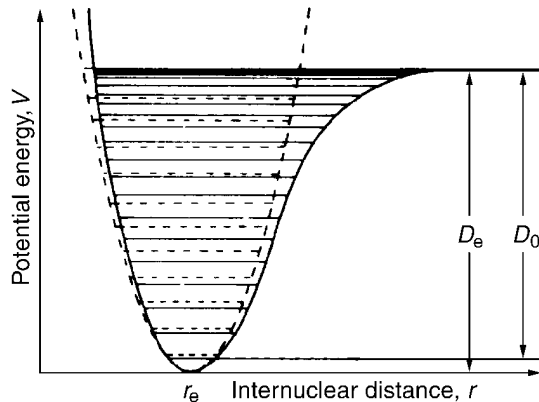


Figure A.1: Harmonic oscillator potential (dashed line) and Morse potential (continuous line). Figure taken from [183].

troscopy it is common to measure vibrational energies in the unit cm^{-1} , which can be obtained by evaluating $\frac{E_v}{hc}$

$$G(v) = \omega\left(v + \frac{1}{2}\right) - \omega x_i\left(v + \frac{1}{2}\right)^2 \quad (\text{A.6})$$

Rotation

The discussion of the previous section explains the presence and the position of line observed in an infrared absorption spectrum at low resolution. Nevertheless spectra of small molecules in the vapor phase show a substructure or fine structure of the lines which cannot be explained

by vibrations alone. Transitions between quantized rotational energy levels which take place at the same time as vibrational transitions cause this structure.

A diatomic molecule can be assumed to be a rigid rotor, that is with a fixed interatomic distance R . By quantum mechanics the expected energy states of this system can be evaluated. The rotational energy is given by the following expression

$$F_J = BJ(J + 1) \quad J = 0, 1, 2, \dots \quad (\text{A.7})$$

where J is the rotational quantum number and B is called rotational constant defined as

$$B = \frac{h}{8\pi^2cI} \quad (\text{A.8})$$

expressed in units of cm^{-1} , being I the moment of inertia of the molecule defined as $I = m_r R^2$ and c the velocity of light. The quantization rule for the angular momentum $|L| = \sqrt{J(J + 1)} \cdot \hbar$ and $L_z = M\hbar$ leads to a $(2J+1)$ - fold degeneracy of the quantum states. The distance between two consecutive levels increases with J . For linear molecules the selection rule for transition between rotational energy states is

$$\Delta J = \pm 1 \quad (\text{A.9})$$

Using this selection rule and the equation for the energy states A.7 the following condition has to be obeyed for a valid transition

$$\tilde{\nu}_{J \rightarrow J+1} = 2B(J + 1) \quad (\text{A.10})$$

The distance between two spectral lines is determined by this relation and it means that each transition has an energy of $2B$ more than the one with the next lower quantum number. As a consequence the emitted lines are equally spaced from each other. Actually this not the reality because a decrease in transition spacings with increasing J is observed in the spectra. This is due to the fact that a molecule cannot be treated as a rigid rotor as the bond between the nuclei is not rigid, and liable to centrifugal forces. This causes a decreasing in the value of B (since R increases) but the contribution of the centrifugal distortion is actually described by the centrifugal distortion constant D linked to B by the expression

$$D = \frac{4B^3}{\omega^2} \quad (\text{A.11})$$

where ω is the vibration wavenumber. The rotational energy E_J is then affected by a decrease and can be written as follows

$$F_J = BJ(J + 1) - DJ^2(J + 1)^2 \quad (\text{A.12})$$

Several factors determine the intensity of the observed lines; most important are the population and the dipole moment. Each state is denoted by a different degeneracy as it increases with larger quantum number J according to $(2J+1)$. Nevertheless it cannot be concluded that transitions between higher quantum numbers have more and more intensity since the thermal occupation of the states plays a role and a transition $J \rightarrow J + 1$ can only be triggered from an already occupied state with quantum number J . The population of the J th level N_J relative to the population of the ground state N_0 is given by the Boltzmann's distribution law and the total occupation probability can be expressed as

$$\frac{N_J}{N_0} = (2J + 1) \exp\left(-\frac{E_r}{kT}\right) = (2J + 1) \exp\left(-\frac{BhcJ(J + 1)}{kT}\right) \quad (\text{A.13})$$

being k is the Boltzmann constant and T the temperature. As can be observed for small J the intensity increases with J but at larger quantum states the exponential decay of the thermal occupation dominates and causes a decrease of intensity.

Coupling of vibrations and rotations

After having consider vibrations and rotations separately it is possible to understand the whole vibrational-rotational spectrum as seen in high-resolution spectroscopy. In the vibrational spectrum a fine structure can be observed corresponding to a rotational transition which takes place at the same time. The energy levels can be written as the sum of the expressions A.6 and A.12 derived previously

$$E(v, J) = G(v) + F(J) = \omega\left(v + \frac{1}{2}\right) - \omega x_i\left(v + \frac{1}{2}\right)^2 + BJ(J + 1) - DJ^2(J + 1)^2 \quad (\text{A.14})$$

In figure (cite) typical rotational transitions accompanying a vibrational transition in a diatomic molecule is shown. The transitions between states with $\Delta J = +1$ form the P-branch whereas the R-branch is originated by transition yielding $\Delta J = -1$. The Q-branch corresponding to $\Delta J = 0$ is in general not allowed but exceptions are molecules with an electronic angular momentum in the ground electronic state (*i.e.* NO). Therefore the infrared spectrum of a diatomic molecule consists of two bands that are fairly symmetric with respect to a central point that is the fundamental vibrational mode $\tilde{\nu}_0$. Due to the effect of the centrifugal distortion the space between the lines in the P-branch increases as the distance from $\tilde{\nu}_0$ increases whereas the opposite effect takes place in the R-branch as shown in the CO spectrum reproduced in figure A.2

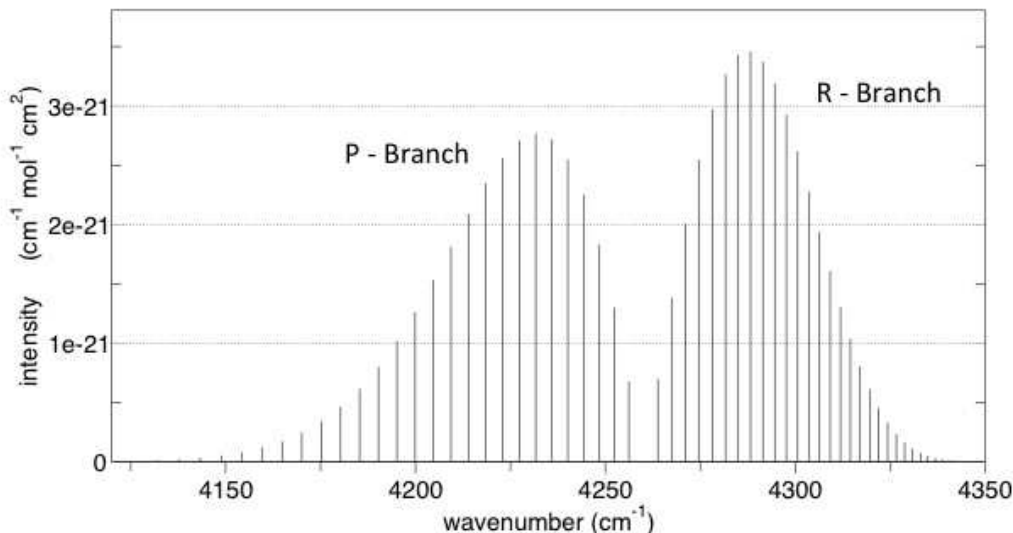


Figure A.2: Vibration-rotation spectrum of CO simulated with the high resolution spectral modeling software SpectralCalc (www.spectralcalc.com).

Spectral line broadening

As shown in the previous sections the absorption spectrum of molecules arises from transitions between rotational and vibrational levels which occur in correspondence of well defined energy values. Thus ideally the lines in a spectrum should be infinitely narrow while in reality they

are characterized by finite width centered around the emission energy. Several processes contribute to the broadening of spectral lines. The first one is due to the evidence that, after having adsorbed radiation, the excited molecule has a finite lifetime τ and eventually returns to the ground state by spontaneous emission. According to the Heisenberg's uncertainty principle which relates the lifetime to the energy spread ΔE for a state

$$\hbar \leq \Delta E \tau \quad (\text{A.15})$$

when the molecule relaxes back, the energy release changes in the range given by ΔE . As a consequence the photon energy is distributed in this interval leading to a broad line profile with a shape of a Lorentzian function which FWHM is called natural line width. In general this effect is negligible in infrared spectroscopy.

Another broadening effect is the Doppler broadening due to the different thermal movements of molecules. Supposing that a molecule absorbs a photon with wavenumber ν_0 in its reference system, an observer sees the molecule traveling towards him with a velocity v and absorbing photons corresponding to a wavenumber $\nu = \nu_0 (1 + v/c)$ where c is the speed of light. Since the velocity follows the Maxwell distribution, the resulting spectral shape has a gaussian profile depending on ν_0 and on the temperature T and given by

$$\Phi_{\nu}^D(\nu_0, T) = \sqrt{\frac{\ln 2}{\pi}} \frac{1}{\gamma_D} \exp\left(-\frac{\ln 2(\nu - \nu_0)^2}{\gamma_D^2}\right) \quad (\text{A.16})$$

where the half width at half maximum, expressed in cm^{-1} is defined by

$$\gamma_D = 3.58 \times 10^{-7} \nu_0 \left(\frac{T}{M}\right)^{1/2} \quad (\text{A.17})$$

being M the molecular mass.

The third origin for broadening in the spectral shape are the collisions between the absorbing molecules themselves and the other molecules of the medium which cause a perturbation of the initial and final energy states. In this case the process is called pressure broadening or collisional broadening. The line is characterized by a Lorentzian profile:

$$\Phi_{\nu}^L(\nu_0, T, P) = \frac{1}{\pi} \frac{\gamma_L}{(\nu - \nu_0)^2 + \gamma_L^2} \quad (\text{A.18})$$

The FWHM is proportional to pressure and depends on the species which take part to the collision, on temperature and on the specific transition. It can be written as the sum of the broadening due to collisions between molecules of different gases and of the same species:

$$\gamma_L = \sum_i \gamma_{L,i}(\nu_0, P_0, T_{ref}) \frac{P_i}{P_0} \left(\frac{T_{ref}}{T}\right)^{n_i} \quad (\text{A.19})$$

where T is the temperature, P_i is the partial pressure of the gas i , T_{ref} and P_0 are respectively the reference temperature and pressure (296 K and 1013,25 hPa), $\gamma_{L,i}$ is the broadening of the gas i and n_i is the temperature dependence. The two line shapes described have different properties, arising from the dependence on the wavenumber. The Gaussian profile has an exponential decay proportional to $\exp[-(\nu_0 - \nu)^2]$ and consequently the emission is dominant corresponding to the peak whereas is weak in the wings of the line. In contrast a large fraction of the total emission is in the tails of the line for a Lorentzian broadening since the intensity decays with the square of the deviation from the central wavelength. In addition, collisional broadening dominates at high pressures while at low values Doppler broadening is no longer

negligible and the resulting line shape is obtained by the convolution of the Gaussian and the Lorentzian line shapes. This profile is called Voigt shape and is given by

$$\Phi_{\nu}^V = \sqrt{\frac{\ln 2}{\pi}} \frac{1}{\gamma_D} \int_{-\infty}^{+\infty} \frac{e^{-t^2}}{(X-t)^2 + Y^2} dt \quad (\text{A.20})$$

where

$$X = \sqrt{\ln 2} \frac{\nu - \nu_0}{\gamma_D} \quad (\text{A.21})$$

and

$$Y = \sqrt{\ln 2} \frac{\gamma_L}{\gamma_D} \quad (\text{A.22})$$

In figure A.3 the shape of a Lorentzian profile (black curve) is compared with a Gaussian one (red curve). The convolution of the two has been calculated in order to draw the Voigt profile (green curve).

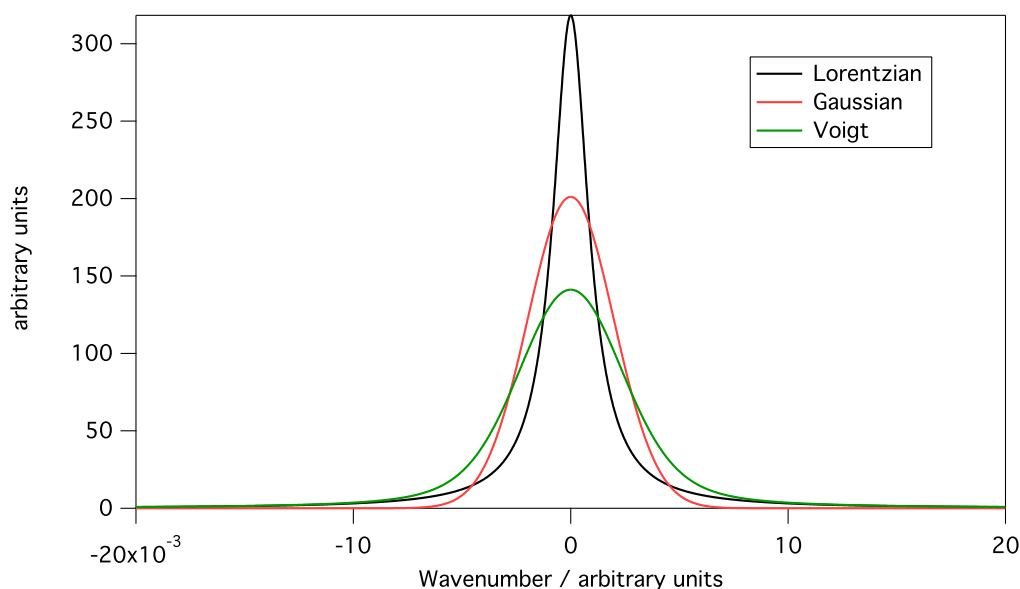


Figure A.3: Comparison between a Lorentzian (black curve) and a Gaussian profile (red curve). The resulting Voigt profile, calculated by the convolution of the two, is also plotted in green color.

A.1.2 Fourier Transform Infrared Spectroscopy (FTIR)

Fourier Transform Infrared Spectroscopy (FTIR) is based on the occurrence of interferences of two beams in an interferometer and on the observation that each wavelength produces a particular interference pattern if the optical path difference (OPD) of the two interfering beams is changed. The radiation is emitted by a source and after having passed through an interferometer is transmitted or reflected by a sample to be analyzed and is finally focused on a detector which provides for the conversion to a digital signal. The data are then transferred to a computer for Fourier transformation. The operating principle of a typical interferometer will be illustrated in the next section.

The Michelson Interferometer

Usually FTIR instruments are based on a Michelson interferometer which main components are a source, two mirrors (one fixed, the other moveable) and a beam splitter arranged as

shown in figure A.4

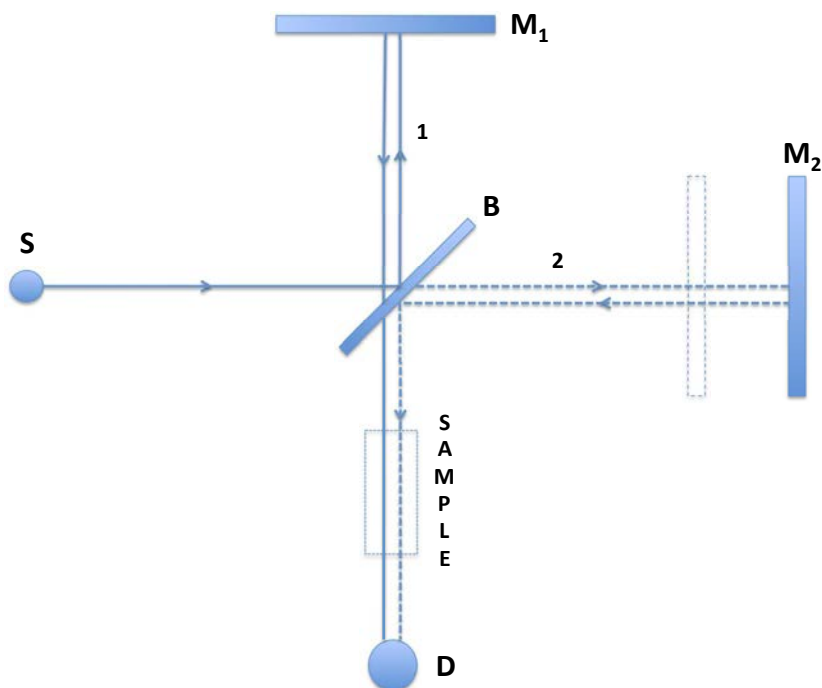


Figure A.4: Scheme of the Michelson interferometer.

In the ideal case the monochromatic source S emits a parallel beam which is equally divided by the beam splitter B: the reflected fraction (1) hits the fixed mirror M_1 and after being reflected is partially transmitted at the beam splitter towards the detector D. The other part of the beam (2) is transmitted by the beamsplitter and then is reflected by the movable mirror M_2 . This beam is reflected by B before reaching the detector D. When rays 1 and 2 reach D, they have traversed different paths with an optical path difference (OPD) δ called *retardation* given by

$$\delta = 2(BM_2 - BM_1) \quad (\text{A.23})$$

As consequence, the OPD depends on the geometrical path difference caused by the movable mirror which introduces a phase difference of the two recombining waves of radiation. If the two waves are in phase they interfere constructively at the detector whereas if they differ by a phase shift of π the interference is destructive and no signal is detected. Therefore if the mirror moves at constant velocity the signal detected is seen to vary sinusoidally and a maximum is registered each time the retardation is an integer multiple of the wavelength emitted by the source, λ_0 . The intensity of the beam at the detector $I'(\delta)$ is expressed in function of the retardation δ and the intensity of the source $I(\tilde{\nu}_0)$ by

$$I'(\delta) = 0.5 I(\tilde{\nu}_0)(1 + \cos 2\pi\tilde{\nu}_0\delta) \quad (\text{A.24})$$

For spectroscopic studies only the modulated component of $I'(\delta)$ is relevant and it is known as *interferogram* $I(\delta)$ and represents the raw FTIR data

$$I(\delta) = 0.5 I(\tilde{\nu}_0) \cos 2\pi\tilde{\nu}_0\delta \quad (\text{A.25})$$

Actually this expression needs to be modified since a beamsplitter which has an ideal behavior

(50% transmission and 50% reflection) does not exist. These devices are characterized by a wavelength - dependent response, too. This needs to be taken in account if the source is not monochromatic. In addition the detector response is normally not uniform for all wavelengths and the amplifiers used for the signal processing contain filters in order to cut light radiation outside the spectral range of interest. As consequence the interferogram depends not only on the intensity of the source but also on instrumental features which can be factored in one term $B(\tilde{\nu}_0)$ referred as single-beam spectral intensity [184]. The interferogram is then given by the expression

$$I(\delta) = B(\tilde{\nu}_0)\cos 2\pi\tilde{\nu}_0\delta \quad (\text{A.26})$$

where $I(\delta)$ from a mathematical point of view is the cosine Fourier transform of $B(\tilde{\nu}_0)$ and the spectrum is then evaluated by computing the cosine Fourier transform of $I(\delta)$. During an usual experiment the source emits radiation at many wavelengths with a spectral irradiance $B(\tilde{\nu})$ (expressed in $\text{W} \cdot \text{m}^{-1}$) and the detected intensity has the following expression

$$I(\delta) = \int_{-\infty}^{\infty} B(\tilde{\nu})\cos(2\pi\tilde{\nu}\delta) d\tilde{\nu} \quad (\text{A.27})$$

The spectral distribution can be calculated by the estimation of the Fourier transform of $I(\delta)$

$$B(\tilde{\nu}) = \int_{-\infty}^{\infty} I(\delta)\cos(2\pi\tilde{\nu}\delta) d\delta \quad (\text{A.28})$$

Being $I(\delta)$ an even function [185] the equation A.28 can be written as follows

$$B(\tilde{\nu}) = 2 \int_0^{\infty} I(\delta)\cos(2\pi\tilde{\nu}\delta) d\delta \quad (\text{A.29})$$

Equation (A.29) leads to the conclusion that it could be possible to measure spectra with a retardation ranging from zero to $+\infty$ that is with infinite path differences. Of course, this is not possible with a real interferometer and the detection of an interferogram scanning the moving mirror of the instrument at finite distances introduces a finite resolution in the measurements. It can be shown [185] that the measured spectrum $\tilde{S}(\tilde{\nu})$ is the convolution of the ideal spectrum $B(\tilde{\nu})$ and the instrument function $f(\tilde{\nu})$:

$$S(\tilde{\nu}) = B(\tilde{\nu}) \otimes f(\tilde{\nu}) \quad (\text{A.30})$$

where $f(\tilde{\nu})$ is related to the maximum optical path difference, namely Δ , by

$$f(\tilde{\nu}) = 2\Delta \frac{\sin(2\pi\tilde{\nu}\Delta)}{2\pi\tilde{\nu}\Delta} \quad (\text{A.31})$$

$$\equiv 2\Delta \text{sinc}(2\pi\tilde{\nu}\Delta) \quad (\text{A.32})$$

being $\text{sinc}(x)=\sin(x)/x$. This function is characterized by quite large oscillations and besides a maximum centered at $\tilde{\nu} = 0$, several additional peak are present. The first minimum corresponds to a negative amplitude which is 22% of the maximum amplitude of the function. In case another weaker line appears corresponding at the wavenumber where this minimum is present, it will not be seen in the spectrum. Furthermore, the side lobes do not correspond to actually measured information but are an artifact caused by the truncation of the interferogram at Δ . This effect can be reduced by multiplying the interferogram by an *apodization function* which attenuates the amplitude of the lobes, thus making less important the effect of the truncation of the interferogram at Δ . Several apodization functions have been proposed (Norton-Beer, triangular, trapezoidal, Happ-Genzel or hamming, ...) and the choice

of one particular function respect to another one depends on the features of the analyzed spectrum. Normally a good quantitative accuracy is obtained performing the analysis with triangle function which leads to a resolution R given by

$$R \approx 0.9/\Delta \tag{A.33}$$

which is the FWHM of the Fourier transform of the triangle apodization function.

Appendix B

Statistical Models on Ozone Photolytic Decomposition

B.1 Full statistical model

Overview of the full statistical model of photolytic decomposition of ozone, which comprises all isotopic variants of molecules and reactions

Table B.1: List of main reactions.

#	# of variants	reaction type
1	27	$O + O_2 \longrightarrow O_3$
2	27	$O_3 + h\nu \longrightarrow O_2 + O$
3	72	$O_3 + O \longrightarrow O_2 + O_2$
4	18	$Q + O_2 \longrightarrow OQ + O$

Table B.2: Species by molecular size.

# of atoms	# of species	species
1	3	O, P, Q
2	6	O_2 , OP, OQ, P_2 , PQ, Q_2
3	18	O_2P , O_2Q , O_3 , OPO, OPQ, OQO, OQP, P_2O , P_2Q , P_3 , POP, POQ, PQP, Q_2O , Q_2P , Q_3 , QOQ, QPQ

Table B.3: Molecules by number of isotope substitutions

# of substitutions	# of molecules	list of molecules
0	3	O, O_2 , O_3
1	8	O_2P , O_2Q , OP, OPO, OQ, OQO, P, Q
2	10	OPQ, OQP, P_2 , P_2O , POP, POQ, PQ, Q_2 , Q_2O , QOQ
3	6	P_2Q , P_3 , PQP, Q_2P , Q_3 , QPQ

Table B.4: Complete list of all reactions.

#	Reaction	Rate coefficient ($\text{s}^{-1}, \text{cm}^3 \text{s}^{-1}$)	Note
1 · 01	$\text{O} + \text{O}_2 \longrightarrow \text{O}_3$	$[\text{M}] 6.0 \times 10^{-34} (300 \text{ K}/T)^{-2.4}$	1
1 · 02	$\text{Q} + \text{O}_2 \longrightarrow \text{O}_2\text{Q}$	$k_{1.01}$	
1 · 03	$\text{O} + \text{OQ} \longrightarrow \text{O}_2\text{Q}$	$1/2 k_{1.01}$	
1 · 04	$\text{O} + \text{OQ} \longrightarrow \text{OQO}$	$1/2 k_{1.01}$	
1 · 05	$\text{P} + \text{O}_2 \longrightarrow \text{O}_2\text{P}$	$k_{1.01}$	
1 · 06	$\text{O} + \text{OP} \longrightarrow \text{O}_2\text{P}$	$1/2 k_{1.01}$	
1 · 07	$\text{O} + \text{OP} \longrightarrow \text{OPO}$	$1/2 k_{1.01}$	
1 · 08	$\text{Q} + \text{OQ} \longrightarrow \text{QOQ}$	$1/2 k_{1.01}$	
1 · 09	$\text{Q} + \text{OQ} \longrightarrow \text{Q}_2\text{O}$	$1/2 k_{1.01}$	
1 · 10	$\text{O} + \text{Q}_2 \longrightarrow \text{Q}_2\text{O}$	$k_{1.01}$	
1 · 11	$\text{Q} + \text{OP} \longrightarrow \text{POQ}$	$1/2 k_{1.01}$	
1 · 12	$\text{Q} + \text{OP} \longrightarrow \text{OPQ}$	$1/2 k_{1.01}$	
1 · 13	$\text{P} + \text{OQ} \longrightarrow \text{POQ}$	$1/2 k_{1.01}$	
1 · 14	$\text{P} + \text{OQ} \longrightarrow \text{OQP}$	$1/2 k_{1.01}$	
1 · 15	$\text{O} + \text{PQ} \longrightarrow \text{OPQ}$	$1/2 k_{1.01}$	
1 · 16	$\text{O} + \text{PQ} \longrightarrow \text{OQP}$	$1/2 k_{1.01}$	
1 · 17	$\text{O} + \text{P}_2 \longrightarrow \text{P}_2\text{O}$	$k_{1.01}$	
1 · 18	$\text{P} + \text{OP} \longrightarrow \text{P}_2\text{O}$	$1/2 k_{1.01}$	
1 · 19	$\text{P} + \text{OP} \longrightarrow \text{POP}$	$1/2 k_{1.01}$	
1 · 20	$\text{Q} + \text{Q}_2 \longrightarrow \text{Q}_3$	$k_{1.01}$	
1 · 21	$\text{Q} + \text{PQ} \longrightarrow \text{Q}_2\text{P}$	$1/2 k_{1.01}$	
1 · 22	$\text{Q} + \text{PQ} \longrightarrow \text{QPQ}$	$1/2 k_{1.01}$	
1 · 23	$\text{P} + \text{Q}_2 \longrightarrow \text{Q}_2\text{P}$	$k_{1.01}$	
1 · 24	$\text{Q} + \text{P}_2 \longrightarrow \text{P}_2\text{Q}$	$k_{1.01}$	
1 · 25	$\text{P} + \text{PQ} \longrightarrow \text{P}_2\text{Q}$	$1/2 k_{1.01}$	
1 · 26	$\text{P} + \text{PQ} \longrightarrow \text{PQP}$	$1/2 k_{1.01}$	
1 · 27	$\text{P} + \text{P}_2 \longrightarrow \text{P}_3$	$k_{1.01}$	
2 · 01	$\text{O}_3 + h\nu \longrightarrow \text{O}_2 + \text{O}$	$J_1 = 2.65 \times 10^{-4}$	2
2 · 02	$\text{O}_2\text{Q} + h\nu \longrightarrow \text{O}_2 + \text{Q}$	$1/2 k_{2.01}$	
2 · 03	$\text{O}_2\text{Q} + h\nu \longrightarrow \text{OQ} + \text{O}$	$1/2 k_{2.01}$	
2 · 04	$\text{OQO} + h\nu \longrightarrow \text{OQ} + \text{O}$	$k_{2.01}$	
2 · 05	$\text{O}_2\text{P} + h\nu \longrightarrow \text{O}_2 + \text{P}$	$1/2 k_{2.01}$	
2 · 06	$\text{O}_2\text{P} + h\nu \longrightarrow \text{OP} + \text{O}$	$1/2 k_{2.01}$	
2 · 07	$\text{OPO} + h\nu \longrightarrow \text{OP} + \text{O}$	$k_{2.01}$	
2 · 08	$\text{QOQ} + h\nu \longrightarrow \text{OQ} + \text{Q}$	$k_{2.01}$	
2 · 09	$\text{Q}_2\text{O} + h\nu \longrightarrow \text{OQ} + \text{Q}$	$1/2 k_{2.01}$	
2 · 10	$\text{Q}_2\text{O} + h\nu \longrightarrow \text{Q}_2 + \text{O}$	$1/2 k_{2.01}$	
2 · 11	$\text{OPQ} + h\nu \longrightarrow \text{PQ} + \text{O}$	$1/2 k_{2.01}$	
2 · 12	$\text{OPQ} + h\nu \longrightarrow \text{OP} + \text{Q}$	$1/2 k_{2.01}$	
2 · 13	$\text{POQ} + h\nu \longrightarrow \text{OP} + \text{Q}$	$1/2 k_{2.01}$	
2 · 14	$\text{POQ} + h\nu \longrightarrow \text{OQ} + \text{P}$	$1/2 k_{2.01}$	
2 · 15	$\text{OQP} + h\nu \longrightarrow \text{OQ} + \text{P}$	$1/2 k_{2.01}$	
2 · 16	$\text{OQP} + h\nu \longrightarrow \text{PQ} + \text{O}$	$1/2 k_{2.01}$	
2 · 17	$\text{POP} + h\nu \longrightarrow \text{OP} + \text{P}$	$k_{2.01}$	
2 · 18	$\text{P}_2\text{O} + h\nu \longrightarrow \text{OP} + \text{P}$	$1/2 k_{2.01}$	
2 · 19	$\text{P}_2\text{O} + h\nu \longrightarrow \text{P}_2 + \text{O}$	$1/2 k_{2.01}$	

Table B.4: continued

#	Reaction	Rate coefficient ($\text{s}^{-1}, \text{cm}^3 \text{s}^{-1}$)	Note
2·20	$\text{Q}_3 + h\nu \longrightarrow \text{Q}_2 + \text{Q}$	$k_{2.01}$	
2·21	$\text{Q}_2\text{P} + h\nu \longrightarrow \text{Q}_2 + \text{P}$	$1/2 k_{2.01}$	
2·22	$\text{Q}_2\text{P} + h\nu \longrightarrow \text{PQ} + \text{Q}$	$1/2 k_{2.01}$	
2·23	$\text{QPQ} + h\nu \longrightarrow \text{PQ} + \text{Q}$	$k_{2.01}$	
2·24	$\text{P}_2\text{Q} + h\nu \longrightarrow \text{P}_2 + \text{Q}$	$1/2 k_{2.01}$	
2·25	$\text{P}_2\text{Q} + h\nu \longrightarrow \text{PQ} + \text{P}$	$1/2 k_{2.01}$	
2·26	$\text{PQP} + h\nu \longrightarrow \text{PQ} + \text{P}$	$k_{2.01}$	
2·27	$\text{P}_3 + h\nu \longrightarrow \text{P}_2 + \text{P}$	$k_{2.01}$	
3·01	$\text{O}_3 + \text{O} \longrightarrow \text{O}_2 + \text{O}_2$	$8.0 \times 10^{-12} \exp(-2060.0 \text{ K}/T)$	1
3·02	$\text{O}_3 + \text{Q} \longrightarrow \text{OQ} + \text{O}_2$	$k_{3.01}$	
3·03	$\text{O}_2\text{Q} + \text{O} \longrightarrow \text{OQ} + \text{O}_2$	$k_{3.01}$	
3·04	$\text{OQO} + \text{O} \longrightarrow \text{OQ} + \text{O}_2$	$k_{3.01}$	
3·05	$\text{O}_3 + \text{P} \longrightarrow \text{OP} + \text{O}_2$	$k_{3.01}$	
3·06	$\text{O}_2\text{P} + \text{O} \longrightarrow \text{OP} + \text{O}_2$	$k_{3.01}$	
3·07	$\text{OPO} + \text{O} \longrightarrow \text{OP} + \text{O}_2$	$k_{3.01}$	
3·08	$\text{O}_2\text{Q} + \text{Q} \longrightarrow \text{Q}_2 + \text{O}_2$	$1/2 k_{3.01}$	
3·09	$\text{O}_2\text{Q} + \text{Q} \longrightarrow \text{OQ} + \text{OQ}$	$1/2 k_{3.01}$	
3·10	$\text{OQO} + \text{Q} \longrightarrow \text{OQ} + \text{OQ}$	$k_{3.01}$	
3·11	$\text{QOQ} + \text{O} \longrightarrow \text{OQ} + \text{OQ}$	$k_{3.01}$	
3·12	$\text{Q}_2\text{O} + \text{O} \longrightarrow \text{OQ} + \text{OQ}$	$1/2 k_{3.01}$	
3·13	$\text{Q}_2\text{O} + \text{O} \longrightarrow \text{Q}_2 + \text{O}_2$	$1/2 k_{3.01}$	
3·14	$\text{O}_2\text{P} + \text{Q} \longrightarrow \text{OQ} + \text{OP}$	$1/2 k_{3.01}$	
3·15	$\text{O}_2\text{P} + \text{Q} \longrightarrow \text{PQ} + \text{O}_2$	$1/2 k_{3.01}$	
3·16	$\text{OPO} + \text{Q} \longrightarrow \text{OQ} + \text{OP}$	$k_{3.01}$	
3·17	$\text{O}_2\text{Q} + \text{P} \longrightarrow \text{PQ} + \text{O}_2$	$1/2 k_{3.01}$	
3·18	$\text{O}_2\text{Q} + \text{P} \longrightarrow \text{OQ} + \text{OP}$	$1/2 k_{3.01}$	
3·19	$\text{OQO} + \text{P} \longrightarrow \text{OQ} + \text{OP}$	$k_{3.01}$	
3·20	$\text{OPQ} + \text{O} \longrightarrow \text{O}_2 + \text{PQ}$	$1/2 k_{3.01}$	
3·21	$\text{OPQ} + \text{O} \longrightarrow \text{OQ} + \text{OP}$	$1/2 k_{3.01}$	
3·22	$\text{OQP} + \text{O} \longrightarrow \text{O}_2 + \text{PQ}$	$1/2 k_{3.01}$	
3·23	$\text{OQP} + \text{O} \longrightarrow \text{OQ} + \text{OP}$	$1/2 k_{3.01}$	
3·24	$\text{POQ} + \text{O} \longrightarrow \text{OQ} + \text{OP}$	$k_{3.01}$	
3·25	$\text{O}_2\text{P} + \text{P} \longrightarrow \text{P}_2 + \text{O}_2$	$1/2 k_{3.01}$	
3·26	$\text{O}_2\text{P} + \text{P} \longrightarrow \text{OP} + \text{OP}$	$1/2 k_{3.01}$	
3·27	$\text{OPO} + \text{P} \longrightarrow \text{OP} + \text{OP}$	$k_{3.01}$	
3·28	$\text{POP} + \text{O} \longrightarrow \text{OP} + \text{OP}$	$k_{3.01}$	
3·29	$\text{P}_2\text{O} + \text{O} \longrightarrow \text{OP} + \text{OP}$	$1/2 k_{3.01}$	
3·30	$\text{P}_2\text{O} + \text{O} \longrightarrow \text{P}_2 + \text{O}_2$	$1/2 k_{3.01}$	
3·31	$\text{Q}_3 + \text{O} \longrightarrow \text{OQ} + \text{Q}_2$	$k_{3.01}$	
3·32	$\text{QOQ} + \text{Q} \longrightarrow \text{OQ} + \text{Q}_2$	$k_{3.01}$	
3·33	$\text{Q}_2\text{O} + \text{Q} \longrightarrow \text{OQ} + \text{Q}_2$	$k_{3.01}$	
3·34	$\text{OPQ} + \text{Q} \longrightarrow \text{OQ} + \text{PQ}$	$1/2 k_{3.01}$	
3·35	$\text{OPQ} + \text{Q} \longrightarrow \text{OP} + \text{Q}_2$	$1/2 k_{3.01}$	
3·36	$\text{OQP} + \text{Q} \longrightarrow \text{OQ} + \text{PQ}$	$k_{3.01}$	
3·37	$\text{POQ} + \text{Q} \longrightarrow \text{PQ} + \text{OQ}$	$1/2 k_{3.01}$	
3·38	$\text{POQ} + \text{Q} \longrightarrow \text{OP} + \text{Q}_2$	$1/2 k_{3.01}$	

Table B.4: continued

#	Reaction	Rate coefficient ($\text{s}^{-1}, \text{cm}^3 \text{s}^{-1}$)	Note
3·39	$\text{Q}_2\text{P} + \text{O} \longrightarrow \text{Q}_2 + \text{OP}$	$1/2 k_{3\cdot 01}$	
3·40	$\text{Q}_2\text{P} + \text{O} \longrightarrow \text{OQ} + \text{PQ}$	$1/2 k_{3\cdot 01}$	
3·41	$\text{QPQ} + \text{O} \longrightarrow \text{PQ} + \text{OQ}$	$k_{3\cdot 01}$	
3·42	$\text{POP} + \text{Q} \longrightarrow \text{OP} + \text{PQ}$	$k_{3\cdot 01}$	
3·43	$\text{P}_2\text{O} + \text{Q} \longrightarrow \text{OP} + \text{PQ}$	$1/2 k_{3\cdot 01}$	
3·44	$\text{P}_2\text{O} + \text{Q} \longrightarrow \text{P}_2 + \text{OQ}$	$1/2 k_{3\cdot 01}$	
3·45	$\text{QOQ} + \text{P} \longrightarrow \text{OQ} + \text{PQ}$	$k_{3\cdot 01}$	
3·46	$\text{Q}_2\text{O} + \text{P} \longrightarrow \text{OQ} + \text{PQ}$	$1/2 k_{3\cdot 01}$	
3·47	$\text{Q}_2\text{O} + \text{P} \longrightarrow \text{Q}_2 + \text{OP}$	$1/2 k_{3\cdot 01}$	
3·48	$\text{OPQ} + \text{P} \longrightarrow \text{PQ} + \text{OP}$	$k_{3\cdot 01}$	
3·49	$\text{OQP} + \text{P} \longrightarrow \text{P}_2 + \text{OQ}$	$1/2 k_{3\cdot 01}$	
3·50	$\text{OQP} + \text{P} \longrightarrow \text{OP} + \text{PQ}$	$1/2 k_{3\cdot 01}$	
3·51	$\text{POQ} + \text{P} \longrightarrow \text{P}_2 + \text{OQ}$	$1/2 k_{3\cdot 01}$	
3·52	$\text{POQ} + \text{P} \longrightarrow \text{OP} + \text{PQ}$	$1/2 k_{3\cdot 01}$	
3·53	$\text{P}_2\text{Q} + \text{O} \longrightarrow \text{P}_2 + \text{OQ}$	$1/2 k_{3\cdot 01}$	
3·54	$\text{P}_2\text{Q} + \text{O} \longrightarrow \text{PQ} + \text{OP}$	$1/2 k_{3\cdot 01}$	
3·55	$\text{PQP} + \text{O} \longrightarrow \text{PQ} + \text{OP}$	$k_{3\cdot 01}$	
3·56	$\text{POP} + \text{P} \longrightarrow \text{OP} + \text{P}_2$	$k_{3\cdot 01}$	
3·57	$\text{P}_2\text{O} + \text{P} \longrightarrow \text{OP} + \text{P}_2$	$k_{3\cdot 01}$	
3·58	$\text{P}_3 + \text{O} \longrightarrow \text{OP} + \text{P}_2$	$k_{3\cdot 01}$	
3·59	$\text{Q}_3 + \text{Q} \longrightarrow \text{Q}_2 + \text{Q}_2$	$k_{3\cdot 01}$	
3·60	$\text{Q}_2\text{P} + \text{Q} \longrightarrow \text{Q}_2 + \text{PQ}$	$k_{3\cdot 01}$	
3·61	$\text{QPQ} + \text{Q} \longrightarrow \text{Q}_2 + \text{PQ}$	$k_{3\cdot 01}$	
3·62	$\text{Q}_3 + \text{P} \longrightarrow \text{PQ} + \text{Q}_2$	$k_{3\cdot 01}$	
3·63	$\text{P}_2\text{Q} + \text{Q} \longrightarrow \text{P}_2 + \text{Q}_2$	$1/2 k_{3\cdot 01}$	
3·64	$\text{P}_2\text{Q} + \text{Q} \longrightarrow \text{PQ} + \text{PQ}$	$1/2 k_{3\cdot 01}$	
3·65	$\text{QPQ} + \text{P} \longrightarrow \text{PQ} + \text{PQ}$	$k_{3\cdot 01}$	
3·66	$\text{Q}_2\text{P} + \text{P} \longrightarrow \text{PQ} + \text{PQ}$	$1/2 k_{3\cdot 01}$	
3·67	$\text{Q}_2\text{P} + \text{P} \longrightarrow \text{Q}_2 + \text{P}_2$	$1/2 k_{3\cdot 01}$	
3·68	$\text{PQP} + \text{Q} \longrightarrow \text{PQ} + \text{PQ}$	$k_{3\cdot 01}$	
3·69	$\text{P}_3 + \text{Q} \longrightarrow \text{PQ} + \text{P}_2$	$k_{3\cdot 01}$	
3·70	$\text{PQP} + \text{P} \longrightarrow \text{PQ} + \text{P}_2$	$k_{3\cdot 01}$	
3·71	$\text{P}_2\text{Q} + \text{P} \longrightarrow \text{PQ} + \text{P}_2$	$k_{3\cdot 01}$	
3·72	$\text{P}_3 + \text{P} \longrightarrow \text{P}_2 + \text{P}_2$	$k_{3\cdot 01}$	
4·01	$\text{Q} + \text{O}_2 \longrightarrow \text{OQ} + \text{O}$	2.9×10^{-12}	3
4·02	$\text{O} + \text{OQ} \longrightarrow \text{O}_2 + \text{Q}$	$1/2 k_{4\cdot 01}$	
4·03	$\text{P} + \text{O}_2 \longrightarrow \text{OP} + \text{O}$	$k_{4\cdot 01}$	
4·04	$\text{O} + \text{OP} \longrightarrow \text{O}_2 + \text{P}$	$1/2 k_{4\cdot 01}$	
4·05	$\text{O} + \text{Q}_2 \longrightarrow \text{OQ} + \text{Q}$	$k_{4\cdot 01}$	
4·06	$\text{Q} + \text{OQ} \longrightarrow \text{Q}_2 + \text{O}$	$1/2 k_{4\cdot 01}$	
4·07	$\text{P} + \text{OQ} \longrightarrow \text{PQ} + \text{O}$	$1/2 k_{4\cdot 01}$	
4·08	$\text{P} + \text{OQ} \longrightarrow \text{OP} + \text{Q}$	$1/2 k_{4\cdot 01}$	
4·09	$\text{O} + \text{PQ} \longrightarrow \text{OP} + \text{Q}$	$1/2 k_{4\cdot 01}$	
4·10	$\text{O} + \text{PQ} \longrightarrow \text{OQ} + \text{P}$	$1/2 k_{4\cdot 01}$	
4·11	$\text{Q} + \text{OP} \longrightarrow \text{OQ} + \text{P}$	$1/2 k_{4\cdot 01}$	
4·12	$\text{Q} + \text{OP} \longrightarrow \text{PQ} + \text{O}$	$1/2 k_{4\cdot 01}$	

Table B.4: continued

#	Reaction	Rate coefficient ($\text{s}^{-1}, \text{cm}^3 \text{s}^{-1}$)	Note
4 · 13	$\text{O} + \text{P}_2 \longrightarrow \text{OP} + \text{P}$	$k_{4.01}$	
4 · 14	$\text{P} + \text{OP} \longrightarrow \text{P}_2 + \text{O}$	$1/2 k_{4.01}$	
4 · 15	$\text{P} + \text{Q}_2 \longrightarrow \text{PQ} + \text{Q}$	$k_{4.01}$	
4 · 16	$\text{Q} + \text{PQ} \longrightarrow \text{Q}_2 + \text{P}$	$1/2 k_{4.01}$	
4 · 17	$\text{Q} + \text{P}_2 \longrightarrow \text{PQ} + \text{P}$	$k_{4.01}$	
4 · 18	$\text{P} + \text{PQ} \longrightarrow \text{P}_2 + \text{Q}$	$1/2 k_{4.01}$	

1 See Ref [150].

2 See section 6.3.

3 See Ref. [186] and [187].

B.2 Statistical model restricted to singly substituted species

The following tables give an overview on the reaction system used for the photolysis of pure ozone. It assumes statistical rate coefficients and considers only reactions which contain at most one heavy isotope. As before, we employ the shorthand notation $O = {}^{16}O$, $P = {}^{17}O$, and $Q = {}^{18}O$.

Table B.5: Species by molecular size.

# of atoms	# of species	species
1	3	O, P, Q
2	3	O ₂ , OP, OQ
3	5	O ₂ P, O ₂ Q, O ₃ , OPO, OQO

Table B.6: Molecules by number of isotope substitutions

# of substitutions	# of molecules	list of molecules
0	3	O, O ₂ , O ₃
1	8	O ₂ P, O ₂ Q, OP, OPO, OQ, OQO, P, Q

Table B.7: List of main reactions.

#	# of variants	reaction type
1	7	$O + O_2 \longrightarrow O_3$
2	7	$O_3 + h\nu \longrightarrow O_2 + O$
3	7	$O_3 + O \longrightarrow O_2 + O_2$
4	4	$Q + O_2 \longrightarrow OQ + O$

Table B.8: Complete list of all reactions.

#	Reaction		Rate coefficient ($\text{s}^{-1}, \text{cm}^3 \text{s}^{-1}$)
1.01	$\text{O} + \text{O}_2$	$\longrightarrow \text{O}_3$	$[\text{M}] 6.0 \times 10^{-34} (300 \text{ K}/T)^{-2.4}$
1.02	$\text{Q} + \text{O}_2$	$\longrightarrow \text{O}_2\text{Q}$	$k_{1.01}$
1.03	$\text{O} + \text{OQ}$	$\longrightarrow \text{O}_2\text{Q}$	$1/2 k_{1.01}$
1.04	$\text{O} + \text{OQ}$	$\longrightarrow \text{OQO}$	$1/2 k_{1.01}$
1.05	$\text{P} + \text{O}_2$	$\longrightarrow \text{O}_2\text{P}$	$k_{1.01}$
1.06	$\text{O} + \text{OP}$	$\longrightarrow \text{O}_2\text{P}$	$1/2 k_{1.01}$
1.07	$\text{O} + \text{OP}$	$\longrightarrow \text{OPO}$	$1/2 k_{1.01}$
2.01	$\text{O}_3 + h\nu$	$\longrightarrow \text{O}_2 + \text{O}$	$J_1 = 2.65 \times 10^{-4}$
2.02	$\text{O}_2\text{Q} + h\nu$	$\longrightarrow \text{O}_2 + \text{Q}$	$1/2 k_{2.01}$
2.03	$\text{O}_2\text{Q} + h\nu$	$\longrightarrow \text{OQ} + \text{O}$	$1/2 k_{2.01}$
2.04	$\text{OQO} + h\nu$	$\longrightarrow \text{OQ} + \text{O}$	$k_{2.01}$
2.05	$\text{O}_2\text{P} + h\nu$	$\longrightarrow \text{O}_2 + \text{P}$	$1/2 k_{2.01}$
2.06	$\text{O}_2\text{P} + h\nu$	$\longrightarrow \text{OP} + \text{O}$	$1/2 k_{2.01}$
2.07	$\text{OPO} + h\nu$	$\longrightarrow \text{OP} + \text{O}$	$k_{2.01}$
3.01	$\text{O}_3 + \text{O}$	$\longrightarrow \text{O}_2 + \text{O}_2$	$8.0 \times 10^{-12} \exp(-2060.0 \text{ K}/T)$
3.02	$\text{O}_3 + \text{Q}$	$\longrightarrow \text{OQ} + \text{O}_2$	$k_{3.01}$
3.03	$\text{O}_2\text{Q} + \text{O}$	$\longrightarrow \text{OQ} + \text{O}_2$	$k_{3.01}$
3.04	$\text{OQO} + \text{O}$	$\longrightarrow \text{OQ} + \text{O}_2$	$k_{3.01}$
3.05	$\text{O}_3 + \text{P}$	$\longrightarrow \text{OP} + \text{O}_2$	$k_{3.01}$
3.06	$\text{O}_2\text{P} + \text{O}$	$\longrightarrow \text{OP} + \text{O}_2$	$k_{3.01}$
3.07	$\text{OPO} + \text{O}$	$\longrightarrow \text{OP} + \text{O}_2$	$k_{3.01}$
4.01	$\text{Q} + \text{O}_2$	$\longrightarrow \text{OQ} + \text{O}$	2.9×10^{-12}
4.02	$\text{O} + \text{OQ}$	$\longrightarrow \text{O}_2 + \text{Q}$	$1/2 k_{4.01}$
4.03	$\text{P} + \text{O}_2$	$\longrightarrow \text{OP} + \text{O}$	$k_{4.01}$
4.04	$\text{O} + \text{OP}$	$\longrightarrow \text{O}_2 + \text{P}$	$1/2 k_{4.01}$

Appendix C

Reaction Schemes for the CCAR Experiments

Table C.1: Chemical Model for the O₃+CO experiments at CCAR.

#	Reaction	Rate coefficient (s ⁻¹ , cm ³ s ⁻¹)	Note
01	O ₃ + hν → O + O ₂	J ₁	1
02	O ₃ + hν → O(¹ D) + O ₂	J ₂	2
03	O + O ₂ → O ₃	6.00 · 10 ⁻³⁴ (300 K/T) ^{2.4} [M]	3
04	O ₃ + O → O ₂ + O ₂	8.00 · 10 ⁻¹² exp(-2060.0 K/T)	
05	O(¹ D) + O ₂ → O + O ₂	3.30 · 10 ⁻¹¹ exp(55.0 K/T)	
06	O(¹ D) + O ₃ → O ₂ + O ₂	1.20 · 10 ⁻¹⁰	
07	O(¹ D) + O ₃ → O ₂ + O + O	1.20 · 10 ⁻¹⁰	
08	O(¹ D) + H ₂ → OH + H	1.20 · 10 ⁻¹⁰	
09	O(¹ D) + H ₂ O → OH + OH	1.63 · 10 ⁻¹⁰ exp(60.0 K/T)	
10	O(¹ D) + N ₂ → O + N ₂	2.15 · 10 ⁻¹¹ exp(110 K/T)	
11	O(¹ D) + CO ₂ → O + CO ₂	7.50 · 10 ⁻¹¹ exp(115 K/T)	
12	O(¹ D) + H ₂ O ₂ → O + 2OH	(5.20 · 10 ⁻¹⁰)/2	4
13	O(¹ D) + H ₂ O ₂ → OH + HO ₂	(5.20 · 10 ⁻¹⁰)/2	4
14	O(¹ D) + CO → CO + O	2.15 · 10 ⁻¹¹ exp(110 K/T)	3
15	O + OH → O ₂ + H	1.80 · 10 ⁻¹¹ exp(180 K/T)	
16	O + HO ₂ → OH + O ₂	3.00 · 10 ⁻¹¹ exp(200 K/T)	
17	O + H ₂ O ₂ → OH + HO ₂	1.40 · 10 ⁻¹² exp(-2000 K/T)	
18	H + O ₂ → HO ₂	k ₀ = 4.40 · 10 ⁻³² (300 K/T) ^{1.3} k _∞ = 7.50 · 10 ⁻¹¹ (300 K/T) ^{-0.2}	3, 5
19	H + O ₃ → OH + O ₂	1.40 · 10 ⁻¹⁰ exp(-470 K/T)	3
20	H + HO ₂ → OH + OH	7.20 · 10 ⁻¹¹	
21	H + HO ₂ → O + H ₂ O	1.60 · 10 ⁻¹²	
22	H + HO ₂ → H ₂ + O ₂	6.90 · 10 ⁻¹²	
23	OH + O ₃ → HO ₂ + O ₂	1.70 · 10 ⁻¹² exp(-940 K/T)	
24	OH + H ₂ → H ₂ O + H	2.80 · 10 ⁻¹² exp(-1800 K/T)	
25	OH + OH → H ₂ O + O	1.80 · 10 ⁻¹²	
26	OH + OH → H ₂ O ₂	k ₀ = 6.90 · 10 ⁻³¹ (300 K/T) k _∞ = 2.60 · 10 ⁻¹¹	3, 5
27	OH + HO ₂ → H ₂ O + O ₂	4.80 · 10 ⁻¹¹ exp(250 K/T)	3
28	OH + H ₂ O ₂ → H ₂ O + HO ₂	1.80 · 10 ⁻¹²	
29	HO ₂ + O ₃ → OH + O ₂ + O ₂	1.00 · 10 ⁻¹⁴ exp(-490 K/T)	
30	HO ₂ + HO ₂ → H ₂ O ₂ + O ₂	3.00 · 10 ⁻¹³ exp(460 K/T) + 2.10 · 10 ⁻³³ exp(920 K/T) [M]	6

Table C.1: Chemical Model for the O₃+CO experiments at CCAR.

#	Reaction	Rate coefficient (s ⁻¹ , cm ³ s ⁻¹)	Note
31	OH + CO → HOCO	$k_0 = 5.90 \cdot 10^{-33} (300 \text{ K}/T)^{1.4}$	7
32	OH + CO → H + CO ₂	$k_\infty = 1.10 \cdot 10^{-12} (300 \text{ K}/T)^{-1.3}$ $k_0 = 1.50 \cdot 10^{-13} (300 \text{ K}/T)^{-0.6}$	7
33	HOCO + O ₃ → OH + O ₂ + CO ₂	$k_\infty = 2.10 \cdot 10^9 (300 \text{ K}/T)^{-6.1}$	3
34	HOCO + O ₂ → HO ₂ + CO ₂	$1.44 \cdot 10^{-11}$	
35	HOCO + O → OH + CO ₂	$2.00 \cdot 10^{-12}$	
36	O + CO → CO ₂	$1.44 \cdot 10^{-11}$ $3.67 \cdot 10^{-33} \exp(-2184 \text{ K}/T)[\text{M}]$	8

1 $J_1 = 1.5 - 6.5 \times 10^{-5}$, value adjusted in the model for each run to obtain the observed amount of unreacted ozone. See section 6.4.1.

2 $J_2 = 2 \times 10^{-7} J_1$ or $J_2 = 1 \times 10^{-6} J_1$ (upper limit). See chapter 5.

3 See Ref.[150].

4 Rate coefficient value is taken from Ref.[188]. In this study the absolute rate for the reaction O(¹D) + H₂O₂ was determined by measuring the attenuation of excited state oxygen atoms. Since the products of the reaction were not detected and no information is available concerning the rate coefficients of the two individual channels 15 and 16, we assume that reaction O(¹D) + H₂O₂ proceeds with probability of 50% via channel 15 and 50% via channel 16.

5 Rate coefficient is calculated using the expression

$$k_f([\text{M}], T) = \left(\frac{k_0(T)[\text{M}]}{1 + \frac{k_0(T)[\text{M}]}{k_\infty(T)}} \right) 0.6^{\frac{1}{1 + \left[\log_{10} \left(\frac{k_0(T)[\text{M}]}{k_\infty(T)} \right) \right]^2}} \quad (\text{C.1})$$

introduced in section 6.2. k_0 and k_∞ values are from Ref.[150].

6 Rate coefficient calculated as the sum of the pressure-independent bimolecular component and the pressure-dependent component. See note B13 in Ref.[150].

7 The OH + CO reaction can proceed via channels 33 and 34. In the former case (association to yield HOCO) the rate coefficient is calculated using C.1, in the latter (chemical activation process to H and CO₂) it is calculated using the expression introduced in Ref.[150]

$$k_f^{ca}([\text{M}], T) = \left(\frac{k_0(T)}{1 + \frac{k_0(T)}{k_\infty(T)/[\text{M}]}} \right) 0.6^{\frac{1}{1 + \left[\log_{10} \left(\frac{k_0(T)}{k_\infty(T)/[\text{M}]} \right) \right]^2}} \quad (\text{C.2})$$

where k_0 and k_∞ values are from Ref.[150]. See note D1 in ref.[150].

8 See section 6.4.1.

Appendix D

Reaction Schemes for the PB06 Experiments

Table D.1: Species by molecular size

# of atoms	# of species	species
1	7	H, O, O(¹ D), P, P(¹ D), Q, Q(¹ D)
2	11	CO, CP, CQ, H ₂ , N ₂ , O ₂ , OH, OP, OQ, PH, QH
3	16	CO ₂ , COP, COQ, H ₂ O, H ₂ P, H ₂ Q, HO ₂ , HOP, HOQ, HPO, HQO, O ₂ P, O ₂ Q, O ₃ , OPO, OQO
4	8	H ₂ O ₂ , H ₂ OP, H ₂ OQ, HOCO, HOCP, HOCQ, HPCO, HQCO

Table D.2: Molecules by number of isotope substitutions

# of substitutions	# of molecules	list of molecules
0	14	CO, CO ₂ , H, H ₂ , H ₂ O, H ₂ O ₂ , HO ₂ , HOCO, N ₂ , O, O(¹ D), O ₂ , O ₃ , OH
1	28	COP, COQ, CP, CQ, H ₂ OP, H ₂ OQ, H ₂ P, H ₂ Q, HOCP, HOCQ, HOP, HOQ, HPCO, HPO, HQCO, HQO, O ₂ P, O ₂ Q, OP, OPO, OQ, OQO, P, PH, Q, QH, P(¹ D), Q(¹ D)

Table D.3: List of main reactions

#	# of variants	reaction type
0001	7	$O_3 + h\nu \longrightarrow O_2 + O$
0002	7	$O_3 + h\nu \longrightarrow O_2 + O(^1D)$
0003	7	$O + O_2 \longrightarrow O_3$
0004	7	$O_3 + O \longrightarrow O_2 + O_2$
0005	9	$O(^1D) + O_2 \longrightarrow O + O_2$
0006	7	$O(^1D) + O_3 \longrightarrow O_2 + O_2$
0007	9	$O(^1D) + O_3 \longrightarrow O_2 + O + O$
0008	3	$O(^1D) + H_2 \longrightarrow OH + H$
0009	7	$O(^1D) + H_2O \longrightarrow OH + OH$
0010	3	$O(^1D) + N_2 \longrightarrow O + N_2$
0011	9	$O(^1D) + CO_2 \longrightarrow O + CO_2$
0012	5	$O(^1D) + H_2O_2 \longrightarrow O + OH + OH$
0013	5	$O(^1D) + H_2O_2 \longrightarrow OH + HO_2$
0014	5	$O(^1D) + CO \longrightarrow O + CO$
0015	5	$O + OH \longrightarrow O_2 + H$
0016	7	$O + HO_2 \longrightarrow OH + O_2$
0017	7	$O + H_2O_2 \longrightarrow OH + HO_2$
0018	3	$H + O_2 \longrightarrow HO_2$
0019	7	$H + O_3 \longrightarrow OH + O_2$
0020	5	$H + HO_2 \longrightarrow OH + OH$
0021	9	$H + HO_2 \longrightarrow O + H_2O$
0022	5	$H + HO_2 \longrightarrow H_2 + O_2$
0023	11	$OH + O_3 \longrightarrow HO_2 + O_2$
0024	3	$OH + H_2 \longrightarrow H_2O + H$
0025	3	$OH + OH \longrightarrow H_2O + O$
0026	3	$OH + OH \longrightarrow H_2O_2$
0027	7	$OH + HO_2 \longrightarrow H_2O + O_2$
0028	7	$OH + H_2O_2 \longrightarrow H_2O + HO_2$
0029	12	$HO_2 + O_3 \longrightarrow OH + O_2 + O_2$
0030	9	$HO_2 + HO_2 \longrightarrow H_2O_2 + O_2$
0031	5	$OH + CO \longrightarrow HOCO$
0032	5	$OH + CO \longrightarrow H + CO_2$
0033	11	$HOCO + O_3 \longrightarrow OH + O_2 + CO_2$
0034	9	$HOCO + O_2 \longrightarrow HO_2 + CO_2$
0035	7	$HOCO + O \longrightarrow OH + CO_2$
0036	5	$O + CO \longrightarrow CO_2$
0037	4	$Q + O_2 \longrightarrow OQ + O$
0038	4	$Q + CO \longrightarrow CQ + O$

Table D.4: Chemical Model for the PB06 experiments.

#	Reaction	Rate coefficient (s^{-1} , $\text{cm}^3 \text{s}^{-1}$)	Note
001 · 001	$\text{O}_3 + h\nu \longrightarrow \text{O}_2 + \text{O}$	J_1	1
001 · 002	$\text{O}_2\text{Q} + h\nu \longrightarrow \text{O}_2 + \text{Q}$	$0.99 \cdot (1/2) \cdot k_{001-001}$	
001 · 003	$\text{O}_2\text{Q} + h\nu \longrightarrow \text{OQ} + \text{O}$	$1.01 \cdot (1/2) \cdot k_{001-001}$	
001 · 004	$\text{OQO} + h\nu \longrightarrow \text{OQ} + \text{O}$	$k_{001-001}$	
001 · 005	$\text{O}_2\text{P} + h\nu \longrightarrow \text{O}_2 + \text{P}$	$0.995 \cdot (1/2) \cdot k_{001-001}$	
001 · 006	$\text{O}_2\text{P} + h\nu \longrightarrow \text{OP} + \text{O}$	$1.005 \cdot (1/2) \cdot k_{001-001}$	
001 · 007	$\text{OPO} + h\nu \longrightarrow \text{OP} + \text{O}$	$k_{001-001}$	
002 · 001	$\text{O}_3 + h\nu \longrightarrow \text{O}_2 + \text{O}({}^1\text{D})$	J_2	2
002 · 002	$\text{O}_2\text{Q} + h\nu \longrightarrow \text{O}_2 + \text{Q}({}^1\text{D})$	$0.94 \cdot (1/2) \cdot k_{002-001}$	
002 · 003	$\text{O}_2\text{Q} + h\nu \longrightarrow \text{OQ} + \text{O}({}^1\text{D})$	$1.06 \cdot (1/2) \cdot k_{002-001}$	
002 · 004	$\text{OQO} + h\nu \longrightarrow \text{OQ} + \text{O}({}^1\text{D})$	$0.972 k_{002-001}$	
002 · 005	$\text{O}_2\text{P} + h\nu \longrightarrow \text{O}_2 + \text{P}({}^1\text{D})$	$0.97 \cdot (1/2) \cdot k_{002-001}$	
002 · 006	$\text{O}_2\text{P} + h\nu \longrightarrow \text{OP} + \text{O}({}^1\text{D})$	$1.03 \cdot (1/2) \cdot k_{002-001}$	
002 · 007	$\text{OPO} + h\nu \longrightarrow \text{OP} + \text{O}({}^1\text{D})$	$k_{002-001}$	
003 · 001	$\text{O} + \text{O}_2 \longrightarrow \text{O}_3$	$6.00 \cdot 10^{-34} (300 \text{ K}/T)^{2.4} [\text{M}]$	3
003 · 002	$\text{Q} + \text{O}_2 \longrightarrow \text{O}_2\text{Q}$	$0.92 k_{003-001}$	
003 · 003	$\text{O} + \text{OQ} \longrightarrow \text{O}_2\text{Q}$	$0.725 k_{003-001}$	
003 · 004	$\text{O} + \text{OQ} \longrightarrow \text{OQO}$	$1/2 k_{003-001}$	
003 · 005	$\text{P} + \text{O}_2 \longrightarrow \text{O}_2\text{P}$	$1.03 k_{003-001}$	
003 · 006	$\text{O} + \text{OP} \longrightarrow \text{O}_2\text{P}$	$0.66 k_{003-001}$	
003 · 007	$\text{O} + \text{OP} \longrightarrow \text{OPO}$	$1/2 k_{003-001}$	
004 · 001	$\text{O}_3 + \text{O} \longrightarrow \text{O}_2 + \text{O}_2$	$8.0 \cdot 10^{-12} \exp(-2060.0 \text{ K}/T)$	
004 · 002	$\text{O}_3 + \text{Q} \longrightarrow \text{OQ} + \text{O}_2$	$k_{004-001}$	
004 · 003	$\text{O}_2\text{Q} + \text{O} \longrightarrow \text{OQ} + \text{O}_2$	$k_{004-001}$	
004 · 004	$\text{OQO} + \text{O} \longrightarrow \text{OQ} + \text{O}_2$	$k_{004-001}$	
004 · 005	$\text{O}_3 + \text{P} \longrightarrow \text{OP} + \text{O}_2$	$k_{004-001}$	
004 · 006	$\text{O}_2\text{P} + \text{O} \longrightarrow \text{OP} + \text{O}_2$	$k_{004-001}$	
004 · 007	$\text{OPO} + \text{O} \longrightarrow \text{OP} + \text{O}_2$	$k_{004-001}$	
005 · 001	$\text{O}({}^1\text{D}) + \text{O}_2 \longrightarrow \text{O} + \text{O}_2$	$3.30 \cdot 10^{-11} \exp(55.0 \text{ K}/T)$	
005 · 002	$\text{O}({}^1\text{D}) + \text{OQ} \longrightarrow \text{Q} + \text{O}_2$	$1/3 k_{005-001}$	
005 · 003	$\text{O}({}^1\text{D}) + \text{OQ} \longrightarrow \text{O} + \text{OQ}$	$2/3 k_{005-001}$	
005 · 004	$\text{Q}({}^1\text{D}) + \text{O}_2 \longrightarrow \text{Q} + \text{O}_2$	$1/3 k_{005-001}$	
005 · 005	$\text{Q}({}^1\text{D}) + \text{O}_2 \longrightarrow \text{O} + \text{OQ}$	$2/3 k_{005-001}$	
005 · 006	$\text{O}({}^1\text{D}) + \text{OP} \longrightarrow \text{P} + \text{O}_2$	$1/3 k_{005-001}$	
005 · 007	$\text{O}({}^1\text{D}) + \text{OP} \longrightarrow \text{O} + \text{OP}$	$2/3 k_{005-001}$	
005 · 008	$\text{P}({}^1\text{D}) + \text{O}_2 \longrightarrow \text{P} + \text{O}_2$	$1/3 k_{005-001}$	
005 · 009	$\text{P}({}^1\text{D}) + \text{O}_2 \longrightarrow \text{O} + \text{OP}$	$2/3 k_{005-001}$	
006 · 001	$\text{O}({}^1\text{D}) + \text{O}_3 \longrightarrow \text{O}_2 + \text{O}_2$	$1.2 \cdot 10^{-10}$	
006 · 002	$\text{O}({}^1\text{D}) + \text{O}_2\text{Q} \longrightarrow \text{OQ} + \text{O}_2$	$k_{006-001}$	
006 · 003	$\text{O}({}^1\text{D}) + \text{OQO} \longrightarrow \text{OQ} + \text{O}_2$	$k_{006-001}$	
006 · 004	$\text{Q}({}^1\text{D}) + \text{O}_3 \longrightarrow \text{OQ} + \text{O}_2$	$k_{006-001}$	
006 · 005	$\text{O}({}^1\text{D}) + \text{O}_2\text{P} \longrightarrow \text{OP} + \text{O}_2$	$k_{006-001}$	
006 · 006	$\text{O}({}^1\text{D}) + \text{OPO} \longrightarrow \text{OP} + \text{O}_2$	$k_{006-001}$	
006 · 007	$\text{P}({}^1\text{D}) + \text{O}_3 \longrightarrow \text{OP} + \text{O}_2$	$k_{006-001}$	
007 · 001	$\text{O}({}^1\text{D}) + \text{O}_3 \longrightarrow \text{O}_2 + \text{O} + \text{O}$	$1.2 \cdot 10^{-10}$	3
007 · 002	$\text{O}({}^1\text{D}) + \text{O}_2\text{Q} \longrightarrow \text{OQ} + \text{O} + \text{O}$	$1/2 k_{007-001}$	
007 · 003	$\text{O}({}^1\text{D}) + \text{O}_2\text{Q} \longrightarrow \text{O}_2 + \text{Q} + \text{O}$	$1/2 k_{007-001}$	
007 · 004	$\text{O}({}^1\text{D}) + \text{OQO} \longrightarrow \text{OQ} + \text{O} + \text{O}$	$k_{007-001}$	
007 · 005	$\text{Q}({}^1\text{D}) + \text{O}_3 \longrightarrow \text{O}_2 + \text{Q} + \text{O}$	$k_{007-001}$	
007 · 006	$\text{O}({}^1\text{D}) + \text{O}_2\text{P} \longrightarrow \text{OP} + \text{O} + \text{O}$	$1/2 k_{007-001}$	

Table D.4: Chemical Model for the PB06 experiments.

#	Reaction	Rate coefficient ($\text{s}^{-1}, \text{cm}^3 \text{s}^{-1}$)	Note
007 · 007	$\text{O}(^1\text{D}) + \text{O}_2\text{P} \longrightarrow \text{O}_2 + \text{P} + \text{O}$	$1/2 k_{007 \cdot 001}$	
007 · 008	$\text{O}(^1\text{D}) + \text{OPO} \longrightarrow \text{OP} + \text{O} + \text{O}$	$k_{007 \cdot 001}$	
007 · 009	$\text{P}(^1\text{D}) + \text{O}_3 \longrightarrow \text{O}_2 + \text{P} + \text{O}$	$k_{007 \cdot 001}$	
008 · 001	$\text{O}(^1\text{D}) + \text{H}_2 \longrightarrow \text{OH} + \text{H}$	$1.20 \cdot 10^{-10}$	
008 · 002	$\text{Q}(^1\text{D}) + \text{H}_2 \longrightarrow \text{QH} + \text{H}$	$k_{008 \cdot 001}$	
008 · 003	$\text{P}(^1\text{D}) + \text{H}_2 \longrightarrow \text{PH} + \text{H}_2$	$k_{008 \cdot 001}$	
009 · 001	$\text{O}(^1\text{D}) + \text{H}_2\text{O} \longrightarrow \text{OH} + \text{OH}$	$1.63 \cdot 10^{-10} \exp(60.0 \text{ K}/T)$	
009 · 002	$\text{Q}(^1\text{D}) + \text{H}_2\text{O} \longrightarrow \text{QH} + \text{OH}$	$k_{009 \cdot 001}$	
009 · 003	$\text{O}(^1\text{D}) + \text{H}_2\text{Q} \longrightarrow \text{QH} + \text{OH}$	$k_{009 \cdot 001}$	
009 · 004	$\text{Q}(^1\text{D}) + \text{H}_2\text{Q} \longrightarrow \text{QH} + \text{QH}$	$k_{009 \cdot 001}$	
009 · 005	$\text{P}(^1\text{D}) + \text{H}_2\text{O} \longrightarrow \text{PH} + \text{OH}$	$k_{009 \cdot 001}$	
009 · 006	$\text{O}(^1\text{D}) + \text{H}_2\text{P} \longrightarrow \text{PH} + \text{OH}$	$k_{009 \cdot 001}$	
009 · 007	$\text{P}(^1\text{D}) + \text{H}_2\text{P} \longrightarrow \text{PH} + \text{PH}$	$k_{009 \cdot 001}$	
010 · 001	$\text{O}(^1\text{D}) + \text{N}_2 \longrightarrow \text{O} + \text{N}_2$	$2.15 \cdot 10^{-11} \exp(110 \text{ K}/T)$	
010 · 002	$\text{Q}(^1\text{D}) + \text{N}_2 \longrightarrow \text{Q} + \text{N}_2$	$k_{010 \cdot 001}$	
010 · 003	$\text{P}(^1\text{D}) + \text{N}_2 \longrightarrow \text{P} + \text{N}_2$	$k_{010 \cdot 001}$	
011 · 001	$\text{O}(^1\text{D}) + \text{CO}_2 \longrightarrow \text{O} + \text{CO}_2$	$7.50 \cdot 10^{-11} \exp(115 \text{ K}/T)$	
011 · 002	$\text{O}(^1\text{D}) + \text{COQ} \longrightarrow \text{Q} + \text{CO}_2$	$1/3 k_{011 \cdot 001}$	
011 · 003	$\text{O}(^1\text{D}) + \text{COQ} \longrightarrow \text{O} + \text{COQ}$	$2/3 k_{011 \cdot 001}$	
011 · 004	$\text{Q}(^1\text{D}) + \text{CO}_2 \longrightarrow \text{Q} + \text{CO}_2$	$1/3 k_{011 \cdot 001}$	
011 · 005	$\text{Q}(^1\text{D}) + \text{CO}_2 \longrightarrow \text{O} + \text{COQ}$	$2/3 k_{011 \cdot 001}$	
011 · 006	$\text{O}(^1\text{D}) + \text{COP} \longrightarrow \text{P} + \text{CO}_2$	$1/3 k_{011 \cdot 001}$	
011 · 007	$\text{O}(^1\text{D}) + \text{COP} \longrightarrow \text{O} + \text{COP}$	$2/3 k_{011 \cdot 001}$	
011 · 008	$\text{P}(^1\text{D}) + \text{CO}_2 \longrightarrow \text{P} + \text{CO}_2$	$1/3 k_{011 \cdot 001}$	
011 · 009	$\text{P}(^1\text{D}) + \text{CO}_2 \longrightarrow \text{O} + \text{COP}$	$2/3 k_{011 \cdot 001}$	
012 · 001	$\text{O}(^1\text{D}) + \text{H}_2\text{O}_2 \longrightarrow \text{O} + \text{OH} + \text{OH}$	$(5.2 \cdot 10^{-10})/2$	4
012 · 002	$\text{O}(^1\text{D}) + \text{H}_2\text{OQ} \longrightarrow \text{O} + \text{QH} + \text{OH}$	$k_{012 \cdot 001}$	
012 · 003	$\text{Q}(^1\text{D}) + \text{H}_2\text{O}_2 \longrightarrow \text{Q} + \text{OH} + \text{OH}$	$k_{012 \cdot 001}$	
012 · 004	$\text{O}(^1\text{D}) + \text{H}_2\text{OP} \longrightarrow \text{O} + \text{PH} + \text{OH}$	$k_{012 \cdot 001}$	
012 · 005	$\text{P}(^1\text{D}) + \text{H}_2\text{O}_2 \longrightarrow \text{P} + \text{OH} + \text{OH}$	$k_{012 \cdot 001}$	
013 · 001	$\text{O}(^1\text{D}) + \text{H}_2\text{O}_2 \longrightarrow \text{OH} + \text{HO}_2$	$(5.2 \cdot 10^{-10})/2$	4
013 · 002	$\text{Q}(^1\text{D}) + \text{H}_2\text{O}_2 \longrightarrow \text{QH} + \text{HO}_2$	$k_{013 \cdot 001}$	
013 · 003	$\text{O}(^1\text{D}) + \text{H}_2\text{OQ} \longrightarrow \text{OH} + \text{HOQ}$	$k_{013 \cdot 001}$	
013 · 004	$\text{P}(^1\text{D}) + \text{H}_2\text{O}_2 \longrightarrow \text{PH} + \text{HO}_2$	$k_{013 \cdot 001}$	
013 · 005	$\text{O}(^1\text{D}) + \text{H}_2\text{OP} \longrightarrow \text{OH} + \text{HOP}$	$k_{013 \cdot 001}$	
014 · 001	$\text{O}(^1\text{D}) + \text{CO} \longrightarrow \text{O} + \text{CO}$	$2.15 \cdot 10^{-11} \exp(110 \text{ K}/T)$	3
014 · 002	$\text{Q}(^1\text{D}) + \text{CO} \longrightarrow \text{Q} + \text{CO}$	$k_{014 \cdot 001}$	
014 · 003	$\text{O}(^1\text{D}) + \text{CQ} \longrightarrow \text{O} + \text{CQ}$	$k_{014 \cdot 001}$	3
014 · 004	$\text{P}(^1\text{D}) + \text{CO} \longrightarrow \text{P} + \text{CO}$	$k_{014 \cdot 001}$	
014 · 005	$\text{O}(^1\text{D}) + \text{CP} \longrightarrow \text{O} + \text{CP}$	$k_{014 \cdot 001}$	
015 · 001	$\text{O} + \text{OH} \longrightarrow \text{O}_2 + \text{H}$	$1.8 \cdot 10^{-11} \exp(180 \text{ K}/T)$	
015 · 002	$\text{Q} + \text{OH} \longrightarrow \text{OQ} + \text{H}$	$k_{015 \cdot 001}$	
015 · 003	$\text{O} + \text{QH} \longrightarrow \text{OQ} + \text{H}$	$k_{015 \cdot 001}$	
015 · 004	$\text{P} + \text{OH} \longrightarrow \text{OP} + \text{H}$	$k_{015 \cdot 001}$	
015 · 005	$\text{O} + \text{PH} \longrightarrow \text{OP} + \text{H}$	$k_{015 \cdot 001}$	
016 · 001	$\text{O} + \text{HO}_2 \longrightarrow \text{OH} + \text{O}_2$	$3.0 \cdot 10^{-11} \exp(200 \text{ K}/T)$	
016 · 002	$\text{Q} + \text{HO}_2 \longrightarrow \text{QH} + \text{O}_2$	$k_{016 \cdot 001}$	
016 · 003	$\text{O} + \text{HOQ} \longrightarrow \text{QH} + \text{O}_2$	$k_{016 \cdot 001}$	
016 · 004	$\text{O} + \text{HQO} \longrightarrow \text{OH} + \text{OQ}$	$k_{016 \cdot 001}$	

Table D.4: Chemical Model for the PB06 experiments.

#	Reaction	Rate coefficient (s^{-1} , $\text{cm}^3 \text{s}^{-1}$)	Note
016 · 005	$\text{P} + \text{HO}_2 \longrightarrow \text{PH} + \text{O}_2$	$k_{016-001}$	
016 · 006	$\text{O} + \text{HOP} \longrightarrow \text{PH} + \text{O}_2$	$k_{016-001}$	
016 · 007	$\text{O} + \text{HPO} \longrightarrow \text{OH} + \text{OP}$	$k_{016-001}$	
017 · 001	$\text{O} + \text{H}_2\text{O}_2 \longrightarrow \text{OH} + \text{HO}_2$	$1.4 \cdot 10^{-12} \exp(-2000 \text{ K}/T)$	
017 · 002	$\text{Q} + \text{H}_2\text{O}_2 \longrightarrow \text{QH} + \text{HO}_2$	$k_{017-001}$	
017 · 003	$\text{O} + \text{H}_2\text{OQ} \longrightarrow \text{OH} + \text{HOQ}$	$1/2 k_{017-001}$	
017 · 004	$\text{O} + \text{H}_2\text{OQ} \longrightarrow \text{OH} + \text{HQO}$	$1/2 k_{017-001}$	
017 · 005	$\text{P} + \text{H}_2\text{O}_2 \longrightarrow \text{PH} + \text{HO}_2$	$k_{017-001}$	
017 · 006	$\text{O} + \text{H}_2\text{OP} \longrightarrow \text{OH} + \text{HOP}$	$1/2 k_{017-001}$	
017 · 007	$\text{O} + \text{H}_2\text{OP} \longrightarrow \text{OH} + \text{HPO}$	$1/2 k_{017-001}$	
018 · 001	$\text{H} + \text{O}_2 \longrightarrow \text{HO}_2$	$k_0 = 4.40 \cdot 10^{-32} (300 \text{ K}/T)^{1.3}$ $k_\infty = 7.50 \cdot 10^{-11} (300 \text{ K}/T)^{-0.2}$	3, 5
018 · 002	$\text{H} + \text{OQ} \longrightarrow \text{HOQ}$	$k_{018-001}$	
018 · 003	$\text{H} + \text{OP} \longrightarrow \text{HOP}$	$k_{018-001}$	
019 · 001	$\text{H} + \text{O}_3 \longrightarrow \text{OH} + \text{O}_2$	$1.4 \cdot 10^{-10} \exp(-470 \text{ K}/T)$	3
019 · 002	$\text{H} + \text{O}_2\text{Q} \longrightarrow \text{QH} + \text{O}_2$	$1/2 k_{019-001}$	
019 · 003	$\text{H} + \text{O}_2\text{Q} \longrightarrow \text{OH} + \text{OQ}$	$1/2 k_{019-001}$	
019 · 004	$\text{H} + \text{OQO} \longrightarrow \text{OH} + \text{OQ}$	$k_{019-001}$	
019 · 005	$\text{H} + \text{O}_2\text{P} \longrightarrow \text{PH} + \text{O}_2$	$1/2 k_{019-001}$	
019 · 006	$\text{H} + \text{O}_2\text{P} \longrightarrow \text{OH} + \text{OP}$	$1/2 k_{019-001}$	
019 · 007	$\text{H} + \text{OPO} \longrightarrow \text{OH} + \text{OP}$	$k_{019-001}$	
020 · 001	$\text{H} + \text{HO}_2 \longrightarrow \text{OH} + \text{OH}$	$7.2 \cdot 10^{-11}$	
020 · 002	$\text{H} + \text{HOQ} \longrightarrow \text{QH} + \text{OH}$	$k_{020-001}$	
020 · 003	$\text{H} + \text{HQO} \longrightarrow \text{OH} + \text{QH}$	$k_{020-001}$	
020 · 004	$\text{H} + \text{HOP} \longrightarrow \text{PH} + \text{OH}$	$k_{020-001}$	
020 · 005	$\text{H} + \text{HPO} \longrightarrow \text{OH} + \text{PH}$	$k_{020-001}$	
021 · 001	$\text{H} + \text{HO}_2 \longrightarrow \text{O} + \text{H}_2\text{O}$	$1.6 \cdot 10^{-12}$	
021 · 002	$\text{H} + \text{HOQ} \longrightarrow \text{Q} + \text{H}_2\text{O}$	$1/2 k_{021-001}$	
021 · 003	$\text{H} + \text{HOQ} \longrightarrow \text{O} + \text{H}_2\text{Q}$	$1/2 k_{021-001}$	
021 · 004	$\text{H} + \text{HQO} \longrightarrow \text{Q} + \text{H}_2\text{O}$	$1/2 k_{021-001}$	
021 · 005	$\text{H} + \text{HQO} \longrightarrow \text{O} + \text{H}_2\text{Q}$	$1/2 k_{021-001}$	
021 · 006	$\text{H} + \text{HOP} \longrightarrow \text{P} + \text{H}_2\text{O}$	$1/2 k_{021-001}$	
021 · 007	$\text{H} + \text{HOP} \longrightarrow \text{O} + \text{H}_2\text{P}$	$1/2 k_{021-001}$	
021 · 008	$\text{H} + \text{HPO} \longrightarrow \text{P} + \text{H}_2\text{O}$	$1/2 k_{021-001}$	
021 · 009	$\text{H} + \text{HPO} \longrightarrow \text{O} + \text{H}_2\text{P}$	$1/2 k_{021-001}$	
022 · 001	$\text{H} + \text{HO}_2 \longrightarrow \text{H}_2 + \text{O}_2$	$6.9 \cdot 10^{-12}$	
022 · 002	$\text{H} + \text{HOQ} \longrightarrow \text{H}_2 + \text{OQ}$	$k_{022-001}$	
022 · 003	$\text{H} + \text{HQO} \longrightarrow \text{H}_2 + \text{OQ}$	$k_{022-001}$	
022 · 004	$\text{H} + \text{HOP} \longrightarrow \text{H}_2 + \text{OP}$	$k_{022-001}$	
022 · 005	$\text{H} + \text{HPO} \longrightarrow \text{H}_2 + \text{OP}$	$k_{022-001}$	
023 · 001	$\text{OH} + \text{O}_3 \longrightarrow \text{HO}_2 + \text{O}_2$	$1.7 \cdot 10^{-12} \exp(-940 \text{ K}/T)$	
023 · 002	$\text{QH} + \text{O}_3 \longrightarrow \text{HOQ} + \text{O}_2$	$1/2 k_{023-001}$	
023 · 003	$\text{QH} + \text{O}_3 \longrightarrow \text{HO}_2 + \text{OQ}$	$1/2 k_{023-001}$	
023 · 004	$\text{OH} + \text{O}_2\text{Q} \longrightarrow \text{HOQ} + \text{O}_2$	$1/2 k_{023-001}$	
023 · 005	$\text{OH} + \text{O}_2\text{Q} \longrightarrow \text{HO}_2 + \text{OQ}$	$1/2 k_{023-001}$	
023 · 006	$\text{OH} + \text{OQO} \longrightarrow \text{HO}_2 + \text{OQ}$	$k_{023-001}$	
023 · 007	$\text{PH} + \text{O}_3 \longrightarrow \text{HOP} + \text{O}_2$	$1/2 k_{023-001}$	
023 · 008	$\text{PH} + \text{O}_3 \longrightarrow \text{HO}_2 + \text{OP}$	$1/2 k_{023-001}$	
023 · 009	$\text{OH} + \text{O}_2\text{P} \longrightarrow \text{HOP} + \text{O}_2$	$1/2 k_{023-001}$	
023 · 010	$\text{OH} + \text{O}_2\text{P} \longrightarrow \text{HO}_2 + \text{OP}$	$1/2 k_{023-001}$	
023 · 011	$\text{OH} + \text{OPO} \longrightarrow \text{HO}_2 + \text{OP}$	$k_{023-001}$	
024 · 001	$\text{OH} + \text{H}_2 \longrightarrow \text{H}_2\text{O} + \text{H}$	$2.8 \cdot 10^{-12} \exp(-1800 \text{ K}/T)$	
024 · 002	$\text{QH} + \text{H}_2 \longrightarrow \text{H}_2\text{Q} + \text{H}$	$k_{024-001}$	

Table D.4: Chemical Model for the PB06 experiments.

#	Reaction	Rate coefficient ($\text{s}^{-1}, \text{cm}^3 \text{s}^{-1}$)	Note
024 · 003	PH + H ₂ → H ₂ P + H	$k_{024-001}$	
025 · 001	OH + OH → H ₂ O + O	$1.8 \cdot 10^{-12}$	
025 · 002	QH + OH → H ₂ Q + O	$1/2 k_{025-001}$	
025 · 003	QH + OH → H ₂ O + Q	$1/2 k_{025-001}$	
026 · 001	OH + OH → H ₂ O ₂	$k_0 = 6.90 \cdot 10^{-31} (300 \text{ K}/T)$ $k_\infty = 2.60 \cdot 10^{-11}$	3, 5
026 · 002	QH + OH → H ₂ OQ	$k_{026-001}$	
026 · 003	PH + OH → H ₂ OP	$k_{026-001}$	
027 · 001	OH + HO ₂ → H ₂ O + O ₂	$4.8 \cdot 10^{-11} \exp(250 \text{ K}/T)$	3
027 · 002	QH + HO ₂ → H ₂ Q + O ₂	$k_{027-001}$	
027 · 003	OH + HOQ → H ₂ O + OQ	$k_{027-001}$	
027 · 004	OH + HQO → H ₂ O + OQ	$k_{027-001}$	
027 · 005	PH + HO ₂ → H ₂ P + O ₂	$k_{027-001}$	
027 · 006	OH + HOP → H ₂ O + OP	$k_{027-001}$	
027 · 007	OH + HPO → H ₂ O + OP	$k_{027-001}$	
028 · 001	OH + H ₂ O ₂ → H ₂ O + HO ₂	$1.8 \cdot 10^{-12}$	
028 · 002	QH + H ₂ O ₂ → H ₂ Q + HO ₂	$k_{028-001}$	
028 · 003	OH + H ₂ OQ → H ₂ O + HOQ	$1/2 k_{028-001}$	
028 · 004	OH + H ₂ OQ → H ₂ O + HQO	$1/2 k_{028-001}$	
028 · 005	PH + H ₂ O ₂ → H ₂ P + HO ₂	$k_{028-001}$	
028 · 006	OH + H ₂ OP → H ₂ O + HOP	$1/2 k_{028-001}$	
028 · 007	OH + H ₂ OP → H ₂ O + HPO	$1/2 k_{028-001}$	
029 · 001	HO ₂ + O ₃ → OH + O ₂ + O ₂	$1.0 \cdot 10^{-14} \exp(-490 \text{ K}/T)$	
029 · 002	HOQ + O ₃ → OH + O ₂ + OQ	$k_{029-001}$	
029 · 003	HQO + O ₃ → OH + OQ + O ₂	$k_{029-001}$	
029 · 004	HO ₂ + O ₂ Q → QH + O ₂ + O ₂	$1/2 k_{029-001}$	
029 · 005	HO ₂ + O ₂ Q → OH + OQ + O ₂	$1/2 k_{029-001}$	
029 · 006	HO ₂ + OQO → OH + OQ + O ₂	$k_{029-001}$	
029 · 007	HOP + O ₃ → OH + O ₂ + OP	$k_{029-001}$	
029 · 008	HPO + O ₃ → OH + OP + O ₂	$k_{029-001}$	
029 · 009	HO ₂ + O ₂ P → PH + O ₂ + O ₂	$1/2 k_{029-001}$	
029 · 010	HO ₂ + O ₂ P → OH + OP + O ₂	$1/2 k_{029-001}$	
029 · 011	HO ₂ + OPO → OH + OP + O ₂	$k_{029-001}$	
029 · 012	HO ₂ + OQO → OH + OQ + O ₂	$1/2 k_{029-001}$	
030 · 001	HO ₂ + HO ₂ → H ₂ O ₂ + O ₂	$3.00 \cdot 10^{-13} \exp(460 \text{ K}/T) +$ $2.10 \cdot 10^{-33} \exp(920 \text{ K}/T) [\text{M}]$	6
030 · 002	HOQ + HO ₂ → H ₂ O ₂ + OQ	$3.00 \cdot 10^{-13} \exp(460 \text{ K}/T) +$ $(1/2) 2.10 \cdot 10^{-33} \exp(920 \text{ K}/T) [\text{M}]$	
030 · 003	HOQ + HO ₂ → O ₂ + H ₂ OQ	$k_{030-002}$	
030 · 004	HQO + HO ₂ → H ₂ O ₂ + OQ	$k_{030-002}$	
030 · 005	HQO + HO ₂ → O ₂ + H ₂ OQ	$k_{030-002}$	
030 · 006	HOP + HO ₂ → H ₂ O ₂ + OP	$k_{030-002}$	
030 · 007	HOP + HO ₂ → O ₂ + H ₂ OP	$k_{030-002}$	
030 · 008	HPO + HO ₂ → H ₂ O ₂ + OP	$k_{030-002}$	
030 · 009	HPO + HO ₂ → O ₂ + H ₂ OP	$k_{030-002}$	
031 · 001	OH + CO → HOCO	$k_0 = 5.90 \cdot 10^{-33} (300 \text{ K}/T)^{1.4}$ $k_\infty = 1.10 \cdot 10^{-12} (300 \text{ K}/T)^{-1.3}$	7
031 · 002	QH + CO → HQCO	$k_{031-001}$	
031 · 003	OH + CQ → HOCQ	$k_{031-001}$	
031 · 004	PH + CO → HPCO	$k_{031-001}$	
031 · 005	OH + CP → HOCP	$k_{031-001}$	

Table D.4: Chemical Model for the PB06 experiments.

#	Reaction	Rate coefficient (s^{-1} , $\text{cm}^3 \text{s}^{-1}$)	Note
032 · 001	OH + CO \longrightarrow H + CO ₂	$k_0 = 1.50 \cdot 10^{-13} (300 \text{ K}/T)^{-0.6}$ $k_\infty = 2.10 \cdot 10^9 (300 \text{ K}/T)^{-6.1}$	7
032 · 002	QH + CO \longrightarrow H + COQ	$k_{032-001}$	
032 · 003	OH + CQ \longrightarrow H + COQ	$k_{032-001}$	
032 · 004	PH + CO \longrightarrow H + COP	$k_{032-001}$	
032 · 005	OH + CP \longrightarrow H + COP	$k_{032-001}$	
033 · 001	HOCO + O ₃ \longrightarrow OH + O ₂ + CO ₂	$1.44 \cdot 10^{-11}$	3
033 · 002	HQCO + O ₃ \longrightarrow OH + O ₂ + COQ	$k_{033-001}$	
033 · 003	HOCQ + O ₃ \longrightarrow OH + O ₂ + COQ	$k_{033-001}$	
033 · 004	HOCO + OQO \longrightarrow OH + O ₂ + CO ₂	$k_{033-001}$	
033 · 005	HOCO + O ₂ Q \longrightarrow QH + O ₂ + CO ₂	$1/2 k_{033-001}$	
033 · 006	HOCO + O ₂ Q \longrightarrow OH + OQ + CO ₂	$1/2 k_{033-001}$	
033 · 007	HPCO + O ₃ \longrightarrow OH + O ₂ + COP	$k_{033-001}$	
033 · 008	HOCP + O ₃ \longrightarrow OH + O ₂ + COP	$k_{033-001}$	
033 · 009	HOCO + OPO \longrightarrow OH + O ₂ + CO ₂	$k_{033-001}$	
033 · 010	HOCO + O ₂ P \longrightarrow PH + O ₂ + CO ₂	$1/2 k_{033-001}$	
033 · 011	HOCO + O ₂ P \longrightarrow OH + OP + CO ₂	$1/2 k_{033-001}$	
034 · 001	HOCO + O ₂ \longrightarrow HO ₂ + CO ₂	$2.00 \cdot 10^{-12}$	
034 · 002	HQCO + O ₂ \longrightarrow HO ₂ + COQ	$k_{034-001}$	
034 · 003	HOCQ + O ₂ \longrightarrow HO ₂ + COQ	$k_{034-001}$	
034 · 004	HOCO + OQ \longrightarrow HOQ + CO ₂	$1/2 k_{034-001}$	
034 · 005	HOCO + OQ \longrightarrow HQO + CO ₂	$1/2 k_{034-001}$	
034 · 006	HPCO + O ₂ \longrightarrow HO ₂ + COP	$k_{034-001}$	
034 · 007	HOCP + O ₂ \longrightarrow HO ₂ + COP	$k_{034-001}$	
034 · 008	HOCO + OP \longrightarrow HOP + CO ₂	$1/2 k_{034-001}$	
034 · 009	HOCO + OP \longrightarrow HPO + CO ₂	$1/2 k_{034-001}$	
035 · 001	HOCO + O \longrightarrow OH + CO ₂	$1.44 \cdot 10^{-11}$	
035 · 002	HQCO + O \longrightarrow OH + COQ	$k_{035-001}$	
035 · 003	HOCQ + O \longrightarrow OH + COQ	$k_{035-001}$	
035 · 004	HOCO + Q \longrightarrow QH + CO ₂	$k_{035-001}$	
035 · 005	HPCO + O \longrightarrow OH + COP	$k_{035-001}$	
035 · 006	HOCP + O \longrightarrow OH + COP	$k_{035-001}$	
035 · 007	HOCO + P \longrightarrow PH + CO ₂	$k_{035-001}$	
036 · 001	O + CO \longrightarrow CO ₂	$4.3 \cdot 10^{-36} \text{ [M]}$	8
036 · 002	Q + CO \longrightarrow COQ	$k_{036-001}$	
036 · 003	O + CQ \longrightarrow COQ	$k_{036-001}$	
036 · 004	P + CO \longrightarrow COP	$k_{036-001}$	
036 · 005	O + CP \longrightarrow COP	$k_{036-001}$	
037 · 001	Q + O ₂ \longrightarrow OQ + O	$2.9 \cdot 10^{-12}$	9
037 · 002	O + OQ \longrightarrow O ₂ + Q	$0.462 k_{037-001}$	
037 · 003	P + O ₂ \longrightarrow OP + O	$k_{037-001}$	
037 · 004	O + OP \longrightarrow O ₂ + P	$0.480 k_{037-001}$	
038 · 001	Q + CO \longrightarrow CQ + O	$8.3 \cdot 10^{-16}$	10
038 · 002	O + CQ \longrightarrow CO + Q	$0.902 k_{038-001}$	
038 · 003	P + CO \longrightarrow CP + O	$k_{038-001}$	
038 · 004	O + CP \longrightarrow CO + P	$0.949 k_{038-001}$	

1 $J_1 = 2.5 \times 10^{-3} \text{ s}^{-1}$. See section 6.4.4. The fractionation factors are taken from [189].

2 $J_2 = 0.05 J_1$. See section 6.4.4. The fractionation factors are taken from [189].

3 See Ref.[150].

4 Rate coefficient value is taken from Ref.[188]. In this study the absolute rate for the

reaction $\text{O}(^1\text{D}) + \text{H}_2\text{O}_2$ was determined by measuring the attenuation of excited state oxygen atoms. Since the products of the reaction were not detected and no information is available concerning the rate coefficients of the two individual channels 15 and 16, we assume that reaction $\text{O}(^1\text{D}) + \text{H}_2\text{O}_2$ proceeds with probability of 50% via channel 15 and 50% via channel 16.

5 Rate coefficient is calculated using the expression

$$k_f([\text{M}], T) = \left(\frac{k_0(T)[\text{M}]}{1 + \frac{k_0(T)[\text{M}]}{k_\infty(T)}} \right) 0.6^{\frac{1}{1 + \left[\log_{10} \left(\frac{k_0(T)[\text{M}]}{k_\infty(T)} \right) \right]^2}} \quad (\text{D.1})$$

introduced in section 6.2. k_0 and k_∞ values are from Ref.[150].

6 Rate coefficient calculated as the sum of the pressure-independent bimolecular component and the pressure-dependent component. See note B13 in Ref.[150].

7 The $\text{OH} + \text{CO}$ reaction can proceed via channels 33 and 34. In the former case (association to yield HOCO) the rate coefficient is calculated using C.1, in the latter (chemical activation process to H and CO_2) it is calculated using the expression introduced in Ref.[150]

$$k_f^{ca}([\text{M}], T) = \left(\frac{k_0(T)}{1 + \frac{k_0(T)}{k_\infty(T)/[\text{M}]}} \right) 0.6^{\frac{1}{1 + \left[\log_{10} \left(\frac{k_0(T)}{k_\infty(T)/[\text{M}]} \right) \right]^2}} \quad (\text{D.2})$$

where k_0 and k_∞ values are from Ref.[150]. See note D1 in ref.[150].

8 See section 6.4.1.

9 See Ref. [186] and [187].

10 See Ref. [180].

Bibliography

- [1] S. E. Braslavsky and M. B. Rubin. The history of ozone Part VIII. Photochemical formation of ozone. *Photochem. Photobiol. Sci.*, 10(10):1515–1520, 2011.
- [2] P. J. Hoolmann. *Mémoire sur l'équivalent calorifique de l'ozone*. Librairie de C. Van der Post, Jr., Utrecht, 1868.
- [3] S. E. Schwartz and P. Warneck. Units for use in atmospheric chemistry. *Pure Appl. Chem.*, 67(8-9):1377–1406, 1995.
- [4] B. J. Finlayson-Pitts and J. N. Pitts. *Chemistry of the Upper and Lower Atmosphere: Theory, Experiments, and Applications*. Elsevier Science, 1999. ISBN 9780080529073.
- [5] S. Sitch, P. M. Cox, W. J. Collins, and C. Huntingford. Indirect radiative forcing of climate change through ozone effects on the land-carbon sink. *Nature*, 448(7155):791–U4, 2007.
- [6] W. M. Haynes. *CRC Handbook of Chemistry and Physics, 93rd Edition*. CRC Handbook of Chemistry and Physics. Taylor & Francis, 2012. ISBN 9781439880494.
- [7] S. E. Harnung and M. S. Johnson. *Chemistry and the Environment*. Cambridge University Press, 2012. ISBN 9781107682573.
- [8] S. Chapman. On ozone and atomic oxygen in the upper atmosphere. *Philos. Mag.*, 10(64, 7TH SERIES):369–383, 1930.
- [9] H. Levy. Normal atmosphere: Large radical and formaldehyde concentrations predicted. *Science*, 173(3992):141–143, 1971.
- [10] B. Weinstock. Carbon monoxide: Residence time in the atmosphere. *Science*, 166(3902):224–225, 1969.
- [11] H. I. Schiff. Laboratory measurements of reactions related to ozone photochemistry. *Ann. Geophys.*, 28(1):67, 1972.
- [12] D. J. Giachard and R. P. Wayne. Photolysis of ozone by ultraviolet-radiation .6. reactions of O(¹D). *Proc. R. Soc. London, Ser. A*, 330(1580):131, 1972.
- [13] J. I. Steinfeld, S. M. Adlergolden, and J. W. Gallagher. Critical survey of data on the spectroscopy and kinetics of ozone in the mesosphere and thermosphere. *J. Phys. Chem. Ref. Data*, 16(4):911–951, 1987.
- [14] R. P. Wayne. The photochemistry of ozone. *Atmos. Environ.*, 21(8):1683–1694, 1987.
- [15] B. M. Smirnov and H. Reiss. *Physics of Ionized Gases*. Wiley, 2008. ISBN 9783527617715.

- [16] J. Bai. Study on surface O₃ chemistry and photochemistry by UV energy conservation. *Atmos. Pollut. Res.*, 1(2):118–127, 2010.
- [17] M. G. Lawrence, P. Jöckel, and R. von Kuhlmann. What does the global mean OH concentration tell us? *Atmos. Chem. Phys.*, 1:37–49, 2001.
- [18] U. Platt and F. Heintz. Nitrate radicals in tropospheric chemistry. *Isr. J. Chem.*, 34(3-4):289–300, 1994.
- [19] U. Platt, G. Lebras, G. Poulet, J. P. Burrows, and G. K. Moortgat. Peroxy-radicals from nighttime reaction of NO₃ with organic-compounds. *Nature*, 348(6297):147–149, 1990.
- [20] M. C. Cooke, S. R. Utembe, P. Gorrotxategi Carbajo, A. T. Archibald, A. J. Orr-Ewing, M. E. Jenkin, R. G. Derwent, D. J. Lary, and D. E. Shallcross. Impacts of formaldehyde photolysis rates on tropospheric chemistry. *Atmos. Sci. Lett.*, 11(1):33–38, 2010.
- [21] A. N. Ajavon, P. A. Newman, J. A. Pyle, and A.R. Ravishankara et al. Scientific assessment of ozone depletion: 2010. Global Ozone Research and Monitoring Project—Report No. 52, National Oceanic and Atmospheric Administration, National Aeronautics and Space Administration, United Nations Environment Programme, World Meteorological Organization, European Commission, 2010.
- [22] S. Lee and S. B. Feldstein. Detecting Ozone- and Greenhouse Gas-Driven Wind Trends with Observational Data. *Science*, 339(6119):563–567, 2013.
- [23] D. W. Waugh, F. Primeau, T. DeVries, and M. Holzer. Recent Changes in the Ventilation of the Southern Oceans. *Science*, 339(6119):568–570, 2013.
- [24] J. C. Farman, B. G. Gardiner, and J. D. Shanklin. Large losses of total ozone in Antarctica reveal seasonal ClO_x/NO_x interaction. *Nature*, 315(6016):207–210, 1985.
- [25] D. Jacob. *Introduction to Atmospheric Chemistry*. Princeton University Press, 1999. ISBN 9780691001852.
- [26] Soddy. Intra-atomic charge. *Nature*, 92:399–400, 1913.
- [27] IUPAC. Compendium of Chemical Terminology, 2nd ed. (the “Gold Book”). Compiled by A. D. McNaught and A. Wilkinson. Blackwell Scientific Publications, Oxford (1997). XML on-line corrected version: <http://goldbook.iupac.org> (2006-) created by M. Nic, J. Jirat, B. Kosata; updates compiled by A. Jenkins. ISBN 0-9678550-9-8. doi:10.1351/goldbook.
- [28] P. J. Mohr, B. N. Taylor, and D. B. Newell. CODATA recommended values of the fundamental physical constants: 2010. *J. Phys. Chem. Ref. Data*, 41(4):043109, 2012.
- [29] Mook, W. G., *Environmental isotopes in the hydrological cycle*, International hydrological programme, UNESCO, IAEA, Paris, 2000.
- [30] R. E. Criss. *Principles of Stable Isotope Distribution*. Oxford University Press, USA, 1999. ISBN 9780195353525.
- [31] R. Gonfiantini. Standards for stable isotope measurements in natural compounds. *Nature*, 271(5645):534–536, 1978.

- [32] W. A. Brand, T. B. Coplen, J. Vogl, and M. Rosner. Assessment of international reference materials for isotope-ratio analysis (IUPAC technical report). *Pure Appl. Chem.*, 2014.
- [33] J. R. De Laeter, J. K. Böhlke, P. De Bièvre, H. Hidaka, H. S. Peiser, K. J. R. Rosman, and P. D. P. Taylor. Atomic weights of the elements: Review 2000 - (IUPAC technical report). 75(6):683–800, 2003.
- [34] J. Bigeleisen. Chemistry of isotopes. *Science*, 147(3657):463–471, 1965.
- [35] H. C. Urey. The thermodynamic properties of isotopic substances. *J. Chem. Soc.*, pages 562–581, 1947.
- [36] J. Bigeleisen and M. Goeppert Mayer. Calculation of equilibrium constants for isotopic exchange reactions. *J. Chem. Phys.*, 15(5):261–267, 1947.
- [37] C. Kendall and J.J. McDonnell. *Isotope Tracers in Catchment Hydrology*. Developments in Water Science Series. Elsevier, 1998. ISBN 9780444501554.
- [38] J. Hoefs. *Stable Isotope Geochemistry*. U.S. Government Printing Office, 2009. ISBN 9783540707035.
- [39] E. D. Young, A. Galy, and H. Nagahara. Kinetic and equilibrium mass-dependent isotope fractionation laws in nature and their geochemical and cosmochemical significance. *Geochim. Cosmochim. Acta*, 66(6):1095 – 1104, 2002.
- [40] J. Bigeleisen and M. Wolfsberg. Theoretical and experimental aspects of isotope effects in chemical kinetics. *Advances in Chemical Physics*, 1:15–76, 1958.
- [41] M. Wolfsberg. Isotope effects. *Ann. Rev. Chem. Phys.*, 20:449–478, 1969.
- [42] R. E. Weston. Anomalous or mass-independent isotope effects. *Chem. Rev.*, 99(8): 2115–2136, 1999.
- [43] J. Bigeleisen and M. Wolfsberg. Theoretical and experimental aspects of isotope effects in chemical kinetics. *Advances in Chemical Physics*, 1:15–76, 1958.
- [44] Stefania Zanconato, Dan M. Cooper, Yaacov Armon, and Samuel Epstein. Effect of increased metabolic rate on oxygen isotopic fractionation. *Respir. Physiol.*, 89(3):319 – 327, 1992.
- [45] T. B. Coplen, J. K. Böhlke, P. De Bièvre, T. Ding, N. E. Holden, J. A. Hopple, H. R. Krouse, A. Lamberty, H. S. Peiser, K. Révész, S. E. Rieder, K. J. R. Rosman, E. Roth, P. D. P. Taylor, R. D. Vocke, and Y. K. Xiao. Isotope-abundance variations of selected elements - (IUPAC technical report). *Pure Appl. Chem.*, 74(10):1987–2017, 2002.
- [46] K. Mauersberger. Measurement of heavy ozone in the stratosphere. *Geophys. Res. Lett.*, 8(8):935–937, 1981.
- [47] K. Mauersberger, P. Lämmerzahl, and D. Krankowsky. Stratospheric ozone isotope enrichments—revisited. *Geophys. Res. Lett.*, 28(16):3155–3158, 2001.
- [48] V. Haverd, G. C. Toon, and D. W. T. Griffith. Evidence for altitude-dependent photolysis-induced ^{18}O isotopic fractionation in stratospheric ozone. *Geophys. Res. Lett.*, 32, 2005.

- [49] D. Krankowsky, P. Lämmerzahl, K. Mauersberger, C. Janssen, B. Tuzson, and T. Röckmann. Stratospheric ozone isotope fractionations derived from collected samples. *J. Geophys. Res.*, 112(D8):D08301, 2007.
- [50] J. R. Hulston and H. G. Thode. Variations in the S^{33} , S^{34} , and S^{36} contents of meteorites and their relation to chemical and nuclear effects. *J. Geophys. Res.*, 70(14):3475–3484, 1965.
- [51] H. C. Urey and L. J. Greiff. Isotopic exchange equilibria. *J. Am. Chem. Soc.*, 57(2):321–327, 1935.
- [52] R. E. Weston. When is an isotope effect non-mass dependent? *J. Nucl. Sci. Tech.*, 43(4):295–299, Apr 2006.
- [53] Y. Matsuhisa, J. R. Goldsmith, and R. N. Clayton. Oxygen isotopic fractionation in the system quartz-albite-anorthite-water. *Geochim. Cosmochim. Acta*, 43(7):1131 – 1140, 1979.
- [54] Y. Matsuhisa, J. R. Goldsmith, and R. N. Clayton. Mechanisms of hydrothermal crystallization of quartz at 250 °C and 15 kbar. *Geochim. Cosmochim. Acta*, 42(2):173, 1978.
- [55] F. Robert, A. Rejouchiel, and M. Javoy. Oxygen isotopic homogeneity of the Earth - new evidence. *Earth Planet. Sci. Lett.*, 108(1-3):1–9, 1992.
- [56] R. N. Clayton, L. Grossman, and T. K. Mayeda. Component of primitive nuclear composition in carbonaceous meteorites. *Science*, 182(4111):485–488, 1973.
- [57] N. J. Turro and M. F. Chow. Magnetic isotope effect on the thermolysis of 9,10-diphenylanthracene endoperoxide as a means of separation of ^{17}O from ^{16}O and ^{18}O . *J. Am. Chem. Soc.*, 102(3):1190–1192, 1980.
- [58] A. L. Buchachenko. *Russ. J. Phys. Chem.*, 51:1445, 1977.
- [59] N. J. Turro. Influence of nuclear-spin on chemical-reactions - magnetic isotope and magnetic-field effects (a review). *Proc. Natl. Acad. Sci. USA*, 80(2):609–621, 1983.
- [60] M. H. Thiemens and J. E. Heidenreich. The mass-independent fractionation of oxygen - a novel isotope effect and its possible cosmochemical implications. *Science*, 219(4588):1073–1075, 1983.
- [61] J. Morton, J. Barnes, B. Schueler, and K. Mauersberger. Laboratory studies of heavy ozone. *J. Geophys. Res.*, 95:901–907, 1990.
- [62] M. F. Miller, T. Röckmann, and I. P. Wright. A general algorithm for the ^{17}O abundance correction to $^{13}\text{C}/^{12}\text{C}$ determinations from CO_2 isotopologue measurements, including CO_2 characterised by ‘mass-independent’ oxygen isotope distributions. *Geochim. Cosmochim. Acta*, 71(13):3145–3161, 2007.
- [63] M. F. Miller. Isotopic fractionation and the quantification of ^{17}O anomalies in the oxygen three-isotope system: an appraisal and geochemical significance. *Geochim. Cosmochim. Acta*, 66(11):1881–1889, 2002.
- [64] M. H. Thiemens. History and applications of mass-independent isotope effects. *Annu. Rev. Earth Planet. Sci.*, 34:217–262, 2006.

- [65] T. A. Berhanu, J. Savarino, S. K. Bhattacharya, and W. C. Vicars. ^{17}O excess transfer during the $\text{NO}_2 + \text{O}_3 \rightarrow \text{NO}_3 + \text{O}_2$ reaction. *J. Chem. Phys.*, 136(4), 2012.
- [66] J. R. Lyons and E. D. Young. CO self-shielding as the origin of oxygen isotope anomalies in the early solar nebula. *Nature*, 435(7040):317–320, 2005.
- [67] K. D. McKeegan, A. P. A. Kallio, V. S. Heber, G. Jarzebinski, P. H. Mao, C. D. Coath, T. Kunihiro, R. C. Wiens, J. E. Nordholt, R. W. Moses, D. B. Reisenfeld, A. J. G. Jurewicz, and D. S. Burnett. The oxygen isotopic composition of the sun inferred from captured solar wind. *Science*, 332(6037):1528–1532, 06 2011.
- [68] A. L. Buchachenko. Mass-independent isotope effects. *J. Phys. Chem. B*, 117(8):2231–2238, 2013.
- [69] V. A. Beliakov, A. L. Buchachenko, E. M. Galimov, and V. I. Maltsev. Enrichment of oxygen by isotope ^{17}O in reactions of liquid-phase oxidation of organic-compounds. *Doklady Akademii Nauk SSSR*, 243(4):924–925, 1978.
- [70] K. Mauersberger. Measurement of heavy ozone in the stratosphere. *Geophys. Res. Lett.*, 8(8):935–937, 1981.
- [71] R. J. Cicerone and J. L. McCrumb. Photo-dissociation of isotopically heavy O_2 as a source of atmosphere. *Geophys. Res. Lett.*, 7(4):251–254, 1980.
- [72] K. Mauersberger. Ozone isotope measurements in the stratosphere. *Geophys. Res. Lett.*, 14(1):80–83, 1987.
- [73] J. A. Kaye and D. F. Strobel. Enhancement of heavy ozone in the Earth’s atmosphere. *J. Geophys. Res., C: Oceans Atmos.*, 88(NC13):8447–8452, 1983.
- [74] J. A. Kaye. Theoretical-analysis of isotope effects on ozone formation in oxygen photochemistry. *J. Geophys. Res.*, 91(D7):7865–7874, 1986.
- [75] B. Tuzson. *Symmetry Specific Study of Ozone Isotopomer Formation*. PhD thesis, Rupertus Carola University of Heidelberg, Germany, 2005.
- [76] D. Krankowsky, P. Laemmerzahl, K. Mauersberger, C. Janssen, B. Tuzson, and T. Roeckmann. Stratospheric ozone isotope fractionations derived from collected samples. *J. Geophys. Res.: Atmos.*, 112(D8), 2007.
- [77] C. E. Miller, R. M. Onorato, M.-C. Liang, and Y. L. Yung. Extraordinary isotopic fractionation in ozone photolysis. *Geophys. Res. Lett.*, 32(14), 2005.
- [78] R. L. Miller, A. G. Suits, P. L. Houston, R. Toumi, J. A. Mack, and A. M. Wodtke. The “ozone deficit” problem: $\text{O}_2(\text{X}, \nu \geq 26) + \text{O}(^3\text{P})$ from 226 nm ozone photodissociation. *Science*, 265(5180):1831–1838, September 1994.
- [79] C. A. Rogaski, J. M. Price, J. A. Mack, and A. M. Wodtke. Laboratory evidence for a possible non - LTE mechanism of stratospheric ozone formation. *Geophys. Res. Lett.*, 20(24):2885–2888, 1993.
- [80] D. Lauvergnat and D. C. Clary. Reactive scattering of highly vibrationally excited oxygen molecules: Ozone formation? *J. Chem. Phys.*, 108(9):3566, 1998.
- [81] P. L. Houston, A. G. Suits, and R. Toumi. Isotopic enrichment of heavy ozone in the stratosphere. *J. Geophys. Res. Atmos.*, 101(D13):18829, 1996.

- [82] D. Krankowski, F. Barteccki, G. G. Klees, K. Mauersberger, K. Schellenbach, and J. Stehr. Measurement of heavy isotope enrichment in tropospheric ozone. *Geophys. Res. Lett.*, 22(13):1713–1716, 1995.
- [83] C. A. M. Brenninkmeijer, C. Janssen, J. Kaiser, T. Rockmann, T. S. Rhee, and S. S. Assonov. Isotope effects in the chemistry of atmospheric trace compounds. *Chem. Rev.*, 103(12):5125–5161, 2003.
- [84] J. C. Johnston and M. H. Thiemens. The isotopic composition of tropospheric ozone in three environments. *J. Geophys. Res.: Atmos.*, 102(D21):25395–25404, 1997.
- [85] W. C. Vicars, S. K. Bhattacharya, J. Erbland, and J. Savarino. Measurement of the ^{17}O -excess ($\Delta^{17}\text{O}$) of tropospheric ozone using a nitrite-coated filter. *Rapid Comm. Mass Spectrom.*, 26(10):1219–1231, 2012.
- [86] M. H. Thiemens and J. E. Heidenreich. The mass-independent fractionation of oxygen - a novel isotope effect and its possible cosmochemical implications. *Science*, 219(4588):1073–1075, 1983.
- [87] J. Morton, J. Barnes, B. Schueler, and K. Mauersberger. Laboratory studies of heavy ozone. *J. Geophys. Res. Atmos.*, 95(D1):901–907, 1990.
- [88] M. H. Thiemens and T. Jackson. Pressure dependency for heavy isotope enhancement in ozone formation. *Geophys. Res. Lett.*, 17(6):717–719, 1990.
- [89] S. K. Bains-Sahota and M. H. Thiemens. Mass-independent oxygen isotopic fractionation in a microwave plasma. *J. Phys. Chem.*, 91(16):4370–4374, 1987.
- [90] MH Thiemens and T Jackson. Production of isotopically heavy ozone by ultraviolet-light photolysis of O_2 . *Geophys. Res. Lett.*, 14(6):624–627, 1987.
- [91] J. Guenther, B. Erbacher, D. Krankowsky, and K. Mauersberger. Pressure dependence of two relative ozone formation rate coefficients. *Chem. Phys. Lett.*, 306(5–6):209 – 213, 1999.
- [92] C. Janssen, J. Guenther, D. Krankowsky, and K. Mauersberger. Temperature dependence of ozone rate coefficients and isotopologue fractionation in ^{16}O - ^{18}O oxygen mixtures. *Chem. Phys. Lett.*, 367(1–2):34 – 38, 2003.
- [93] J. Morton, B. Schueler, and K. Mauersberger. Oxygen fractionation of ozone isotopes $^{48}\text{O}_3$ through $^{54}\text{O}_3$. *Chem. Phys. Lett.*, 154(2):143 – 145, 1989.
- [94] K. Mauersberger, J. Morton, B. Schueler, J. Stehr, and S. M. Anderson. Multi-isotope study of ozone - implications for the heavy ozone anomaly. *Geophys. Res. Lett.*, 20(11):1031–1034, 1993.
- [95] S. M. Anderson, D. Hulsebusch, and K. Mauersberger. Surprising rate coefficients for four isotopic variants of $\text{O}+\text{O}_2+\text{M}$. *J. Chem. Phys.*, 107(14):5385–5392, 1997.
- [96] C. Janssen, J. Guenther, D. Krankowsky, and K. Mauersberger. Relative formation rates of $^{50}\text{O}_3$ and $^{50}\text{O}_3$ in ^{16}O - ^{18}O mixtures. *J. Chem. Phys.*, 111(16):7179–7182, 1999.
- [97] K. L. Feilberg, A. A. Wiegel, and K. A. Boering. Probing the unusual isotope effects in ozone formation: Bath gas and pressure dependence of the non-mass-dependent isotope enrichments in ozone. *Chem. Phys. Lett.*, 556(0):1 – 8, 2013.

- [98] Y. Q. Gao and R. A. Marcus. Strange and unconventional isotope effects in ozone formation. *Science*, 293(5528):259–263, 2001.
- [99] A. L. Van Wyngarden, A. Kathleen, K. A. Boering, J. J. Lin, Y. T. Lee, S. Y. Lin, H. Guo, and G. Lendvay. Nonstatistical behavior of reactive scattering in the $^{18}\text{O}+^{32}\text{O}_2$ isotope exchange reaction. *J. Am. Chem. Soc.*, 129(10):2866–2870, 2007.
- [100] C. Janssen, J. Guenther, K. Mauersberger, and D. Krankowsky. Kinetic origin of the ozone isotope effect: a critical analysis of enrichments and rate coefficients. *Phys. Chem. Chem. Phys.*, 3:4718–4721, 2001.
- [101] G. Michalski, Z. Scott, M. Kabling, and M. H. Thiemens. First measurements and modeling of $\Delta^{17}\text{O}$ in atmospheric nitrate. *Geophys. Res. Lett.*, 30(16), 2003.
- [102] J. Savarino, C. C. W. Lee, and M. H. Thiemens. Laboratory oxygen isotopic study of sulfur (IV) oxidation: Origin of the mass-independent oxygen isotopic anomaly in atmospheric sulfates and sulfate mineral deposits on Earth. *J. Geophys. Res. Atmos.*, 105(D23):29079–29088, 2000.
- [103] Y. L. Yung, W. B. DeMore, and J. P. Pinto. Isotopic exchange between carbon-dioxide and ozone via $\text{O}(^1\text{D})$ in the stratosphere. *Geophys. Res. Lett.*, 18(1):13–16, 1991.
- [104] T. Röckmann, J. Kaiser, J. N. Crowley, C. A. M. Brenninkmeijer, and P. J. Crutzen. The origin of the anomalous or “mass-independent” oxygen isotope fractionation in tropospheric N_2O . *Geophys. Res. Lett.*, 28(3):503–506, 2001.
- [105] M. H. Thiemens. Atmosphere science - Mass-independent isotope effects in planetary atmospheres and the early solar system. *Science*, 283(5400):341–345, 1999.
- [106] S. Chakraborty, P. Yanchulova, and M. H. Thiemens. Mass-Independent Oxygen Isotopic Partitioning During Gas-Phase SiO_2 Formation. *Science*, 342(6157):463–466, 2013.
- [107] T. Röckmann, P. Jöckel, V. Gros, M. Braunlich, G. Possnert, and C. A. M. Brenninkmeijer. Using ^{14}C , ^{13}C , ^{18}O and ^{17}O isotopic variations to provide insights into the high northern latitude surface CO inventory. *Atmos. Chem. Phys.*, 2:147–159, 2002.
- [108] T. Röckmann, C. A. M. Brenninkmeijer, G. Saueressig, P. Bergamaschi, J. N. Crowley, H. Fischer, and P. J. Crutzen. Mass-independent oxygen isotope fractionation in atmospheric CO as a result of the reaction $\text{CO}+\text{OH}$. *Science*, 281(5376):544–546, 1998.
- [109] M. H. Thiemens, T. Jackson, K. Mauersberger, B. Schueler, and J. Morton. Oxygen isotope fractionation in stratospheric CO_2 . *Geophys. Res. Lett.*, 18(4):669–672, 1991.
- [110] S. Kawagucci, U. Tsunogai, S. Kudo, F. Nakagawa, H. Honda, S. Aoki, T. Nakazawa, M. Tsutsumi, and T. Gamo. Long-term observation of mass-independent oxygen isotope anomaly in stratospheric CO_2 . *Atmos. Chem. Phys.*, 8(20):6189–6197, 2008.
- [111] P. Lämmerzahl, T. Röckmann, C. A. M. Brenninkmeijer, D. Krankowsky, and K. Mauersberger. Oxygen isotope composition of stratospheric carbon dioxide. *Geophys. Res. Lett.*, 29(12), 2002.
- [112] MJ Perri, AL Van Wyngarden, KA Boering, JJ Lin, and YT Lee. Dynamics of the $\text{O}(^1\text{D})+\text{CO}_2$ oxygen isotope exchange reaction. *J. Chem. Phys.*, 119(16):8213–8216, 2003.

- [113] R. Shaheen, C. Janssen, and T. Roeckmann. Investigations of the photochemical isotope equilibrium between O-2, CO₂ and O-3. *Atmos. Chem. Phys.*, 7:495–509, 2007.
- [114] J. Wen and M. H. Thiemens. Multi-isotope study of the O(⁴D) + CO₂ exchange and stratospheric consequences. *J. Geophys. Res.*, 98(D7):12801–12808, 1993.
- [115] Renato Winkler, Amaelle Landais, Camille Risi, Melanie Baroni, Alexey Ekaykin, Jean Jouzel, Jean Robert Petit, Frederic Prie, Benedicte Minster, and Sonia Falourd. Inter-annual variation of water isotopologues at Vostok indicates a contribution from stratospheric water vapor. *Proc. Nat. Acad. Sci. USA*, 110(44):17674–17679, 2013.
- [116] R. Winkler, A. Landais, C. Risi, M. Baroni, A. Ekaykin, J. Jouzel, J. R. Petit, F. Prie, B. Minster, and S. Falourd. Interannual variation of water isotopologues at Vostok indicates a contribution from stratospheric water vapor. *Proc. Natl. Acad. Sci. USA*, 110(44):17674–17679, 2013.
- [117] A. Zahn, P. Franz, C. Bechtel, J. U. Grooß, and T. Röckmann. Modelling the budget of middle atmospheric water vapour isotopes. *Atoms. Chem. Phys.*, 6:2073–2090, 2006.
- [118] A. Pandey and S. K. Bhattacharya. Erratum: “Anomalous oxygen isotope enrichment in CO₂ produced from O+CO: Estimates based on experimental results and model predictions” [J. Chem. Phys. 124, 234301 (2006)]. *J. Chem. Phys.*, 125(14):149903, 2006.
- [119] S. K. Bhattacharya and M. H. Thiemens. New evidence for symmetry dependent isotope effects: O + CO → CO₂ reaction. *Z. Naturforsch. A*, 44:435 – 444, 1989.
- [120] J. Viallon, P. Moussay, J. E. Norris, F. R. Guenther, and R. I. Wielgosz. A study of systematic biases and measurement uncertainties in ozone mole fraction measurements with the NIST standard reference photometer. *Metrologia*, 43(5):441–450, Oct 2006.
- [121] A. Gratien, B. Picquet-Varrault, J. Orphal, J. F. Doussin, and J. M. Flaud. New laboratory intercomparison of the ozone absorption coefficients in the mid-infrared (10 μm) and ultraviolet (300–350 nm) spectral regions. *J. Phys. Chem. A*, 114(37):10045–10048, 08 2010.
- [122] B. Picquet-Varrault, J. Orphal, J.-F. Doussin, P. Carlier, and J.-M. Flaud. Intercomparison of the ozone absorption coefficients in the mid-infrared (10 μm) and ultraviolet (300–350 nm) spectral regions. *J. Phys. Chem. A*, 109(1):1008 – 1014, 2005.
- [123] C. Viatte, M. Schneider, A. Redondas, F. Hase, M. Eremenko, P. Chelin, J. M. Flaud, T. Blumenstock, and J. Orphal. Comparison of ground-based FTIR and Brewer O₃ total column with data from two different IASI algorithms and from OMI and GOME-2 satellite instruments. *Atmos. Meas. Tech.*, 4(3):535–546, 2011.
- [124] M. Guinet, D. Mondelain, C. Janssen, and C. Camy-Peyret. Laser spectroscopic study of ozone in the 100←000 band for the SWIFT instrument. *J. Quant. Spectrosc. Radiat. Transfer*, 111(7-8):961–972, 5 2010.
- [125] A. Barbe, S. Mikhailenko, E. Starikova, M. R. De Backer, V.G. Tyuterev, D. Mondelain, S. Kassi, A. Campargue, C. Janssen, and S. Tashkun. Ozone spectroscopy in the electronic ground state: high-resolution spectra analyses and update of line parameters since 2003. *J. Quant. Spectrosc. Radiat. Transfer*, 130:172–190, 2013.

- [126] B. Daudé. *Développement d'un photomètre UV pour des mesures de référence de gaz d'intérêt atmosphérique : ozone et COVs*. thesis, Université Pierre et Marie Curie, Paris, November 2012.
- [127] M. Guinet, D. Mondelain, C. Janssen, and C. Camy-Peyret. Laser spectroscopic study of ozone in the 100←000 band for the SWIFT instrument. *J. Quant. Spectrosc. Radiat. Transfer*, 111(7-8):961–972, 5 2010.
- [128] U. Kogelschatz. Dielectric-barrier discharges: Their history, discharge physics, and industrial applications. *Plasma Chem. Plasma Process.*, 23(1):1–46, 2003.
- [129] D. Hanson and K. Mauersberger. The vapor-pressures of solid and liquid ozone. *J. Chem. Phys.*, 85(8):4669–4672, 1986.
- [130] J. Mattauch and R. Herzog. About a new Mass Spectrograph. *Zeitschrift Fur Physik*, 89(11-12):786–795, NOV 1934.
- [131] A. O. Nier and D. J. Schlutter. High performance double focusing mass spectrometer. *Rev. Sci. Instrum.*, 56(2):214–219, 1985.
- [132] J. Roboz. *Introduction to mass spectrometry; instrumentation and techniques*. Interscience Publishers, 1968.
- [133] C. Janssen, D. Simone, and M. Guinet. Preparation and accurate measurement of pure ozone. *Rev. Sci. Instrum.*, 82(3), 2011.
- [134] A. Pandey and S. K. Bhattacharya. Anomalous oxygen isotope enrichment in CO₂ produced from O+CO: Estimates based on experimental results and model predictions. *J. Chem. Phys.*, 124(23):234301–234313, 2006.
- [135] P. Richet, Y. Bottinga, and M. Javoy. A review of hydrogen, carbon, nitrogen, oxygen, sulphur, and chlorine stable isotope enrichment among gaseous molecules. *Annu. Rev. Earth Planet. Sci.*, 5:65–110, 1977.
- [136] J. A. Kaye. Isotope effects in gas-phase chemical-reactions and photodissociation processes - overview. *ACS Symp. Ser.*, 502:1–14, 1992.
- [137] S. K. Bhattacharya, J. Savarino, and M. H. Thiemens. A new class of oxygen isotopic fractionation in photodissociation of carbon dioxide: Potential implications for atmospheres of Mars and Earth. *Geophys. Res. Lett.*, 27(10):1459–1462, 2000.
- [138] D. L. Baulch, D. D. Drysdale, J. Duxbury, and S. J. Grant. *Homogeneous Gas Phase Reactions of the O₂-O₃ Systems, the CO-O₂-H₂ System, and of Sulphur-containing Species*, volume 3 of *Evaluated Kinetic Data For High Temperature Reactions*. Butterworth, London, 1976.
- [139] D. Bauer, L. D'Ottone, and A. J. Hynes. O(¹D) quantum yields from O₃ photolysis in the near UV region between 305 and 375 nm. *Phys. Chem. Chem. Phys.*, 2(7):1421–1424, 2000.
- [140] W. Tsang and R. F. Hampson. Chemical kinetic database for combustion chemistry 1. Methane and related compounds. *J. Phys. Chem. Ref. Data*, 15(3):1087–1279, 1986.
- [141] C. Janssen and B. Tuzson. Isotope evidence for ozone formation on surfaces. *J. Phys. Chem. A*, 114(36):9709–9719, 2010.

- [142] J. E. Morgan and H. I. Schiff. Diffusion coefficients of O + N atoms in inert gases. *Can. J. Chem.*, 42(10):2300, 1964.
- [143] K. L. Feilberg, D. W. T. Griffith, M. S. Johnson, and C. J. Nielsen. The ^{13}C and D kinetic isotope effects in the reaction of CH_4 with Cl. *Int. J. Chem. Kinet.*, 37(2): 110–118, 2005.
- [144] E. J. K. Nilsson, L. M. T. Joelsson, J. Heimdal, M. S. Johnson, and O.J. Nielsen. Re-evaluation of the reaction rate coefficient of $\text{CH}_3\text{Br} + \text{OH}$ with implications for the atmospheric budget of methyl bromide. *Atmos. Environ.*, 80(0):70 – 74, 2013.
- [145] M. C. Dodge. Chemical oxidant mechanisms for air quality modeling: critical review. *Atmos. Environ.*, 34(12–14):2103 – 2130, 2000.
- [146] E. Jaekel, M. Wendisch, and B. L. Lefer. Parameterization of ozone photolysis frequency in the lower troposphere using data from photodiode array detector spectrometers. *J. Atmos. Chem.*, 54(1):67–87, 2006.
- [147] J. U. White. Long optical paths of large aperture. *J. Opt. Soc. Am.*, 32(5):285–288, 1942.
- [148] E. J. K. Nilsson, C. Eskebjerg, and M. S. Johnson. A photochemical reactor for studies of atmospheric chemistry. *Atmos. Environ.*, 43(18):3029 – 3033, 2009.
- [149] R. R. Sowell, R. E. Cuthrell, D. M. Mattox, and R. D. Bland. Surface cleaning by ultraviolet-radiation. *J. Vac. Sci. Technol.*, 11(1):474–475, 1974.
- [150] S. P. Sander, J. Abbatt, J. R. Barker, J. B. Burkholder, R. R. Friedl, D. M. Golden, R. E. Huie, C. E. Kolb, M. J. Kurylo, G. K. Moortgat, V. L. Orkin and P. H. Wine “Chemical Kinetics and Photochemical Data for Use in Atmospheric Studies, Evaluation No. 17,” JPL Publication 10-6, Jet Propulsion Laboratory, Pasadena, 2011 <http://jpldataeval.jpl.nasa.gov>.
- [151] T. G. Slanger, B. J. Wood, and G. Black. Kinetics of $\text{O}(^3\text{P}) + \text{CO} + \text{M}$ recombination. *J. Chem. Phys.*, 57(1):233–238, 1972.
- [152] J. Wolfrum, T. Dreier, V. Ebert, and C. Schultz. *Laser-Based Combustion Diagnostics*. John Wiley & Sons, Ltd, 2006.
- [153] P. Warneck. *Chemistry of the Natural Atmosphere*. Academic Press, 2 edition, 1999.
- [154] D. Griffith (2008), *Malt5 User guide, Version 5.4*, University of Wollongong, NSW 2522, Australia.
- [155] L. S. Rothman, I. E. Gordon, Y. Babikov, A. Barbe, D. Chris Benner, P. F. Bernath, M. Birk, L. Bizzocchi, V. Boudon, L. R. Brown, A. Campargue, K. Chance, E. A. Cohen, L. H. Coudert, V. M. Devi, B. J. Drouin, A. Fayt, J. M. Flaud, R. R. Gamache, J. J. Harrison, J. M. Hartmann, C. Hill, J. T. Hodges, D. Jacquemart, A. Jolly, J. Lamouroux, R. J. Le Roy, G. Li, D. A. Long, O. M. Lyulin, C. J. Mackie, S. T. Massie, S. Mikhailenko, H. S. P. Mueller, O. V. Naumenko, A. V. Nikitin, J. Orphal, V. Perevalov, A. Perrin, E. R. Polovtseva, C. Richard, M. A. H. Smith, E. Starikova, K. Sung, S. Tashkun, J. Tennyson, G. C. Toon, Vl. G. Tyuterev, and G. Wagner. The HITRAN2012 molecular spectroscopic database. *J. Quant. Spectrosc. Radiat. Transfer*, 130(SI):4–50, 2013.

- [156] I. Arnold, F. J. Comes, and G. K. Moortgat. Laser flash photolysis: Quantum yield of $O^1(D)$ formation from ozone. *Chem. Phys.*, 24(2):211–217, 1977.
- [157] G. D. Smith, L. T. Molina, and M. J. Molina. Temperature Dependence of $O^1(D)$ Quantum Yields from the Photolysis of Ozone between 295 and 338 nm. *J. Phys. Chem. A*, 104(39):8916–8921, 2000.
- [158] K. Bogumil, J. Orphal, J. P. Burrows, and J. M. Flaud. Vibrational progressions in the visible and near-ultraviolet absorption spectrum of ozone. *Chem. Phys. Lett.*, 349(3-4):241–248, 2001.
- [159] D. E. Freeman, K. Yoshino, J. R. Esmond, and W. H. Parkinson. High-resolution absorption cross-section measurements of ozone at 195 K in the wavelength region 240–350 nm. *Planet. Space Sci.*, 32(2):239, 1984.
- [160] S. Yu. Grebenshchikov, Z.-W. Qu, H. Zhu, and R. Schinke. New theoretical investigations of the photodissociation of ozone in the hartley, huggins, chappuis, and wulf bands. *Phys. Chem. Chem. Phys.*, 9:2044–2064, 2007.
- [161] J. Orphal. A critical review of the absorption cross-sections of O_3 and NO_2 in the ultraviolet and visible. *J. Photochem. Photobiol., A*, 157(2):33 – 31, 2003.
- [162] Y. Matsumi and M. Kawasaki. Photolysis of atmospheric ozone in the ultraviolet region. *Chem. Rev.*, 103(12):4767–4781, 2003.
- [163] Y. Matsumi, F. J. Comes, G. Hancock, A. Hofzumahaus, A. J. Hynes, M. Kawasaki, and A. R. Ravishankara. Quantum yields for production of $O^1(D)$ in the ultraviolet photolysis of ozone: Recommendation based on evaluation of laboratory data. *J geophys Res*, 107(D3):4024, 2002.
- [164] Valeriu Damian, Adrian Sandu, Mirela Damian, Florian Potra, and Gregory R Carmichael. The kinetic preprocessor KPP—A software environment for solving chemical kinetics. *Comp. Chem. Eng.*, 26(11):1567–1579, 2002.
- [165] A. Sandu and R. Sander. Technical note: Simulating chemical systems in Fortran90 and Matlab with the Kinetic PreProcessor KPP-2.1. *Atmos. Chem. Phys.*, 6:187–195, 2006.
- [166] S. Gromov, P. Jöckel, R. Sander, and C. A. M. Brenninkmeijer. A kinetic chemistry tagging technique and its application to modelling the stable isotopic composition of atmospheric trace gases. *Geosci. Model Dev.*, 3(1):201–272, 2010.
- [167] P. Eller, K. Singh, A. Sandu, K. Bowman, D. Henze, and M. Lee. Implementation and evaluation of an array of chemical solvers in a global chemical transport model. *Geosci. Model Dev.*, 2(2):89–96, 2009.
- [168] A L Nagy, D Papp, and J Tóth. ReactionKinetics—A Mathematica package with applications. *Chem. Eng. Sci.*, 83:12–23, 2012.
- [169] Scot T Martin. Employing complex kinetic diagrams to understand the Belousov-Zhabotinskii Reaction. *Math. J.*, 8(1):114–125, 2001.
- [170] International Union of Pure and Applied Chemistry, editor. *Compendium of Chemical Terminology: Gold Book*. 2012.

- [171] R. T. Pack, R. B. Walker, and B. K. Kendrick. Three-body collision contributions to recombination and collision-induced dissociation. I. Cross sections. *J. Chem. Phys.*, 109(16):6701–6713, 1998.
- [172] J. Troe. Theory of thermal unimolecular reactions at low-pressures. 1. solutions of master equation. *J. Chem. Phys.*, 66(11):4745–4757, 1977.
- [173] J. Troe. Theory of thermal unimolecular reactions at low-pressures. 2. strong collision rate constants - applications. *J. Chem. Phys.*, 66(11):4758–4775, 1977.
- [174] J. Troe. Toward a quantitative analysis of association reactions in the atmosphere. *Chem. Rev.*, 103(12):4565–4576, 2003.
- [175] S. P. Sander, R. R. Friedl, D. M. Golden, M. J. Kurylo, G. K. Moortgat, H. Keller-Rudek, P. H. Wine, A. R. Ravishankara, C. E. Kolb, M. J. Molina, B. J. Finlayson-Pitts, R. E. Huie, and V. L. Orkin. Chemical kinetics and photochemical data for use in atmospheric studies, evaluation number 15. JPL Publication 06-2, 2006.
- [176] P. Baertschi. Absolute ^{18}O content of standard mean ocean water. *Earth Planet Sci. Lett.*, 31(3):341–344, 1976.
- [177] W. J. Li, B. L. Ni, D. Q. Jin, and Q. G. Zhang. Measurement of the absolute abundance of ^{17}O in V-SMOW. *Kexue Tongbao*, 33(19):1610–1613, 1988.
- [178] A. S. Cole and K. A. Boering. Mass-dependent and non-mass-dependent isotope effects in ozone photolysis: Resolving theory and experiments. *J. Chem. Phys.*, 125(18), NOV 14 2006.
- [179] R. Atkinson, D. L. Baulch, R. A. Cox, J. N. Crowley, R. F. Hampson, Jr, J. A. Kerr, M. J. Rossi, and J. Troe. Summary of evaluated kinetic and photochemical data for atmospheric chemistry. Web version, December 2001.
- [180] S. Jaffe and F. S. Klein. Isotopic exchange reactions of atomic oxygen produced by photolysis of NO_2 at 3660 Å. *Trans. Faraday Soc.*, 62(527P):3135–3141, 1966.
- [181] C. Janssen. Intramolecular isotope distribution in heavy ozone ($^{16}\text{O}^{18}\text{O}^{16}\text{O}$ and $^{16}\text{O}^{16}\text{O}^{18}\text{O}$) (vol 110, art no D08308, 2005). *J. Geophys. Res. Atmos.*, 111(D18), 2006.
- [182] W. Demtröder. *Atoms, Molecules And Photons: An Introduction to Atomic-, Molecular-, and Quantum-physics*. Springer, 2006.
- [183] J. M. Hollas. *Modern Spectroscopy*. Wiley, 2004. ISBN 9780470094716.
- [184] S. P. Davis, M. C. Abrams, and J. W. Brault. *Fourier Transform Spectrometry*. Elsevier Science, 2001. ISBN 9780080506913.
- [185] P. R. Griffiths and J. A. De Haseth. *Fourier Transform Infrared Spectrometry*. Chemical Analysis: A Series of Monographs on Analytical Chemistry and Its Applications. Wiley, 2007.
- [186] S. M. Anderson, F. S. Klein, and F Kaufman. Kinetics of the isotope exchange-reaction of ^{18}O with NO and O_2 at 298 K. *J. Chem. Phys.*, 83(4):1648–1656, 1985.
- [187] P. Fleurat-Lessard, S. Yu. Grebenshchikov, R. Schinke, C. Janssen, and D. Krankowsky. Isotope dependence of the $\text{O}+\text{O}_2$ exchange reaction: Experiment and theory. *J. Chem. Phys.*, 119(9):4700–4712, SEP 1 2003.

- [188] I. S. Fletcher and D. Husain. Collisional quenching of electronically excited oxygen atoms, $O(2^1D_2)$, by gases NH_3 , H_2O_2 , C_2H_6 , C_3H_8 , and $C(CH_3)_4$, using time-resolved attenuation of atomic resonance radiation. *Can. J. Chem.*, 54(11):1765–1770, 1976.
- [189] S. A. Ndengue, R. Schinke, F. Gatti, H-D. Meyer, and R. Jost. Ozone Photodissociation: Isotopic and Electronic Branching Ratios for Symmetric and Asymmetric Isotopologues. *J. Phys. Chem. A*, 116(50):12271–12279, DEC 20 2012.

Acknowledgements

I would like to thank my supervisor Dr.Christof Janssen for having advised and encouraged me during these years of doctoral program. Thanks to my co-supervisor, Prof. Matthew Johnson who gave me the opportunity to work in the Chemistry Department of University of Copenhagen in a friendly environment and for the helpful suggestions in performing the experiments. I would like also to thank my referees Dr. A. Landais and Prof. M. Rotger for having accepted to read and comment my manuscript and Prof. Röckmann and Prof. Krim for agreeing to be part of the jury. I wish to thank all my colleagues of LPMAA for their support and the members of the IntraMif project for having granted my PhD, for the collaboration and the good time spent together during our meetings.

Grazie a tutti gli amici che ho incontrato qui a Parigi, per i sorrisi ed il sostegno che mi hanno donato specialmente negli ultimi mesi e a coloro che, pur distanti, sono riusciti ugualmente a farmi sentire la loro vicinanza.

Ringrazio i miei genitori e mio fratello per le parole di incoraggiamento e per il supporto che mi hanno sempre offerto in questi anni e per essere riusciti sempre a farmi sentire, nonostante la lontananza, parte attiva della nostra famiglia.

Un grazie particolare a Matteo che con il suo amore e la sua pazienza ha reso speciali questi anni.